Control-oriented modeling and model-based control of a blowdown supercharged HCCI engine

July 2015

Michael Jagsch

（千葉大学審査学位論文）

Control-oriented modeling and model-based control of a blowdown supercharged HCCI engine

July 2015

Michael Jagsch

Abstract

This PhD introduces model-based design tools for design and tests of model-based closed-loop control schemes of a Blowdown Supercharge (BDSC) Homogeneous Charge Compression Ignition (HCCI) engine. It first introduces common control concepts for automotive combustion engines, after which detailed modeling, in the commercial 1-D software tool AVL BOOST, and additionally a control-oriented 0-D modeling approach with a pressure wave functionality to provide a suitable model-based platform for model-based closed-loop control tests.
For the design of advanced control concepts, a Mean-Value Engine Model (MVEM) for the BDSC HCCI engine is introduced for linearization to obtain an LTI state-space model, together with a concept of an automated parameterization scheme for the MVEM.
A framework for the design of a robust control scheme based on H-Infinity theory was presented, where the simplicity and a special feature of the MVEM was exploited for a better robustness analysis based on structured singular values (SSV).
Additionally, the potential of Sliding-Mode Control for the BDSC HCCI engine was analyzed and compared to the robust controller in simulation.
The thesis ends with an extensive literature research for switching strategies between traditional spark-ignition (SI) combustion and HCCI, and switching considerations for BDSC HCCI are given.
Additionally, the application of the previously introduced closed-loop control schemes for combustion mode switch from SI to HCCI are demonstrated in simulation.

Acknowledgement

This work was supported by AVL List GmbH in Graz, and I would like sincerely express my deepest gratitude to Dr. Gotthard Rainer, the Vice President of AVL AST. Without the generous funding from AVL, this work would not have been possible.

Aside from the financial aspect, a PhD would not have been possible without a research topic, and for that, I would like to express special appreciation to Prof. Dr. Yasuo Moriyoshi for paving the way for me during my first time in Japan in 2007 and for offering me use of his laboratories at Chiba University to complete my PhD as well as his invaluable academic input and support.
I would also like to thank the team behind the BDSC HCCI project, particularly, Dr. Junichi Takanashi of Honda for providing me detailed information on the engine and his feedback on my ideas. I would also like to thank the students at the engine lab for the great time I had, especially Kyohei Fujita, particularly, Masato Nagayoshi. I would like to thank the post-docs, especially Dr. Tsukasa Hori for the great collaboration during his time in the lab. Additionally, I would like to extend my appreciation to the staff, especially Yuuichi Sugibuchi, for patiently answering my questions and providing me the support I needed, not to mention all of the fun over the years and the ”salad-battle” that decided who got to have the last large salad at the convenience store for dinner.

Outside of the laboratory, my deepest gratitude goes to Professor Dr. Kenzo Nonami for his care and support, as well as his tremendous expertise on control engineering that he was always willing to share. I truly appreciated his supportive advice on my PhD, my career path, as well as the introduction to the Multi-Career Program that ultimately fulfilled my dream of a collaboration on HCCI control research together with Stanford University in California.
In relation to this, I would like to thank Mark Haley for having me in his program as well as the entire team of Chiba University's Multi-Career Center, Prof. Satoshi Inuoe, Prof. Satoshi Fujii, as well as Sunyoung Lim and Reiko Ohata.
On the California side, I deeply thank Oliver Miersch-Wiemers, Nikhil Ravi, and Joel Oudart for accepting me in their HCCI research team at Robert Bosch LLC in a project with Stanford University. To the entire team, I send my thanks. Aleksandar Kojic, Eric Doran, Arjun Sharma, David Cook, Nalin Chatuverdi, and Li Jiang of Michigan. I especially thank my fellow intern and project partner, Karthik Ravishankar, of the University of Michigan for the great work and the great times outside of Bosch. Together with all other Bosch members, as well the students, all of whom who provided a great source of inspiration, I truly had a great time in California! Lastly, I would also like to thank the staff and students at Stanford University.
At Chiba University, I would also like to express my deepest gratitude to Prof. Kang-Zhi Liu for sharing his profound expertise on control theory and his useful comments on my work.
Outside of my PhD research, I thank all the great people I met and great friends I made. They have brought sunshine in my life and often provided a great balance to my PhD work.
I thank Tanner Brooks for proofreading my English of this thesis and the useful advises.

I would like to thank the people who supported me during my entire career path. I deeply thank Ulrike Frey-Schlager and Erguen Yildiz for his extremely competent career advises, as

well as Dr. Amin Velji of the Institut fuer Kolbenmaschinen (Institute of Reciprocating Engines) at Karlsruhe Institute of Technology (KIT), in Karlsruhe Germany.

Last but not least, I would like to thank my aunt, Renate Preussler, for all of her support throughout the years. It was a shock for me to hear that my cousin Oliver Preussler passed away while I was in Japan and preparing for my stay in California. I will always remember his last visit in Japan and our goodbye at Nishi-Chiba Station in Japan. He won't be forgotten, and I would like to dedicate my work to him.

Widmung - Dedication

Ich widme diese Arbeit meinem Cousin Oliver Preussler, der waehrend dieser Arbeit im Januar 2012 viel zu frueh verstarb.

This work is dedicated to my cousin Oliver Preussler, who unexpectedly passed away in January 2012.

Contents

Nomenclature

CA_{50} Crank angle at which 50% of the heat during combustion has been released

$IMEP$ Indicated mean effective pressure

$PIDT_1$ Proportional-integral-derivative lag element (DT_1) output controller

340 340deg CAD - equals 20deg CAD BTDC (as index)

ABS Antilock breaking system

ANN Artificial neural networks

ARE Algebraic Riccati Equation

ATDC After top dead center

BD Blow-down - Position during exhaust after blow-down process has finished and in-cylinder pressure is equal exhaust pressure (as index)

BDC Bottom dead center - the lower position of the piston and nearest to the crankshaft

BDSC Blowdown supercharge

BIBO Bounded input, bounded output

BMEP Brake mean effective pressure (IMEP minus measured brake torque)

BTDC Before top dead center

CAD Crank angle degrees

CFD Computational fluid dynamics

CFL Courant-Friedrich-Lewy condition

Cyl Cylinder (as index)

disp displaced (as index)

ECU Electronic control unit

EGR Exhaust gas recirculation

EVC Exhaust valve closing - position at which the exhaust valve closes (in CAD)

Exh Exhaust (as index)

Exp Experiment

FDM Finite difference method

FFT Fast Fourier Transformation

FTM Fast thermal management

HCCI Homogeneous charge compression ignition

HIL Hardware-in-the-loop

HT Heat-transfer (as index)

IMC Internal model control

Int Intake (as index)

IVC Intake valve closing - position at which the intake valve closes (in CAD)

Junc Junction (as index)

LFT Linear fractional transformation

LHV Lower heating value of fuel

LNT Lean NO_x trap (catalyst)

LPV linear parameter-varying

LQ Linear quadratic

LQI Linear quadratic regulator with integral action

LQR Linear quadratic regulator

LTI Linear time-invariant

MAP Manifold absolute pressure

MBD Model-based design

mfb Mass fraction burned

MIL Model-in-the-loop

MIMO Multiple-input, multiple-output

MOC Method of characteristics

MPC Model-predictive control

MVEM Mean-value engine model

MW Molecular weight

NL Non-linear (as index)

NMEP Net mean effective pressure

NVO Negative valve overlap

ODE Ordinary differential equation

PDE Partial differential equation

PID Proportional-integral-derivative output controller

PVO Positive valve overlap

RCP Rapid control prototyping

RHS Right-hand side of an equation

RON Research octane number

RT Real-time

SACI Spark-assisted compression ignition

SCP Start of compression phase - position at which the exhaust valve closes after EGR re-breathing (in CAD)

SI Spark ignition

Sim Simulation

SISO Single-input, single-output

SMC Sliding Mode Control

SOC Start of combustion (as index)

SOI Start of injection in CAD (as index)

SSV Structured Singular Value

SVD Singular value decomposition

TDC Top dead center - the upper position of the piston and farthest from the crankshaft

TWC Three-way catalyst

VCR Variable compression ratio

Vol Volume (as index)

VVT Variable valve timing

WOT Wide open throttle

Chapter 1

Introduction

The combustion engine, invented by August Otto in Germany, and the Diesel engine by Rudolf Diesel has played a vital role for conversion of thermal energy into mechanical energy for mobility and other uses, including electrical power generation.
Especially the invention of the passenger car by Carl Benz and Gottfried Daimler (well known as Daimler-Benz) has started the era of mobility for individuals that was until now ensured by combustion engines that provided the mechanical energy.
Recent advances in electric powered cars may call traditional combustion engines into question, but they still face many challenges making it likely that combustion engines will still dominate cars within the next two decades.

It is commonly agreed that climate change is man-made and the combustion engine in automotive applications is a major source of CO_2 which necessitates the development of more fuel efficient propulsion systems.
Diesel has the advantage that it is low in fuel consumption, but this comes at the expense of emission formation, especially soot, and due to complicated aftertreatment, NO_x. In contrast, gasoline engine may have better emissions than Diesel engines, but they do not feature the fuel efficiency of a Diesel engine.
Homogeneous Charge Compression Ignition (HCCI) as an alternative to traditional combustion engine concepts has been suggested in the late 80s. Due to recent advances in engine technologies, such as variable valve systems, direct injection, and advanced control concepts, HCCI engines have been in the focus of research world-wide to combine the advantages of diesel and gasoline engines.
HCCI uses controlled knocking to initiate combustion so that a spark plug can be omitted. This relaxes the tight air to fuel requirements of common SI engines in which the amount of air must not vary too much from stoichiometric since combustion may become unstable or aftertreatment becomes ineffective. Although Diesel engines work without spark ignition too, they however utilize fuel injection into the cylinder during the compression stroke to initiate combustion. Hence, combustion phasing can be controlled via spark timing in SI engines, whilst in diesel engines, combustion phasing can be controlled by timing of fuel injection.
In HCCI engines, a mixture of fuel and air is compressed until the mixture auto-ignites and combustion sets in. Although combustion duration for each ignition pocket may be longer in HCCI engines than in SI engine, the mixture ignites practically simultaneously inside the cylinder such the apparent heat release is eventually faster. Due to this rapid combustion process,

thermodynamic advantages of HCCI combustion arise due to the closer proximity to the ideal SI cycle. Furthermore, since the mixture auto-ignites simultaneously inside the cylinder, a flame front does not exist and consequently the peak temperatures are much lower than in SI. This explains why raw emission, especially NO_x is much lower in HCCI combustion than in SI engines.
Another strength of HCCI is that a spark plug is not necessary and consequently a tight air/fuel control by the intake throttle not required. This reduces pumping losses and raises fuel efficiency at low loads remarkably.

Despite the many advantages that an HCCI engine concept may bring, some major disadvantages and challenges exist.
Firstly, due to fast combustion, high pressure rise rates lead to audible noise which may exceed acceptable levels. Such pressure rates are typically higher at high loads which set the operational upper limit of HCCI engines. At low loads on the other hand, HCCI is limited by lack of thermal energy to trigger combustion.
Thereby, a severe problem of HCCI engines is that their possible operation is confined only in a small area at low speeds and lower loads. To cover the remaining operational ranges required for an ordinary combustion engine, an HCCI engine must be able to run in ordinary SI as well. This poses another challenge, as switching between the SI and HCCI modes is due to the different operation conditions in HCCI and SI not straightforward. Thereby, a simple switch would lead to undesired behavior or abnormal combustion during the switch. For that reason, elaborate switching strategies are required.
Apart from the problems mentioned above, a basic problem of an HCCI is that they are inherently different to control due to the indirect control of combustion phasing. Further control challenges exist due to the extreme sensitivity of HCCI combustion on the in-cylinder conditions, which in turn depend on atmospheric conditions and other external disturbances, such as different quality of fuel.

In order to bring HCCI engines to the market, their advantages must first outperform other propulsion concepts, as well as stratified direct injection SI and secondly, the control issues mentioned above must be tackled.

1.1 Motivation of this work

HCCI combustion is extremely sensitive to in-cylinder conditions which vary constantly during high transient engine operation, with varying speed and load and due to external disturbances, such as atmospheric conditions, humidity, quality of the fuel, and others. This may cause abnormal combustion with premature or delayed combustion phasing, or even a misfire which may stall the engine. For increasing robustness despite disturbances, static maps do not suffice and a closed-loop controller is necessary for controlling combustion timing (e.g. [110]). Other control objectives, such as pressure rise rate reduction may be included in the control requirements as well. Furthermore, the dynamics of HCCI combustion are extremely fast and only of time-scales of a few cycles, and the control objective of combustion phasing is within around ten angle degrees ATDC very tight. Premature combustion leads to excessive audible noise, and delayed combustion to high cycle-to-cycle variations, which deteriorate the quality of combustion remarkably. Additionally, it may be desired to control several control outputs simultaneously, and due to the high sensitivity of HCCI combustion, strong cross-coupling between one control input for a different control objective to HCCI combustion exist. This is especially the case if the amount of fuel is to be varied in order to control the power output of the engine, which causes a phase shift in HCCI combustion. In such cases, to keep combustion phasing within the desired range, simultaneous control of ignition becomes necessary.
With these strict control performance requirements, and the desire of multivariable control, ordinary PID controllers may not provide satisfactory results. Furthermore, heuristically tuned PID controllers lack the possibility of model-based performance and robustness judgment before implementation into the actual engine.

This work introduces a control approach of a blow-down supercharge (BDSC) HCCI engine and analysis based on simulation with advanced control concepts. The control concepts presented in this work are a viable alternative to the control attempts of the research team of BDSC HCCI who pursued the idea of using a full 1-D simulation engine model, created in the commercial code GT-Power by Gamma Technologies Inc., as a model-based controller for control of the BDSC HCCI engine online on an ordinary ECU. As an alternative to this, a ”model-based design” approach in which PI controllers are tuned manually on the 1-D simulation model before implementation was proposed by a research team-member who was in charge of the control design of the BDSC HCCI engine.
However, as for the latter solution, drawbacks for control performance analysis were already mentioned, and the fact that a 1-D simulation software runs slow means this solution has rather limited value. Furthermore, for the first approach additional questions remain unanswered:

1. How can a complex simulation model be used as a controller? In other words, is it possible to invert the model, such that control inputs can be calculated from desired outputs? Alternatively, would it be possible to run the model online in an optimization loop, such that inversion of the model can be omitted, and control inputs optimized online such that a desired trajectory of the engine transients is tracked?

2. Is the model computationally cheap enough, or can its performance be optimized, such that it can compute at least as fast as in real-time, or preferably faster than that to save computation resources, and additionally be implemented on a production ECU?

To date, 1-D simulation codes have been limited primarily to engine design and performance analysis, and their use in control design are still very limited. This is due to the fact that such simulation models commonly run multiple times slower than real-time, so that control design and testing becomes tedious. Furthermore, many modeling details common in 1-D models are not required in control engineering (such as pipe junction angles), so that simplified control-oriented models with fair accuracy and low complexity are preferred. This leads to so-called mean-value engine models (MVEM, e.g. [49]), or 0-D modeling approaches for real-time simulation (e.g. [112]), which resemble 1-D codes, with the difference that pressure wave action is not simulated, and intake and exhaust manifolds are lumped into large volumes ("filling and emptying method" [52]).
However, for a BDSC HCCI engine, in which pressure wave action play a pivotal role, traditional 0-D engine modeling approaches would fail here and other approaches must be found.

This work introduces a novel approach for 0-D simulation of a combustion engine with pressure waves, which is derived from a standard 0-D model, and augmented by a pressure wave functionality. In order to ensure consistency of the model, a novel correction procedure by coupling typical 0-D modeling approaches with a 1-D approach is introduced. The model has been adjusted such that it has the potential to run in real-time and is therefore a promising candidate for control design and hardware-in-the-loop (HIL) applications. Since the model was only used for a particular purpose on a particular HCCI engine, this concept may be extended for simulating intake pressure wave actions.
In order to design advanced controllers, control-oriented models that can be linearized for control design are necessary. For this purpose, a simplified mean-value modeling approach is introduced which has been reduced to only four states for a cylinder the exhaust manifold to represent the entire engine together. This model helps for a quick assessment of controllers since it runs faster than real-time and since a linear state-space model can be derived from it. This model can be utilized for design of advanced controllers, such as state control, or robust control. As an additional feature, the model states were chosen such that almost all states are measurable and an observer for state controller could be omitted.
Several control concepts are introduced and compared. Since state-controllers based on LQ optimization or pole-placement algorithms have been reported already in other researches, the feasibility and advantages of a sliding-mode controller (SMC) for HCCI and a robust μ controller based on H_∞ theory are analyzed and compared. The latter has been designed by estimation of structured uncertainties of the HCCI engine and implemented in the control design.
All controllers were tested on the 0-D simulation model, and in order to demonstrate the validity of the suggested control-design approaches, an SMC controller was implemented and tested on a 1-D engine model built on on the commercial software BOOST by the Austrian company AVL List GmbH.
Switching from SI to HCCI is introduced and discussed at the end of this work, and considerations for the combustion mode switch from SI to HCCI are discussed by analyzing an HCCI ignition correlation, and conclusions demonstrated in simulation with the AVL BOOST engine model. Since the switch from SI to HCCI is highly sensitive to changing conditions, the application of closed-loop control for combustion phasing during the switch is presented. Since the switching process is highly dynamic, a closed-loop controller would increase the robustness of the switch greatly and reduce calibration efforts.

Chapter 2

Introduction to HCCI engines

Homogeneous Charge Compression Ignition (HCCI) combustion was first reported in a publication by [109] and firstly termed HCCI in [101], and research in the recent years has shown dramatic interest in HCCI engines to overcome fuel consumption and emission problems (e.g. [1]). HCCI works without a spark plug, and combustion is initiated by controlled auto-ignition, so that tight air/fuel conditions for stable SI combustion can be relaxed and pumping losses due to the throttled intake minimized. This is considered as one of the major reasons for the lower fuel-consumption of HCCI, in comparison to traditional SI engines. Since the mixture is homogeneously distributed inside the cylinder before ignition, combustion occurs simultaneously throughout the entire cylinder and no flame-front from the ignition point exists. Hence although combustion process may be slower than in SI engines, due to the simultaneous fuel ignition however, the apparent heat-release is faster than in SI engines which brings the combustion process closer to the ideal cycle. This is another reason for higher efficiency of HCCI combustion. However, a negative side-effect of this fast combustion process is that pressure rise is very steep, causing high audible noise. In order to overcome this, the cylinder charge contains high amount of dilution, fresh air, as well as EGR, which helps limiting the pressure rise rate during combustion. Although EGR has higher heat-capacity than fresh air, helping to reduce the pressure rise rate and peak temperatures even more, and external EGR is a common strategy for SI engines to reduce NO_x emissions, its amount is limited by the air necessary to burn all fuel inside the cylinder. A common strategy for HCCI is therefore ensuring lean mixture with high levels of EGR for the cylinder charge.
This high dilution, together with the missing flame-front additionally helps to keep peak temperature levels low and to minimize NO_x as raw-emissions.
Although this high dilution and missing spark as a combustion initiator resembles very much common Diesel engines, the crucial difference is that in HCCI, a homogeneous mixture of air and fuel is compressed until ignition, instead of compressing air only until fuel injection for combustion initiation.
Hence, unlike SI engines, where a spark plug serves as an ignition actuator, and Diesel engines, where combustion sets in roughly at the time when fuel is injected, ignition cannot be controlled directly in HCCI engines. Instead, proper in-cylinder conditions during the compression stroke must be identified to ensure ignition at a thermodynamically reasonable ignition timing. It is commonly agreed that the ignition is a chemically driven process due to the pre-reactions that already occur during compression.
It is therefore obvious that the process during compression must be understood and control

strategies found to ensure stable HCCI combustion. In general, ignition needs enough energy to occur and it is thereby clear that the in-cylinder temperatures must be maintained at a certain range to ensure ignition. In order to control the temperature, the energy from a previous cycle is recycled by maintaining some of the hot exhaust gases inside the cylinder for the next cycle. Thereby, by regulating the amount of internal EGR, combustion phasing can be controlled.
To control internal EGR for HCCI, two major engine concept exits, which are:

- Negative Valve Overlap (NVO) HCCI
- Re-breathing HCCI

In NVO HCCI, the exhaust valve closes early before TDC to retain some of the exhaust gas for the next cycle, while the re-breathing strategy re-opens the exhaust valve during the intake stroke, such that besides fresh air from the intake, hot exhaust gas from the exhaust is breathed in.
Both HCCI concepts will be introduced more in detail in the following sections.

Besides the difficulty of controllability of HCCI engines due to the indirect combustion initiation, another critical shortcoming affects the nature of HCCI engines, which is that their operational ranges are only limited to low loads and low speeds.
While the speed constraints stem from gas-exchange dynamics, and fuel ignition delay limitation, the high load HCCI is bounded by too high pressure rise rates during combustion due to high amount of fuel and low dilution, and the lower HCCI bound is set by the insufficient thermal energy to ignite the fuel.
Due to the operational limit of HCCI, an HCCI-capable engine must be able to run in traditional SI in tandem, such that SI combustion is set when necessary, and HCCI operation when possible. For that reason, switching strategies between both combustion modes are crucial for mass-production of HCCI engines.

2.1 Negative Valve Overlap (NVO) HCCI

Negative valve overlap (NVO) HCCI retains hot exhaust gas by closing the exhaust valve early. Part of the exhaust gas is then trapped, and in order to avoid exhaust gas to be pushed out into the intake port. The intake valve opens late and symmetrical to the exhaust valve-closing event to avoid pumping losses stemming from the higher in-cylinder pressure from the intermediate compression between exhaust and intake.
This phase between the two breathing strokes is called re-compression and can be seen in the figure below 2.1.
In this figure, combustion occurs at TDC around 720 degrees and two re-compression peaks before and after combustion can be seen at around 360 degrees and 1080 for the next cycle. By inspecting this figure, it can be seen that during re-compression, pressure levels exceed 10 bar, but due to pure compression expansion, energy losses are rather low.
NVO HCCI is the most common HCCI concept, since control is more straightforward, with control actuators that already exist due to recent down-sizing technology trends of combustion engines.
These are besides turbocharging, cam phasing (VVT), and direct fuel injection technologies.

Cam phasers help regulate the EGR content, while direct injection can control combustion phasing due to the cooling effect of the evaporation of the fuel and pre-reactions that occur during re-compression.

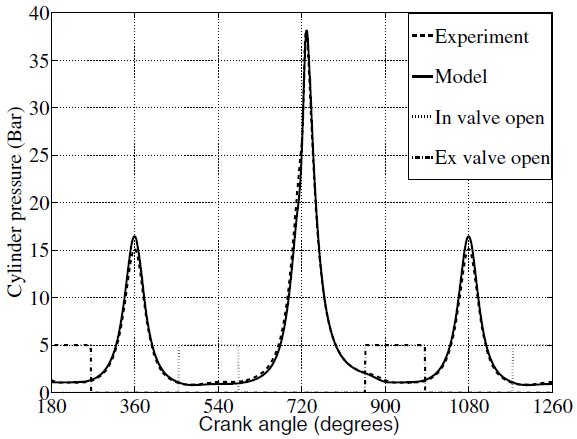

Figure 2.1: Pressure traces of an NVO HCCI engine with re-compression (from [118])

2.2 depicts typical valve lifts for the intake, exhaust for SI with high valve lifts and positive valve overlap, and NVO HCCI with a lower lift and the negative valve overlap.

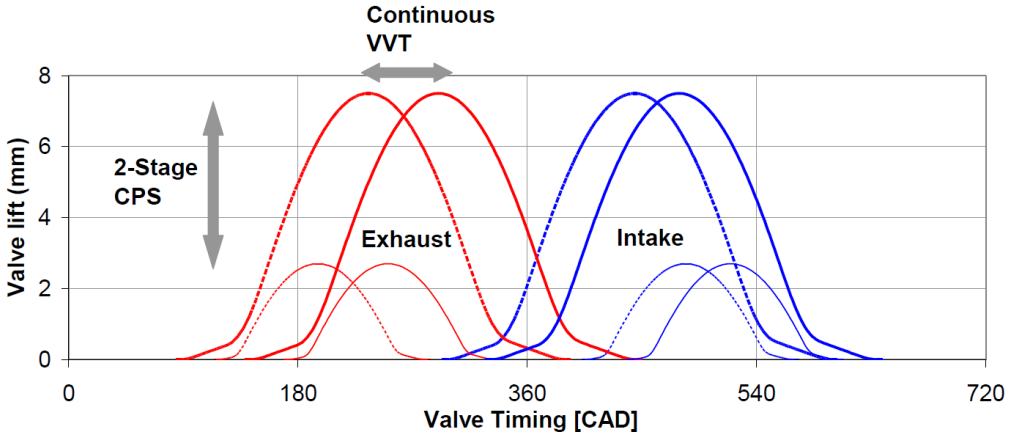

Figure 2.2: Typical Valve lifts of NVO HCCI (from [43])

Since fuel evaporates when injected into the cylinder, it cools the charge and can delay HCCI combustion. However, for NVO HCCI another powerful control actuation of direct injection for combustion phasing exist if the fuel is injected during re-compression phase. The underlying effect is that fuel already decomposes and breaks into smaller molecule chains during re-compression phase due to the higher pressures and temperatures inside the cylinder, denoted as pyrolisis. This effect even has been reported to dominate over the competing effect of evaporation and and combustion advance and retard is both possible with injection timing during re-compression. This is more in detail introduced in [95, 95] and a model-based control approach is presented.

2.2 Re-breathing HCCI

Re-compression HCCI has been presented as a different variant of HCCI. Unlike NVO systems, the valve timing is commonly not varied to control the EGR content. Intake and exhaust valve lifts are similar to SI engines, and the exhaust valve re-opens during intake stroke to re-breathe exhaust gas from the exhaust port. EGR then is typically controlled by varying the re-breathing valve lift, which complicates the HCCI operation, and may explain the popularity of NVO HCCI.
Typical re-breathing HCCI valve-lifts are shown in the following figure 2.3:

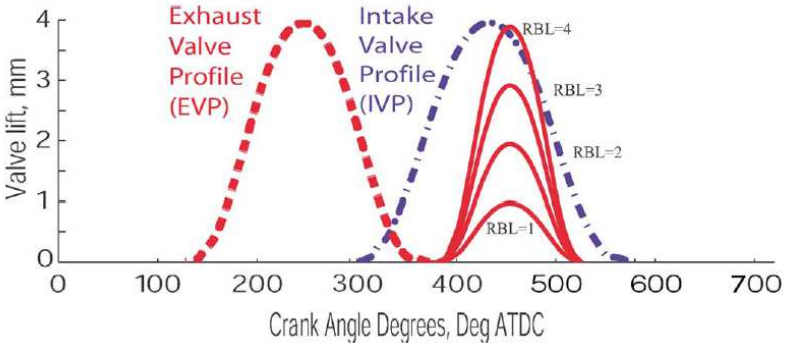

Figure 2.3: Valve Lifts for Exhaust and Intake of a re-breathing HCCI engine (from [23])

In this depiction, the exhaust valve is shown in red and the intake valve shown in blue. It can be seen that, unlike NVO HCCI, a positive valve overlap exists. During the intake stroke, while the piston is moving downward, the exhaust valve opens again to intake some of the exhaust gas from the exhaust port. In this figure, it can be seen that this is roughly between 400 and 500 deg ATDC and that the exhaust valve closes before the intake valve closes. Additionally, four different valve lifts for the re-breathing stroke for regulating the amount of exhaust gas can be seen.

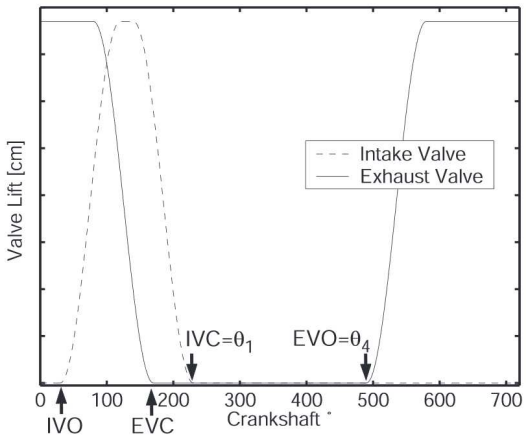

Figure 2.4: Valve Lifts for Exhaust and Intake of a re-breathing HCCI engine where exhaust valve remains open during beginning of intake stroke (from [113])

As an alternative to opening the exhaust valve twice, [113] has demonstrated a re-breathing

strategy, where the exhaust valve remains open longer and closes long after TDC during the intake stroke. This is depicted in figure 2.4, where the late closing of the exhaust valve can be seen to re-breath exhaust gas. Although this research has been done on a fully-flexible valve actuation system, such systems are not common in production engines, and this strategy might be difficult to implement.
Advantages of re-breathing HCCIs are that they can be extended to higher loads due to heat losses in exhaust ports, and better mixing of air/fuel mixture with exhaust gases.

2.3 Blow-Down Supercharge HCCI engine

Blow-Down Supercharge (BDSC) HCCI may be classified as a re-breathing strategy since in this HCCI variant, the exhaust valve re-opens to let hot exhaust gases in, and this concept was first reported in [45]. However, contrary to ordinary re-breathing HCCI, the exhaust valve re-opens after the intake stroke and closes when a blow-down pressure wave from an interconnected cylinder arrives at the valve. This second cylinder is connected via an exhaust pipe, and the blow-down pressure wave is generated during the early stage of exhaust when the in-cylinder pressure is higher than the exhaust pressure. This higher pressure blows exhaust gas out of the cylinder until the cylinder pressure reaches the exhaust pressure levels. After that, the exhaust gas is mainly pushed out by the upward movement of the piston. During the blow-down stage, a pressure wave is generated at the exhaust manifold and it travels at the speed of sound along the pipe.

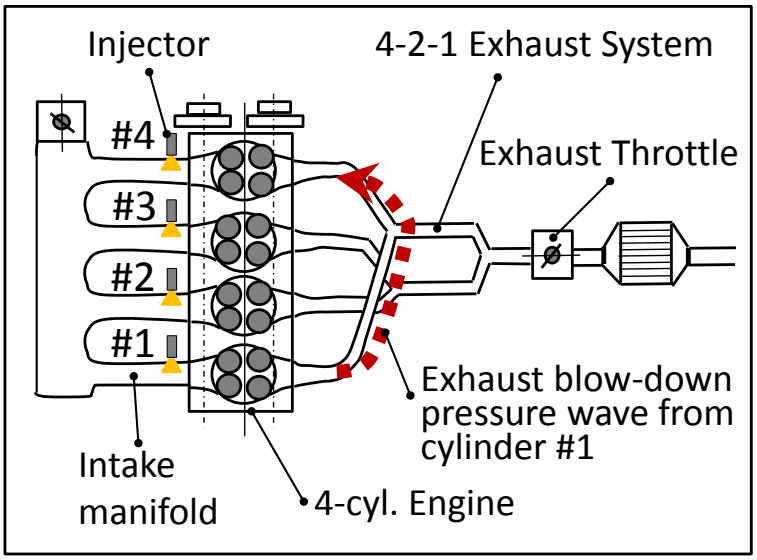

Figure 2.5: Schematic of the blow-down pressure wave system of a 4-cylinder BDSC HCCI engine

The concept of BDSC utilizes a 4-2-1 exhaust manifold, in which two pipes from two cylinders merge to one pipe, and merges with another one from the other two cylinders of a four-cylinder engine. This configuration connects two cylinders with a junction between them, which combines the two pipes. In such a configuration, a blow-down pressure wave would not only leave the exhaust into the atmosphere but also could reach the connected cylinder. This is depicted in the figure 2.5 above.
In this figure, a four cylinder engine can be seen, where the intake port is shown to the left with port fuel injector for each cylinder, and a 4-2-1 exhaust manifold to the right with an exhaust throttle for regulating the pressure levels in the exhaust. It can be seen in this schematic how the 4-2-1 exhaust manifold connects two cylinders, such that blow-down pressure waves can propagate in this figure from cylinder #1 to cylinder #4.
The underlying idea behind BDSC is to utilize this pressure wave for increasing the amount of EGR inside the cylinder. This is accomplished by designing the re-breathing lift such that it closes just when the blow-down from another cylinder arrives. Thereby additional EGR can be pushed into the cylinder, and since re-breathing happens after the intake, the volumetric efficiency is hardly affected.

The following figure 2.6 shows a schematic of the valve lifts for the intake- and exhaust valves for two cylinders, and the pressure wave, traveling from one cylinder to the other:

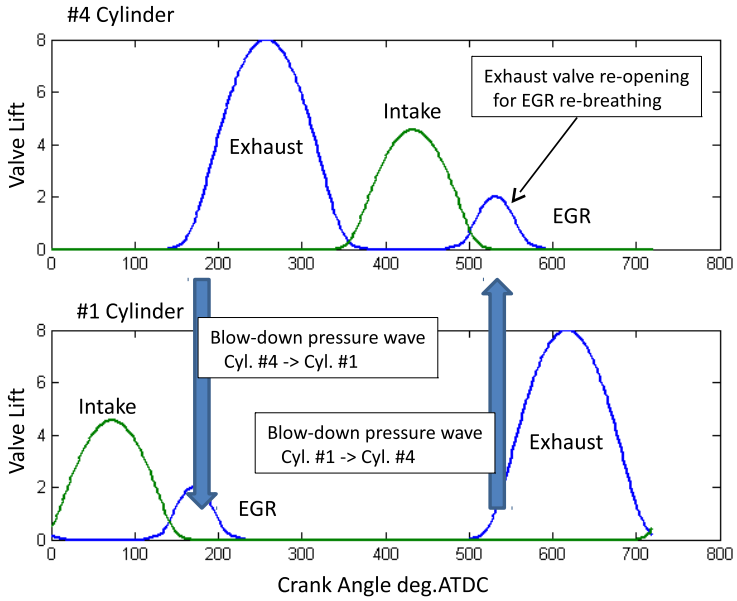

Figure 2.6: Valve lift concept of BDSC HCCI for two cylinders, where intercoupling via the blow-down pressure wave is depicted

Since the re-breathing event happens after the intake stroke when the piston is moving up toward top-dead center, the exhaust pressure must be elevated to prevent mixture inside the cylinder from escaping to the exhaust manifold. For that reason, a throttle in the exhaust manifold is required to increase the exhaust pressure. This throttle also provides a powerful control actuator, since with higher exhaust pressure, more EGR is re-introduced into the cylinder which increases the temperature and consequently advances ignition timing. Opposite to that, the combustion phasing can be retarded by decreasing the exhaust pressure.
However, although this control actuation may be a powerful control input for controlling combustion phasing of a BDSC HCCI engine, it cannot be used for individual cylinder control.
As introduced above, direct fuel injection can be used in NVO systems to control combustion phasing by varying the injection timing during re-compression. In BDSC HCCI however, re-compression does not exist, and evaporation of the fuel cools the mixture such that more exhaust pressure is needed to keep combustion phasing in a desired range. For that reason, only port fuel injection is considered with BDSC HCCI.
As an alternative control actuation, the secondary air injection has been proposed for controlling combustion phasing in each individual cylinder [9], which is shown in the following figure.

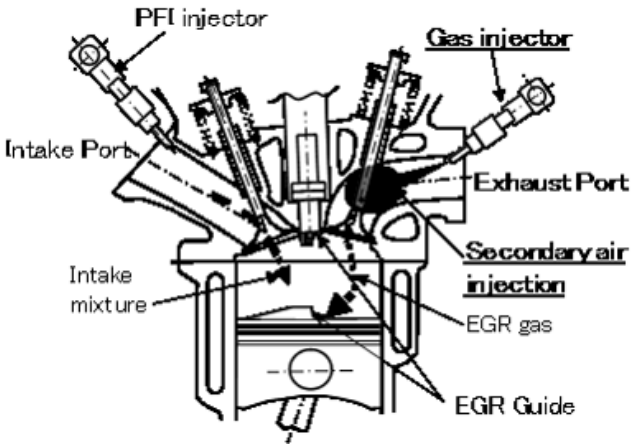

Figure 2.7: Schematic of the Secondary Air Injector

Such systems are common in SI combustion engines and operated during start-up when the engine is cold and more fuel must be injected to ensure stable combustion. This on the other hand leads increased emissions where injection of air in the exhaust port allows for oxidation of partially burned fuel fractions and a faster heating up of the catalyst. After the engine has reached its operating temperature and the engine operated in stoichiometric mode, secondary air is usually switched off [105].
As of BDSC HCCI, this injector injects compressed cooled air directly into the cylinder during the re-breathing phase so that the mixture can be cooled and combustion delayed.
Unlike ordinary secondary air systems of SI combustion engines, the injector must work continuously in BDSC HCCI, which requires energy due to the pump that is required for compressing the air for injection.

Chapter 3

Fundamentals of Control Theory

This chapter gives an introduction into control theory which was used and is therefore necessary for this work.
It starts with linear systems, where fundamental properties and notations are introduced.
It continues with linear control concept, of which the most important ones in automotive control namely simple output control (e.g. PID), and MIMO controllers are explained. The latter ones are mainly state controllers which receive the states of a system as a control input instead of the outputs, which gives great flexibility in control design (e.g. pole placement). MIMO controllers are often also designed in a robust control framework, which mainly comprises controllers based on H_2 and H_∞ optimization techniques. One of the advantages of one of these control approaches is that they already include an observer in the controller structure by definition. Further, design of robust controllers may also include robustness analysis in order to judge the controller performance already during control design instead of during the testing phase. Although the underlying math behind the robust theory maybe a hard one, common design tools, such as the Robust Control ToolBox by Mathworks are nowadays widely available.
As a non-linear control concept, the sliding-mode control has been reported as a suitable control strategy for automotive applications. Its advantages are mainly the simple control design, as well as the robust control performance due to a non-linear switching term included in the control algorithm, which may under certain circumstances cancel out any possible unmodeled dynamics or disturbances.

3.1 Signals and Systems

3.1.1 Norms of Signals and Systems

As defined in [67], a norm of a signal $u(t)$ must fulfill the following criteria:

(i) $\| u \| \geq 0$

(ii) $\| u \| = 0 \Leftrightarrow u(t) = 0 \, \forall \, t$

(iii) $\| au \| = \| a \| \| u \| \;\; \forall a \in R$

(iv) $\| a + u \| = \| a \| + \| u \|$

The first two properties are self-explaining, the latter two clearly require linearity properties of the norm-operator.
The 1-norm of a signal $u(t)$ is defined as:

$$\|u\|_1 = \int_{-\infty}^{\infty} \mid u(t) \mid dt \tag{3.1}$$

Equivalently, the 2-norm of a signal $u(t)$ is:

$$\|u\|_2 = \sqrt{\int_{-\infty}^{\infty} u(t)^2 dt} \tag{3.2}$$

It is evident here that this norm can be considered as the square-root of the energy of a signal.
In control-engineering, the ∞-norm is of special interest, which is defined as:

$$\|u\|_\infty = \sup_t \left[\int_{-\infty}^{\infty} u(t) dt \right] \tag{3.3}$$

Where sup denotes the supremum of of the signal norm over all times.

As with signals, the norm of a linear system can be defined accordingly.
Suppose, the output $y(t)$ of a linear system with a given input signal $u(t)$ can be described by the convolution integral:

$$y(t) = \int_{-\infty}^{\infty} g(t-\tau) u(\tau) d\tau \tag{3.4}$$

then the Laplace-transformed is:

$$Y(s) = G(s) \cdot U(s) \tag{3.5}$$

Here, it is of interest how much a linear system $G(s)$ can "amplify" a signal $u(t)$.
For that reason, the following norms of the transfer functions are defined:

2-Norm:

$$\|G\|_2 = \sqrt{\int_{-\infty}^{\infty} G(j\omega)^2 d\omega} \tag{3.6}$$

and the Infinity-Norm:

$$\|G\|_\infty = \sup_\omega \left[\int_{-\infty}^{\infty} G(j\omega) d\omega \right] \tag{3.7}$$

Note that the norms here are evaluated in the frequency domain instead of the time domain. The infinity norm is of interest in control engineering, since it represents the maximum peak of the bode magnitude and one can thereby judge the stability of a system. This analysis may give sufficient criteria for stability of SISO systems which are commonly analyzed by the so-called Nyquist theorem (e.g. [81]). A peak value of the norm of a system smaller than unity would never cross the critical point $(-1 + j0)$ in the complex plane and the closed-loop system may therefore be judged as stable.

Furthermore, the condition number as a numerical analysis tool is often used in control design. A plant with a high condition number is denoted as ill-conditioned and may cause control problems and are therefore inherently difficult to control. The euclidean condition number of a plant G is defined as:

$$\gamma(G(j\omega)) = \frac{\bar{\sigma}(G(j\omega))}{\underline{\sigma}(G(j\omega))} \tag{3.8}$$

where $\underline{\sigma}$ and $\bar{\sigma}$ denote the maximum and minimum singular values as:

$$\underline{\sigma} = \underset{u\neq 0}{min}\frac{\parallel Gu \parallel_2}{\parallel u \parallel_2} \qquad and \qquad \bar{\sigma} = \underset{u\neq 0}{max}\frac{\parallel Gu \parallel_2}{\parallel u \parallel_2} \tag{3.9}$$

Hence, a high condition number means that signals in one input direction are stronger amplified than signals into another direction. This requires that high gains of the feedback control need to compensate for the plant's deficit in one direction which may not give the desired performance especially in presence of plant uncertainties and unknown dynamics. Hence, efforts in pushing an ill-conditioned system into a low-gain direction may eventually be misaligned into the high-gain directions, causing unwanted transients. Hence, ill-conditioned plants may indicate control problems and are for such reasons considered difficult to handle.

A further introduction into singular values is provided in the following section.

3.1.2 Singular Value Decomposition (SVD) & Singular Values

Singular value decomposition (SVD) of matrices and singular values have been emerged as an important tool for control design and analysis and an example was already indicated in the previous section. They give a better measure for the gains of a MIMO system, than eigenvalues. To begin with, the following lemma states that any complex matrix Q can be decomposed by SVD ([89]):

Lemma 1. *Any complex matrix Q of dimensions mxp, there exists an unitary matrix Y of dimension mxm, a pxp matrix U and a real matrix Σ, such that the following condition holds:*

$$Q = Y \begin{pmatrix} \Sigma & 0 \\ 0 & 0 \end{pmatrix} U^* \tag{3.10}$$

with

$$\Sigma = diag(\sigma_1, \sigma_2, ..., \sigma_r) \tag{3.11}$$

and

$$\sigma_1 \geq \sigma_2 \geq ... \geq \sigma_r \geq 0 \tag{3.12}$$

and $min(m, p) \geq r$, and $\sigma_{r+1} = ... = \sigma_p = 0$.
If Q is a real matrix, Y and U are orthogonal.

Due to the orthogonal properties of matrices Y and U, they form the orthogonal input and output space of matrix Q. The singular values are the positive square roots of the eigenvalues of Q^*Q as:

$$\sigma_i = \sqrt{\lambda_i(Q^*Q))} \tag{3.13}$$

Here, the term Q^* is the complex conjugate of the matrix Q.
Expression 3.10 is denoted as a singular value decomposition (SVD) and 3.12 are singular values. Thereby, the following definition holds:

$$\begin{aligned} \sigma(Q) &= \{\sigma_i : i = 1, ..., p\} \\ \bar{\sigma}(Q) &= \sigma_1 \\ \underline{\sigma}(Q) &= \sigma_p \end{aligned} \tag{3.14}$$

Similar as in equation 3.9 the following identities hold for the maximum and minimum singular value of a matrix:

$$\begin{aligned} \bar{\sigma}(Q) &= \underset{\|u\|_2=1}{max} \parallel Qu \parallel \\ \underline{\sigma}(Q) &= \underset{\|u\|_2=1}{min} \parallel Qu \parallel \end{aligned} \tag{3.15}$$

Singular values play an important role in control stability and robustness analysis, where the minimum singular value and especially the maximum singular value are important. Unlike the eigenvalue decomposition, the SVD gives a better information about the plant gains, and the directions are orthogonal. In fact, eigenvalues might be misleading when analyzing the gain of a system and the true gains only coincide with the eigenvalues if the input-vector is in the same direction as the eigenvector [116].
Hence, the maximum and minimum singular values of a matrix Q are the maximum and the minimum gain of the matrix Q.

3.1.3 Linear Dynamical Systems

A dynamic model of the plant is commonly given as a non-linear relation of the inputs into the system u, to the variables of the system, commonly referred to as states x, and to the outputs of the system, y. The outputs are a combination of the states and the inputs and are commonly measurable, while states are often not detectable but characterize the transients of a system.
A common formulation of a non-linear system reads like:

$$\begin{aligned} \dot{x} &= f(x, u) \\ y &= h(x, u) \end{aligned} \tag{3.16}$$

The first equation maps the evolution of the states $\dot{x}$ to the current states x and control inputs u. These states describe the system entirely and their dynamics, but they are often not measurable.
The second equation describes the outputs depending on the current states and inputs into the system. As can be seen, these are rather a static mapping from the states and inputs to the measured outputs, while the state-equation involves the history of the states and inputs for each current state evolution.

As an illustrative example, one may think of the ideal gas equations where the pressure is commonly measured, but not the mass inside a volume. In a simplified version by assuming constant temperature, the conservation of mass-law provides hereby the system dynamics.
Well-understood control theory requires in most cases a linear representation of a plant. This can be achieved by analytical approaches by identifying the non-linear part of a system and replacing it by a linear term. As in the example above, by setting the temperature of the ideal gas equation constant (and assuming that the volume is constant as well), then the pressure depends only on the mass inside the volume as introduced before. If the mass flows are approximated by linear equations too, then a non-linear representation of the system has been obtained.
In most cases however, it is advisable to linearize a plant by means of Taylor series around a steady-state operating point at a given input u_0 and a resulting steady-state state x_0.
Hence, a linear approximation of a non-linear plant is then obtained by:

$$\begin{aligned} A &= \tfrac{\partial}{\partial x} f(x,u)\big|_{x_0,u_0} \quad B = \tfrac{\partial}{\partial u} f(x,u)\big|_{x_0,u_0} \\ C &= \tfrac{\partial}{\partial x} h(x,u)\big|_{x_0,u_0} \quad D = \tfrac{\partial}{\partial u} h(x,u)\big|_{x_0,u_0} \end{aligned} \tag{3.17}$$

The resulting system is considered as a linear time-invariant (LTI) system, since the obtained matrices form a linear combination of the state- and input vectors and do not vary with time. The resulting equations of the linearized system are:

$$\begin{aligned} \dot{x}(t) &= Ax(t) + Bu(t) \\ y(t) &= Cx(t) + Du(t) \end{aligned} \tag{3.18}$$

As an alternative to state-space description of systems, SISO (single-input single-output) system can be conveniently represented as a complex transfer function:

$$G(s) = \frac{Y(s)}{U(s)} \tag{3.19}$$

with $Y(s)$ and $U(s)$ as the Laplace transformed input and output vectors. Hence, the input-output relation is given by:

$$Y(s) = G(s)U(s) \tag{3.20}$$

This transfer function can be derived by a given differential equation of a linear system in the time-domain as:

$$a_n \frac{d^n y}{dt^n} + ... + a_1 \frac{dy}{dt} + a_0 y(t) = b_q \frac{d^q u}{dt^n} + ... + b_1 \frac{du}{dt} + b_0 u(t) \tag{3.21}$$

with $u(t)$ as system inputs, $y(t)$ as the outputs and a_x ($x \in 1, ..., q$) and b_y ($y \in 1, ..., q$).
Laplace transformation of equation 3.21 gives the transfer function:

$$G(s) = \frac{b_q s^q + b_{q-1} s^{q-1} + ... + b_1 s + b_0}{a_n s^n + a_{n-1} s^{n-1} + ... + a_1 s + a_0} \tag{3.22}$$

Note that for a given system 3.22 the following criterion must hold, in order to ensure causality of a system:

$$n \geq q \tag{3.23}$$

A system 3.22 which fulfills equation 3.23 is called proper.
Moreover, a system 3.22 that fulfills the following inequality (3.24):

$$n > q \tag{3.24}$$

is called strictly proper.

It is easy to show the relationship between the linear state space system 3.18 and the transfer function 3.20 is:

$$G(s) = C\left(sI - A\right)^{-1} B + D \tag{3.25}$$

In case of a MIMO (multiple-input multiple-output) system, the transfer function may be condensed in a single transfer matrix, as:

$$G(s) = \begin{pmatrix} G_{1,1}(s) & G_{1,2}(s) & \cdots & G_{1,n}(s) \\ G_{2,1}(s) & G_{2,2}(s) & \cdots & G_{2,n}(s) \\ \vdots & \vdots & \ddots & \vdots \\ G_{m,1}(s) & G_{m,2}(s) & \cdots & G_{m,n}(s) \end{pmatrix} \tag{3.26}$$

The diagonal elements are the direct mappings of the inputs to their respective outputs, and the other elements describe the dynamic cross-coupling between the inputs and outputs.

3.1.4 Stability of linear systems

One fundamental property of a dynamic system besides its dynamics is its stability. It is obvious that the designer wants to avoid any instability of a system, and it is well-known that an unstable system can be stabilized by proper closed-loop control design. In some cases it is even desired to design a system purposely unstable to facilitate special dynamic properties. A closed-loop controller becomes then indispensable to stabilize the system. The design of a jet-fighter might be taken here as an example, where the aeroengine is located in the back of the plane which allows for swift maneuvers, but obviously destabilizes the plane since the engine pushes the plane from behind and may lead to uncontrolled movements. Here, closed-loop control is necessary to ensure safe operation of such an aircraft. Despite significant improvements of dynamic systems that can be achieved by proper control design, a stable system can conversely be made unstable by poor feedback control and the control engineer needs tools and criteria to judge the closed-loop stability properties of a system.
To proceed with this matter, a definition for stability of a system is first required, which is described by the following definition:

Definition 1 (Stability, Asymptotic Stability)**.** *A homogeneous system 3.18 with* $u(t) = 0 \; \forall \; t > 0$ *is said to be stable if for every initial state* x_0 *the states tend to the origin* $x = 0$ *and remain in a vicinity* $\epsilon > 0$ *for* $t \to \infty$

$$\lim_{t \to \infty} \mid x(t) \mid \leq \epsilon \tag{3.27}$$

Moreover, it is said to be asymptotic stable if 3.28 is fulfilled.

$$\lim_{t\to\infty} x(t) = \mathbf{0} \tag{3.28}$$

Furthermore, exponential stability can be defined if the motion of the states x towards the origin **0** follows an exponential law, e.g. the analytic solution of a homogeneous system 3.18 with $u(t) = 0 \; \forall \; t > 0$ is an exponential function.

In order to analyze a given system, by its state-space description, the following theorem holds:

Theorem 1. *The system 3.18 is stable if, and only if, the eigenvalues of the system-matrix A lie in the left side of the complex plane, i.e. the real-value of all eigenvalues are negative:*

$$Re\{\lambda_i(A)\} < 0 \quad (i = 1, 2..., n) \tag{3.29}$$

A system matrix A with such properties is called stable or Hurwitz.

This stability criterion is useful if the state-space representation of a system is given. This in many cases true for MIMO system.
In case of a system descried by a linear and dynamical transfer function, the following theorem is relevant:

Theorem 2. *A system described by a linear and dynamic transfer function $G(s)$ 3.24 is stable if, and only if, the roots of the characteristic equations of denominator are located on the right side of the complex plane, i.e. the real-value of all poles of the transfer function $G(s)$ are positive.*

These theorems assume a homogeneous system with no system inputs, i.e. $u = 0$. The following theorem gives a statement of a system that is stable and has a system input, other than 0 ($u \neq 0$):

Theorem 3. *The system 3.18 is said to be BIBO (bounded inputs, bounded outputs) stable, if the outputs are bounded with bounded inputs. For a given constant input u_0 the output tends then to an infinite constant y_∞, such that*

$$Y_\infty = G(0)U_0 \tag{3.30}$$

where $G(s = 0)$ is a transfer function realization of the state-space system 3.18.

The next theorem states that if a system is asymptotically stable, then it is also BIBO stable ([81]).

Definition 2. *A linear system is said to be bounded-input bounded-output stable if for a given state near the origin*

$$x_0 = 0 \tag{3.31}$$

and a limited input signal

$$\mid u(t) \mid < u_{max} \; \forall \; t > 0 \tag{3.32}$$

the output signal stays in a bounded region for all times:

$$\mid y(t) \mid < y_{max} \; \forall \; t > 0 \tag{3.33}$$

The following corollary gives a criteria for BIBO stability in time-domain:

Corollary 1. *A linear is BIBO stable if for the function $g(t)$ the following inequality applies:*

$$\int_0^\infty \mid g(t) \mid dt < \infty \tag{3.34}$$

Equivalently, the next corollary gives a criteria for BIBO stability of transfer functions in the Laplace domain:

Corollary 2. *A linear is BIBO stable if for the poles of the transfer function $G(s)$ the following inequality applies:*

$$Re\{s_i\} < 0 \; (i = 1, 2, ..., n) \tag{3.35}$$

This corollary gives a trivial conclusion, which is given in the next corollary:

Corollary 3. *A linear system that is asymptotically stable is also BIBO stable.*

3.1.5 Controllability and Observability

State controllers need the states of a system as a feedback signal at all times. However, in most cases the states are not measurable and must be computed online with an observer. A common observer is the Luenberger Observer, which has a similar structure as the linear state-space system but it additionally includes a correction term which computes the error between the measured system outputs y and the simulated system outputs $\hat{y}$. Similar to the Luenberger Observer is the Kalman Filter that has been commonly used as a state estimator for feedback control, and the basic difference is that the correction gain is derived from noise estimations of the feedback signal, while the Luenberger only ensures stability of the observer error $y - \hat{y}$ and convergences to zero.

Although a state-space model of the system may be available, it is not guaranteed that the states can be tracked and a state estimator utilized. In order to analyze the observability of the states of a system, analysis tools need to be derived.

Furthermore, by employing a state-controller, controllability of the states must be ensured also. Namely, it must be guaranteed that all states can be driven to any desired location at a desired time.

The following definition describes the controllability:

Definition 3 (Controllability)**.** *A linear and dynamic system is said to be completely controllable, if all states can be transferred from any initial location x_0 to any arbitrary location x_e in finite time t_e and by the choice of appropriate input signals $u_{[0,t_e]}$.*

$$S_S = \begin{pmatrix} B & AB & A^2B & \dots & A^{n-1}B \end{pmatrix} \tag{3.36}$$

It can be shown that this matrix has the dimensions $n, n \cdot m$.

Proposition 1 (Controllability according to Kalman)**.** *Given a state-space system, with the matrix pair (A,B), it is completely observable, if the controllability matrix S_S has full rank:*

$$RankS_S = n \tag{3.37}$$

It can be shown that this is a necessary criterion [82].

The following definition is for observability:

Definition 4 (Observability)**.** *A linear and dynamic system is said to be observable if the initial states x_0 at time $t_0 = 0$ can be reconstructed by the information of the inputs $u[0, t_0]$ and the outpus $y[0, t_0]$ within a finite interval $[0, t_e]$.*

The observability of a linear system can be analyzed by the Kalman criterion ([82]). According to this criterion,the observability matrix S_B needs to be defined:

$$S_B = \begin{pmatrix} C \\ CA \\ CA^2 \\ \vdots \\ CA^{n-1} \end{pmatrix} \tag{3.38}$$

It is easy to show that this matrix has the dimensions $(r \cdot n \times n)$.
The following preposition gives a statement about the observability:

Proposition 2 (Observability according to Kalman)**.** *Given a state-space system, with the matrix pair (A,C), it is completely observable, if the observability matrix S_B has full rank:*

$$RankS_B = n \tag{3.39}$$

As with the controllability, it can be shown that this is a necessary criterion [82].

While the criterion above may give good results, in some cases they may lead to numerical problems, such that Gramian matrices may be used as an analysis tool instead. Interested readers may refer to [82].

3.1.6 Final Value Theorem

The final value theorem is an important anaylzis tool for estimation of the final output value of a stable system, without comprehensive numerical analysis.
The theorem states that for a stable system, the final constant value is ([35]):

$$\lim_{t \to \infty} x(t) = \lim_{s \to 0} sX(s) \tag{3.40}$$

with $X(s)$ the Laplace transformed of $x(t)$. Hence, by solving RHS of equation 3.40, the final output of a system can be computed.

3.1.7 Discrete-Time Systems

Discrete-time systems are inherently different than their continuous-time counterpart which must be considered in control design. Instead of differential equations for a continuous time system, a sampled discrete-time system is described by differences equations:

$$\begin{gathered} a_n y(k+n) + a_{n-1} y(k+n-1) + ... + a_1 y(k+1) + a_0 y(k) = \\ b_q u(k+q) + b_{q-1} u(k+q-1) + ... + b_1 u(k+1) + b_0 u(k) \end{gathered} \tag{3.41}$$

which leads to a discrete-time state-space system:

$$\begin{aligned} x_{k+1} &= A_D x_k + B_D u_k \\ y_k &= C_D x_k + D_d u_k \end{aligned} \tag{3.42}$$

A transformation from a continuous state-space system into a discrete-time system with the sample time T is done as follows:

$$\begin{aligned} A_d = exp(AT) \qquad & B_d = \textstyle\int_0^T exp(A\alpha) d\alpha B \\ C_d = C \qquad & D_d = D \end{aligned} \tag{3.43}$$

Unlike the convolution integral for continuous time systems, the convolution sum applies in discrete-time systems:

$$y_k = \Sigma_{j=k-\tilde{k}+1}^{k} g(k-j)u(j) = \Sigma_{j=0}^{\tilde{k}-1} g(j)U(k-j) \tag{3.44}$$

This implies that time-signals earlier than $\tilde{k}$ have no influence on the current output signal.

By introducing the z-transformation, instead of Laplace-transformation a discrete-time transfer function can be formulated.
The z-Transformed $F(z)$ of a sampled signal $f(k)$ is defined as:

$$F(z) = \Sigma_{k=0}^{\infty} f(k) z^{-1} \tag{3.45}$$

Thereby, the convolution integral in time-domain becomes a straightforward multiplication in the Z-domain, and a transfer function for sampled systems can be conveniently defined as:

$$G(z) = \frac{Y(z)}{U(z)} \tag{3.46}$$

Stability and other properties of Discrete-Time Systems

Although most properties of a discrete-time system are the same as for a continuous systems, the stability criterion differs, which is stated in the following theorem for a sampled state-space system:

Theorem 4. *A discrete-time system 3.42 is stable if all eigenvalues of the system-matrix A fulfill the following inequality:*

$$|\lambda(A)| \leq 1 \tag{3.47}$$

Furthermore, the system 3.42 is asymptotically stable if, and only if the following condition holds

$$|\lambda(A)| < 1 \tag{3.48}$$

This can be easily verified by considering that due to the time-sampling a space is warped through the exponential function into a different space ($e^{sT} = z$). For all negative eigenvalues with negative real-parts which cover the entire left side region of the complex plane, the exponential conversion leads to a contraction of that space into the unit disc centered at the origin $(0 + j0)$. This is obvious since the largest exponential value of negative arguments is inevitably one for an argument of zero.
Since, like in continuous systems, the poles of a transfer function are the same as the eigenvalues of the system matrix A_D of the discrete state-space system, stability of a time-sampled system is ensured if, and only if, the poles of the transfer functions are within the unit circle, centered around the origin of the complex plane.

As of observability and controllability of the pairs (A_D, C_D) and (A_D, B_D) of a sampled system, the same holds as in continuous time systems.

Dead-Beat Control

The time-domain solution of equation 3.18 of an asymptotically stable time-continuous system is an exponential function in which the states approach the origin. Contrary to that, due to its discrete-time character, an asymptotically stable discrete-time system 3.42 can reach the origin in a finite time, and within maximum n time-steps.
This is equivalent to reaching a desired system output y_k in a finite time. Namely:

$$y_k = r \; for \; k \geq n \tag{3.49}$$

By assuming state feedback control, with a feed-forward control for reference tracking:

$$u_k = -Kx_k + Nr_k \tag{3.50}$$

the following state equation can be obtained:

$$x_{k+1} = \tilde{A}x_k + B_D N\tilde{r} \tag{3.51}$$

with $\tilde{r}$ as a constant reference tracking value:

$$\tilde{r} = r_k \tag{3.52}$$

and $\tilde{A}$ as the closed-loop system matrix:

$$\tilde{A} = (A_D - B_D K) \tag{3.53}$$

It can be shown that the closed-loop controlled system 3.51 reaches its final value in no more than n sampling time-steps if and only if, all eigenvalues of the closed-loop system matrix $\tilde{A}$ are exactly zero ([82]):

$$\tilde{\lambda}_1 = \tilde{\lambda}_2 = ... = \tilde{\lambda}_n = 0 \tag{3.54}$$

A controller with these properties is referred to as a Dead-Beat Controller.

3.2 Linear Control

3.2.1 Linear Output Control (PID)

Output control is the most common control approach. It is easy to tune since only maximum three constant gains need to be found, it does not require a plant model, and it often can satisfy many control problems.
The control law for PID control is:

$$u = K_P \cdot e + K_I \int_t e \cdot dt + K_D \cdot \frac{de}{dt} \tag{3.55}$$

where the constants K_P, K_I, K_D can be found by trial and error approaches, heuristic approaches (Ziegler and Nichols, or Chien, Hrones and Reswick) or by more powerful approaches, such as root-locus. The latter is only useful if a model of the plant is available. With this approach, poles of the closed-loop system can be placed by setting new zeroes into the system and by tuning the overall gain. By doing so, the poles can be moved from undesired locations (e.g. positive real values) to desired ones (e.g. negative real values). The rules behind this approach also make it clear that the zeros of a system limit the bandwidth of the actuators and the dynamics of the system.
Note that control law 3.55 is not proper and is usually replaced by $PIDT_1$ during implementation.

While this control approach may give satisfactory control results and sufficient robustness analysis by applying the Nyquist Theorem, it does not allow for arbitrarily placement of poles and has limitations in MIMO control design. Additionally, better control performance may be expected with more advanced control concepts.

3.2.2 State control - Optimal Control

While output control is limited to controlling the outputs of a system only, state control controls the states x of a system and, thereby, can shape the dynamic features of the system. It has advantages especially MIMO control problems and usually requires a control-oriented LTI model. A common control input with state feedback is as follows:

$$u = -K \cdot x \tag{3.56}$$

where x is the state that is fed back as a control signal, and K the static gain of the controller. Inserting this into the state space equations (3.18) gives:

$$\dot{x} = A \cdot x - B \cdot K \cdot x \tag{3.57}$$

and by re-arranging:

$$\dot{x} = (A - BK) \cdot x \tag{3.58}$$

In this equation, it is obvious that the term $(A - BK)$ can be considered as a new system matrix $\tilde{A}$, which has different properties than the original system matrix A. The eigenvalues have been relocated so that an unstable system can be made stable. Pole-placement algorithms are often employed to put the poles at desired locations.

Optimal Control - LQR

Pole-placement for control design is more of a frequency-domain tuning technique, whereas time-domain techniques such as Linear-Quadratic design (LQ) designs are very popular and often preferred due to their flexibility. By choosing suitable diagonal and positive-definite design matrices R and Q, the LQ algorithm aims at minimizing the quadratic cost function:

$$J = \int_0^\infty x(t)^T Q x(t) + u(t)^T R u(t) dt \tag{3.59}$$

Here it can be seen that by proper weights of Q and R, the dynamics and actuation of the closed-loop controlled plant can be shaped. In general, a higher r_i gain of the matrix R penalizes the respective control input u_i of control vector u and makes this actuator slower.

A solution to the optimization problem of the cost function 3.59 is usually obtained by solving the Algebraic Riccati Equation:

$$A^T P + PA - PBR^{-1}B^T P + Q = 0 \tag{3.60}$$

where with the solution P of this equation one obtains the controller K:

$$K = R^{-1}B^T P \tag{3.61}$$

State Observer for State Control

In most control problems, all states cannot be measured since either the values are not accessible in real-time due to missing sensing devices, or employing such devises are too expensive so that they are omitted in the final control system design.
In case of combustion engines, the instantaneous in-cylinder pressure may be measured for each cylinder by dedicated sensors and the measured values processed in real-time to estimate the engine torque or combustion states. This approach has become popular with Diesel engines recently, but it is not a standard in gasoline as of yet.

In order to track the states of a process in real-time and use them as feedback signals for the controller, online estimation based on simple models are commonly used. These are either Luenberger observers, or Kalman filters which are conceptionally the same as Luenberger observers, except for the correction term, which is derived in a different way. This corrector is used to correct model imperfections or temporal plant deviations by comparing the outputs of the model with the measured outputs of the system. In order to keep the algorithm computationally as simple as possible, observer models are often based on linear state-space descriptions of the model.
The following equation shows the structure of a linear observer:

$$\begin{aligned} \dot{\hat{x}} &= A\hat{x} + Bu + L(y - \hat{y}) \\ \hat{y} &= C\hat{x} + Du \end{aligned} \tag{3.62}$$

Note the L correction term that has been introduced here. This equation compares the actual measurement y of the system with the estimated output $\hat{y}$ from the second equation. This gain can be found by applying stability theorems for linear systems, as introduced above (Luenberger Observer), or optimization in presence of measurement noise (Kalman Filter).

Reference Tracking - Feed-Forward Control

Tracking of a reference value r, such that $y(t \to \infty) = r$, can be achieved by a feed-forward control which is formulated as:

$$u_{FF} = N \cdot r \tag{3.63}$$

and added to the overal control law

$$u = -Kx + Nr \tag{3.64}$$

To begin with, a steady-state system-state x_{ss} and inputs u_{ss} are introduced:

$$u = -K(x - x_{ss}) + u_{ss} \tag{3.65}$$

where K is the state controller as above.
By defining Nx and N_u as:

$$\begin{aligned} \dot{x}_{ss} &= Ax_{ss} + Bu_{ss} = (AN_x + BN_u)r = 0 \\ y_{ss} &= Cx_{ss} + Du_{ss} = (CN_x + DN_u)r = r \end{aligned} \tag{3.66}$$

which can be re-arranged into the form of matrices:

$$\begin{pmatrix} A & B \\ C & D \end{pmatrix} \begin{pmatrix} N_x \\ N_u \end{pmatrix} = \begin{pmatrix} 0 \\ 1 \end{pmatrix} \tag{3.67}$$

by solving for the unknowns N_x and N_u:

$$\begin{pmatrix} N_x \\ N_u \end{pmatrix} = \begin{pmatrix} A & B \\ C & D \end{pmatrix}^{-1} \begin{pmatrix} 0 \\ 1 \end{pmatrix} \tag{3.68}$$

equation 3.65 can be re-formulated as:

$$u = -K(x - N_x r) + N_u r \tag{3.69}$$

or

$$u = -Kx + \tilde{N}r \tag{3.70}$$

for

$$\tilde{N} = N_u + KN_x \tag{3.71}$$

This approach ensures fast tracking of desired references and is especially useful if fast response times are required. However, tracking is only perfect if the modeled plant is error-free and does not differ from the actual plant. In case of uncertainties or strong non-linearities, this approach may give undesired results. Furthmore, in case of strong intercoupling between inputs and outputs, this feed-forward term may result in unfavorable transients before the steady-state values are reached.

The following section addresses this problem and introduces a control action for the closed-loop system for tracking control and increased robustness in presence of disturbances.

Reference Tracking - Augmented State-Space Model

As introduced in the previous section, tracking a reference can be achieved by proper feed-forward design which is generally a static gain. However, as mentioned in this section, aside from fast transients for reference tracking, this approach does not account for unmodeled disturbances and has only very limited robustness against it.
In order to allow for tracking of a reference in presence of disturbances, an integral action can be included in the overall control design. The underlying idea is to include the time derivative of the tracking error as an artificial state, as:

$$\dot{x}_{aug} = e = r - y \tag{3.72}$$

and assuming that $D = 0$:

$$\dot{x}_{aug} = e = r - C \cdot x \tag{3.73}$$

the original model is then augmented to:

$$\dot{x} = \begin{pmatrix} \dot{x}_{aug} \\ \dot{x} \end{pmatrix} = \begin{pmatrix} 0 & -C \\ 0 & A \end{pmatrix} x + \begin{pmatrix} 0 \\ B \end{pmatrix} u + \begin{pmatrix} I & 0 \end{pmatrix} r \tag{3.74}$$

Design of a closed-loop control is then straightforward. The additional state can for example be included in LQR design as well and be tuned by selecting an appropriate weighting constant q_i in the design matrix Q. However, this approach should not exceed the control authorities of the actual state controller to maintain the actual control dynamics.

3.2.3 Robust Control

Robust control is a fairly new control theory that emerged in the late 70s and was greatly advanced in the 80s and early 90s. Since classical control approaches allow for design of controllers and the estimation of their robustness properties by analyzing the sensitivity function, for example, this analysis is rather crude and they do not explicitly include robustness in their design.
The most well-known controller for robust control is the H_∞ controller, which aims to reduce the infinity norm of the closed-loop system $F_l(P, K)$ with plant P and controller P for all relevant frequencies as:

$$\|F_l(P, K)\|_\infty = \sup_\omega \left[\int_{-\infty}^{\infty} F_l(P, K) d\omega \right] \tag{3.75}$$

Here, the term $F_l(P, K)$ denotes the lower linear fractional transformation (LFT), which is depicted in figure 3.1 for a plant M and a controller K.

Given that the plant can be decomposed to

$$M = \begin{bmatrix} M_{11} M_{12} \\ M_{21} M_{22} \end{bmatrix} \tag{3.76}$$

the lower linear fractional transformation is:

$$F_l(M, K) = M_{11} + M_{12} K (I - M_{22} K)^{-1} M_{21} \tag{3.77}$$

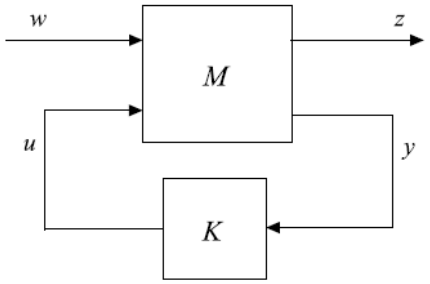

Figure 3.1: Example of a lower Linear Fractional Transformation (LFT) [27]

The H_∞ controller is hereby a controller that optimizes the minimum of the infinity norm of a closed loop signal. This may ensure robustness for SISO systems, when the frequency response is below the magnitude of one, as it can be shown with the Nyquist theorem.
For MIMO systems however, the critical point $(-1 + j0)$ is not valid for stability and other criteria have been suggested, based on the small-gain theorem, which will be introduced in the the following theorem:

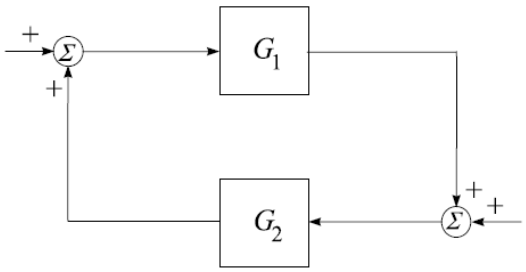

Figure 3.2: Small Gain Theorem: Interconnection of two stable plants [27]

Theorem 5 (Small-Gain Theorem)**.** *Consider an interconnected system of two sub-systems* $G_1 \in RH_\infty$ *and* $G_2 \in RH_\infty$ *as shown in figure 3.3, consisting of two systems, and suppose there exists a* $\gamma > 0$*. The interconnected system is well-posed and internally stable and converges to zero, if the following conditions apply:*

$$\begin{aligned} &(a) \qquad \|G_1\|_\infty \leq 1/\gamma \quad \textit{if and only if} \quad \|G_2\|_\infty < \gamma \\ &(b) \qquad \|G_1\|_\infty < 1/\gamma \quad \textit{if and only if} \quad \|G_2\|_\infty \leq \gamma \end{aligned} \tag{3.78}$$

The proof is provided in [128].
To analyze robustness of a closed-loop system with an interconnected uncertainty Δ, the small-gain theorem may be applied by replacing G_1 by an uncertainty block Δ and G_2 by a plant M. This theorem is only sufficient since it does not take phase margin into account and makes only

use of the magnitude. Hence, since it is not a necessary condition it may lead to rather conservative results to sub-optimal controllers.

When using the small-gain theorem as an analyzing tool for control design, modeling of a system is only considered complete if besides the nominal model itself, also the uncertainty is identified and included in the model as well. Modeling of uncertainties will be introduced in a later section.

The H_∞ control problem is an optimization problem, and algorithms for solving this problem have been suggested, of which the two Algebraic Riccati Equation (ARE) solution is the commonly used solution. A newer approach is based on Linear Matrix Inequalities has recently emerged as an alternative to the two Riccati Equation, of which an introduction is given in [83].

Two Algebraic Riccati Equation (ARE) Solution - Simplified Version

The H_∞ optimization problem poses challenges in the algorithms in finding an optimized solution and the underlying maths are too complex to be presented in this section. One of the most common ones is the the Two Riccati Equation approach of which only the simplified solution will be only outlined here, which however introduces the necessary features of the H_∞ theory ([128]). Interested reader may refer to [83], [128], [89], or [27].

First, starting from a plant model in state-space form, a general plant of the form is structured as:

$$G(s) = \left[\begin{array}{c|cc} A & B_1 & B_2 \\ \hline C_1 & D_{11} & D_{12} \\ C_2 & D_{21} & D_{22} \end{array}\right] \tag{3.79}$$

such that it can be interconnected to a controller K to give the lower linear fractional transformation (LFT) $F_l(G, K) = F_{ZW}$.
For the plant G, the following assumptions are made:

(A1) (A, B_1) is stabilizable and (C_1, A) is detectable

(A2) (A, B_2) is stabilizable and (C_2, A) is detectable

(A3) $D_{12}^T C_1 = 0$ and $D_{12} D_{12}^T = I$

(A4) $B_1 D_{21}^T = 0$ and $D_{21} D_{21}^T = I$

(A5) $D_{11} = 0$ and $D_{22} = 0$

Then the following two Algebraic Riccati Equations are used:

(i) There exist a solution $X_\infty > 0$ to

$$X_\infty A + A^T X_\infty + X_\infty(\gamma^{-2} B_1 B_1^T - B_2 B_2^T) X_\infty + C_1^T C_1 = 0 \tag{3.80}$$

such that

$$Re\lambda_i[A + (\gamma^{-2}B_1B_1^T - B_2B_2^T)X_\infty] < 0, \forall i \tag{3.81}$$

and

(ii) There exist a solution $Y_\infty > 0$ to

$$AY_\infty + Y_\infty A^T + Y_\infty(\gamma^{-2}C_1C_1^T - C_2C_2^T)Y_\infty + B_1^TB_1 = 0 \tag{3.82}$$

such that

$$Re\lambda_i[A + Y_\infty(\gamma^{-2}C_1C_1^T - C_2C_2^T)] < 0, \forall i \tag{3.83}$$

with

$$\rho(X_\infty Y_\infty) < \gamma^2 \tag{3.84}$$

where the closed-loop system fulfills:

$$\parallel F_{ZW} \parallel_\infty < \gamma \tag{3.85}$$

Since the infinity-norm of the transfer function is only below a pre-defined threshold γ, further reductions may be possible. Hence, a controller with such properties is denoted as suboptimal controller.
Solving the two algebraic Riccati equations 3.80 and 3.82 is not a trivial task and Hamilton matrices are utilized for obtaining a solution, which are:

$$H_\infty = \begin{bmatrix} A & \gamma^2B_1B_2^T - B_2B_2^T \\ -C_1^TC_1 & -A^T \end{bmatrix} \tag{3.86}$$

and

$$J_\infty = \begin{bmatrix} A^T & \gamma^2C_1^TC_1 - C_2^TC_2 \\ -B_1B_1^T & -A \end{bmatrix} \tag{3.87}$$

The following theorem, as directly taken from [83], defines the approach for finding a suboptimal controller.

Theorem 6. *Suppose assumption (A1) - (A5) hold. Then there exists an admissible controller with* $\parallel F_{zw} \parallel_\infty < \gamma$ *if and only if the following conditions are fulfilled:*

(i) $H_\infty \in dom(Ric)$ *and* $X_\infty = Ric(H_\infty \geq 0)$

(ii) $J_\infty \in dom(Ric)$ *and* $Y_\infty = Ric(H_\infty \geq 0)$

(iii) $\rho(X_\infty Y_\infty) < \gamma^2$

If these conditions hold, such a controller is:

$$K_{sub}(s) = \left[\begin{array}{c|c} \hat{A}_\infty & -Z_\infty L_\infty \\ \hline F_\infty & 0 \end{array}\right] \tag{3.88}$$

with

$$\begin{gathered} \hat{A} = A + \gamma^2B_1B_1^TX_\infty + B_2F_\infty + Z_\infty L_\infty C_2 \\ F_\infty = -B_2^TX_\infty,\ L_\infty = Y_\infty C_2^T,\ Z_\infty = (I - \gamma^{-2}Y_\infty X_\infty)^{-1} \end{gathered} \tag{3.89}$$

Although it is not initially evident, this controller has a controller-observer structure, also known as in common state-controllers.
This can be shown if the controller 3.88 is rewritten in the form

$$\begin{gathered}\dot{\tilde{x}} = A\tilde{x} + B_1\tilde{w}_{worst} + B_2u + Z_\infty L_\infty(C_2\tilde{x} - y) \\ u = F_\infty\tilde{x},\ \tilde{w}_{worst} = \gamma^{-2}B_1^T X_\infty\tilde{x}\end{gathered} \tag{3.90}$$

The first equation is obviously an observer, which estimates the states and includes the term $\tilde{w}_{worst} = \gamma^2 B_1^T X_\infty \tilde{x}$, which can be considered as a disturbance estimator ([83]). The term $\tilde{x}$ is obviously the estimate of the true states x. This controller is similar to the H_2 (not introduced in this work) control problem, where in the H_{infty} problem the term B_1 is incorporated into the observer equation.
However, the assumptions (A1)-(A5) here are often too restrictive, and other approaches for more relaxed assumptions also exist.

The two Riccati approach is the classical approach and has been used widely in many control problems. It provides useful solutions in most cases.
In cases where this approach cannot provide any results, an alternative approach to the H_∞ optimization problem, based on matrix inequalities has been proposed.

Description of uncertainty

As outlined in the previous sections, analysis or robustness of a system requires a description of the uncertainty. Therefore, in order to make modeling of a plant complete, a model of the uncertainty is necessary and needs to be implemented in the model where two different kinds of uncertainties exist: structured and unstructured.
An unstructured uncertainty is usually described by transfer functions, which typically have small magnitudes at low frequencies, and higher error magnitudes at higher frequencies, which is normally due to poorly modeled high frequency dynamics.
These unstructured uncertainties can be placed at the output of a plant, where measurement of the true plant at different frequencies and magnitudes can be determined and put in relation to the nominal plant model as in equation (relative uncertainty):

$$l_y = \max_{G_p \in \pi} \left| \frac{G_p(j\omega) - G(j\omega)}{G(j\omega)} \right| \tag{3.91}$$

An upper bound of a transfer function can then be fitted to cover all identified uncertainties, as:

$$|w_y| \geq l_y(j\omega) \forall \omega \tag{3.92}$$

The following picture shows an unstructured output uncertainty of a nominal plant $G_0(s)$:

An uncertainty representation can also be set at the intake port of a nominal model in a similar way. In case of combustion engines, where the injection of fuel into the port delays fuel transport to the successive cycle, this delay can be modeled as an unstructured uncertainty and implemented on the input-side of the model.

In a general approach, the uncertainty is separated from the disturbed plant as shown in the following figure to allow for stability analysis:

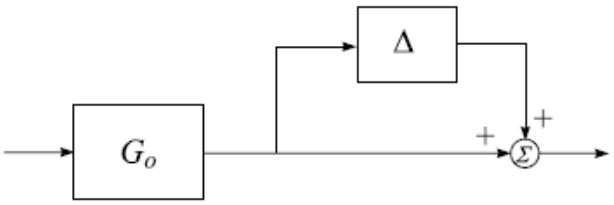

Figure 3.3: Output Uncertainty at nominal Plant G_0 [27])

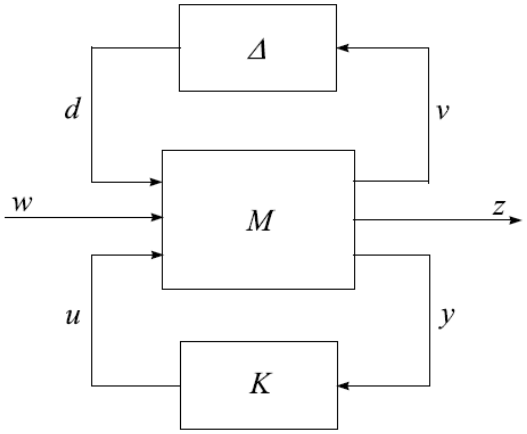

Figure 3.4: Generalized Plant with nominal plant (M), controller (K), and uncertainty (Δ) (from [27])

Here, the uncertainty is a matrix Δ whose elements may include dynamic transfer functions, as well as static scalars.
For each element Δ_i of Δ, the following inequality holds:

$$|\Delta_i| \leq 1 \tag{3.93}$$

Structured perturbations on the other hand are often derived from parametric uncertainties, when only bounds of certain parameters are known. Examples are the mass of a rope of a mining cart, whose thickness and varying length determine the weight of the rope. Other examples may be friction, of which only upper and lower bounds are known.
Such uncertainties can often be extracted to form a block-diagonal matrix, as shown in the following equation:

$$\Delta = diag\{\Delta_i\} = \begin{pmatrix} \Delta_{1,1} & 0 & \cdots & 0 \\ 0 & \Delta_{2,2} & \cdots & 0 \\ \vdots & \vdots & \ddots & \vdots \\ 0 & 0 & \cdots & \Delta_{m,n} \end{pmatrix} \tag{3.94}$$

Due to the known structure of the matrix, this kind of uncertainty is called structured uncertainty and has crucial advantages over unstructured uncertainties, when robust performance of a controlled plant is required.

Since in MIMO systems, not only the magnitude can make a plant unstable or lead to undesired control performance, but also the interaction of different the inputs, namely the direction of the input vector. Using the small-gain theorem does not consider the structure of the uncertainties and requires that all single uncertainties are below a common boundary. This may lead to conservative solutions, while more optimized solutions may exist.
For that reason, it is also desired to include the perturbation structure into the control design, where the structured uncertainty is a promising candidate for a better control design.
This leads to structured singular value (SSV), which will be introduced in the next section.

Structured Singular Values (SSV)

By inspection of the generalized plant M, as

$$M = \begin{pmatrix} M_{1,1} & M_{1,2} \\ M_{2,1} & M_{2,2} \end{pmatrix} \tag{3.95}$$

with an uncertainty block, the upper linear fractional transformation (LFT), the transfer function from input w to z is defined as:

$$z = \boldsymbol{F}_u(M, \Delta)w = [M_{22} + M_{21}\Delta(I - M_{11}\Delta)^{-1}M_{12}]w \tag{3.96}$$

Since it is assumed that the plant M and the disturbance Δ are each stable, instabilities may arise if the term $(I - M_{11}\Delta)$ has negative zeros on the right-hand complex plane ($\mathbb{RH}_\infty$).
If a structured uncertainty matrix is given as:

$$\triangle = \{diag[\delta_1 I_{r1}, ..., \delta_s I_{rs}, \Delta_1, ..., \Delta_F] : \delta_i \in \mathbb{C}^{m_j x m_j}\} \tag{3.97}$$

and the following relation must hold:

$$\Sigma_{i=1}^{S} r_i + \Sigma_{j=1}^{F} m_j = n \tag{3.98}$$

The idea is to find structured disturbances at each frequency, that can make a plant unstable. With the above equations given, the structured singular value (SSV) μ_Δ of a plant M can be defined.

Definition 5. *For a given plant M, and a structured uncertainty Δ, the structured singular value (SSV) is defined as*

$$\mu_\Delta(M) := \frac{1}{min\{\bar{\sigma}(\delta) : \Delta \in \underline{\Delta}, det(I - M\Delta) = 0\}} \tag{3.99}$$

In cases, where at a particular frequency, there is no uncertainty $\Delta \in \Delta$ that makes $(I - M\Delta)$ singular, the structured singular value is zero ($\mu_\Delta(M) = 0$)

This definition is the same as for unstructured singular values, except for the uncertainty Δ, which is unstructured.
It can be shown that the following inequality applies, which states the lower conservativeness of structured singular values:

$$\rho(M) \leq \mu_\Delta(M) \leq \bar{\sigma}(M) \tag{3.100}$$

In fact, the structured singular values becomes the maximum singular value if the disturbance is unstructured, hence:

$$\mu_{\Delta}(M) = \bar{\sigma}(M) \; for \; \underline{\Delta} \; unstructured \tag{3.101}$$

As introduced above, the structured singular values give a better insight into robust stability and especially robust performance.
The theorems in the following sections give the criteria for robust stability and robust performance of perturbed systems.

Robust Stability and Robust Performance

Robust stability is the stability of a open-loop or closed-loop system despite of model uncertainties and perturbations. While the nominal unperturbed system may be stable, perturbations may destabilize a system. Hence, estimation of robustness is vital for design of closed-loop control design and it is advantageous to assess control stability and robust performance during control design.
For SISO system, robustness of a closed-loop system may be judged by the bode plot of the open loop, where the distance of the frequency response plot "does not cross" or "does not encircle" the -1 point on the complex plane. This is a simplified Nyquist criterion for SISO systems.
In MIMO systems however, the critical point -1 diminishes since the determinant of a matrix comes into play when stability is analyzed ([89]).
As introduced above, for an interconnected system, the small gain theorem is a suitable candidate for judgement of stability of a system, where depending on the modeling approach for the uncertainty, different stability criteria exist which are listed below.

- **Robust Stability**
  As previously stated, for different unstructured disturbance modeling approaches different robust stability criteria exist, of which for the sake of brevity, the most important once are listed in table 3.1.

	Uncertain Plant	Robust Stability
Additive Uncertainty	$G_P = G + W_1 \Delta W_2$	$\parallel W_2 K S_o W_1 \parallel_{\infty} \leq 1$
Input (actuator) multiplicative uncertainty	$G_P = G(I + W_1 \Delta W_2)$	$\parallel W_2 T_i W_1 \parallel_{\infty} \leq 1$
Output (sensor) multiplicative uncertainty	$G_P = (I + W_1 \Delta W_2) G$	$\parallel W_2 T_o W_1 \parallel_{\infty} \leq 1$

Table 3.1: Robustness Criteria for different uncertainty descriptions

  Here, T_i is the input complementary sensitivity function, T_o the output complementary sensitivity function, and K the controller.

- **Structured Robust Stability** of closed-loop systems with structured perturbation ([83])

  Theorem 7. *Let the nominal feedback system $M = F_l(P, K)$ be internally stable and let $\gamma > 0$. Then the following assertions are equivalent:*

(i) $\mu_{\underline{\Delta}}(M_{11}(s) \leq \gamma)$ *for every* $s \in \bar{C}_+$

(ii) The perturbed feedback system in Fig. 13.4 is well-posed and internally stable for all perturbations $\Delta \in M(\underline{\Delta})$ *with* $\| \Delta \| < 1/\gamma$

- **Robust Performance** for output multiplicative uncertainty: Suppose the goal is to minimize the tracking error e. The energy of the error signal over all unit disturbances $\tilde{d}$ is defined as ([128]):

$$\sup_{\|\tilde{d}\|_2 \leq 1} \| e \|_2 \leq \epsilon \tag{3.102}$$

Then the robust performance criterion can be defined as:

$$\| T_{e\tilde{d}} \|_\infty \leq 1, \ P_\Delta \ \in \Pi \tag{3.103}$$

where $T_{e\tilde{d}}$ is the transfer function from disturbance $\tilde{d}$ to the error signal e.
The perturbed error model, as an unstructured error, is

$$\Pi := \{(I + W_1 \Delta W_2)P : \ \Delta \in RH_\infty, \ \| \Delta \|_\infty < 1\} \tag{3.104}$$

with some disturbance scaling transfer functions W_1 and W_2.
The transfer function from disturbance to tracking error then becomes:

$$T_{e\tilde{d}} = W_e S_0 (I + W_1 \Delta W_2 T_0)^{-1} W_d \tag{3.105}$$

Robust performance is then satisfied if, and only if:

$$\| W_2 T_0 W_2 \|_\infty \leq 1 \tag{3.106}$$

and the following inequalities hold

$$\| T_{e\tilde{d}} \|_\infty \leq 1, \ \forall \Delta \ \in \ RH_\infty, \| \Delta \|_\infty < 1 \tag{3.107}$$

Although these simple conditions are sufficient for assessment of robust performance, they are not necessary and therefore not exact. Exact analysis is based on structured singular values and will be introduced next.

- **Structured Robust Performance** of closed-loop systems with structured perturbation ([83]): Robust performance can be treated in the same way as robust stability. Namely, a system is considered robust in terms of performance, if for any admissible uncertainty the norm of the system stays under a pre-defined limit. Hence, if $\| F_u(M, \Delta) \|_\infty \leq \gamma_p$. This criterion can be reformulated by treating the performance as a disturbance. By introducing a robust performance uncertainty Δ_l which can be unstructured, and by setting $w = \Delta_l z$, the disturbance can be re-cast into:

$$\underline{\Delta}_p = \left\{ \begin{pmatrix} \Delta & 0 \\ 0 & \Delta_l \end{pmatrix} \mid \Delta \in \underline{\Delta}, \Delta_l \in C^{q_2 x p_2} \right\} \tag{3.108}$$

With the upper linear fractional transformation for the plant M:

$$F_u(M, \Delta) = M_{22} + M_{21}\Delta(I - M_{11}\Delta)^{-1}M_{12} \tag{3.109}$$

The following theorem is a criterion for robust stability ([83]):

Theorem 8. *Let the nominal feedback system $M = F_l(P, K)$ be internally stable and let $\gamma > 0$. Then the following assertions are equivalent.*

(i) For every $\Delta \in M(\underline{\Delta})$ with $\| \Delta \|_\infty < 1/\gamma$ the feedback system depicted in Fig. 13.4 is well-posed, internally stable and fulfills the inequality

$$\| F_u(M, \Delta) \|_\infty \leq \gamma \tag{3.110}$$

(ii) The following inequality holds:

$$\sup_{\omega \in R} \mu_{\underline{\Delta}^P}(M(i\omega)) \leq \gamma \tag{3.111}$$

D-K Iteration

Although the control design approaches presented in the previous sections consider disturbance, they do not explicitly include disturbance in the control design, such that this becomes an iterative and tedious procedure. Contrary to that, the D-K Iteration is a proposed iterative algorithm to shape robust controllers under consideration of modeled structured uncertainties.

The nominal plant can be merged with the controller K to give the linear fractional transformation (LFT) M, as

$$M(P, K) = F_l(P, K) \tag{3.112}$$

For control of robust controllers, the following inequality must be fulfilled:

$$\sup_{\omega \in R} \mu[M(P, K)] \leq 1 \tag{3.113}$$

or the optimized solution:

$$\inf_{K(s)} \sup_{\omega \in R} \mu[M(P, K)] \tag{3.114}$$

Ideally equation 3.114 would be solved directly for K. However, since computing μ alone is not straightforward, solving for the optimal controller K becomes unfeasible.
For that reason, the D-K iteration for finding the optimal controller has been suggested, which will be introduced in this section.
Equation 3.114 can be augmented with a diagonal scaling matrix D:

$$\inf_{K(s)} \sup_{\omega \in R} \inf_{D \in \mathbf{D}} \bar{\sigma}[DM(P, K)D^{-1}] \tag{3.115}$$

The scaling matrix D is defined as ([27]):

$$\mathbf{D} = \{D = diag[D_1, ..., D_s, d_1 I_m, ..., d_f I_{mf}] : D_i \in C^{r_i x r_i}, D_i = D_* > 0, d_j > 0\} \quad (3.116)$$

The objective of the D-K iteration is to minimize the left hand side of equation 3.115 by scaling D and controller K, while keeping all other terms fixed.
The optimization problem then becomes a classical H_∞ problem, with

$$\inf_K \parallel DMD^{-1} \parallel_\infty = \inf_K \parallel DF_l(P,K)D^{-1} \parallel_\infty = \inf_K \parallel F_l(\tilde{P},K) \parallel_\infty \quad (3.117)$$

with

$$\tilde{P} = \begin{bmatrix} D & 0 \\ 0 & I \end{bmatrix} P \begin{bmatrix} D^{-1} & 0 \\ 0 & I \end{bmatrix} \quad (3.118)$$

The D-K Iteration consists then of the following steps:

Step 1: Start with an initial D. Usually, D is set to I

Step 2: Solve the H_∞ optimization problem to obtain controller K

$$K = arg \inf_K \parallel F_l(\tilde{P},K) \parallel_\infty \quad (3.119)$$

Step 3: Solve the convex optimization problem for new scaling matrix D for each frequency

$$D(j\omega) = arg \inf_{D \in (D)} \bar{\sigma}[DF_l(P.K)D^{-1}(j\omega)] \quad (3.120)$$

Step 4: Find a $D(s)$ to fit all identified $D(j\omega)$ and go to Step 2 until convergence is reached.

3.3 Non-Linear Systems and Control

Non-linear systems are difficult to characterize and well-known linear analysis and control synthesis tools often fail in non-linear systems. In most cases, a non-linear system is linearized around a chosen operating point, and it is often assumed that the linearized system matches the original non-linear system well in a vicinity around that operating point. It is not difficult to imagine that a the performance of linear controller degrades when it is operated further away from the linearization point.
Therefore, in finding a control scheme, it is of superior interest to analyze the control performance of a linear controller far away from the linearization point. Generally speaking, a linear controller will perform well if robustness is considered in control design and if the targeted plant has fairly linear characteristics. On the other hand, a strong non-linear plant will cause problems with linear controllers and may require the design of non-linear control schemes.
Popular design tools are back-stepping and sliding mode control ([74]), of which sliding mode control as a popular control concept in automotive applications will be introduced in the next sections.
The following section starts off with the Lyupanov criterion for non-linear stability.

3.3.1 Stability of non-linear systems

For non-linear plants, Lyuapunov stability has been accepted as common criterion for stability of a non-linear system.
It is stated as follows [74]:

Theorem 9 (Lyupanov Stability)**.** *For any autnomous system $\dot{x} = f(x)$, let $x_0 = 0$ be an equilibirium point and $D \subset R^n$ a domain that contains x_0. Define a continuous differentiable function $V : D \to R$, with the following properties:*

$$V(0) = 0 \qquad \textit{and} \qquad V(x) > 0 \qquad inD - \{0\} \tag{3.121}$$

Then x is stable if

$$\dot{V}(x) \leq 0 \quad \textit{in} \quad D \tag{3.122}$$

Moreover, it is asymptotically stable if

$$\dot{V}(x) < 0 \quad \textit{in} \quad D - \{0\} \tag{3.123}$$

The function V is not defined and one must be found that fulfills the conditions 3.121. For that reason V is often referred to Lyupanov function candidate. A frequent candidate for scalar systems is of the form $V(x) = \frac{1}{2}x^2$ which is continuous, positive definite and its derivative easy to handle.
In case of LTI systems, this theorem can be reformulated with a Lyupanov function candidate as:

$$V(x) = x^T P x \tag{3.124}$$

and with $Q > 0$ and $P > 0$, to a Lyupanov Equation as:

$$A^T P + PA + Q = 0 \tag{3.125}$$

A system $\dot{x} = Ax$ is globally asymptotically stable if 3.125 is fulfilled.

Lyupanov stability plays a key-role in case of Sliding-Mode Control (SMC), a fairly simple but powerful control tool that has been applied frequently in automotive applications and will be introduced in the next sections.

3.3.2 Non-linear control: Sliding Mode Control (SMC)

Sliding Mode Control (SMC) is a control technique that was first recognized in the English-speaking world by Utkin in 1977, who translated a paper from the Russian language into English ([121]).
It dates back to the times when relays in electrical circuits where heavily used and could be used to switch between two distinct modes.
Two introductory examples are given as follows:
A boat with a rudder that can only switch between two positions, which are opposite to each other. Hence, one position would lead the boat to turn left, while the other to turn right. Consequently, keeping one position would make the boat sail in a circle (and move away towards

infinity by presence of a flow). However, by continuously switching between the two positions, the boat can potentially move in a forward direction.
Another, and more abstract, example is a system with two unstable configurations. Keeping one configuration would make the system drift away from the origin. Therefore it would theoretically go to infinity and can be considered as unstable. However, if in this example, the other configuration is unstable too, but moving in the opposite direction, the overall system can be stabilized by continuous switching between the two unstable configuration. This is illustrated in figure 3.5

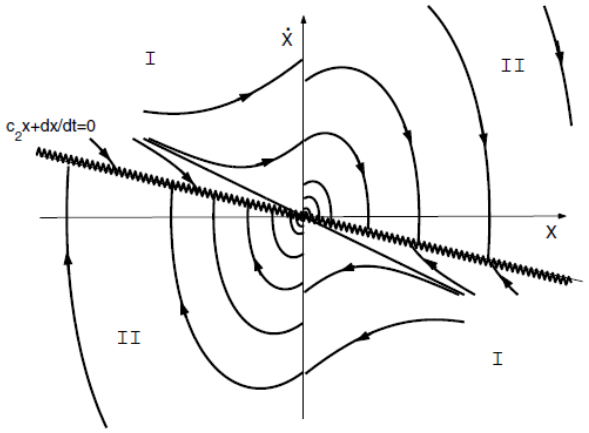

Figure 3.5: Illustration of a sliding manifold between two unstable configurations of a system [11]

This figure illustrates two systems I, and II, which are each unstable in itself, such that the system would move away from zero along the illustrated lines, which is especially true for system I. A switching manifold is depicted with a negative slope, which is required for system stability reasons to ensure that the states move toward origin. The controller would switch such that the states move towards the sliding manifold from either side and stay there once they have reached it. This phase is called the reaching mode, and once the states have reached the sliding manifold, they slide in direction to the origin, which is called the sliding mode.
Hence, in Sliding-Mode Control, two distinct modes can be defined:

1 Reaching Mode:
Starting from an initial point x_0 away from the sliding manifold ($\sigma(x_0) \neq 0$), the states move monotonically to the sliding manifold, and once they reach there:

2 Sliding Mode:
Once the states have reached the sliding manifold ($\sigma(x) = 0$) and remain there hereinafter

Since the sliding manifold generally does not vary, the dynamics of the controlled system remain the same during sliding mode, regardless of the non-linearity and disturbances of the plant. However, ideal sliding mode is only possible in theory. Since real systems have actuation with only limited bandwidth, they can only switch with some delay and the states ”overshoot” a bit before the switching controller forces the states back towards the sliding manifold. This, overall, creates the unfavorable property of sliding mode control, which is denoted as chattering.

One of the main advantages over other control schemes have been reported as the robustness of the scheme.
The static switching term can be designed such that it cancels out any disturbance or modeling error, which explains the robustness feature.

The following sections give a brief introduction into sliding-mode control design and elaborates its robustness feature more in detail.

Sliding-Mode Control Design

To begin with Sliding-Mode Control design, a hyperplane as the sliding manifold needs to be designed.
It is defined as:

$$\sigma(x) = S \cdot x = 0 \tag{3.126}$$

Once the states are on the sliding manifold, it is assumed that they remain there and slide along it where they approaches the origin of the state plane in finite time.
Therefore, the time derivative of the switching function equals zero:

$$\begin{aligned} \dot{\sigma} = 0 &= S \cdot \dot{x} \\ &= S \cdot (A \cdot x + B \cdot u_{ctrl}) \end{aligned} \tag{3.127}$$

solving for u_{ctrl} gives:

$$u_{ctrl} = -\left(SB\right)^{-1} SAx \tag{3.128}$$

which is denoted as the equivalent control and will be marked as u_{equ} hereinafter.
It is obvious that this control law requires the states as a feedback, and that an observer becomes necessary.
To ensure that the states reach the sliding manifold from any arbitrary position in finite time, a switching term is introduced. The derivation of this term is based on the Lyupanov stability theorem, with a Lyupanov function candidate, of which one of the most popular ones is:

$$V = \frac{1}{2} x^T \cdot P \cdot x \tag{3.129}$$

with a positive definite matrix P, and a derivative as:

$$\dot{V} = x^T \cdot P \cdot \dot{x} \tag{3.130}$$

where $\dot{x}$ can be replaced by the linear state-space formulation as 3.18. Then, the nonlinear system is stable if:

$$\dot{V} < 0 \tag{3.131}$$

With this definition, convergence of a state towards the sliding manifold can be states as:

$$V = S^T \cdot P \cdot S \tag{3.132}$$

whilst satisfying

$$\dot{V} < 0 \tag{3.133}$$

fulfills the reaching property. It is then easy to show that

$$u_{nl} = -k \cdot sgn(\sigma(x)) \tag{3.134}$$

satisfies the above criterion for any k greater than any uncertainty.
The overall Sliding-Mode Control law then becomes:

$$u_{SMC} = u_{equ} + u_{nl} \tag{3.135}$$

If the frequency of the switching term is high enough, then the states remain around a the sliding manifold in a small range at any time.
Despite its easy design and robustness feature, the switching term often causes an unwanted chattering effect, which might in some cases lead to undesired effects. Remedies are using a ramp function around the sliding manifold instead of a signum function to ensure that the switching magnitude is smaller the nearer the states are at the manifold.

Sliding-Mode Control Robustness

As shown in the design overview in the previous section, Sliding-Mode Control is known for its robustness against uncertainties due to the switching function.
However, this is only true, if the uncertainties are located in the input ports of the controlled system.
Suppose, a system has a disturbance $h(x,t)$:

$$\dot{x} = Ax + Bu + Dh(x,t) \tag{3.136}$$

Robustness of Sliding-Mode Control against any disturbance $h(x,t)$ is ensured and sliding mode on manifold $\sigma(x) = 0$ is unaffected if the matching condition holds, as expressed in the following theorem ([28]):

Theorem 10. *The sliding mode on manifold $\sigma(x) = 0$ is entirely insensitive to the uncertainty $h(x,t)$ if:*

$$rank(D) \subset rank(B) \tag{3.137}$$

As it can be seen, if a disturbance does not comply with the matching condition, then this control-scheme is not resistant against this disturbance. Such a disturbance is called unmatched disturbance.

Sliding Mode for Discrete Systems

The theory of sliding mode control introduced above accounts for continuous time systems as well as for discrete-time systems although some differences and special features of the latter one exist that will be introduced in this section.
First consider again a discrete time linear and time-invariant system, as:

$$\begin{aligned} x_{k+1} &= Ax_k + Bu_k \\ y_k &= Cx_k + Du_k \end{aligned} \tag{3.138}$$

and as for the switching law with the sliding manifold S, as:

$$\sigma_k = S \cdot x_k \tag{3.139}$$

hence:

$$\sigma_{k+1} = S \cdot x_{k+1} \tag{3.140}$$

gives

$$\sigma_{k+1} = S\left(Ax_k + Bu_k\right) \tag{3.141}$$

Setting $\sigma_{k+1} = \sigma_k = 0$ and solving after u_k one obtains the linear control law:

$$u_k = -(S \cdot B)^{-1} S \cdot A \cdot x_k \tag{3.142}$$

It is again easy to see the state feedback of this scheme.
Inserting this control law into the function 3.141 shows that the sliding manifold is reached after one time-step. This additionally implies that a switching term can be omitted in discrete sliding mode control, which is a fundamental difference to continuous sliding mode control. This was pointed out by Hui and Zak ([57]) who furthermore stated that a switching law in the control scheme would impair the robustness of the controller.

Despite of this, several reaching schemes for discrete sliding mode control have been discussed in the past, of which the most important ones will be introduced here:

- **Sapturk**
  The Sapturk ([34]) reaching scheme as one of the simplest schemes is derived from the continuous time sliding mode condition:

  $$\dot{s}_i(x) s_i(x) < 0 \tag{3.143}$$

  which is translated into its discrete-time counterpart:

  $$[s_i(k+1) - s_i(k)] s_i(k) < 0 \tag{3.144}$$

  This however is a necessary but not sufficient condition and therefore this condition may still allow a chattering around the i^{th} sliding surface with increasing amplitude.
  To prevent this instability, a condition was suggested, which allows for both, sliding motion and convergence onto the hyperplane toward the origin, and it is stated as:

  $$|s_i(k+1)| < |s_i(k)| \tag{3.145}$$

  This can be reformulated as:

  $$\begin{aligned} |s_i(k+1) - s_i(k)| sgn(s_i(k)) &< 0 \\ |s_i(k+1) + s_i(k)| sgn(s_i(k)) &> 0 \end{aligned} \tag{3.146}$$

The first condition is for ensuring that the sliding manifold is reached in finite time, while the second ensures that the closed-loop system does not move too far away from it, which creates a quasi-sliding mode within an upper and lower bound around the sliding manifold.
The control-law suggested by Sapturk is then:

$$u(k) = -K(x, s_i)x(k) \tag{3.147}$$

where K is defined as:

$$K_{i,j} = \begin{cases} K_{i,j}^{+} & \text{if } s_i(k)x(k) > 0 \\ K_{i,j}^{-} & \text{if } s_i(k)x(k) < 0 \end{cases} \tag{3.148}$$

- **Gao**
Similar to the Sapturk scheme, the Gao ([34]) reaching scheme has been derived from a continuous scheme and discretized.
For a reaching scheme, the following attributes were desired and are recited below from the original text:

1. "Starting from any initial state, the trajectory will move monotonically toward the switching plane and cross it in finite time"
2. "Once the trajectory has crossed the switching plane the first time, it will cross the plane again in every successive sampling period, resulting in a zigzag motion about the switching plane"
3. "The size of each successive zigzagging step is non-increasing and the trajectory stays within a specified band"

Beginning with a reaching law for a continuous system defined as:

$$\dot{s}(t) = -\epsilon sgn(s(t) - qs(t)),\ \epsilon > 0, q > 0 \tag{3.149}$$

an equivalent reaching law for discrete systems has been then defined as:

$$s(k+t) - s(k) = -q^T s(k) - \epsilon T sgn(s(k)),\ \epsilon > 0, q > 01 - qT > 0 \tag{3.150}$$

where T is the sampling period.
With this reaching law, all the desired attributes listed above are satisfied, where k and q are tuning parameters.
The control law can be now derived as follows:

Given a linear switching function

$$s(x) = c^T x \tag{3.151}$$

the equivalent control can be obtained as:

$$u_c = -(c^T b)^{-1} c^T A x(k) \tag{3.152}$$

Then the incremental change of $s(k)$ is:

$$s(k+1) - s(k) = c^T x(k+1) - c^T x(k) = c^T A x(k) + c^T B u(k) - c^T x(k) \tag{3.153}$$

By comparison with the equation above, which gives

$$s(k+1) - s(k) = -qTs(k) - \epsilon T sgn(s(k)) = c^T A x(k) + c^T B u(k) - c^T x(k) \tag{3.154}$$

one can obtain the control law:

$$u(k) = -(c^T b)^{-1}[c^T A x(k) - c^T x(k) + qTc^T x(k) + \epsilon T sgn(c^T x(k))] \tag{3.155}$$

- **Bartoszewicz**
  Bartoszewicz suggested a scheme ([12]) whose reaching law approaches the sliding manifold in finite time, but stays in a vicinity around it such that the subsequent sliding mode is only a quasi-sliding motion parallel to the manifold. This reduces chattering since frequent crossing of the sliding manifold is avoided. Furthermore, in his paper, he suggests that his reaching mode brings more robustness than the Gao scheme, introduced above.

  The Bartoszewicz reaching law is defined as follows:

$$s(k+1) = d(k) - d_0 + s_d(k+1) \tag{3.156}$$

  with $d(k)$ as:

$$d_l <= d(k) = c^T \Delta A x(t) + c^T f(k) <= d_u \tag{3.157}$$

  where d_l and d_u are the lower and upper bound of the disturbance and ΔA are the parameter uncertainties. $f(k)$ denotes external disturbances.
  By further defining

$$d_0 = \frac{d_l + d_u}{2} \; \delta_d = \frac{d_u - d_l}{2} \tag{3.158}$$

  and $s_d(k)$ an a priori defined function, such that the following holds:

$$\begin{aligned} \text{If} \quad s(0) > 2\delta_d, & \qquad \text{then} \\ s_d(0) = s(0) & \\ s_d(k) \cdot s_d(0) \geq 0 & \qquad \forall \quad k \geq 0 \\ s_d(k) = 0, & \qquad \forall \quad k >= K^* \\ |s_d(k+1)| < |s_d(k)| - 2\delta_d, & \qquad \forall \quad k < k^* \end{aligned} \tag{3.159}$$

As a possible definition for $s_d(k)$ for $s(0) > 2\delta_d$ is:

$$\begin{gathered} s_d(k) = \frac{k^* - k}{k^*} s(0) \\ k^* < \frac{s(0)}{2\delta_d} \end{gathered} \tag{3.160}$$

$$\begin{gathered} s(k+1) = c^T Ax(k) c^T \Delta Ax(k) c^T bu(k) c^T f(k) \\ s(k+1) = c^k Ax(k) + d(k) c^T bu(k) \end{gathered} \tag{3.161}$$

and compared with the reaching law:

$$s_d(k+1) - d_0 = c^T Ax(k) + c^T bu(k) \tag{3.162}$$

the following sliding-mode control law is obtained:

$$u(k) = -(c^T b)^{-1}[c^T Ax(k) + d_0 - s_d(k+1)] \tag{3.163}$$

Then for any $k >= k^*$, the following inequality holds:

$$|s(k)| = |d(k-1) - d_0| \leq \delta_d \tag{3.164}$$

All these schemes can be easily implemented in a control algorithm, where a linear equivalent control u_{equ} already exists. In accordance to the statements of Hui and Zak [57], where the non-linear switching term should be avoided if not necessary, an extensive Sliding-Mode Control scheme can be devised with one of the reaching laws above for the switching term that is activated if necessary (e.g. to increase control performance far away from the sliding manifold) and deactivated if not required. The basic control scheme would then be an ordinary linear state-feedback controller, whose gains are found by sliding mode control theory.

Chapter 4

Control in Automotive Application

4.1 Linear Control

Different kinds of control concepts are found nowadays in the automotive industry and automotive research.
Use of static maps is predominantly used for feed-forward control and for estimating the amount of fuel injected, depending on either the intake mass-flow signal or the intake pressure as a feedback signal. In the same manner, ignition timing, if no unwanted engine knocking occurs, is usually read from a map in dependency of the engine speed for instance.
Often, these maps are accompanied by simple output control as PID control, and this scheme is often used where no stringent control requirements exist and where simple controller tuning methods are desired. This may be for control of idling speed for example where the engine speed should be as low as possible, but at the same time, not be interrupted of even stall due to unpredictable loads from air conditioner, heater, and others. In such a case, pure feed-forward control would not be enough. In some cases, however, PID control may be unsuitable. Since, for example, the PID controller cannot compensate for the time-delay due to film formation of the fuel in the intake port before it enters the cylinder, a state-space based control for engine idling was suggested in [76]. Here, the time-delay of one engine cycle was included in the model for control design. LQG control was also suggested for driveline control. Contrary to that, a PI control for air/fuel ratio is introduced in [2] and to overcome the time-delay difficulty, the PI controller was extended by a Smith-Predictor.
A robust model-based H_∞ controller for air/fuel feedback control in order to adapt the bandwidth of the controller with changing operating points was demonstrated in [42]. This SISO system was extended to a MIMO to an engine speed controller and compared with a two-SISO loops as an industrial solution. In experiments, it was found that the robust H_∞ controller performed better at external load-step disturbances at idle speed.
A robust H_∞ controller for air/fuel ratio was also suggested in [24], where based on a control-oriented model, structured disturbances were modeled, and directly included in the robust control design.
In [91], a PI controller was extended with a mean-value engine model for feedforward control for controlling of engine torque, where stability was assured by Lyupanov analysis and the results were shown in simulation.
With the popularity of downsized gasoline engines, control of turbochargers have drawn attention to researchers. A model-based MIMO state controller for controlling an electronic intake

throttle in combination with a wastegate control was presented in [25], and a coordinated two-loop approach with P and PI controllers was presented in [103]. An H_∞ controller for the airpath pressure for the intake throttle and turbocharger was suggested in [41]. In the design, frequential identification by using sine-inputs at different frequencies was done to estimate the uncertainty model.
A robust controller for a diesel fuel-metering system was presented in [53] where uncertainty descriptions were obtained by linearization of a non-linear plant around different temperatures. With three linearization points, of which the nominal was in the middle of these temperature ranges, the relative uncertainty could be computed.
With new gasoline engine technologies, such as lean NO_x trap (LNT) aftertreatment systems, new challenges in engine control emerge. In LNT control, switching between lean combustion and stoichiometric modes for purging the LNT filter become necessary. Modeling and control strategies are addressed in [62] and [64].
However, with the advantages a linear output or state controller might bring, it is usually limited to a limited operational area around the operating point it was designed for. It is well-known that including robustness into the control design might alleviate degradation of linear controllers due to linearity issues, another technique to combine linear controllers for different operating points has been used in automotive control extensively. This technique is known as Gain-Scheduling, where the gains of controllers are connected with varying operating conditions. Gain scheduled controllers for charge control for example, based on Linear Parameter Varying (LPV) approaches was presented for SI in [3] and of a Diesel in [88].

4.2 Sliding-Mode Control

Apart from classical state-control and modern H_∞ control schemes, Sliding-Mode Control (SMC) has been popular in automotive applications as well.
[44] discusses different possible applications in automotive control, of SMC for online optimization, disturbance and state estimation and friction compensation. It is reported that the challenge in automotive control problems are normally highly nonlinear and affected by disturbances and uncertainties. This was reported as a motivation for sliding-mode control. Examples are given with a comprising control strategy for traction control with a sliding mode spark timing controller. Further examples are given for a position control of a throttle body, including friction compensation.
A throttle controller for a drive-by-wire system on a racing motorcycle engine, based on discrete-time sliding mode controller with an observer, is presented in [13]. The control problem was reported as challenging since the throttle was not directly actuated by an electrical motor but linked over several linkages and joints in order to fit the throttle-body into a system with tight space. Due to the numerous linkages, the mathematical model has become complicated and the system highly non-linear. Also here, friction as a disturbance was reported as critical for a smooth operation of the throttle body. It was shown in experiments that the proposed controller handled disturbances well with only small overshoot. The discrete-time sliding mode observer was found to be very similar in terms of performance in comparison to a continuous time sliding-mode observer, although the latter one showed better performance of the output estimation error.
An adaptive sliding-mode control concept for control of the air/fuel ratio was presented in [117].

In this work, update laws were introduced to reduce the control gains, which needed to be increased if uncertainty is large. With this approach, tracking performance could be improved despite of time-delays in the system. Furthermore, the tracking problem was considered in the design by designing the sliding manifold as the error of the error between the reference and actual air/fuel ratio. By using a Lyapunov function, a non-linear mean-value model was incorporated and adaption schemes for the volumetric efficiency. The adaption scheme has been further extended to two modeling parameters of the fuel time delay.
An SMC control for idling control of an SI combustion engine was introduced in [28]. Good disturbance rejection from activating the electric drive fan and headlights, heater and rear window defroster was shown in experiments on a real engine.
In [14] it was stated that with the advancement of model-based design and higher computation power, more sophisticated robust controllers may become more popular. This comes together with the higher burden of more model-calibration parameters, such that a trade-off between model accuracy and robust control performance is desired. Robustness of a controller was also reasoned with the broader range of operating points that a single robust controller can cover, unlike heuristic tuned output controllers.
This is depicted in the following picture 4.1:

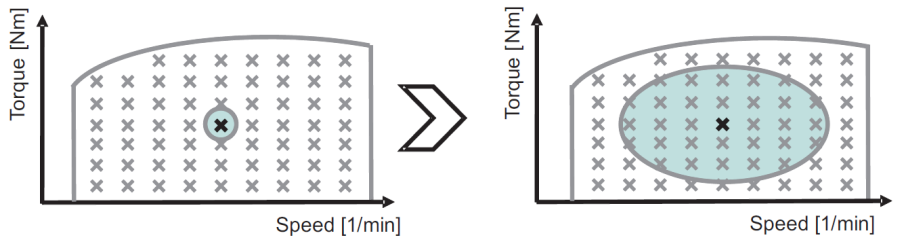

Figure 4.1: Schematic comparison of operating ranges of heuristically tune PI or PID controllers (left) and robust SMC controller (right); from [14]

Sliding mode control has been also reported as an online estimation concept for on-board diagnostic applications. An on-line estimator for the indicated engine torque is introduced in [33], and an overview over further concepts is given in [77].

Apart from sliding-mode control for robust control of a combustion engine, other automotive applications have been reported as well.
An observer for a truck trainer was published in [59] with the observed states as lateral velocity of the tractor, yaw rates of tractor and trailer and the articulation angle, which also served as the measured output. The model used here was linearized around a constant longitudinal speed, and the task is to track the states during a driving maneuver with the steering angle of the front tires of the tractor. The model has been additionally discretetized in order to compare continuous time and discrete time sliding mode observers, where both have shown very short response time in tracking error, however, the discrete-time observer has shown oscillations due to the dead-beat character.
An observer for a drive-by-wire vehicle steering system has been published in [122] as well. The motivation of using a sliding-mode controller was due to the system non-linearities of vehicle steering system states.
[79] compared internal model control (IMC) with a sliding mode control in simulation. Here,

it was shown that both controllers worked well in terms of disturbance rejection and reference tracking. On the other hand, it was found that the SMC was less aggressive than the IMC, despite of same performance. In turn, the sliding-mode control has shown some chattering, which was stated as a possible concern.
A further introduction of sliding mode control in automotive control engineering, for control of an ABS (antilock breaking system), and TCS (traction control system) is presented in [2]. In this example, for a traction control, switching functions for accelerating and for braking, depending on the tire slip $\lambda = \frac{\omega_w - \omega_v}{\omega_v}$ are defined and a simple switching logic, depending on the sign of the switching logic, are presented.

4.3 Control in HCCI engines

Several control approaches have been suggested in the past in automotive engineering, and for example, different advanced control schemes for air/fuel control exist since tight control is critical for reducing emissions. On the other hand, HCCI is still a fairly new combustion concept, and reports and publications for controllers suggested for controlling HCCI combustion are rather limited.
An early paper for closed-loop HCCI control [61], introduces a closed-loop control of an HCCI engine with the use of two fuels for combustion control and PID controllers for CA_{50} and $IMEP$ control. It was stated that the controller gains had to be conservative to avoid instability and experiments have shown that the controller acts rather slow.
A more advanced PID concept was presented in [93], where the PID gains were obtained online by an extremum seeking (ES) algorithm. It was stated that ES might be a suitable approach for gain-scheduling of the PID controllers and that the gains can be effectively be found by this algorithm. By using this algorithm online during stationary engine phases, it was further stated that ES can reduce fuel consumption by including this in the optimization algorithm dynamically during engine operation. The effectiveness of the controller, together with feed-forward control, was demonstrated in experiments.
[15] gives a comprehensive overview about 0-dimensional modeling for control, with a comparison of different ignition models for HCCI, and system identification to obtain a linear state-space model for control design. In this publication, static non-linearities were identified and included in the linear control design for compensation. As for the linear state-space model, it was stated that a second-order model was sufficient to capture the HCCI combustion dynamics. This shown with Hankel singular values of the identified linear model. A PID controller for control of CA_{50} was tested in experiments and was found to be able to track the reference values around one operating point. However at later phasings, the control performance drastically decreased, which was accredited due to the non-linearity of the HCCI engine. It was furthermore stated that at another operating point the closed-loop system showed limited bandwidth and the controller performance decreased drastically. With the parameterization of the first operating point, it was even reported that the PID controller could not be used in the second operating point, due to instability problems.
In comparison to that, a Model-Predictive Control (MPC) was tested, which has shown superb tracking performance, where a step-response could be achieved within 5-6 engine cycles.
Furthermore, the motivation of designing a MIMO engine model for control was addressed. Here, it was stated that simultaneous control of CA_{50}, the load $IMEP$ and to avoid too much noise, a sub-model for prediction of pressure-rise rate during combustion was desirable. An

MPC controller was employed in tests. It was concluded that the MPC controller gave the best results in terms of performance and robustness, although it was additionally stated that gain-scheduling of several linear controller may be necessary to cover all necessary operating points.
A similar approach with MPC for combustion control is shown in [66] and [8]. Here, an introduction into modeling of HCCI engines is given, and different ignition models for HCCI are presented, after which an MPC controller for control of combustion phasing CA_{50} is introduced, based on a cycle-resolved physical engine model. On an engine testbench, it was shown that the controller was able to track CA_{50} and that it had good disturbance rejection capabilities.
In order to overcome non-linearities of an HCCI engine and the different temperature dynamics inside the cylinder with different combustion phasing, a switching controller was suggested in [56]. Here a non-linear physical engine model was linearized at three different operating points between very early and very late phasing and the control-oriented model was linearized around these points. Thereby, a linear LQR controller was synthesized with three different control gains with the aim of switching between the three gains during operations. The linear model has been compared against a model which switches between the three linear models and compared to an engine testbench where it could be shown that the switched engine model showed better agreement with the test-data.
A model-based control of an NVO HCCI engine, where cause and compensation of non-linearity issues was discussed, is presented in [98]. Here, amount of fuel for $IMEP$ control, and intake-valve closing (IVC) together with exhaust-valve closure (EVC) was selected for combustion phasing control. Although it might be intuitive to use the crank angles for IVC and EVC as a controller-output, it was shown in simulation that by using the cylinder volume as controller outputs instead avoids non-linearities and the controller performance could be improved substantially. The effectiveness of the state-controller with Kalman Filter was tested in experiments on a multi-cylinder engine. This four-cylinder engine had fully flexible VVA systems for each cylinder individually, and it could be shown that the combustion stability could be improved and cyclic-variability reduced by closed-loop control.
In order to address the non-linearity issues of HCCI combustion control, [23] suggested a non-linear controller with a non-linear observer based on a positive semidefinite Lyapunov function with a simplified engine model. The performance of the proposed controller was demonstrated in simulation.
A control-oriented physical model for NVO systems with split injection for CA_{50} control has been presented in [96] and [95]. In order to consider the effect of injection timing during re-comopression on combustion phasing, the ignition model was extended to injection timing as a further input. This model was linearized and a state-controller with a feed-forward term was presented, and it was shown in experiments that the controller with injection timing as a control actuator for combustion phasing could favorably regulate CA_{50} and reject disturbances due to $IMEP$ tracking requirements.

A crank-angle resolved model for a two-stroke HCCI engine was proposed in [87], and two discrete-time PI controllers for control of $IMEP$ and CA_{50} with feed-forward maps were presented. Simulation results have shown that the controllers were able to track $IMEP$ requirements while keeping combustion phasing CA_{50} in a required range.
A modeling approach and an LQG controller with a Kalman filter for an NVO HCCI engine with turbo-charger was presented in [10]. The model for prediction of CA_{50} was fitted to experimental data, and the inverse of this fitted equation was used as a feed-forward controller,

together with other parts of the engine model. By using split-injection for combustion phasing control, cylinder balancing could be achieved, and CA_{50} could be kept at a designated reference, while large $IMEP$ steps were tracked.
An LQG controller with a Kalman filter for control of a multi-cylinder HCCI engine for a driving cycle was reported in [38]. A Fast Thermal Management (FTM) for combustion control was used here, on a multi-cylinder engine with variable compression ratio (VCR), which broaden the FTM's bandwidth at higher engine speed. The controller was synthesized using systems identification and tested on an EC2000 driving cycle. In a similar work, a PID controller was reported in [39] for control of combustion phasing of an HCCI engine with VCR and in [40] with FTM.
Further examples for linear state controller obtained from thermodynamic and non-linear engine models are presented for NVO HCCI engines are presented in [97], and in [99], it could be shown that the closed-loop controller could reduce cycle-to-cycle variability of combustion, especially at later combustion phasing.
Based on the work by Ravi et al. a control-oriented model was devised in [125] and with this model, a model-based closed-loop controller was developed and tested in [110]. Similar work was done in [78] where a control-oriented model similar to Ravi et al. was developed but difficulties in linearization was reported.
In [70], stability analysis of HCCI combustion was done on an NVO HCCI engine, and after the stable operating points were identified, and a closed-loop control with cold external EGR and NVO as actuation. The controller was investigated for cylinder balancing control, idling control and switch between SI and HCCI.
[92] presents closed-loop control of air/fuel ratio and CA_{50} simultaneously with two PI controllers of an exhaust gas re-breathing HCCI engine. The intake throttle was used for the air/fuel ratio control, and a throttle for cold external EGR was used for control of combustion phasing. In another setting, the CA_{50} controller was augmented by a combustion efficiency feedback signal in which a threshold calculation limits the introduction of EGR. If cycle-to-cycle variations become too big, the combustion efficiency threshold on the controller is reached and the controller closes the EGR throttle of EGR a little bit. In experiments on a single-cylinder engine it could be shown that the closed-loop control for combustion phasing via cold EGR could track CA_{50} step changes fairly fast in less than 50 cycles, which in turn caused disturbance on the air/fuel ratio. This was handled by the second controller, which brought back the air/fuel ratio to its desired value, which was at range of nearly 200 engine cycles. Furthermore, the late combustion phasing control was investigated, which normally has high cycle-to-cycle variations, and it is desired to reduce those by means of feedback control. It could be shown that the augmented controller could handle the variations much better than the other one. However, the control performance in comparison to open-loop control was not shown in this publication. Nonetheless, this publication presented the effectiveness of cold EGR for combustion control of HCCI engines, and this actuation was found to be fairly fast.
For attenuation of strong cyclic variation at late combustion phasing, several closed-loop control strategies were reported. In [48], the cause of variability was investigated, of which the findings could be included in modeling for control to obtain a controller, which reduces the cyclic variability. In this paper, it was stated that imperfect combustion and fuel residuals are carried over to the next cycle, which in turn impact the combustion of this subsequent cycle. Therefore, a cyclic coupling through not only temperature but also through carried over unburned fuel mass was identified. A model which captures the recycling of the unburned fuel fraction is presented

in [30], and a controller with fuel injection timing for reducing cyclic variations was presented in [29].
In a report of University of Michigan [4], a machine learning algorithm was implemented on the low-cost hardware system Raspberry Pi in a Linux environment, and it was shown in experiments that the control algorithm could reduce the cyclic variations remarkably.
Contrary to all the control concepts presented above, in [73], a non-linear control approach based on Artificial Neural Networks (ANN) was presented. In this work, detailed results and insights from a CFD combustion model were first applied on a 1-D simulation model, which was further reduced to a non-linear Artifical Neural Networks (ANN) for predictive control of combustion phasing. Although, the approach presented in this paper may give good control results, the controller may be too complex for online-optimization, especially due to its non-linear nature, and no test results were reported.
Contrary to using non-linear neural networks for control alone, in [65] a closed-loop control was optimized by introducing adaptions with neural networks.

Use of a real-time capable, crank-angle resolved 0-D model with pressure wave action for HCCI control was proposed in [68]. The model was implemented as rather an observer for estimating the engine states.
While this control concept may be able to control HCCI combustion, it may be rather judged that the computation overhead is too high for real-time implementation of the controller on an actual ECU hardware and this concept might be interesting in the future when the hardware gets more computation power.

Chapter 5

Experimental Set-Up

The engine under consideration is an HCCI engine with BDSC functionality. It is based on a Honda 4-cylinder inline engine, with a bore and a stroke of $89mm$ each and a compression ratio of 11.5. Each cylinder is equipped with a port fuel-injector, and the exhaust ports are connected to a 4-2-1 exhaust system, which couples two cylinders pairwise through an exhaust pipe. Although this engine features four cylinders in its original setup, a reduced version with only two active cylinders has been designed as well for basic analysis of BDSC HCCI. In this particular engine, the valves for the two middle cylinders are deactivated that hinder mass-flow through the cylinders, and the injectors were removed. With the BDSC concept in mind, it is clear that a single-cylinder version for BDSC HCCI cannot be operated and the minimum of two cylinders is required.
The engine has been prepared with valve lifts that were specifically designed for BDSC HCCI, which required low intake valve lift and a re-opening of the exhaust valve after intake stroke. To cover all possible engine loads for HCCI, three different intake valve lifts were designed where the lowest valve lift was designed for low engine load and the the largest valve opening for the highest load. The overall valve-lift setting is depicted in 5.1.

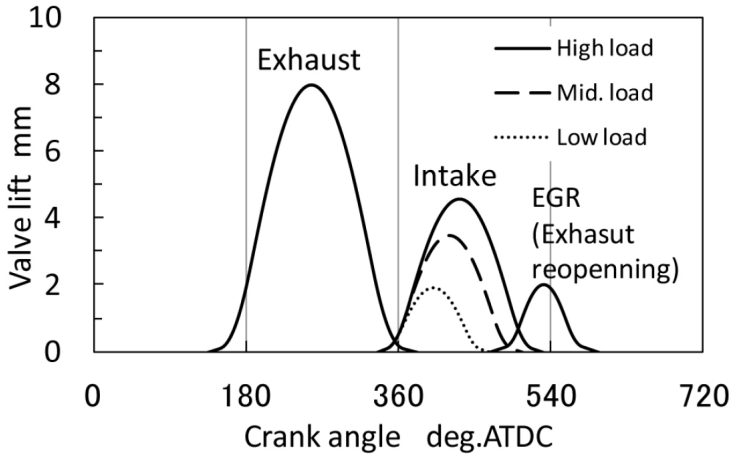

Figure 5.1: Different intake valve-lifts for different engine loads of a BDSC HCCI engine (from [119])

The different lifts for the intake valves were made possible by three different cam shafts which had to be replaced manually. No variable valve system existed which could be actu-

ated online. This was different for re-breathing stroke which could be deactivated so that no re-breathing of exhaust gases would occur. The underlying technology is based on the Honda VTEC system, which makes it possible to switch between two different cam profiles. Furthermore, since the Honda VTEC system is mechanically driven, actuation is very fast and activation or deactivation of the re-breathing lift can be achieved in a time-scale of about one engine cycle. It is thereby possible to operate the engine in SI by switching the EGR-lift off, and a switch between combustion modes is possible too.
To regulate the intake pressure for SI, a throttle body was installed on the intake side, and for regulating the exhaust pressure in HCCI, an additional throttle was installed on the exhaust side of the engine. It should be noted here that the latter one is necessary for BDSC HCCI operation since at too low exhaust pressures the lower amount of re-breathed hot EGR would not suffice to trigger HCCI combustion. To control HCCI combustion, in addition to regulating the exhaust pressure, a secondary air injector was attached to the exhaust port of each cylinder, which injects cold, compressed air directly into the cylinder during exhaust re-breathing for charge-cooling and, consequently, ignition delay.
The fuel used here was common gasoline with a research octane number (RON) of 91.

The table 5.1 gives a quick overview of the most important engine parameters.

Number of Cylinders	2, 4
Bore [mm]	89
Stroke [mm]	89
ShaftLength [mm]	129
Compression Ratio [-]	11.5
Engine Speed [rev/min]	1500

Table 5.1: Engine Specification

Chapter 6

Detailed modeling of BDSC HCCI

In this chapter, modeling approaches for a detailed and crank-angle resolved simulation of an HCCI engine are introduced. First, the modeling theory is explained after which an engine model in the commercial simulation tool BOOST from AVL is presented.
After that, a control-oriented 0-D model, with pressure wave functionality is introduced. The advantage of such a modeling approach is not only the flexibility that an open modeling tool brings, where any sub-model can be implemented or existing ones simplified, but also the insight is a big advantage in research applications, since some information can be used in a more reduced mean-value model. The last point is computation speed: despite being still detailed, it is simple enough that is has potential to run in real-time. For that reason, such 0-dimensional models are well-suited for control design and the preference of control engineers and have been mentioned in numerous engine control publications ([18, 31, 37, 47, 58, 63, 75, 84, 102, 111]).

6.1 Theory

Common simulation models are based on conservation of energy, conservation of mass and if gas dynamics are involved, conservation of momentum. Since the volume of the cylinder is changing with crank angle, an equation for the volume and volume rate becomes additionally necessary. Further required sub-models are for mass-flow over the intake- and exhaust valves, a wall-heat transfer model, and a combustion model for prediction of fuel mass burned during a cycle.
To make an entire engine model complete, models based on conservation principles for the intake and exhaust manifolds are required. In order to implement HCCI simulation capabilities, a model for predicting start of combustion is necessary.

The displacement volume and the necessary volume rate can be computed via the slider-crank formula:

$$V(\theta) = 1 + \frac{1}{2}(r_c - 1)[R + 1 - cos\theta - (R^2 - sin^2\theta)^{\frac{1}{2}}] \tag{6.1}$$

and the volume rate as:

$$\dot{V}(\theta) = \frac{\pi}{4} B^2 a \dot{\theta} sin\theta \left(1 + a \frac{cos\theta}{\sqrt{L^2 - a^2 sin^2\theta}}\right) \tag{6.2}$$

As it can be seen, the volume depends on the engine parameters, which remain fixed during simulation, and the crank-angle, which is changing in this work at a fixed engine speed. Hence, a model for crank-shaft, inertia, and other mechanical models are not required.

Mass-flow through the valves can be calculated as a compressible flow through an orifice ([52]). Due to the fact that gas is compressible, flow through an orifice is limited when the gas velocity reaches speed of sound at the narrowest part (”throat”) of the orifice. This phenomenon is called ”choking” and occurs if the pressure before and after the orifice which drive the flow reach a critical ratio.
The equation employed in this work is for unchoked flows:

$$\dot{m} = \frac{C_D A_R p_0}{\sqrt{RT_0}} \left(\frac{p_T}{p_0}\right)^{\frac{1}{\gamma}} \left[\frac{2\gamma}{\gamma - 1}\left[1 - \left(\frac{p_T}{p_0}\right)^{\frac{\gamma-1}{\gamma}}\right]\right]^{1/2} \tag{6.3}$$

and choked flows:

$$\dot{m} = \frac{C_D A_R p_0}{\sqrt{RT_0}} \sqrt{\gamma} \left[\frac{2}{\gamma + 1}\right]^{\frac{\gamma+1}{2(\gamma-1)}} \tag{6.4}$$

The flow is unchoked when the ratio of upstream pressure to downstream pressure is above a limit as defined as:

$$\frac{p_T}{p_0} > \left(\frac{2}{\gamma + 1}\right)^{\frac{\gamma}{\gamma-1}} \tag{6.5}$$

and the flow is choked otherwise.

By defining the internal thermal energy as a function of temperature:

$$U = m \cdot c_v \cdot T \tag{6.6}$$

and the enthalpy, which is internal energy plus a mechanical work contribution from pressure and volume as:

$$H = U + p \cdot V \tag{6.7}$$

The equation for Conservation of Energy can be derived:

$$\frac{d(m_c u_c)}{dt} = \dot{W} + \dot{Q}_c - \dot{Q}_w + \sum (\dot{m}h)_{valves,i} \tag{6.8}$$

The only mechanical work found in the cylinder is the changing cylinder volume due to the movement of the piston, which causes mechanical work by compression or expansion.
It is defined as:

$$\dot{W} = -p \cdot \dot{V} \tag{6.9}$$

where the change of volume is taken from equation 6.2 and p the in-cylinder pressure.

Combustion can be modeled in many ways, where for HCCI a detailed combustion chemistry

a tabulation technique was suggested in [108] to reduce computation time, or in a global two-step reaction scheme based on [20], as presented in [115]. In order to keep the modeling effort and model complexity in this work low, the combustion model modeled by a Wiebe Function ([36, 52]) was selected here, which reads:

$$x_b(\theta) = 1 - exp\left[-a\left(\frac{\theta - \theta_0}{\Delta\theta}\right)^{m+1}\right] \tag{6.10}$$

and the derivative of the Wiebe function becomes:

$$\frac{dx_b}{d\theta} = a(m+1)\left(\frac{\theta - \theta_i}{\Delta\theta}\right)^{m} exp\left[-a\left(\frac{\theta - \theta_i}{\Delta\theta}\right)^{m+1}\right] \tag{6.11}$$

This equation can be converted to $\frac{dx_b}{dt}$ by using the inverse of $\frac{d\theta}{dt}$.
The heat released from combustion is calculated by using the derivative of the Wiebe function 6.11, and the amount of energy for fuel LHV:

$$\frac{dQ_c}{dt} = \dot{x_b} \cdot m_{fuel,ign} \cdot LHV \tag{6.12}$$

where $m_{fuel,ign}$ is the total amount of fuel before combustion. With this approach, and using the value of 6.9 for the constant a, complete combustion is assumed and the Wiebe function converges to the value of one 6.10.

To account for heat losses during high in-cylinder temperatures and heating of the gas after a gas exchange, a model for heat transfer with the cylinder walls is needed. A general approach for heat exchange is:

$$\frac{dQ_W}{dt} = h_c \cdot A_w \cdot (T - T_w) \tag{6.13}$$

Heat transfer due to radiation is commonly neglected, especially in HCCI engines, where the temperature levels are too low and heat transfer due to convection dominates ([52]).
In this equation, A_w is the instantaneous cylinder wall surface as a function of crank angle, T the temperature of the gas inside the cylinder, T_w the cylinder-wall temperature, and a transfer coefficient h_c. This transfer coefficient is commonly modeled by the Woschni correlation [124] as:

$$h_c(W/m^2 \cdot K) = 3.26B(m)^{-0.2}p(kPa)^{0.8}T(K)^{-0.55}w(m/s)^{0.8} \tag{6.14}$$

with

$$w = \left[C_1\bar{S}_p + C_2\frac{V_d T_r}{p_r V_r}(p - p_m)\right] \tag{6.15}$$

and the constants:

$$\begin{aligned} &C_1 = 6.18, C_2 = 0 && \text{for the gas exchange period} \\ &C_1 = 2.28, C_2 = 0 && \text{for the compression period} \\ &C_1 = 2.28, C_2 = 3.24 \cdot 10^{-3} && \text{for the combustion and expansion period} \end{aligned} \tag{6.16}$$

An alternative, often employed correlation is that from Hohenberg [54], which reads:

$$h_c(W/m^2 \cdot K) = 130 \cdot B(m)^{-0.2} p(kPa)^{0.8} T(K)^{-0.55} w(m/s)^{0.8} \tag{6.17}$$

Hohenberg has taken in reference to the Woschni correlation, taken measurements on a Diesel engine ([52]).
The wall-temperture is commonly set to $400K$ [114], however, to investigate varying wall-temperature effects in HCCI, a simplified wall-temperature model can be inserted as well, of which one is described in [85].

In order to extract combustion parameters, such as start of combustion, combustion duration, from pressure traces from experiments, the apparent heat-release rate can be obtained via the first law of thermodynamics and by including the wall heat transfer. However, the estimation of combustion parameters can be simplified by neglecting the heat-transfer coefficient and the first law of thermodynamics, which eventually gives:

$$\frac{dQ}{d\theta} = \frac{\gamma}{\gamma - 1} p(\theta) \frac{dV}{d\theta} + \frac{1}{\gamma - 1} V(\theta) \frac{dp}{d\theta} \tag{6.18}$$

γ is the polytropic compression coefficient, where as a simple approach, wall-heat losses can be considered by adjusting this coefficient.

Internal energy U and enthalpy H can be both calculated from the temperature as:

$$\begin{aligned} U &= m \cdot c_v(T) \cdot T \\ H &= m \cdot c_p(T) \cdot T \end{aligned} \tag{6.19}$$

where the temperature-dependent heat capacities $c_v(T)$ and $c_p(T)$ are calculated from polynomials, with coefficients from NASA tables ([52]).
The polynomial reads:

$$\frac{c_p}{R} = a_1 + a_2 T + a_3 T^2 + a_4 T^3 + a_5 T^4 \tag{6.20}$$

By knowing the volume and temperature, pressure can be calculated by the ideal gas equation:

$$p = \frac{m}{V} \cdot R \cdot T \tag{6.21}$$

with R as the specific ideal gas constant, derived from the universal gas constant:

$$R = \frac{R_u}{MW} \tag{6.22}$$

with MW as the molecular weight.
The underlying combustion chemistry is:

$$C_a H_b + \left(a + \frac{b}{4}\right)(O_2 + 3.773 N_2) = a CO_2 + \frac{b}{2} H_2O + 3.773 \left(a + \frac{b}{4}\right) N_2 \tag{6.23}$$

It can be seen that N_2 does not play a role during combustion, it is nonetheless important to track nitrogen for calculation of the heat-capacities.
Isooctane (C_8H_{18}) has been used in the analysis as a fuel-substitute, due to the properties, close to regular fuel. Hence, with $a = 8$ and $b = 18$:

$$C_8H_{18} + \phi 12.5(O_2 + 3.773N_2) = 8CO_2 + \phi 9H_2O + 58.95N_2 \tag{6.24}$$

where ϕ is defined as the fuel/air equivalence ratio:

$$\phi = \frac{(F/A)_{actual}}{(F/A)_s} \tag{6.25}$$

commonly (especially in Germany), λ is used instead, which is the inverse of ϕ and reads:

$$\lambda = \phi^{-1} = \frac{(F/A)_s}{(F/A)_{actual}} \tag{6.26}$$

In SI engines, exhaust gas is often recirculated into the intake to reduce NO_x emissions. A number which quantifies this recycled exhaust gas is the EGR (exhaust gas residual), and it is often defined in %, as:

$$EGR(\%) = \frac{m_{Exhaust}}{m_{Cylinder}} \cdot 100 \tag{6.27}$$

Here, $m_{Exhaust}$ is the total amount of exhaust gases inside a cylinder before combustion, and $m_{Cylinder}$ the total in-cylinder mass.

In order to allow for HCCI combustion, a model for prediction of start of combustion is needed. This differs from SI where the start of combustion is controlled by timing of the spark, and correlations for a ignition delay can be included [80]. For predicting the onset of combustion in HCCI, several approaches have been suggested in the literature.
The Shell autoignition model has been suggested in [16], which reads:

$$\begin{aligned}
RH + O_2 &\xrightarrow{k_q} 2\bar{R} && \text{(initiation)}\\
\bar{R} &\xrightarrow{k_p} \bar{R} + \ products\ and\ heat && \text{(propagation cycle)}\\
\bar{R} &\xrightarrow{f_1 k_p} \bar{R} + B && \text{(propagation forming B)}\\
\bar{R} + Q &\xrightarrow{f_2 k_p} \bar{R} + B && \text{(propagation forming B)}\\
\bar{R} &\xrightarrow{f_3 k_p} out && \text{(linear termination)}\\
\bar{R} &\xrightarrow{f_4 k_p} \bar{R} + Q && \text{(propagation forming Q)}\\
2\bar{R} &\xrightarrow{k_t} out && \text{(quadratic termination)}\\
B &\xrightarrow{k_b} 2\bar{R} && \text{(degenerate branching)}
\end{aligned} \tag{6.28}$$

Autoignition is governed by the set of equations, as formulated in 6.29:

$$\begin{aligned}
\frac{d[\bar{R}]}{dt} &= 2\left\{k_q[RH][O_2] + k_b[B] - k_t[\bar{R}]^2\right\} - f_3 k_p[\bar{R}] \\
\frac{d[B]}{dt} &= f_1 k_p[\bar{R}] - f_2 k_p[Q][\bar{R}] - k_b[\bar{R}] \\
\frac{d[Q]}{dt} &= f_4 k_p[\bar{R}] - f_2 k_p[Q][\bar{R}] \\
\frac{d[O_2]}{dt} &= -g k_p[\bar{R}]
\end{aligned} \tag{6.29}$$

As another approach for HCCI calculation, a more common way is a Knock-Integral Method (KIM), referred to as the Integrated Arrhenius Rate Threshold ([113, 114]) as shown in the following equation 6.30

$$K_{th} = \int_{\theta_{IVC}}^{\theta} A \cdot [Fuel]^a \cdot [O_2]^b \cdot exp(E_a/R_u T) d\theta \tag{6.30}$$

Another ignition model that resembles that one above is the Livengood-Wu method, in which the inverse of the ignition delay of a fuel is integrated over time. The model reads with crank angle θ as a substitute for time s:

$$1 = \int_{\theta_{IVC}}^{\theta} \frac{1}{\tau_{ign}} d\theta \tag{6.31}$$

Start of integration is done during compression from any arbitrary point where no chemical reactions are expected yet. Often, this is done at intake-valve closing or some point before TDC. In this work, 20 degress BTDC has been chosen as the start of integration point. Integration is complete when the value of the integral 6.31 reaches unity and it is assumed that combustion starts at this angle. Here, it should be noted that τ_{ign} is not constant but depends mainly on temperature and other combustion-related values. The integral 6.31 can be thought as a time-equivalent that is necessary for the ignition under varying ignition duration conditions, which is the case during compression. If τ_{ign} was constant, then the time-equivalent of the integral 6.31 would equal the constant time delay.
An ignition delay correlation for HCCI has been given by [46]:

$$\tau_{ign} = 1.3 \cdot 10^{-4} P^{-1.05} \phi^{-0.77} \chi_{O_2}^{-1.41} exp(33,700/R_{(cal/mol/K)} T) \tag{6.32}$$

This correlation is taken from measurements under HCCI specific conditions with ϕ as the equivalence ratio, and χ the mole-fraction of oxygen.

With correlations for combustion duration, and Wiebe exponent m, the HCCI-specific combustion model is complete.

6.2 1-D modeling with BOOST

The equations for engine modeling above are included in commercial simulation tools where, for this work, the engine simulation tool BOOST by AVL was used.
This tool allows for easy creation of complex simulation models for combustion engines. The cylinders are treated in a 0-D manner, such that full homogeneity inside the cylinders is assumed

and only one temperature and pressure at each time-step represents the entire cylinder content. Hence, the model is a crank-angle resolved model. To account for pressure waves in the intake and exhaust, a 1-dimensional finite-volume approach is included in the pipes. Therefore, the intake and exhaust manifolds can be modeled as volumes and pipes, where unlike the pipes, the volumes are treated in 0-D. Due to the pressure-wave functionality along the pipes, without multi-dimensional consideration of the pipes, this simulation tool is classified as 1-D simulation tool.
In AVL BOOST, the Wiebe function is included and Woschni, as well as a Hohenberg correlation can be set to account for wall-heat losses. By specifying valve lift curves as a function of crank angle degree, and discharge coefficients as function of valve lifts, mass-flows into and out of the cylinders are considered. The discharge coefficients account for non-isentropic flow conditions, such as turbulence, and these discharge coefficients used in this work were measured on real intake- and exhaust ports for this particular BDSC HCCI engine on a testbench. A port fuel injector was modeled in this work and the amount of injected fuel was specified according to steady-state experiments. This model setup was in agreement with the test engine, which was equipped with port fuel injectors as well.
Although the AVL BOOST simulation tool includes several combustion models, including a single Wiebe function, an ignition model was not included in the BOOST package, and it had to be implemented. Here, the Livengood-Wu approach 6.31 was pursued but with slightly different ignition delay correlation than equation 6.32 and this modification was published in [119]. The ignition delay correlation suggested here is based on the above correlation, but to account for regular gasoline as fuel instead of octane the following relation has been considered here:

$$\tau_{ign} \propto (ON)^{3.402} \tag{6.33}$$

This proportionality was taken from the Douaud and Eyzat (e.g. in correlation [52]) for prediction of knocking in gasoline engines, which reads:

$$\tau_{ign} = 17.68 \left(\frac{ON}{100}\right)^{3.402} p^{-1.7} exp\left(\frac{3800}{T}\right) \tag{6.34}$$

In this relation, the proportionality 6.34 is evident. By using 6.34 and defining the air/gas and fuel/gas ratio A/G and F/G, where the term "gas" comprises fresh air and recycled exhaust gas, the correlation for ignition 6.32 can be re-arranged as:

$$\tau_{ign} = 1.66 \cdot 10^{-4} P^{-1.05} (F/G)^{-0.77} (A/G)^{-0.64} exp(33,700/R_{(cal/mol/K)}T) \tag{6.35}$$

and a combustion duration correlation that has been fitted by means of least-square to match experimental data was defined as:

$$t_{CombDur} = (F/G)^{-1.31} \cdot (A/G)^{1.60} \cdot exp(507/T_{20}) \cdot (1.2 \cdot 10^{-3} \cdot CA_{10} \cdot 5.1 \cdot 10^{-3}) \cdot N_e^{0.09} \tag{6.36}$$

with

$$CA_{10} = \theta_{ign}(-0.2712 \cdot (G/F) + 16.802) \tag{6.37}$$

The advantage of this approach is that information of moles of species is not accessible during simulation in AVL BOOST so that direct implementation is not possible and an estimate for

the original ignition model is necessary.

To account for different heat-transfer mechanisms in HCCI than in ordinary SI engines, the Hohenberg relation has been found very suitable, and a motivation for this model is well explained in [55]. Although other HCCI-specific wall-heat transfer models have been suggested in [51] and [71], both have been either found unsuitable or too complex for implementation, while the Hohenberg correlation has, despite its simplicity, provided good results.

As for the combustion model, the Wiebe function was chosen here, and the ignition model has been implemented in AVL BOOST by using Function Interpreter Modules, where custom models can be coded in a programming language that resembles ordinary C/C++ with a similar syntax. Since per default an integration functionality does not exist in AVL BOOST, a trapezoidal integration scheme was pursued here, which requires to store the integrated value of the previous time-step, but increases the accuracy compared to Euler forward integration schemes. To ensure proper integration, a fixed time-step solvation scheme has been set in AVL BOOST, with a time-step size of 0.1 degrees crank-angle. This small time-step size is also required for stable pressure wave simulation in the intake and exhaust manifolds.

In order to tune and test the ignition model, a single-cylinder engine model has been created with reduced intake and exhaust pipes. The idea behind this approach is to use experimental pressure traces for the intake and exhaust, which were measured 700mm away from the intake and exhaust ports, and to apply them as boundary conditions in simulation. Furthermore, the mean value for the temperature was taken from experiments and set at the boundaries. With this approach, simulation if intake and exhaust pressures can be excluded which increases the accuracy of the cylinder filling simulation, and as a side-effect increases computation speed is increased.
Using this simulation model, the ignition model can be tuned by altering the pre-exponential factor of the employed ignition model 6.35.
Figure 6.1 shows the single-cylinder engine model in AVL BOOST:

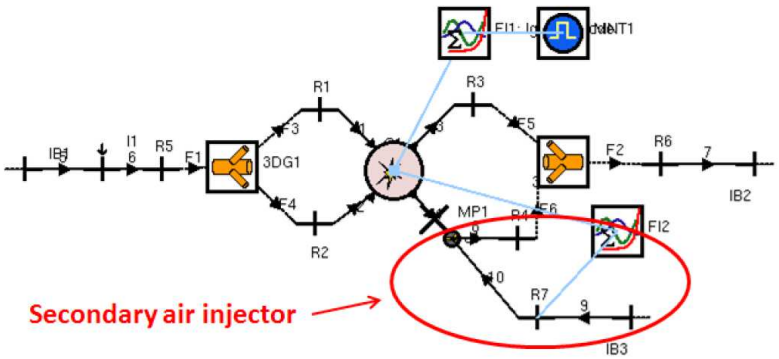

Figure 6.1: Boost single-cylinder engine model for combustion model tuning

In this figure, the cylinder can be seen in the middle, while the intake is on the left-hand side and the exhaust to the right. Above the cylinder, the BOOST Formula Interpreter Mod-

ule, which includes the modeled ignition model together with the integration scheme, can be seen directly connected to the cylinder to set the start of combustion where the Wiebe function is processed by BOOST itself inside the cylinder. Below the cylinder model, a secondary air functionality has been attached to allow for simulation of secondary air.

The ignition model was implemented in a full-engine model in AVL BOOST, with an entire intake, an exhaust manifold, a simple silencer model and a catalyst. Since only two of the four cylinders were activated in experiments, the same was done here by omitting injectors for the two middle cylinders, and setting the valve lifts for intake- and exhaust side to zero to avoid cylinder mass-flows.
An example of such a full-engine model is shown in the following figure:

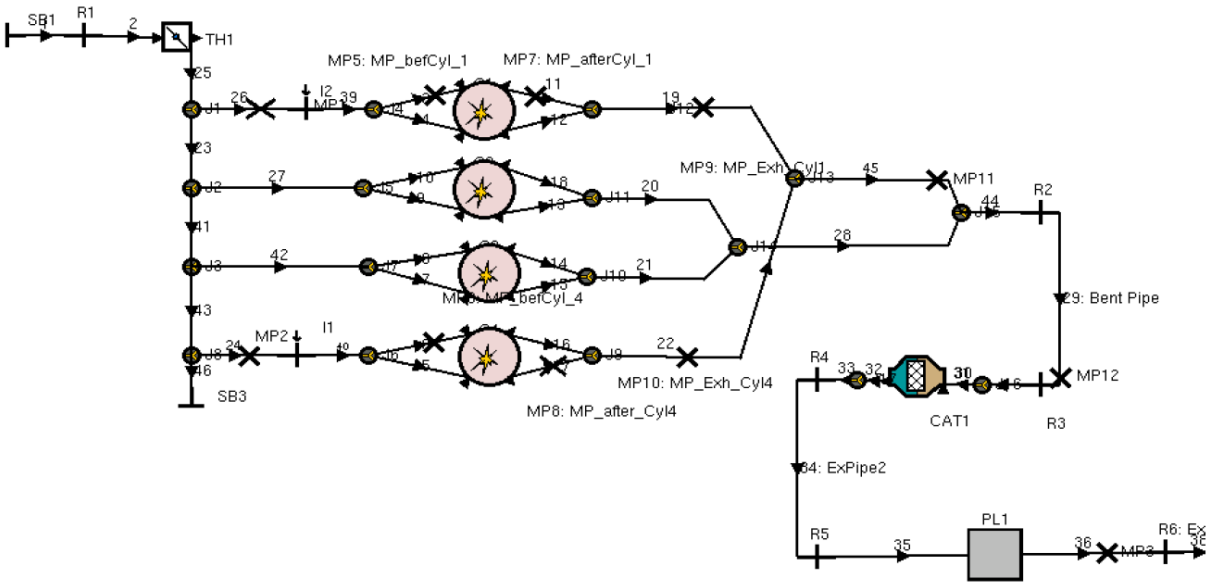

Figure 6.2: BOOST full-engine model

However, to comply with the reference model, which was modeled in GT-Power by Gamma Technologies, the geometrical dimensions of this model have been transferred directly without any modification to a second full-engine BOOST model. Taking this step was decided since the dimensions of the pipes were measured on the real engine for the GT-Power model only and were not available for the BOOST model.
This model is shown in figure 6.2.

It can be seen that this model incorporates many volume-modules in the intake- and exhaust manifold, which replace the simple junction models of the BOOST model.
It should be noted here that this not a common modeling way in AVL BOOST and this model has been found to run much slower and it was suspected that this was due to the increased model complexity.
Although the first full-engine model has lower complexity than the latter one, it still runs multiple times slower than real-time, which makes test of controllers not only tedious but especially for research including tests of different control concepts almost impossible.
Additionally, since AVL BOOST is a commercial simulation tool, and the code is not open to

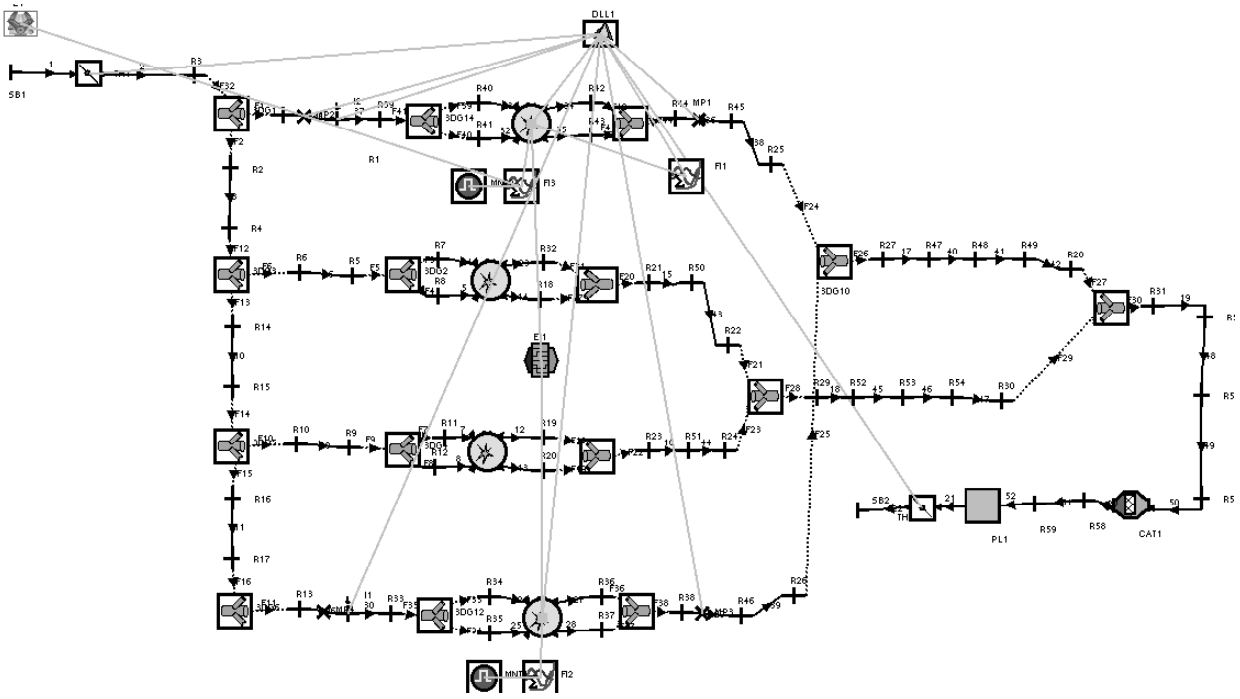

Figure 6.3: BOOST full-engine model as modeled according to the GT-Power model

the user, some information and simulation results are not accessible which may cause difficulties in creating a reduced mean-value model for control design. As an example, the exhausted enthalpy into the exhaust manifold needs to be known, which could only be estimated on the BOOST model.

For these reasons, an own simulation code for research has been created in MATLAB/Simulink, which will be presented in the next section.

6.3 0-D modeling in Matlab

0-D modeling of combustion engines is a common practice in engine control. 0-D models are commonly preferred over 1-D codes, which are useful for engine performance analysis and engine design but are usually too slow for tests of controllers. 1-D models can be still used for Model-in-the-loop simulations where a control algorithm, commonly written in a model-based approach, such as in Simulink, can be tested on a simulation model first. Although this approach may be possible, it however becomes cumbersome if different control concepts and numerous controllers need to be tested, due to the time needed. Furthermore, real-time capabilities become compulsory if applications like Hardware-in-the-loop (HIL) tests are intended (e.g. [112]).
In this work, a 0-D model was created not only for speed reasons as explained above, but also to have an open model at hand for analysis reasons. Such an open model is especially useful since it can be simplified if possible and information extracted for a more simplified mean-value model, which will be introduced in the next chapter.
The approach here was to implement the model in MATLAB/Simulink, which is a common

software tool for control engineering. The equations presented above have been implemented in S-Functions in Simulink. To increase calculation speed, the S-Functions were written in the programming language C, which allows for compilation of the S-Function blocks to speed up execution of the model.
In a 0-D approach uniform temperatures and pressures are calculated inside the cylinder and stratification effects are not considered at all. Intake and exhaust are normally modeled via filling- and emptying methods, where a single volume represents the entire intake or exhaust. This, however, becomes problematic for simulation of the BDSC HCCI engine, where exhaust blow-down pressure wave is essential and must be included in the simulation model as well. Commercial RT models are able to fulfill the real-time requirements. They, however, are based on the filling and emptying principle and are not able to resolve pressure wave dynamics.
To overcome this issue, several pressure-wave modeling approaches may be considered. These include:

1 Extract pressure wave characteristics from experiments and add them on the mean exhaust pressure

2 Model the dominant blow-down exhaust pressure wave as a rigid wall that travels from cylinder to cylinder

3 Include gas dynamics functionality in the model

As for option 1, the instantaneous pressure can be taken from measurements, and the mean value of the pressure traces subtracted such as:

$$p_{add} = p_{exp}(\theta) - \bar{p}_{exp}(\theta) \qquad \forall\, \theta \in [0, 720[\tag{6.38}$$

where $\bar{p}$ is the mean value of the pressure. This mean value would then be replaced in simulation by the pressure from the exhaust manifold volume. This would allow for simulation of the pressure traces with varying exhaust pressures, by actuation of the exhaust throttle for instance. On the other hand, it would be limited to a fixed speed and fixed exhaust valve timings, since it may be expected that the pressure wave characteristics change if engine speed and valve timings are changed.
In option 2, the traveling time of the blow-down pressure wave can be estimated by knowing the speed of sound from the exhaust temperature, which is defined as

$$a = \sqrt{\kappa \cdot R_{spec} \cdot T} \tag{6.39}$$

and by neglecting the macroscopic fluid velocity. This may be justified since the speed of sound is much higher than the speed of the fluid. However, the magnitude of the peak of the pressure wave remains unknown and must be identified from experiments.
With these considerations, option 3 was chosen in this work and a novel modeling approach for simulation of a pressure wave whilst keeping high computation speed was developed.
To begin with, the engine was modeled in a 0-D approach so that the cylinders were simulated as introduced above, and the intake and exhaust manifolds were both modeled in a common filling and emptying manner (e.g. [52]), and the exhaust pipe, which connects the two cylinders, was modeled as an extra volume.
The overall engine model is depicted in the figure 6.4 below.

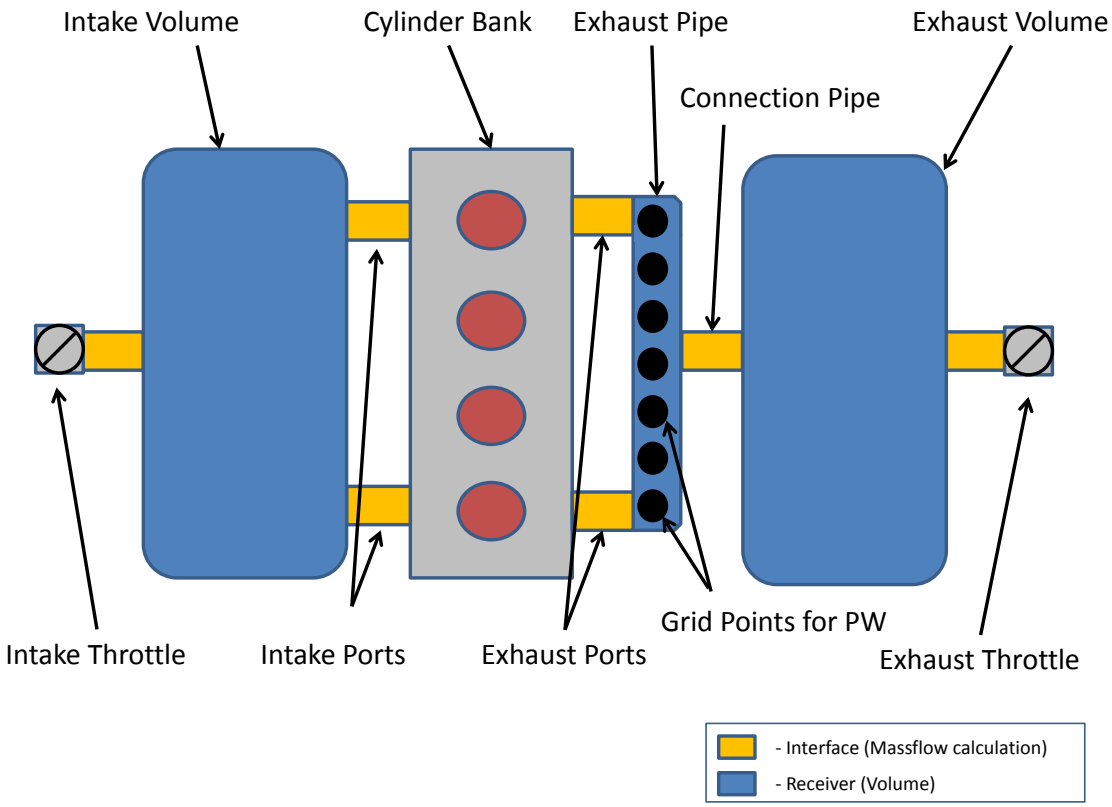

Figure 6.4: Description of the 0-D engine modeling approach

In this figure, the volumes are displayed in blue, of which the aforementioned three can be seen: the intake, the exhaust volume, and the volume of the pipe between the two cylinders. The boundaries of the intake and exhaust volumes are interfaced to the atmosphere by throttle bodies, where the mass- and enthalpy-flows into and out of the volumes are calculated with the equations for compressible flows 6.4 and 6.3. Furthermore, grid points for spatial discretization for simulation of pressure waves in the exhaust pipe are depicted, the theory of which will be introduced in the next section.
Mass-flow elements between volumes are depicted in yellow in the figure, where the intake and exhaust mass-flows are calculated between the intake volume and cylinder, and cylinders and exhaust pipe respectively. Another mass-flow element is placed between the exhaust pipe and the exhaust volume. This ensures that the mean-value exhaust pressure dynamics, as controlled by the exhaust valve, are captured in the exhaust pipe as well.
While all volumes, including the cylinders are modeled as 0-D volumes, the pressure wave is not captured with this model at all. However, with the additional volume for the pipe, another modeling approach for the pressure wave becomes possible: here, the pressure wave is rather imitated, by strongly reducing the discharge coefficient of the orifice between the exhaust pipe and exhaust volume to reduce high transient flows into the exhaust volume during blow-down. Hence, during the blow-down process, the pipe volume would strongly be filled with the exhausted gas before it can escape to the exhaust volume. Thereby, the pressure inside the pipe

volume would increase and act as a blow-down pressure wave to increase the EGR content in the connected exhaust gas re-breathing cylinder.
This approach, however, would require to tune the discharge coefficient for the part between the exhaust pipe and the exhaust volume and not guarantee physically meaningful results, since the pressure increase might change with changing mean exhaust pressure and not reproduce the expected results. Furthermore, a time-delay of the pressure wave of several crank angle degrees before it reaches the other cylinder is not reflected with this model.
For that reason, a pressure wave calculation functionality, based on a finite-difference method (FDM) ([123]) was pursued in this work and will be introduced in the next section.

6.3.1 Pressure Wave

Gas dynamics are generally governed by Euler Equations [52], which resemble Navier-Stokes Equations but omit viscosity.
The euler equations for gas dynamics are as follows:

$$\frac{\partial}{\partial t}\begin{pmatrix}\rho\\ \rho U\\ \rho e\end{pmatrix}+\frac{\partial}{\partial x}\begin{pmatrix}\rho U\\ \rho U^2+p\\ \rho U+\rho U u\end{pmatrix}=\begin{pmatrix}-\rho U\frac{dA}{dx}\\ \rho\frac{U^2}{A}\frac{dA}{dx}+\rho\frac{2\xi U|U|}{D}\\ -\frac{4h_c(T-T_w)}{D\rho}-\frac{1}{A}\frac{dA}{dx}\left(\frac{1}{2}\rho U^3+\frac{\gamma}{\gamma-1}Up\right)\end{pmatrix} \tag{6.40}$$

with U as the fluid velocity and e as the energy as $e = c_v T + 1/2u^2$.
To solve for these Partial Differential Equations (PDE), the Method of Characteristics (MOC) has traditionally been used in commercial simulation tools [17]. Additional methods are the Finite Volume Method (FVM), in which the volume is divided in discrete volumes (cells), in which all variables are averaged over an entire cell. These methods are popular especially in 3-D Computational Fluid Dynamics (CFD) applications.
Another opportunity to deal with these equations is the finite differences method (FDM). This is the most intuitive approach, in which the differential spatial derivative $\frac{\delta}{\delta x}$ is replaced by discrete differences $\frac{\Delta}{\Delta x}$.
In the current case, it was desired to solve these PDE's in Simulink, which, on the other hand, can only treat Ordinary Differential Equations (ODE). For that reason, a procedure to convert these PDEs into ODEs was saught after.
A PDE is of the general form:

$$\frac{\partial F}{\partial t}+\frac{\partial G}{\partial x}=H \tag{6.41}$$

where the PDEs for gas dynamics introduced above 6.46 are of mathematical hyperbolic character which makes numerical treatment of these equations difficult [123]. In fact, if for such equations were solved by using ordinary PDE solvers, such as those available in standard MATLAB, the solution would not converge and go to infinity instead.
For treating such hyperbolic PDEs, special numerical solvers has been suggested, such as the Lax-Friedrich, or the Lax-Wendroff scheme, which reads:

$$F_j^{n+1} = F_j^n - \frac{1}{2}\frac{\Delta t}{\Delta x}(G_{j+1}^n - G_{j-1}^n) + \Delta t H_j^n + \frac{1}{4}\left(\frac{\Delta t}{\Delta x}\right)^2 [(G'^n_{j+1} G'^n_j)(G_{j+1}^n - G_j^n) - (G'^n_j G'^n_{j-1})(G_j^n - G_{j-1}^n)] \tag{6.42}$$

where $G' = \partial G / \partial \delta$.
To ensure stability of the integration scheme, the time step-size is confined by the grid size by the distance of each grid point to each other. This is called the Courant-Friedrich-Lewy criterion [123], and it states that one variable may not surpass one grid point for each time step and reads:

$$C = (|U| + a)\frac{\Delta t}{\Delta x} < 1 \tag{6.43}$$

This solvation scheme 6.42 is easy to implement in an ordinary simulation code. On the other hand, it becomes inconvenient when it needs to be implemented in Simulink where flexibility in terms of solver settings are desired. As an additional feature, it may be desired to set the number of grid points without complicated re-coding. In a [94], for the development of a control-oriented engine model, a fully discretized approach of the Euler Equations 6.46 was implemented as Simulink blocks where the discretization was determined by the number of employed Simulink blocks. Additionally, a separate solver for the partial differential equations was implemented based on a CIR (Courant, Isaacson and Rees) method that is closely related to the method of characteristics (MOC), which decouples this solvation scheme from the Simulink solver. A similar approach with a fully discrete solver was presented in [32].
This overall reduces the flexibility, and as an alternative to this, a different procedure was followed here.

The underlying idea is, unlike full-discretization schemes such as the Lax-Wendroff scheme 6.42, to discretize the spatial term of the Euler equations only, such that the differential time derivative remains, such that the modified PDEs as newly obtained ODEs can be solved by standard Simulink ODE solvers.
Hence, discretizing the spatial term of a general PDE 6.41 by introducing grid-points at defined spatial positions in direction x:

$$\frac{\partial G}{\partial x} = \frac{\Delta G}{\Delta x} \tag{6.44}$$

the overall partial differential equation becomes:

$$\frac{\partial F}{\partial t} + \frac{\Delta G}{\Delta x} = H \tag{6.45}$$

Here, with a fixed number of grid points n, these grid points can be considered as newly introduced states, similar to states of a state-space system in control engineering. The variable vector F has then been increased by three times the number of grid nodes, since the Euler equations 6.41 is a set of three equations. The converted equation then reads:

$$\frac{\partial F}{\partial t} = H - \frac{\Delta G}{\Delta x} \tag{6.46}$$

where the ODE structure is evident.
As introduced above, an intuitive approach would be to discretize the spatial terms where the central-differential scheme is a very popular approach, while the temporal term remains left as it is. However, this would cause numerical instabilities creating the need for a new approach.
As a solution to this, the solvation scheme proposed by Kurganov and Tadmor [6] was chosen here which isn't only of higher order, but also has the capabilities to capture shock phenomena that are diffictult deal with an ordinary solver, due to their sharp discontinuity character. An outline of the Kruganov Tadmor scheme will be introduced next.
Starting with a partial-differential equation (PDE) as:

$$\frac{\partial}{\partial t}u(x,t) + \frac{\partial}{\partial x}f(u(x,t)) = 0 \tag{6.47}$$

according to Kurganov and Tadmor, by letting $\Delta t \downarrow 0$ of a proposed discrete second-order central scheme, a semi-discrete central scheme can be obtained as:

$$\begin{aligned}\frac{d}{dt}u_j(t) = -\frac{(f(u^+_{j+1/2}(t)) + f(u^-_{j+1/2}(t))) - (f(u^+_{j-1/2}(t)) + f(u^-_{j-1/2}(t)))}{2\Delta x} + \\ \frac{1}{2\Delta x}\left\{a_{j+1/2}(t)[u^+_{j+1/2} - u^-_{j+1/2}(t)] - a_{j-1/2}(t)[u^+_{j-1/2} - u^-_{j-1/2}(t)]\right\}\end{aligned} \tag{6.48}$$

with Δx as the grid-point difference and $a_{j+1/2}(t)$ the maximal local speed.
This equation can be cast in the *conservative form*:

$$\frac{d}{dt}u_j(t) = -\frac{H_{j+1/2}(t) - H_{j-1/2}(t)}{\Delta x} \tag{6.49}$$

where the numerical flux H is defined as:

$$H_{j+1/2}(t) = \frac{f\left(u^+_{j+1/2}(t)\right) + f\left(u^-_{j+1/2}(t)\right)}{2} - \frac{a_{j+1/2}(t)}{2}\left[u^+_{j+1/2}(t) - u^-_{j+1/2}(t)\right] \tag{6.50}$$

and the intermediate values u are defined as:

$$\begin{aligned}u^+_{j+1/2} := u_{j+1}(t) - \frac{\Delta x}{2}(u_x)_{j+1}(t) \\ u^-_{j+1/2} := u_j(t) + \frac{\Delta x}{2}(u_x)_j(t)\end{aligned} \tag{6.51}$$

and the maximum local speed, calculated as the spectral radius:

$$a_{j+1/2}(t) := max\left\{\rho\left(\frac{\delta f}{\delta u}\left(u^+_{j+1/2}(t)\right)\right), \rho\left(\frac{\delta f}{\delta u}\left(u^-_{j+1/2}(t)\right)\right)\right\} \tag{6.52}$$

However, calculating the Jordan Matrix in 6.52 would be computationally expensive, and a simplified approach was chosen here where the above expression was replaced by the maximum and minimum velocities as defined as:

$$\begin{aligned} a_{plus} &= \mid u_i + \sqrt{\kappa \cdot R_{spec} \cdot T_i} \mid \\ a_{minus} &= \mid u_i - \sqrt{\kappa \cdot R_{spec} \cdot T_i} \mid \end{aligned} \tag{6.53}$$

Furthermore, in equation 6.48 a flux limiter $(u_x)_j^n$ is calculated, of which the $minmod$ scheme was used here, which reads:

$$(u_x)_j^n = minmod\left(\phi\frac{u_j^n - u_{j-1}^n}{\Delta x},\ \phi\frac{u_{j+1}^n - u_{j-1}^n}{2\Delta x},\ \phi\frac{u_{j+1}^n - u_j^n}{\Delta x}\right) \tag{6.54}$$

which completes the basic model.
This scheme is easy to implement in a Simulink S-Function and has good robustness features so that the solver runs stably. However, in order to maintain the robustness of the solver, the CFL condition 6.43 must be obeyed. This means that either the time-step size must be kept small enough such that the condition is fulfilled, or the grid-size must be decreased and the distance between grid-points increased. The first measure increases the accuracyW but has the disadvantage of increased computational cost and makes real-time simulation impossible with the hardware available at present. The second measure of increasing the distance of two grid-points allows for increasing the time-step size such that the CFL condition remains fulfilled. However, by reducing the number of grid points, the accuracy would strongly decrease and one might be at risk to lose conservation of mass and energy.
Since filling and emptying approaches have been used with confidence in automotive control engineering for decades, the idea is to merge the 1-D modeling approach that was presented above with the well-known 0-D approach. Hereby, the 0-D volume would serve as a reference and to account for conservation of mass and energy while the 1-D approach in the same volume would ”distort” the volume and introduce spatial resolution of pressure. With this approach, it would be possible to simulate a pressure wave in a control-oriented 0-D framework.
The idea is depicted in figure 6.5.

This figure shows a volume and a pressure, which is evenly distributed in the first case on the left hand side. In this volume, values for the pressure and temperature, as well as the moles are calculated and treated constant over the entire volume. In the second approach on the right hand side of the figure 6.5, grid points are inserted into the volume to account for different pressures at different locations in the same volume. This figure also implies that the set of Euler Equations is evaluated at each grid point, while at the same time, a spatial distribution of the species in terms of moles remains condensed in the volume and is not included in the Euler Equations. This drastically simplifies the model, since the numerical complexity raises only three-fold with every grid-point but not with the five species additionally. The numerical treatment of the five species remains in the filling-and-emptying approach for the volume and such is an equation for conservation of energy for the volume. With this additional set of equations, modeling of the volume itself is complete and may serve as a reference correction of the numerical dissipation due to the reduced grid points.
The motivation for reducing the grid points is shown in figure 6.6, taken from [17]. This figure shows the numerical results of pressure traces at two locations with a graphical solution (shown in this graph in points), numerical with 50 meshes (shown as a solid line), 30 meshes (dashed line) and only 10 meshes (solid-dashed line). This figure shows that with decrease of mesh size, the solution ”smears” and becomes less accurate, while a the same time, the main characteristics remain.

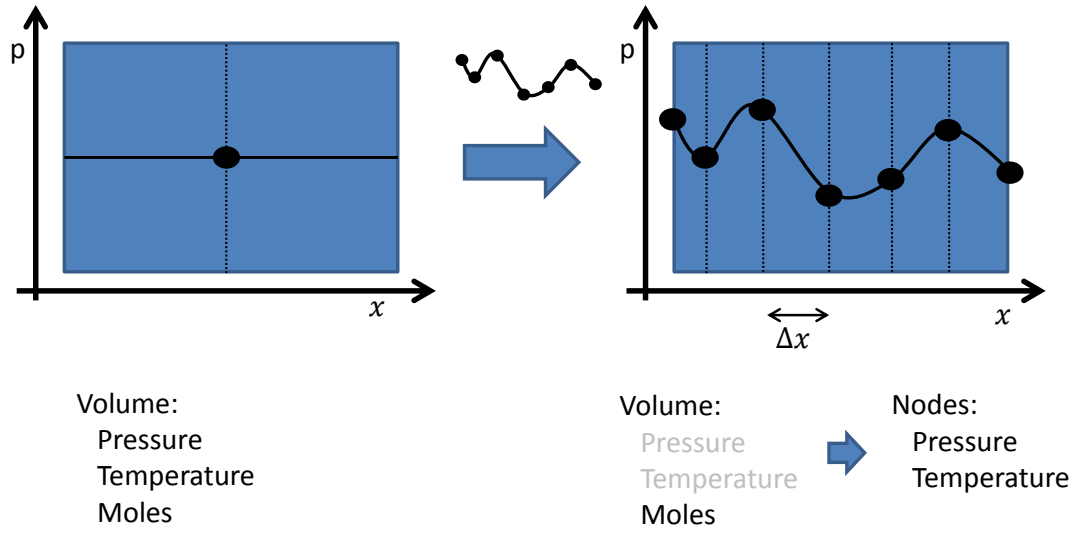

Figure 6.5: Insertion of discrete grid-points into a volume

As mentioned above, to reduce numerical errors and increase the robustness of the solution, the volume here serves as a corrector for the Kurganov-Tadmor scheme. This was achieved by including additional source terms in the Euler Equations 6.41 as:

$$\frac{\partial F}{\partial t} + \frac{\partial G}{\partial x} = H + S_{Volume} \tag{6.55}$$

with S_{Volume} as the source term from the volume which the grid-points are referenced to. Since it may serve as a source term for the conservation of mass, conservation of energy, and conservation of momentum, this source term can be described as a vector, as:

$$S_{Volume} = \frac{d}{dt} \begin{pmatrix} S_{Vol,e} \\ S_{Vol,\rho} \\ S_{Vol,u} \end{pmatrix} \tag{6.56}$$

of which each of the elements can be a vector of the length of number of grid-points. Hence, this source term corrects the Euler Equation at each grid point.
Note that this source term is expressed in terms of the time-derivative. The reason for this is that this term was evaluated after each integration step in the S-Function in Simulink and not

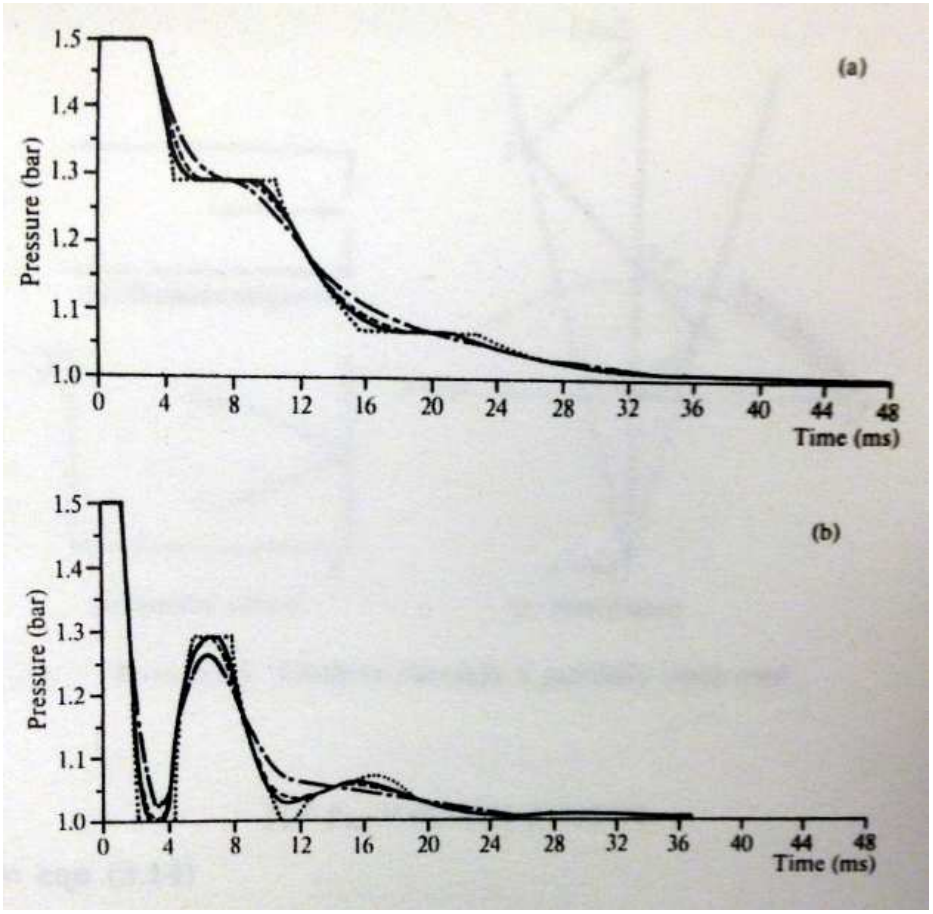

Figure 6.6: Comparison of Pressure Simulation with different number of grid points (from [17])

included as a derivative to make implementation easier.
Hereby, the source term to update the mass and energy equation is derived as:

$$\Delta e = e_{ExhVol} - \Sigma e_i \tag{6.57}$$

with e_{ExhVol} as the energy of the volume, and e_i the energy of each grid-point.
The same approach for the mass reads:

$$\Delta m = m_{ExhVol} - \Sigma m_i \tag{6.58}$$

with m_{ExhVol} the mass of the volume, which is calculated from the moles, and m_i the mass of each grid-point.
The energy- and mass-error 6.57 and 6.58 are used to calculate the update-source terms as follow:

$$S_{u,i} = \frac{\Delta e}{V_{Pipe}} \tag{6.59}$$

and

$$S_{m,i} = \frac{\Delta m}{V_{Pipe}} \tag{6.60}$$

The volume of the pipe was used in this correction term to comply with the Euler Equations 6.46 above.

In order to account for wall-heat losses, an extra source term has been implemented, which is:

$$\dot{Q}_{wall,i} = -k_t \cdot \alpha_w \cdot (T_i - T_{Wall}); \tag{6.61}$$

with k_t as a manual tuning factor to match the temperatures to experiments, and α_w, as taken from [42], as:

$$\begin{aligned} \alpha_w &= 28.6 + 4.0 \cdot |u_i| \qquad \text{for} \qquad |u| < 5m/s \\ \alpha_w &= 21.0 \cdot |u_i|^{0.52} \qquad \text{for} \qquad |u| \geq 5m/s \end{aligned} \tag{6.62}$$

and the final source term has been implemented for each cell i as:

$$S_{WHT,i} = \dot{Q}_{wall,i} \cdot \rho_i \tag{6.63}$$

The junction has been simplified by adding a source term for the grid point that is affected. Hereby, the enthalpy source term reads:

$$S_{U,Junc} = \frac{\dot{H}}{V_{cell}} \tag{6.64}$$

and the equation for density is given the following source term:

$$S_{\rho,Junc} = \frac{\dot{m}_{Junc}}{V_{cell}} \tag{6.65}$$

This mass-flow $\dot{m}_{Junc}$ was simply calculated via the flow equation for compressible flows 6.4, as introduced above. With the knowledge of the upstream temperature, the enthalpy flow for the source-term above 6.64 can be calculated as well.
In order to account for pressure losses that may occur in a junction, a non-dimensional loss-term can be implemented at the grid point at the junction.
Since conservation of momentum is not considered in a 0-D modeling approach for the volume, a correction term for the momentum equation is not available and has been omitted.
While maintaining the 0-D character of the model, which has been used in engine control extensively, adding 1-D elements have enhanced this model.
It should be also emphasized here that by assuming perfect mixing of the species, as in filling and emptying methods, the five different species are not captured in each node separately which helps to achieve higher calculation speed.

The following figure shows the exhaust pressure of the model in comparison with the experimental data. The in-cylinder pressure of the simulation is given in green.

It can be clearly seen that the blow-down pressure wave is generated right after the exhaust valve opens. After the reaching the peak pressure during exhaust, the exhaust pressure equalizes with the in-cylinder pressure and follows its trend, until the valve closes.
During the subsequent intake stroke, at which the in-cylinder pressure falls to the pressure level of the intake, it rises again when the exhaust valve opens, which can be seen at the exhaust

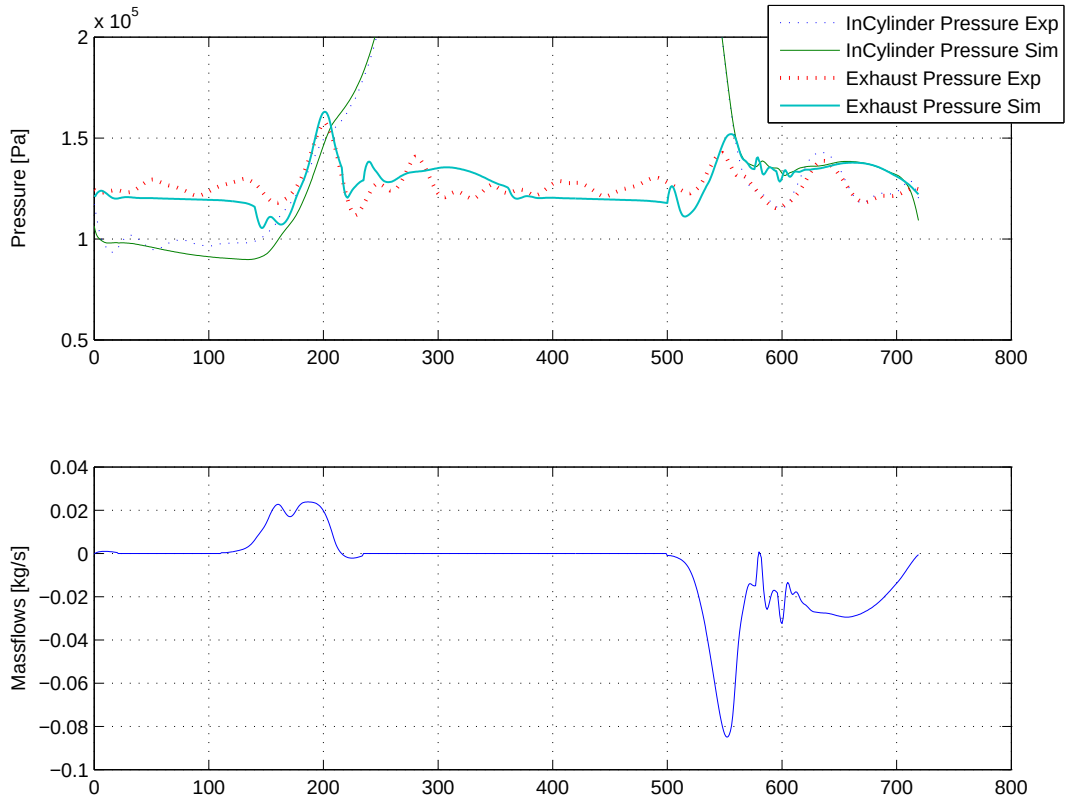

Figure 6.7: Comparison of Exhaust Pressure with Experiments

mass-flows. It can be further seen that a second ”bump” in the re-breathing stroke due to the pressure wave appears, which pushes more exhaust gas in the cylinder.
Also, the pressure peaks during exhaust and re-breathing do not coincide, but there is an expected delay of roughly ten degrees, when the pressure wave travels at the speed of sound along the exhaust pipe that connects the two cylinders.
Figure 6.8 shows the exhaust pressure dynamics, following a steady-state condition when the exhaust pressure is opened in one step. Thereby, it can be expected that the pressure drops with rather slow dynamics due to the emptying of the exhaust manifold. This assumption is in accordance with the results seen in this figure by the mean pressure dynamics plotted in red, while the instantaneous pressure from pressure waves plotted in blue. An example of exhaust pressure traces is shown in figure 7.3 in a later chapter where the similarity is obvious. The reason for the less ripples in simulation is due to the fact that the experimental data were taken from a 4-cylinder engine with more pressure wave characteristics, and that pressure wave simulation was only modeled in the exhaust pipe between the cylinders, while the remaining part was treated in a mean-value fashion.

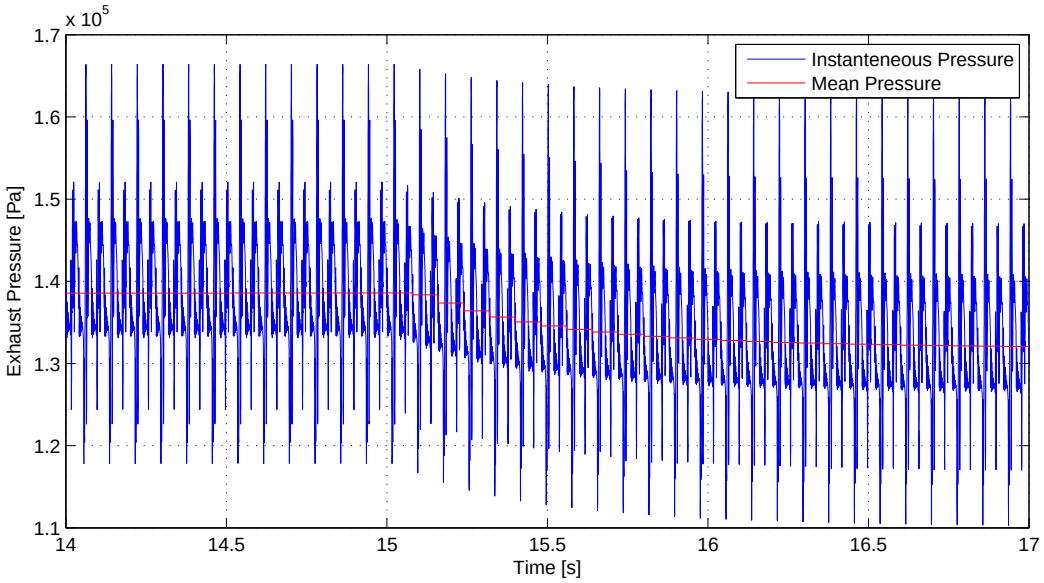

Figure 6.8: Dynamics of the crank-angle resolved pressure traces from the 0-D model by opening the exhaust valve in one step

6.3.2 Combustion Model

For combustion analysis, the well-known Rassweiler-Withrow method has been used to extract the rate of heat release from the in-cylinder pressure traces from experiments [52].
The Rassweiler-Withrow method is based on the assumption that the apparent heat release can be extracted from the pressure difference between pressure rise from combustion Δp_c, and a pressure change due to pure compression of the combustion chamber Δp_v. This difference of both pressures is expressed as:

$$\Delta p = \Delta p_c + \Delta p_v \tag{6.66}$$

The pressure change due to volume change can be estimated via the well-known polytropic relation:

$$p_i V_i^n = p_j V_j^n \tag{6.67}$$

Hence,

$$\Delta p_v = p_j - p_i = p_i \left[\left(\frac{V_i}{V_j} \right)^n - 1 \right] \tag{6.68}$$

The mass fraction burned (mfb) can be estimated by assuming that within the interval $\Delta\theta$, it is proportional to the pressure rise due to combustion. Hence, the mass fraction burned at the i_{th} interval is given by

$$x_{mbf,i} = \frac{m_{b(i)}}{m_{b(total)}} = \frac{\Sigma_0^i \Delta p_c}{\Sigma_0^N \Delta p_c} \tag{6.69}$$

After extracting the mass fraction burned curves ($x_{mbf,Exp}$) from experimental data, the Wiebe combustion parameters, combustion start, combustion duration (defined as start of com-

bustion until combustion end, estimated at 99% fuel burned), and the Wiebe exponent are automatically fitted for each case by means of a least squares optimization algorithm.
The optimization procedure is then subject to:

$$J = min\left(x_{mbf,Exp} - x_{mbf,Wiebe}\right) \tag{6.70}$$

The following figure 6.9 shows the pressure trace of case #3 with the identified mass fraction burnt plotted below in comparison to the fitted Wiebe function.

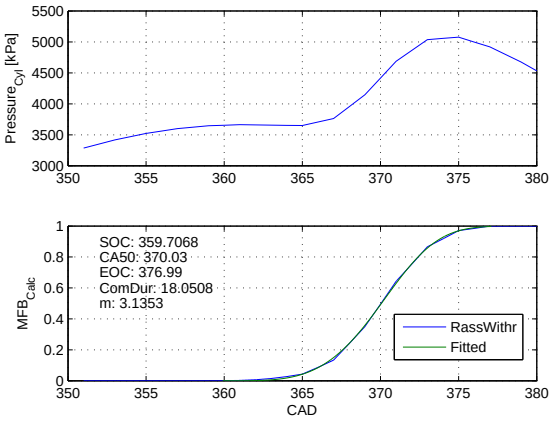

Figure 6.9: Results of fitting of combustion parameters for case #3

Although it may be difficult to estimate the correct mfb from experimental data, finding the right Wiebe parameters is straightforward with an optimization algorithm, as the match in this figure shows. Figure 6.10 shows the same plot for case #19, and 6.11 for case #26.

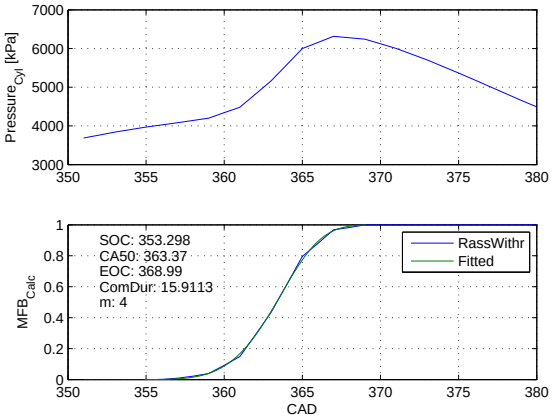

Figure 6.10: Results of fitting of combustion parameters for case #19

In order to find a correlation for combustion duration $\Delta\theta$ and the exponent m_{Wiebe}, which should be kept simple enough such that it could potentially be also implemented in a mean-value engine model for control design, a linear approach has been followed here, which is similar to [114].
The correlation for for combustion duration thereby reads:

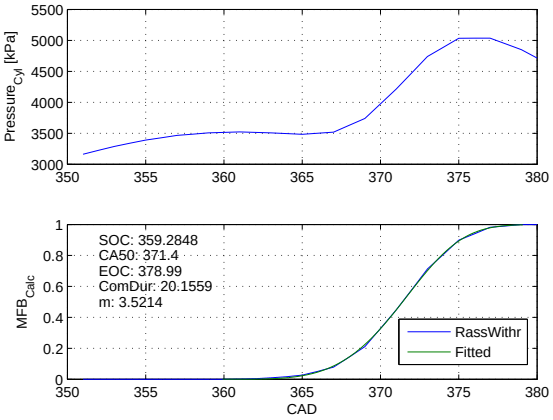

Figure 6.11: Results of fitting of combustion parameters for case #26

$$\Delta\theta = c_{CombDur,1} + c_{CombDur,2}\theta_{SOC} \tag{6.71}$$

with

$$\begin{aligned} c_{CombDur,1} &= -118.8174 \\ c_{CombDur,2} &= 0.3822 \end{aligned} \tag{6.72}$$

and the Wiebe coefficient m_{Wiebe} as:

$$m_{Wiebe} = c_{CombExpo,1} + c_{CombExpo,2}\theta_{SOC} \tag{6.73}$$

$$\begin{aligned} c_{CombExpo,1} &= 37.0749 \\ c_{CombExpo,2} &= -0.0938 \end{aligned} \tag{6.74}$$

for start of combustion (SOC) values around 360 CAD.

The results from the correlations above are shown in the figures 6.13 and 6.12.

Although a tight fit could be found, the correlation used specifically for combustion duration showed some larger deviation, which is not too critical, since combustion duration in HCCI engines is typically very short at an order of roughly 20deg, compared to those from SI engines, which may reach durations far beyond 50 degrees ([80]).

The mathematically simplicity of these correlations, the easy inversion, and general handling outweigh the accuracy. In comparison, an exponential function including more factors might provide higher accuracy, though their handling could become cumbersome if it is considered to implement them in a model-based control scheme. Furthermore, due to the short combustion duration, the gain of a more complex model would be only marginal.

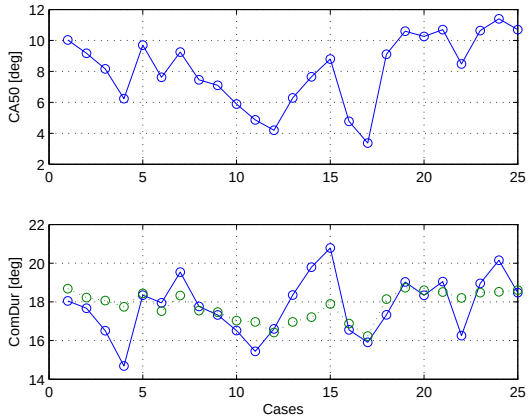

Figure 6.12: Identified CA_{50} and Combustion Duration, in comparison with the simplified model

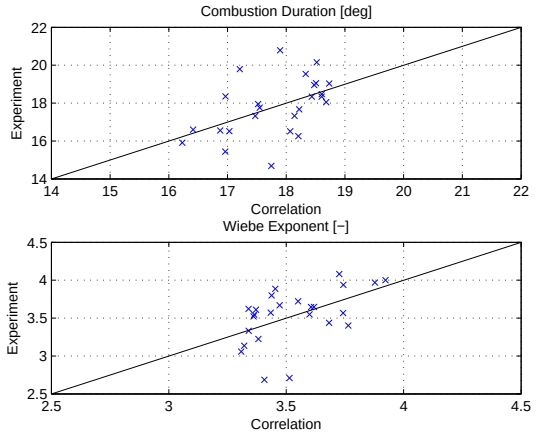

Figure 6.13: Comparison of Identified Values and Fitted Correlations for Wiebe Exponent and Combustion Duration

6.3.3 Results of the 0-D model

HCCI

The models presented above have been included in Simulink S-Functions, written in the programming language C to increase execution speed of the model. Unlike the single-cylinder approach as presented for the 1-D BOOST model, where measured pressure traces on the intake- and exhaust side were applied as boundaries to the model, to allow for combustion model tuning, the calibration approach pursued here is different. Since execution speed of the model is very high, it is more appropriate to use the full-engine model, including the intake and exhaust manifolds. A simple I-controller was used to control the exhaust pressure via the exhaust throttle and to match it with mean exhaust pressure data from experiments. The ignition model was then tuned, by altering the pre-exponential factor, until satisfactory results were obtained.
Figures 6.14 and 6.15 show the results of the 0-D full engine model, of which the in-cylinder pressure is in comparison with the experimental data.

The upper left corner shows the plot of the calculated temperature, whose level is well in

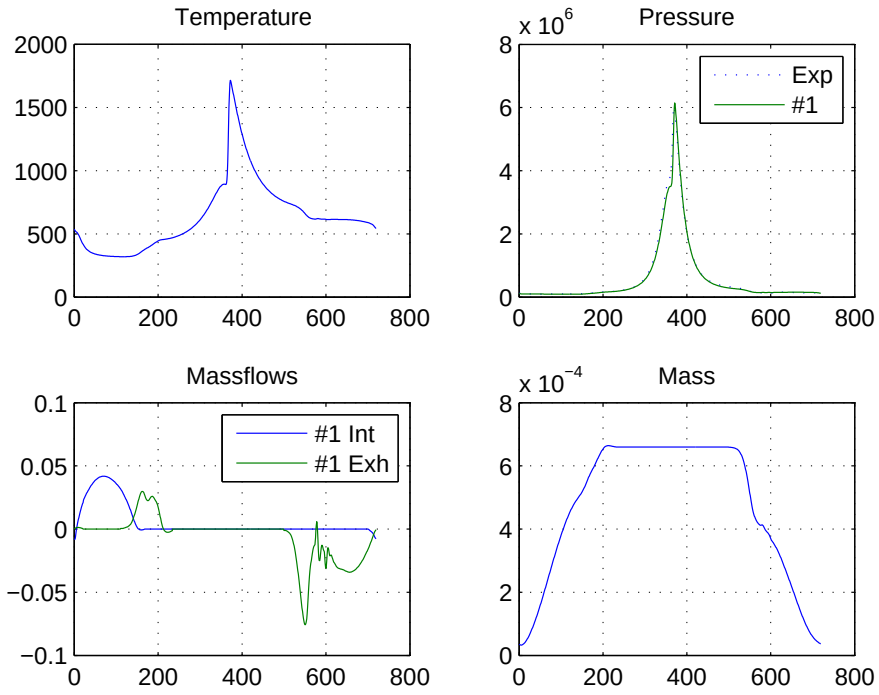

Figure 6.14: Results of 0-D model in comparison with experiments

accordance to the expected temperature levels of HCCI engines. The plot next to it shows the calculated pressure traces in comparison to experimental data, which show a tight match between both curves. The lower plots show the calculated mass inside the cylinder and the respective mass-flows. Note that the intake mass-flow, given in blue, is a smooth and round curve, which is due to the 0-D characteristics of the intake, where no pressure waves are present. This is different to the exhaust mass-flow, where a ”bump” at the end of the EGR stroke can be seen, which is attributed to the pressure wave, which is included in this model. At this point, it should be noted that an ordinary 0-D model would not be able to simulate this pressure wave, such that the EGR amount would be underpredicted. This would not only lead to lower temperature levels inside the cylinder and delayed combustion (which could be corrected by tuning the ignition model), but also a lower cylinder filling which could be recognized in the pressure traces. For this reason, it is essential to have a sub-model for the pressure wave included.

Figure 6.16 shows the $IMEP$ of the 0-D model in comparison with experimental data. Although a rather constant offset can be seen in this plot, of which the reason is not entirely clear, the trend is the same. This kind of offset has been found in other engine models, including AVL BOOST and GT-Power, such that the results here were accepted.
The last result in figure 6.17 are the combustion location (CA_{50}) over all cases in comparison with experimental data. Despite the simplicity of the model and the fact that the full-engine model was used and the exhaust mean pressure was closed-loop controlled, instead of applying measured data for intake and exhaust pressure, the results presented here show a very close match with the experimental data. The second plot in this figure shows the A/F ratio of the model in comparison to experimental data, which also contains a slight offset though the trend remains the same.

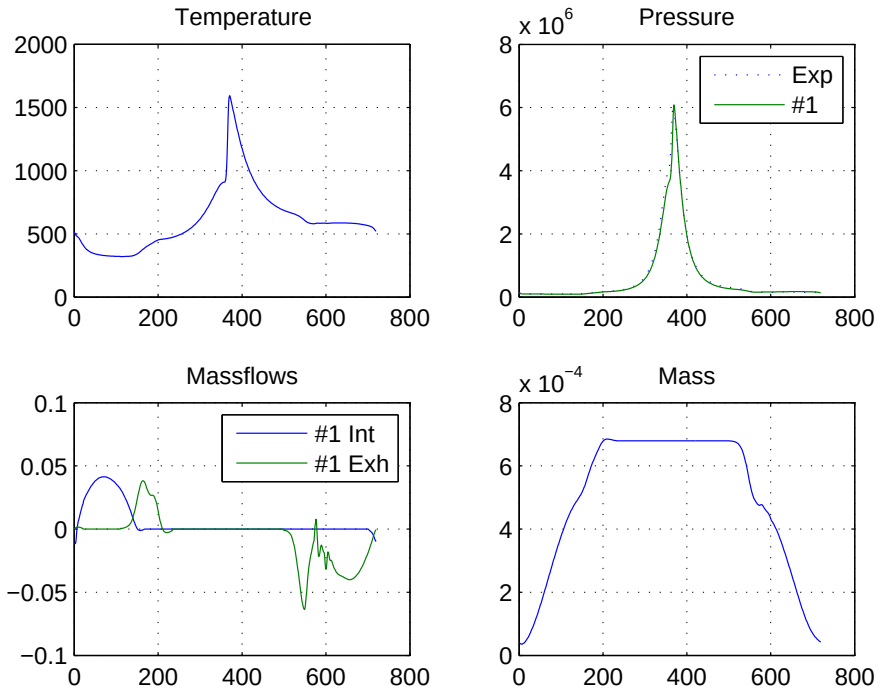

Figure 6.15: Results of 0-D model in comparison with experiments

Overall, it can be concluded that this engine model is well-suited for control analysis. In spite of the strong reduction of some sub-models and the in overall simplicity, the results shown here can be judged as good. Furthermore, since this is an entirely open model, all sub-models and simulation results can be accessed for further use in a mean-value engine model, which is required for control design. Considering the high computation speed, where real-time capabilities are likely, it substantially helps in tests of different control concepts before actual implementation on a real engine. One of the great differences to a mean-value model, as presented in a subsequent section, is that the 0-D model is crank-angle resolved, and signal feedback algorithms (such as fast CA_{50} or $IMEP$ online processing can be tested on this model before such algorithms are directly implemented on a rapid control prototyping (RCP) system or engine control unit (ECU).
The modeling approach presented here is, therefore, a promising candidate for model-based design (MBD) of a HCCI capable combustion engine, in which pressure waves may be crucial.

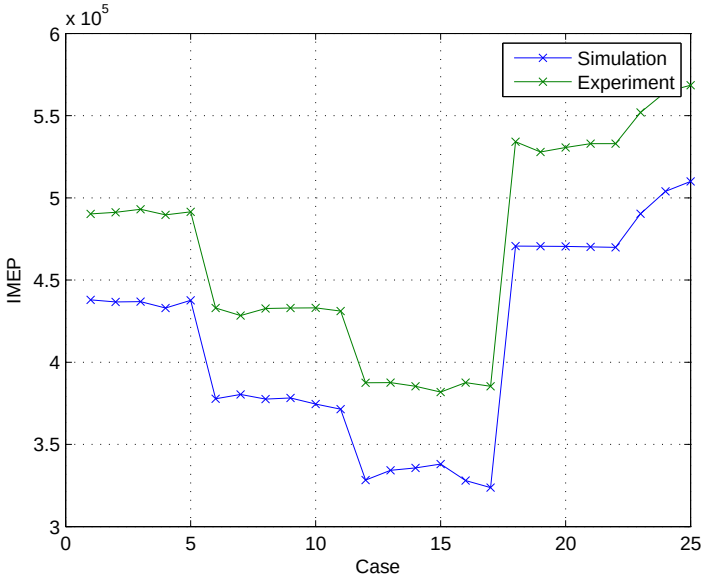

Figure 6.16: Comparison of $IMEP$ 0-D model with Experiments

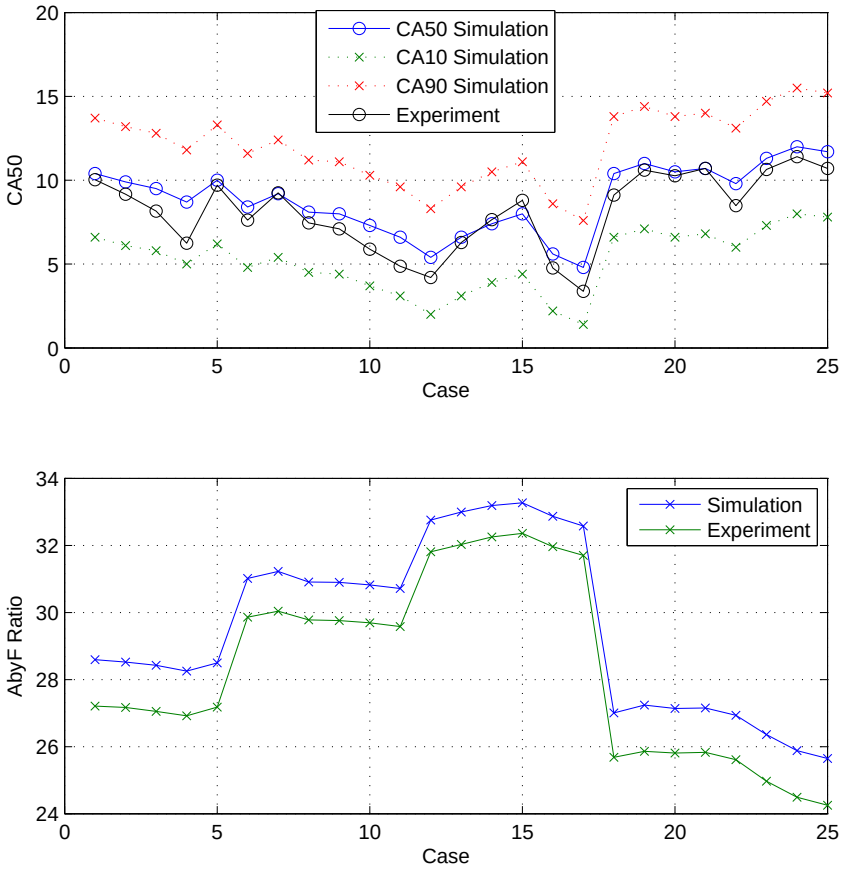

Figure 6.17: Results of the 0-D full engine model in comparison with experimental data

SI

The model presented above has been also prepared to allow for spark ignition combustion simulation. Major differences are the combustion durations and Wiebe exponents that are used for the combustion model. As for the wall-heat model, the standard Woschni correlation has been used instead of the Hohenberg, which was used for HCCI.
Since the EGR valve is deactivated in SI operation, the second valve lift of the exhaust valve was not simulated, while the other valve lifts remained the same as in HCCI.
Since stoichiometric conditions inside the cylinders must be ensured, the intake pressure needed to be decreased by the intake throttle to limit the amount of air coming into the cylinders. As a solution to this, a simple I-controller was implemented to regulate the A/F ratio during SI. Since no special requirements existed for the A/F control, such a simple controller was sufficient.
As for the combustion model, a standard Wiebe function has been used, and the combustion model parameters identified from experimental data, with the Rassweiler-Withrow method as introduced above. Since SI combustion is not the focus of this work, and only necessary for the analysis of the combustion mode switch, the identified combustion parameters have been kept fixed during simulation with no correlation for exponent, ignition delay, etc. being considered.

The following results show the cylinder pressure traces of one case in comparison with the experimental data 6.18. In this figure, it can be seen that the fit of the in-cylinder pressure is not as tight as in the case of HCCI. However, since a fixed value for fuel amount for each case is known from experiments and thereby the cylinder-filling is fixed too, the only tuning parameter would be the heat transfer model by either the heat transfer coefficient or the wall-temperatures. On the other hand, an excessive tuning of this sub-model would lead to a simulation model that is not very credible. As another measure to improve the results, the combustion model parameters would have to be revised.
Figure 6.19 shows the results of combustion phasing, $IMEP$ and exhaust temperature. As for $IMEP$, a close match with experiments is shown, although a steady offset for all cases can be seen. The last plot shows the exhaust temperature, which is the most important part of this simulation model, since this gives the starting conditions for HCCI during a combustion mode switch. Although some deviation is apparent, in the form of a few Kelvin, the model follows the general trend.
Overall, some parts of this model can be still optimized. However since HCCI is the main focus of this research, and only the exhaust temperature before the combustion mode switch, the results here for SI have been accepted.

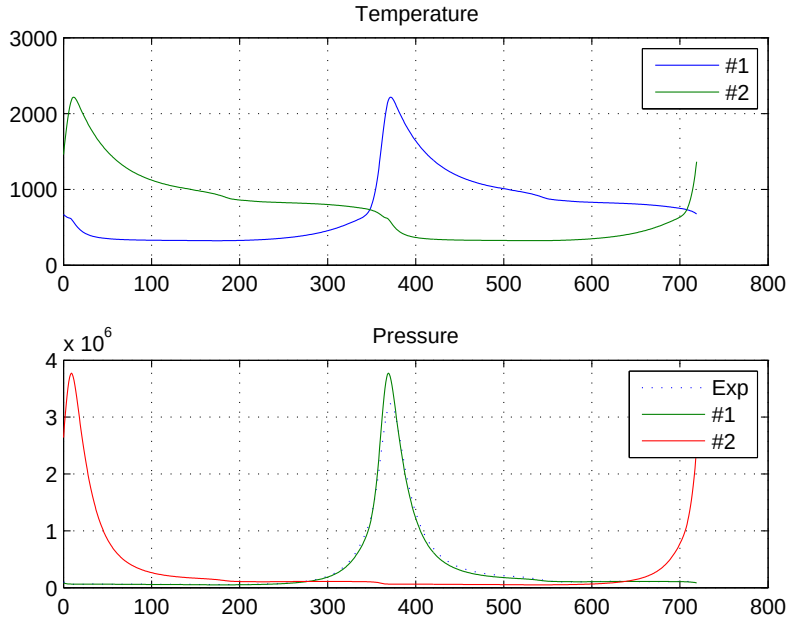

Figure 6.18: Results of 0-D model for SI case 0x

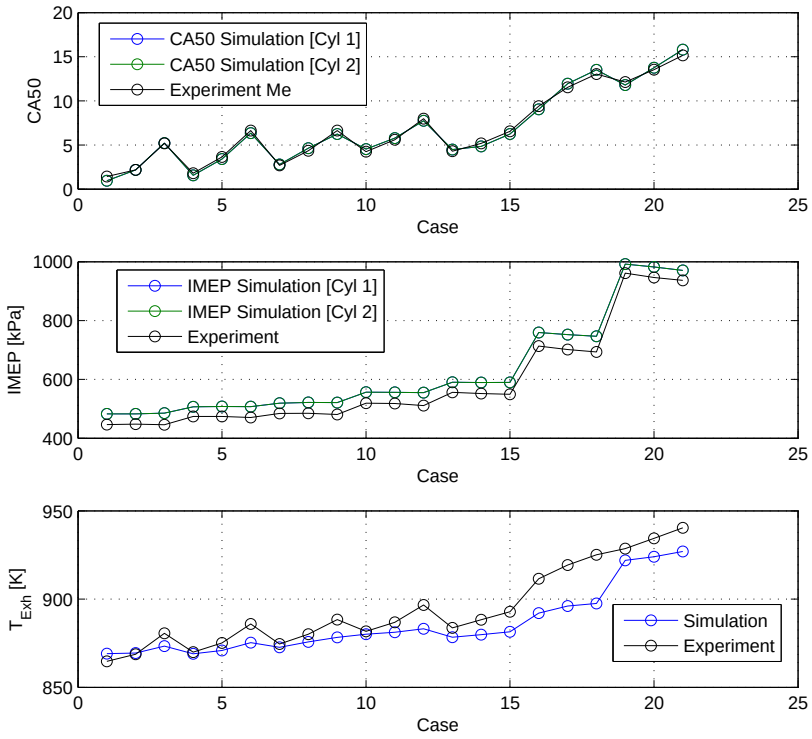

Figure 6.19: Overall Results of 0-D model for SI

Chapter 7

Control-Oriented Mean-Value Modeling

Mean-Value modeling for HCCI has been mentioned in the literature (e.g. [26]), it is not yet standard in commercial software or books.
Common Mean-Value Engine Models (MVEM) for SI engines usually consists of intake manifolds that are modeled as volumes where the intake throttle body can be modeled, as in the 0-D or 1-D case, by using equation 6.17 with the same holding true for the exhaust.
To calculate the mean cylinder flow, the engine speed and volumetric efficiency (usually taken from experiments) are utilized here with look-up tables typically used to calculate the volumetric efficiency. Together with the intake manifold pressure, the intake flow is then calculated.
By limiting the amount of fuel injected to stoichiometric, and thus depending on the amount of air breathed in, the power output, torque, or indicated mean effective pressure can be gathered from tables as well. By including a crank-shaft and a transmission model, the engine speed transients can be simulated.
Such modeling approaches are commonly used for control testing and hardware in the loop applications (HIL), where real-time capabilities of the model are required. However, in many other applications, such models can be also used for advanced air by fuel control designs where such a model can be linearized around an operating point in order to obtain a linear state-space description 3.18.
In case of HCCI, the main cylinder outputs are the work output, typically expressed as $IMEP$ or torque, and the combustion phasing (e.g. CA_{50}). Since $IMEP$ is rather a static process depending on the fuel injected and intake manifold pressure, a table can be used as well. However, as for the combustion phasing output of an HCCI engine, dynamics inside the cylinder exist which must be covered in a simulation model as well. Since HCCI combustion depends heavily on the in-cylinder temperature, varying the amount of fuel brings a shift in combustion phasing due to cooling effects during fuel evaporation processes, or due to the varying gas temperatures of the exhaust gases that are retained from a previous cycle. Therefore, cyclic coupling exists and must be modeled as well to obtain a controller that is suitable for HCCI control.
In the following sections, a generic model for an HCCI model will be presented that suits not only BDSC but may be applied to other HCCI variants as well.
It is based on physical principles, but in order to simplify the complicated gas exchange process of a BDSC engine, as well as to increase the accuracy of the model, some empiric correlations had to be included, which overall gives a so-called grey-box model.

7.1 Mean-Value Engine Model (MVEM) of the BDSC HCCI Engine

In this modeling approach, an engine cycle is broken down to discrete events within one cycle. Specifically:

1) Gas-exchange and compression phase
   (a) Calculation of in-cylinder states, such as pressure and temperature from mixing of air and hot exhaust gases
   (b) Calculation of the combustion phasing, based on pressure and temperature from the previous calculation (a)
   (c) Calculating temperature and pressure after compression at some point before combustion
2) Combustion
   (a) Calculating temperature and pressure after combustion by assuming isochoric combustion
3) Expansion and Exhaust
   (a) Calculating temperature and pressure after expansion and before exhaust valve opens
   (b) Calculating temperature after exhaust by assuming same pressure as in exhaust port
4) Going back to first step 1) and using exhaust gas temperature from step 3)

From this sequence, the cycling coupling becomes evident and that the exhaust gas temperature after exhaust is taken over to the next cycle.
The overall sequence is again illustrated in the following figure 7.1.

The single steps are introduced more in detail in the following sections.

Gas-Exchange and Compression Phase

For calculating the in-cylinder conditions before compression phase and for avoiding complex models for the gas exchange, a correlation for EGR and for the in-cylinder pressure at the end of gas-exchange are necessary and can be read from steady-state experiments or simulation results since their transients are negligible.

In case of EGR, a polynomial function with fitted parameters depending on the exhaust mean pressure and the in-cylinder temperature during exhaust and at the end of the blow-down process has been found suitable, which reads:

$$EGR = f(P_{Exh}, T_{BD}) \tag{7.1}$$

while at the same time, the pressure can be found by a static affine correlation, depending only on the mean exhaust pressure as:

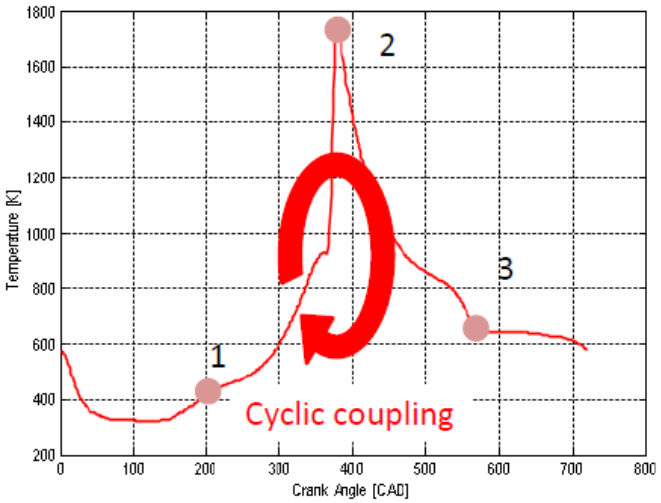

Figure 7.1: Depiction of the discrete steps and cyclic coupling for the MVEM

$$P_{SCP} = c_1 \cdot P_{Exh} + c_2 \tag{7.2}$$

with the pressure and EGR known at start of compression, the temperature inside the cylinder at start of compression can be calculated by assuming perfect mixing with hot exhaust gas from the previous cycle and fresh air:

$$T_{SCP} = k_1 \cdot x_{EGR} \cdot T_{BD} + k_2 \cdot (1 - x_{EGR}) \cdot T_{Int} \tag{7.3}$$

with

$$k_1 = \frac{c_{v,Int}}{c_{v,Mix}} \cdot \chi_{HT,Int} \qquad \text{and} \qquad k_2 = \frac{c_{v,Exh}}{c_{v,Mix}} \cdot \chi_{HT,Exh} \tag{7.4}$$

Note that the fuel has been neglected here to further simplify the model. It can be included into the equation, and by also including the heat capacity of the fuel into it, cooling effects may be simulated, which may retard combustion phasing, despite of neglecting the cooling effect of evaporation.
The unknown constants of heat transfer with walls and heat capacities have been condensed into unknown constants k_1 and k_2 in equation 7.4, which must be found when parameterizing the model. Furthermore, due to the compression of the upward moving piston before the EGR re-breathing valve closes, some temperature and pressure rise may occur, which can be considered in the constants as well.

Once the temperature and the pressure are known, combustion phasing can be estimated at this point.
The following figure 7.2 depicts a map of identified CA_{50} from the 0-D model and it shows a clear trend of early combustion phasing with increasing temperature and pressure, where the temperatures and pressures are taken from a reference model as well. At this point it should be noted that a strong intercoupling between pressure and temperature exists. The higher the temperature, due to higher EGR, which is due to higher exhaust pressure, the higher the in-cylinder pressure.

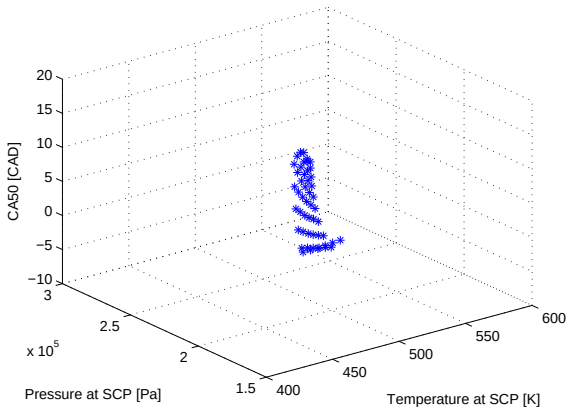

Figure 7.2: Identified Dependency of CA_{50} on In-Cylinder Temperature and Pressure at Start of Compression Phase (SCP)

In order to find a correlation for combustion phasing, the ignition delay model from He et al. [46] has been taken as a reference and modified to match the target values from the reference model. It is formulated as:

$$CA_{50} = A \cdot {P_{SCP}}^{B} \cdot exp(E_{mod}/T_{SCP}) \tag{7.5}$$

The motivation for reducing the ignition model to evaluate pressure and temperature only is explained by [22] and [21].
Additionally, the integral as in equation 6.31 has been omitted here for reasons that will be explained later.

After the location of CA_{50} has been found, compression from the start of compression to a virtual start of combustion point can be calculated as:

$$T_{SOC} = \left(\frac{V_{CA_{50}}}{V_{SCP}}\right)^{\frac{\gamma}{\gamma-1}} \cdot T_{SCP} \tag{7.6}$$

and

$$P_{SOC} = \left(\frac{V_{CA_{50}}}{V_{SCP}}\right)^{\gamma} \cdot P_{SCP} \tag{7.7}$$

The term virtual start of combustion point refers to the fact that this information cannot be obtained from the reference model due to the simulated combustion and, hence, higher temperatures and pressures than in compression only. For that reason, the information has to be extrapolated with the equation above 7.6 and 7.7.

Combustion

There are several ways to model combustion. One common way is to condense the entire combustion process at the end of combustion and to evaluate the pressure and temperature only

there. The Wiebe function from the more detailed 0-D model can be taken here, with the simplified correlations for Wiebe exponent and especially the extremely simplified combustion duration correlation as introduced above. In such an approach one would calculate the actual start of combustion point so that the ignition model 7.5 has to be fitted to SOC location instead of CA_{50}. By knowing the actual start of combustion and the combustion duration, the in-cylinder conditions could be calculated by assuming isochoric combustion at this point and including a zero-dimensional wall-heat transfer term to tune the model and match it with temperatures and pressures. However, this approach makes calculation of CA_{50} more complicated, and the Wiebe function must be processed to estimate CA_{50}. Alternatively, a linear interpolation between combustion starting point and ending point has been used by other authors (e.g. [96]).

In the approach here, the location of CA_{50} has been chosen for simplicity. The assumption that the entire combustion process is not only isochoric, it also occurs only at the location of CA_{50}. This can be justified in case of HCCI, since combustion is typically fast and close to the ideal cycle.
Hence, by knowing the temperature from equation 7.6, temperature at the end of combustion is then derived from the isochoric relationship:

$$T_{EOC} = T_{SOC} + \frac{Q_{LHV} \cdot m_{fuel} \cdot \chi}{m_{Cyl} \cdot c_v} \tag{7.8}$$

where the in-cylinder mass m_{Cyl} can be calculated by the ideal gas law:

$$m_{Cyl} = \frac{p_{SOC} \cdot V_{SOC}}{R_{cyl} \cdot T_{SOC}} \tag{7.9}$$

with p_{SOC} the pressure, V_{SOC} the cylinder volume, R_{cyl}, the gas constant of the mixture, and T_{SOC} the temperature at start of combustion (SOC), or at any other point during compression. Note that χ considers wall-heat losses and is a non-dimensional constant that needs to be tuned.

Expansion and Exhaust

From the peak temperature 7.9 and pressure after combustion, the pressure and temperature at exhaust valve opening after the expansion phase are calculated again from polytropic expansion relations. The subsequent blow-down process is then commonly modeled by assuming that the pressure inside the cylinder is equal the mean pressure of the exhaust after blow-down so that the following relation holds:

$$T_{BD} = \left(\frac{P_{Exh}}{P_{EVO}} \right)^{\frac{\gamma}{\gamma-1}} \cdot T_{EVO} \tag{7.10}$$

During blow-down and exhaust, the exhausted mass and enthalpy needs to calculated. The exhausted mass was calculated by assuming that the exhausted mass is equal to the cylinder displacement volume and by substracting the re-breathed exhaust gas as EGR. This is also a simplification and in accordance to the ideal gasoline cycle where the substraction of EGR implicitly includes the volumetric efficiency.
Calculation of the exhausted enthalpy is then straightforward by knowing the exhaust mass-flow and by assuming a constant in-cylinder temperature, of which the blow-down temperature from

equation 7.10 was taken.
The two equations for exhausted mass and enthalpy are then:

$$\begin{aligned} \dot{m}_{Exh} &= m_{disp} \cdot 0.5 \cdot N \\ \dot{H}_{Exh} &= \dot{m}_{disp} \cdot c_p \cdot T_{BD} \end{aligned} \tag{7.11}$$

Where m_{disp} is the displaced mass.
Note that the engine speed N in the unit $[rev/s]$ has been included in order to convert the exhausted mass into the mass-flow. The term 0.5 considers two revolutions per cycle to account for being a four-stroke engine.

The two equations 7.11 couple the cylinder model, which is in discrete-time, with the exhaust model, which is in time-continuous domain. It should be emphasized here that back-coupling from the exhaust to the cylinders is not modeled and that modeling of the exhaust ports has been entirely omitted. The reason for this and further discussions are given below.

Power Output (IMEP)

Since unlike in NVO systems, the valve phasings are fixed in BDSC HCCI, calculation of the indicated mean effective pressure (IMEP) is straightforward.
In the approach here, a simple equation taken from the ideal gasoline process has been utilized [52] and is shown in the equation 7.12:

$$IMEP = Q^* \left(\frac{1}{\gamma - 1}\right) \left(\frac{r_c}{r_c - 1}\right) \left(1 - \frac{1}{r_c^{\gamma - 1}}\right) p_1 - \Delta p \tag{7.12}$$

with

$$Q^* = \left(\frac{m_f Q_{LHV}}{m \cdot c_v T_1}\right) \tag{7.13}$$

and pumping losses Δp due to elevated exhaust pressures have been added as:

$$\Delta p = p_{Exh} - p_{atm} \tag{7.14}$$

Thereby some minor dynamics of the $IMEP$ are included as well, such that $IMEP$ drops when the exhaust pressure increases, and conversely rises when the exhaust pressure falls. The dynamics of $IMEP$ are then governed by the dynamics of the exhaust pressure.
Including this $IMEP$ loss is a sensible step, in order to obtain a controller that considers the cross-coupling of exhaust valve and engine load.

Exhaust Model

Modeling of the exhaust is straightforward, by just applying conservation of mass and energy for calculation of mass and temperature.
By knowing the mass-flows and enthalpy flows from the cylinders from equation 7.11, the mass-balance in the exhaust manifold is:

$$\dot{m}_{Exh} = \Sigma \dot{m}_{Cyl} - \dot{m}_{ExhThro} \tag{7.15}$$

where the $\dot{m}_{Cyl}$ are the exhausted mass-flows and the term $\dot{m}_{ExhThro}$ is the mass-flow through the exhaust throttle as modeled as 6.4.
And the first-law of thermodynamics gives the energy-balance for temperature calculation with:

$$\dot{m}_{Exh} = \Sigma \dot{H}_{Cyl} - \dot{H}_{ExhThro} - \dot{Q}_{Wall} \tag{7.16}$$

Where $\dot{H}_{ExhThro}$ is the enthalpy-flow through the exhaust throttle. Note that a term $\dot{Q}_{Wall}$ for the wall-heat losses is included and can be used to tune the model.
The exhaust pressure can be calculated from the ideal gas equation 6.21.

Remarks on the Mean-Value Engine Model for BDSC HCCI

The presented model consists of a discrete-time part, which are the cylinders, and a continuous-time part, which is the exhaust manifold. By utilizing a zero-order hold approach, the discrete-time cylinder model can be coupled with the time continuous exhaust system to give the overall engine model.
As a special feature, the model has been designed such that the blow-down pressure wave calculation has been omitted, and only the mean exhaust pressure is considered in the model. The justification for this can be explained in the following figures, where figure 7.3 shows the transients of the pressure traces from experiments where the throttle was opened in one step and engine speed kept fixed:

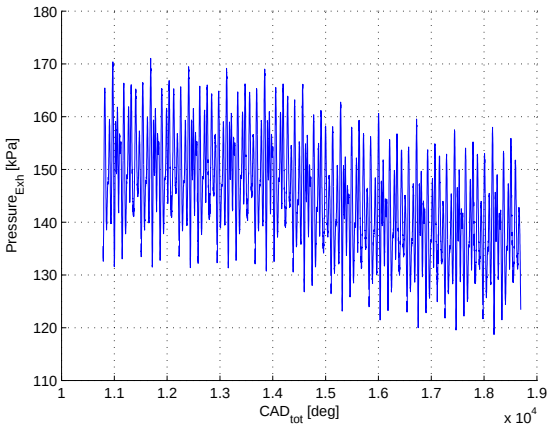

Figure 7.3: Exhaust pressure changes with exhaust throttle opening

While the ripples of the pressure waves can clearly be seen in this plot, the mean pressure shows a slowed transient when dropping from higher pressures to a steady-state lower pressure value. These transients closely resemble first-order dynamics, while it seems that the pressure characteristics do not change at all.
This is confirmed in the next two figures which depict a close-up of the pressure traces for one engine cycle at steady state before and one cycle after these transients. Figure 7.4 shows the pressure traces of one cycle before the step, while the next figure 7.5 shows the pressure traces of one cycle after the step.

Both plots clearly show that the pressure traces hardly change and are very similar if the mean pressure is taken out. This is not surprising, since engine speed was kept fixed, so that

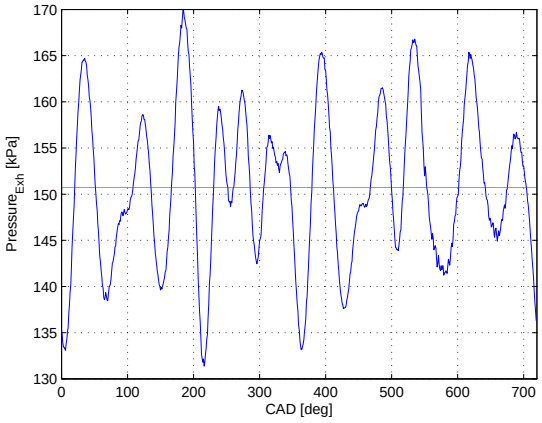

Figure 7.4: Exhaust Pressure traces of one cycle before the exhaust throttle step change

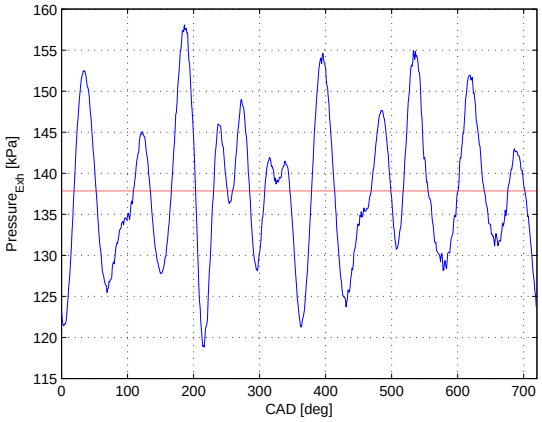

Figure 7.5: Exhaust Pressure traces of one cycle after the step change

pressure wave travels at constant distances (e.g. exhaust port to catalyst) and at constant time-scales. Hence, pressure wave interference happens at one point in space always at the same time-instance such that, eventually, the apparent instantaneous pressures have similar characteristics. This is true for both mean pressure levels, and consequently, the pressure traces in both figures look the same despite of different pressure levels. Hence, with varying engine speed, it may expected that the pressure traces differ, and as another source may be mentioned variable valve timings such that the blow-time pressure wave timing varies with changing exhaust opening time. However, since in a BDSC HCCI engine variable-valve systems are not employed, this does not need to be considered in a simplified model.
This clearly motivates the use of a mean exhaust pressure for control only and the correlation of the EGR and in-cylinder pressure as given above.
In order to account for engine speed, it might be conceivable to apply the same engine model with different parameters for the correlations for different engine speeds and to interpolate between the discrete engine speed points. Such an approach might be useful in control design, when engine speed variations are to be modeled as known disturbances. A control-oriented model that accounts for speed effects for NVO HCCI has been presented in [106].

As a further model reduction measure, since the pressure wave is not modeled at all, re-breathing has been simplified by assuming simply that the gas condition inside the cylinder at exhaust is directly influencing the next cycle, regardless of the exhaust port condition. Hence, there is no feedback in terms of temperature from the exhaust system to the cylinders. Wall-heat losses in the exhaust ports can be compensated by tuning the constants k_1 and k_2 for the ideal mixing in equation 7.4. By omitting a sub-model for the exhaust port temperatures, additional states for control design can be avoided, which greatly helps in control design.

An additional feature of this model is given by the simplified ignition model. Since the pressure at start of compression is known by expression 7.2, the temperature at start of compression can be back-calculated by inverting the ignition model 7.5 and by knowing the combustion phasing from the previous cycle. Here, in order to prevent mathematical imaginary values for the temperature, combustion has been assumed to be around a value of 360 deg instead of around 0 deg to avoid negative values.

The same holds for the amount of fuel, which can be back-calculated by knowing $IMEP$ from the previous cycle only.
Thereby, a cycle start at start of compression, and the amount of fuel injected before that instant is taken over to the next cycle, when it gets burnt. This simulated a port fuel injector where it is assumed that amount of fuel injected into the port is first trapped as a film at the port, until it evaporates and is carried over to the next cycle.

So far, only exhaust pressure has been discussed as a dynamic sub-model for the mean-value engine model for BDSC HCCI, however, the combustion phasing transients have not been discussed as of yet.
From experimental data, the following figure 7.6 shows the CA_{50}, $IMEP$ and exhaust pressure transients when the amount of fuel is changed and the exhaust valve kept fixed.

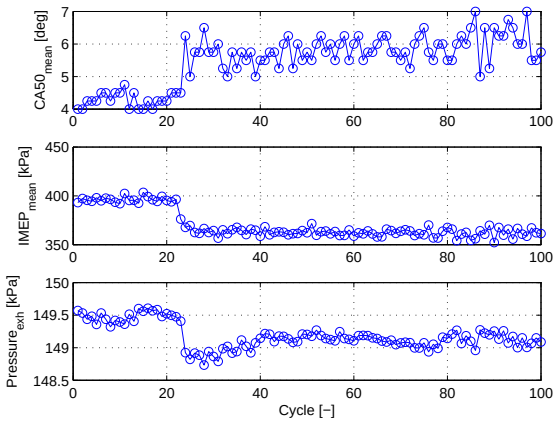

Figure 7.6: Step Input of the Fuel of the real engine

And the figure 7.7 shows the fuel step change, from lower values to higher values from experiments.

Both examples show that combustion phasing changes greatly when the amount of fuel is injected. This is easily explained by the hotter exhaust gas temperatures after combustion with

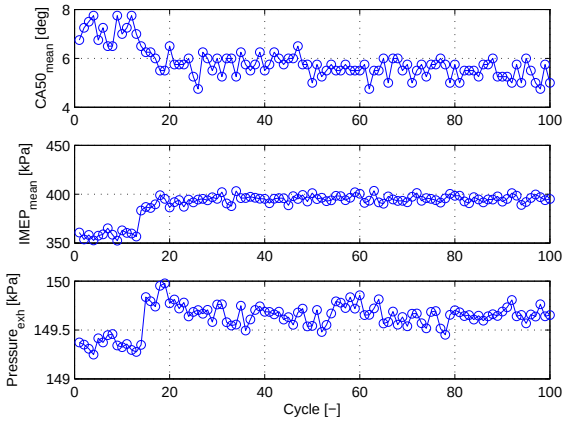

Figure 7.7: Step Input of the Fuel of the real engine

higher amount of fuel. The next engine cycle then reuses these hotter exhaust gases which raise the in-cylinder temperature and advance ignition. Conversely, with less fuel, combustion temperatures reduce and delay point of ignition.
This is a cycle-to-cycle coupling through the exhaust gas temperatures, which has been considered in the mean-value engine model by design, as discussed above. It may therefore be expected that the model behaves in a similar way and with similar transients, although mass of injected fuel is not considered in the presented simplified ignition model (equation 7.5) at all.

The overall modeling approach presented here allows for a change of the states, of which the temperature at start of pressure (while pressure at this point is only a static mapping from the exhaust pressure) as a possible state can be converted in CA_{50} as a new state variable. It is therefore now possible to link the cycles by knowing only combustion phasing CA_{50} and the mean indicated effective pressure $IMEP$, which extremely simplifies control design.

The equations have been implemented as Level-2 S-Functions in Simulink for the cylinder and for the exhaust, respectively. The separation the models was done due to the different time domains of both engine parts. Simulink S-Functions are convenient due to control-oriented functions provided. These comprise a function for the inputs and outputs, an update function for the discrete-time states, and a derivative function for the continuous-time states where the integration scheme is already included. The MATLAB programming language M, used in both functions is sufficient, even for simulation execution time much faster than real-time, due to the extremely low complexity of the model. This helps greatly in control design and offline evaluation tests.
By inserting time-delay properties in each cylinder S-Function block, a phase shift between the cylinders can be simulated.
The built-in variable-time solver ODE15s, which incorporates an algorithm for mathematically stiff problems, has provided good results.

This model has shown to be a suitable model for control design for BDSC HCCI engines, but due to the correlations for EGR and pressure at start of compression phase as well as several unknown parameters, parameterization and tuning of this model becomes cumbersome. An au-

tomated two-step tuning methodology has been developed for this purpose and is presented in the next section.

7.2 Engine Parameter Identification

The mean-value engine model, as introduced in the previous section, incorporates several unknown parameters that need to be found for parameterization. In this section, an automated tuning scheme will be introduced that finds suitable parameters for the engine model to match with reference data and to increase the accuracy of the model.
For that purpose, reference data is needed, and since values for in-cylinder temperatures and others that cannot be measured in experiments are necessary, a more detailed simulation model is required.
In order to collect enough data for fitting the presented control-oriented model, an additional identification routine was created that ran the reference engine model at different operating points until cyclic convergence was achieved. The 0-D model presented in an earlier chapter was used here due to its low complexity and faster simulation speed such that this identification procedure is only a matter of less than an hour. The collected input and output data, as well as in-cylinder information for a wider range of the engine operating points, were then used as a reference for the control-oriented model.
The range of the fuel was between 11mg and 16mg per cylinder and the exhaust throttle angle was between 0.1 degrees and 1.5 degrees. Cases which misfired due to exhaust throttle opened too wide were excluded in this analysis.
The following figure 7.8 shows the outcome of this identification on the 0-D model where a clear and physically reasonable trend of combustion phasing with amount of fuel and exhaust throttle angle can be seen.

Values for CA_{50} from $-10deg\ ATDC$ until up to $+20deg\ ATDC$ were taken into consideration for the two-step calibration routine, which will be presented in the next section.

7.3 MVEM Calibration

In order to find the right parameters for the mean-value model with respect to reference data from the 0-D model (or a 1-D model), a parameterization routine is suggested here that tunes the model automatically.
Not only the static correlations for EGR and in-cylinder pressure at start of compression (P_{SCP}) need to be found, but the condensed parameters k_1 and k_2 in equation 7.3 also need to be determined, consisting of the heat capacities and contribution of the heat transfer from and to the walls. Other parameters, such as heat capacities c_p and c_v or polytopic coefficients can be taken from the reference model, a conflict due to the variability with temperature exists here. The heat capacities depend on the mixture of the gas but especially on the temperature, and this influence of the temperature is considerably high during compression and expansion as well as during combustion. Including a variable heat capacity would bring mode fidelity into the model, and wall-heat transfer effects with varying wall temperatures might be included with variable polytropic exponents (e.g $\kappa = f(T)$). This, on the other hand, would make modeling much more complex and bring a negligible advantage. Wall-temperatures typically vary with time-scales of at least one hundred engine cycles [19], and these dynamics can be compensated for by using

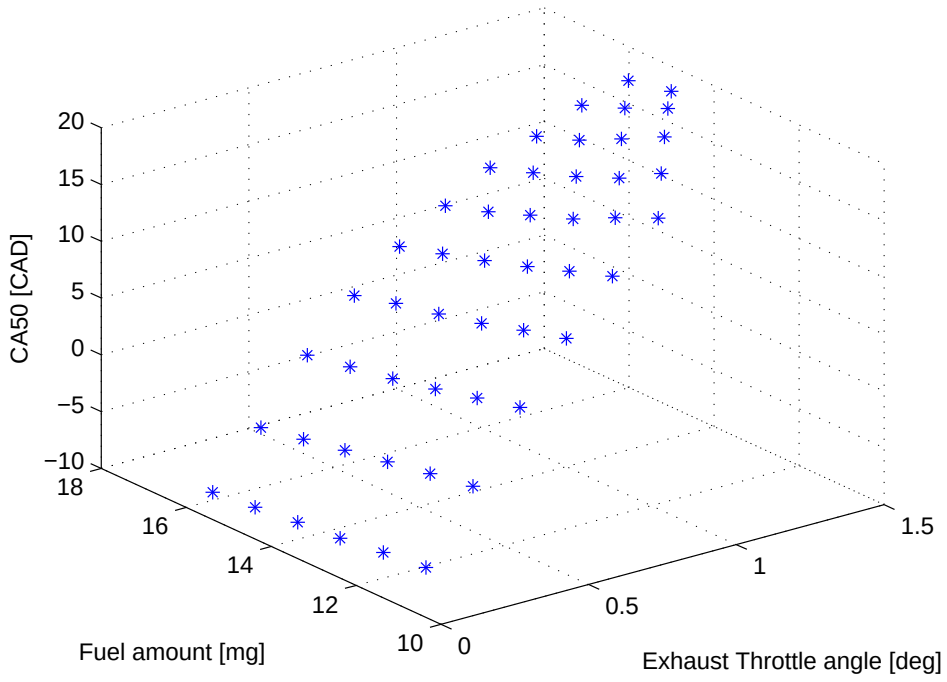

Figure 7.8: Identification Points, taken from the Reference Model

an integral action in the control algorithm. Therefore, one single, static heat capacity is needed that applies to all identified engine operating points.

With all identified parameters, they can be applied to the mean-value engine model, but due to inherent modeling errors the model might not converge to the targeted reference points causing slight deviation. To increase the accuracy of the final model, a second calibration step has been developed here to run and automatically fine-tune the entire model.
The overall calibration approach consist of two major steps, which are:

1. **First Step: Static Parameter Calibration**
   Fitting unknown constants for each stage in a cycle

2. **Second Step: Dynamic Parameter Calibration**
   Applying the constants to the model and fine-tune a selected parameter during simulation runs to ensure cyclic convergence

The next section explains the two tuning steps more in detail.

7.3.1 First calibration step: Static Parameter Calibration

This step tunes the parameters of each stage in a cycle and equation presented in the introduction of the mean-value model above.

For step 1. an engine cycle from a reference model (e.g. 0-D model) is taken and split into different stages, and a usually non-linear function with known inputs ($u_{fitting}$) and outputs ($y_{fitting}$), as

$$y_{fitting} = f(u_{fitting}) \tag{7.17}$$

where parameters of the function f are unknown.
The calibration stages in one engine cycle are:

1. **Start of compression**

   - **Correlations for EGR and $\mathbf{P_{SCP}}$**
     At this stage, the correlations for EGR and the pressure at start of compression P_{SCP} must be fitted. This is done by simple curve fitting procedures with the data directly taken from the reference model.
     Thereby, for the EGR polynom, the input-values $u_{fitting}$ and output-values $y_{fitting}$ are:

     $$u_{fitting} = \begin{pmatrix} P_{exh} \\ T_{BD} \end{pmatrix}, \qquad y_{fitting} = \begin{pmatrix} EGR \end{pmatrix} \tag{7.18}$$

     with the mean-exhaust pressure P_{exh} taken from the reference model. The values from the mean-values model are still unknown for T_{BD} and is taken from the reference model at a certain point after the blow-down process.
     The correlation for the pressure P_{SCP} is straightforward, since this is only an affine function that only depends on the mean exhaust pressure. The input data reduced then to only one as shown in the following vectors:

     $$u_{fitting} = \begin{pmatrix} P_{exh} \end{pmatrix}, \qquad y_{fitting} = \begin{pmatrix} P_{SCP} \end{pmatrix} \tag{7.19}$$

     In accordance with the reasons above, the data is directly taken from the reference model.
   - **Mixing of fresh air and exhaust gases from previous cycle** The unknowns from the equations 7.7 and 7.6 are fitted such that the right temperature at start of compression is achieved. The starting temperatures after blow-down are taken from the reference model as well for tuning the model since the values from the mean-value models are not available as of yet.

     $$u_{fitting} = \begin{pmatrix} T_{Intake} \\ T_{BD} \end{pmatrix}, \qquad y_{fitting} = \begin{pmatrix} T_{SCP} \end{pmatrix} \tag{7.20}$$

     Here, the T_{Intake} was set to atmospheric temperature at $20degC$.
   - **Ignition model for prediction of CA_{50}**
     The constants for the ignition model have been tuned with data from the reference model, which are the temperature and pressure at start of compression, and the targeted CA_{50} values.

$$u_{fitting} = \begin{pmatrix} T_{SCP} \\ P_{SCP} \end{pmatrix}, \qquad y_{fitting} = \begin{pmatrix} CA_{50} \end{pmatrix} \tag{7.21}$$

- **Compression** With the knowledge of the starting temperature and pressure and the values for CA_{50}, the polytropic coefficient can be tuned to match the targeted pressure and temperature. However, since isochoric combustion at CA_{50} is assumed in this model, the targeted values from the reference model are usually unknown. They can be determined from additional simulation in the reference model by skipping combustion. This however would unnecessarily increase the workload for tuning of the model, with little benefit. Instead, the temperature at -20 degrees ATDC have been taken, and a fitting between SOC and -20 ATDC carried out to gain the polytropic coefficents for compression of the mean-value model until CA_{50} and before combustion.
  For fitting, the input and output vectors are:

$$u_{fitting} = \begin{pmatrix} T_{SCP} \\ P_{SCP} \end{pmatrix}, \qquad y_{fitting} = \begin{pmatrix} T_{CA_{50}} \\ P_{CA_{50}} \end{pmatrix} \tag{7.22}$$

2. **Combustion**

- **Isochoric combustion** Combustion is assumed to be isochoric at CA_{50}, and the peak temperatures and pressures after combustion need to be found. This poses two problems: first, the temperatures and pressures before combustion are unknown, which has already been addressed in the previous step. Second, the peak temperatures and pressures from the time-continuous reference model are not located at the end of combustion, which is the assumption for the mean-value model. To overcome the first problem, the starting temperatures and pressures are found by using the polytropic compression with the polytropic exponents from the previous fitting step, where the target values at were set at -20 deg BTDC, which are known from the reference model. The extrapolation looks then like:

$$T_{SOC} = \left(\frac{V_{CA_{50}}}{V_{340}} \right)^{\frac{\gamma}{\gamma-1}} \cdot T_{340} \tag{7.23}$$

  and

$$P_{SOC} = \left(\frac{V_{CA_{50}}}{V_{340}} \right)^{\gamma} \cdot P_{340} \tag{7.24}$$

  where the index 340 stands for -20 deg BTDC and γ is the polytropic compression coefficient identified from the reference model for compression between start of compression phase (SCP - when EGR valve closes) and -20 deg BTDC.
  As for the second conflict with the peak values for temperature and pressure after combustion, the peak values during have been nonetheless taken from the reference model and used without any modification for the fitting procedure.
  The input and output vectors for the fitting routine for combustion are:

$$u_{fitting} = \begin{pmatrix} T_{SOC} \\ P_{SOC} \\ m_{Fuel} \\ m_{Cylinder} \end{pmatrix}, \qquad y_{fitting} = \begin{pmatrix} T_{max} \\ P_{max} \end{pmatrix} \tag{7.25}$$

The temperatures and pressures of the input vector have been extrapolated by using equation 7.23 and 7.24 and using T_{340} and P_{340} from the reference as starting values, and κ from the previous optimization step. m_{Fuel} is an input into the system that is known from the identification of the reference model, and $m_{Cylinder}$ is the total cylinder mass, either taken from the reference model, or calculated via ideal gas equation 6.21 and with known in-cylinder pressure and temperature at some point after gas exchange.

3. **Expansion and Exhaust**

- **Expansion**
  Expansion can be easily fitted as done for the compression stroke explained above, such that the temperatures and pressures at exhaust valve opening can be calculated by polytropic relations for temperatures and pressures only. Here, only the polytropic coefficient needs to be found. However, it should be noted here that starting point for expansion are the peak values for temperatures and pressures at CA_{50}, so this approach is physically not entirely correct. However, since this simplifies the entire model, this modeling abstraction has been chosen over model fidelity.
  The optimization values for this step are:

$$u_{fitting} = \begin{pmatrix} T_{EOC} \\ P_{EOC} \end{pmatrix}, \qquad y_{fitting} = \begin{pmatrix} T_{EVO} \\ P_{EVO} \end{pmatrix} \tag{7.26}$$

  where these values are taken from the reference model.

- **Exhaust**
  By knowing the starting and pressures and temperatures, the exhaust model can be easily fitted. As a target pressure, the mean exhaust pressure has been selected. However, since the temperature at the reference model varies during exhaust a fixed location towards the end of exhaust and before intake has been chosen. Here, the location was set at 300 degrees after combustion TDC.

$$u_{fitting} = \begin{pmatrix} T_{EVO} \\ P_{EVO} \\ P_{Exh} \end{pmatrix}, \qquad y_{fitting} = \begin{pmatrix} T_{BD} \end{pmatrix} \tag{7.27}$$

  where the values have been taken directly from the reference model.

All equations constants to be found were optimized by means of least-squares, with function $f(u)$, the provided input vectors $u_{fitting}$, the output vectors $y_{fitting}$, and the function constants k_i to be found by least squares subject to:

$$min_{k_i} \Sigma (f(u_{fitting}) - y_{fitting})^2 \tag{7.28}$$

In almost all optimization steps, input and output data were taken from the reference model, and since the mean-value model has some imperfections and differences to the reference model, applying the optimized constants on the engine model the model would not exactly converge to the targeted reference data. Accuracy could be greatly increased by tuning one selected parameter again on the running model until the right target values are met.
This step is explained in the next section.

7.3.2 Second calibration step: Dynamic Parameter Calibration

In the second step of this optimization routine, the parameters that have been found in the first stage are applied to the model, and selected parameters are fine-tuned again to reach cyclic convergence. This step is necessary, since for each stage in one cycle, ideal starting and target values have been taken from the reference model. However, if they are applied to the mean-value model, these starting and target values at each stage will differ due to cyclic coupling and the overall simulation results will move away from the actual target when reaching cyclic convergence.
Since at this stage an entire engine model will be parameterized, the overall optimization task will become complicated and optimization might become difficult due to many different optimization parameters. Optimization then might only sub-optimal results or even abort due to numerical errors.

Therefore, as in the first optimization step, the second optimization step is also divided into several sub-tasks, which are:

1. **Cylinder**
   Simulate the cylinder alone, by setting the boundary conditions (e.g. exhaust pressures) fixed according to the reference model. Hereby, the temperature at start of compression has been fine-tuned to ensure cyclic convergence to the targeted combustion phasing values. Also, like in the first optimization step, input and output vectors can be defined, which are:

$$u_{fitting} = \begin{pmatrix} m_{Fuel} \\ P_{Exh} \end{pmatrix}, \qquad y_{fitting} = \begin{pmatrix} CA_{50} \end{pmatrix} \tag{7.29}$$

   $IMEP$ has not been fine-tuned here, since this is a static relation and hardly converges to a steady-state value.

2. **Exhaust Manifold**
   Simulate the exhaust manifold alone by setting the boundary conditions (mass-flows and enthalpy flows) fixed to the values from the reference model. Thereby, the influence of the cylinders is excluded. The input and output vectors are:

$$u_{fitting} = \begin{pmatrix} \dot{m}_{Exh,Cyl} \\ \dot{H}_{Exh,Cyl} \end{pmatrix}, \qquad y_{fitting} = \begin{pmatrix} P_{Exh} \\ T_{Exh} \end{pmatrix} \tag{7.30}$$

   The values for the cylinder mass-flows $\dot{m}_{Exh,Cyl}$ and enthalpy flows $\dot{H}_{Exh,Cyl}$ are taken directly from the reference model.

To fit the model, the heat capacity c_v for the exhaust manifold has been taken for fine-tuning. The initial value has been estimated and not parameterized before.
The target values are here the exhaust pressure and temperature. Care should be taken due the different units and their magnitudes of pressure, which is simulated in Pascal, and temperature, which is simulated in Kelvin. This would privilege the pressure and optimization might stop, although the targeted temperature may not have been reached. As a solution to this problem, the values can be normalized, such that the influence of the magnitude of the pressure has been diminished.
As an alternative to the heat capacity as a tuning factor, the heat transfer could be tuned as well. However, with a fixed wall temperature for all considered cases, an increase of the wall-heat transfer coefficient would flatten the temperature profile over all cases and approximate them to the wall temperature. In the worst case, at a very high heat transfer coefficient, the exhaust temperature would be the same as for the wall of the exhaust manifold. Tuning the heat capacity has therefore found as a more effective measure for tuning the exhaust manifold.

3. **Engine Model**
   Simulate the cylinder with the exhaust manifold together. Here, the already tuned cylinder is coupled with the tuned exhaust manifold, and again the ignition model has been adjusted to optimize the results. Here, it has been found to optimize the offset to reach the targeted values for combustion phasing.
   Finally, with the entire model tuned, the input and output vectors are the same as for the final model, except for $IMEP$, which has been excluded in the tuning procedure. The vectors are:

$$u_{fitting} = \begin{pmatrix} m_{Fuel} \\ \theta_{Exh} \end{pmatrix}, \qquad y_{fitting} = \begin{pmatrix} CA_{50} \end{pmatrix} \tag{7.31}$$

   Where m_{Fuel} is the amount of fuel injected and θ_{Exh} and the exhaust throttle angle.

It should be noted here that this approach may ensure optimized steady-state values. This, however, does not guarantee the right transients, which must be considered during modeling.
This calibration routine has proven to be a useful tool for optimization the grey box model for control design. As mentioned in the introduction, it might help to find the variables for different operating points at different engine speeds and loads (when other intake cams are used), such that interpolation between the parameters may ensure full coverage of the simplified model over all necessary operating points.
Thus, different controllers for different operating points could be designed and connected via gain scheduling, which is commonly done in engine control.
Additionally, speed variations for example could be modeled and included in the controller design as known perturbation, which might enhance the quality of the controller.

7.3.3 Results of the MVEM optimization routine

In this section, the final results of the calibration routine from above is shown in plots. The results from the first calibration step are shown first, after which the results of the second calibration step will be introduced.

First step

Figure 7.9 shows the most important results from the first calibration step, where the target values (here: from the 0-D model) are depicted as "Aim" in blue, and the results from the equations above in green "Simplified". Here (from top to bottom and left to right), the plots for combustion phasing (CA_{50}), temperature at -20deg BTDC (T_{340}), combustion peak temperature(T_{max}), temperature at exhaust valve opening (T_{EVO}), temperature after blow-down ($T_{BlowDown}$), and temperature after EGR re-breathing, when the EGR valve closes, denoted as "start of compression phase" (T_{SCP}) are plotted over the 37 randomly sampled cases.

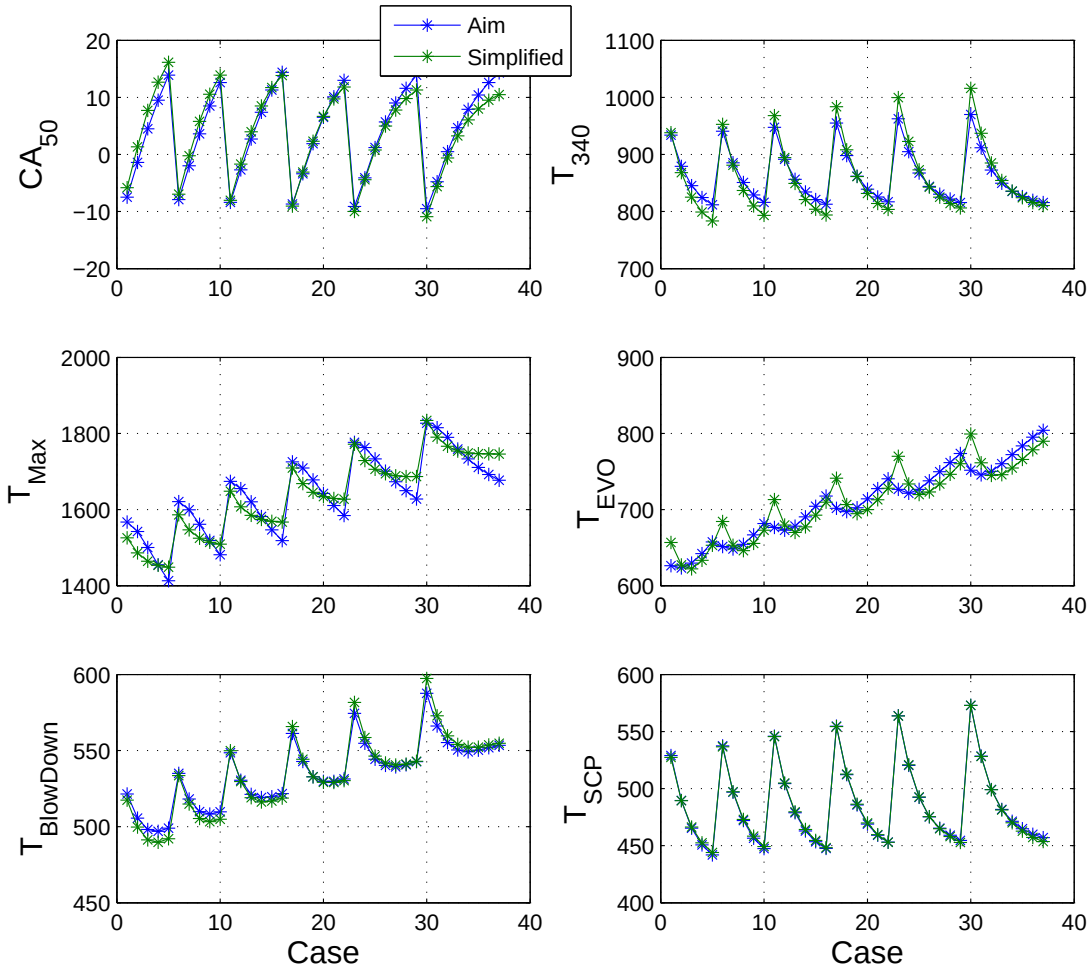

Figure 7.9: Fitting Routine Results: Overall Results

Second Step

The final results of the second calibration step are shown in the following plot 7.10. Here, the $IMEP$ in the first plot, and CA_{50} are shown in the second plot, together with their respective residuals. The blue values are the reference values, while the red ones are those with the parameterization directly from the first parameterization step (”prev”). The green ones (”optim”) are the optimized ones that have been fine-tuned on the entire MVEM. It can bee seen that little improvement has resulted from the second calibration routine and that the values from the first step were adequate.
Furthermore, the residuals for combustion phasing become larger at extreme values of early combustion phasing or late.

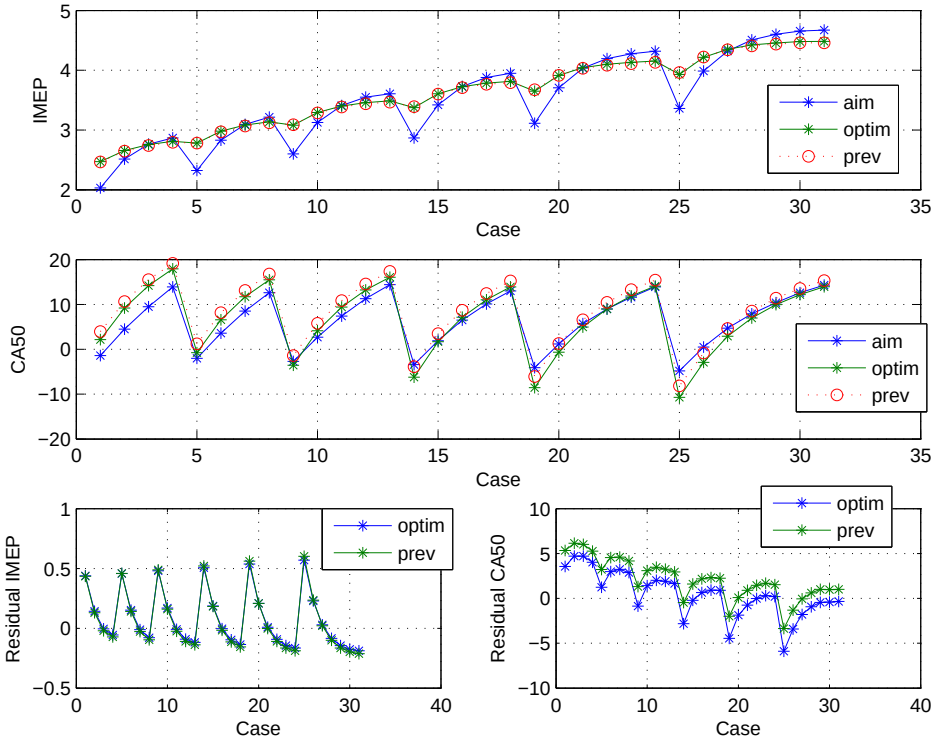

Figure 7.10: Fitting Routine Results: Second Step, Final: Full Engine

However, despite the ultra simplification of the presented MVEM, including its extremely simple combustion model, the maximum residuals have been found around 6deg cad, and this is mainly the case for extreme combustion. This result is surprising, since this accounts for CA_{50}, which not only includes ignition timing, but also indirectly combustion duration, which are all included in the presented model.

7.3.4 Remarks on the MVEM calibration routine

The calibration routine introduced here is a convenient calibration tool for the mean-value engine model (MVEM). By splitting the overall calibration routine into several sub-routines more robustness is brought into the scheme.

The employed ignition model here has been found as accurate and simple enough for control despite the presence of a shortcoming explained here.
This is depicted in the following figure 7.11, where the combustion phasing, as CA_{50}, is plotted over the in-cylinder pressure and the temperature at start of compression phase (SCP).

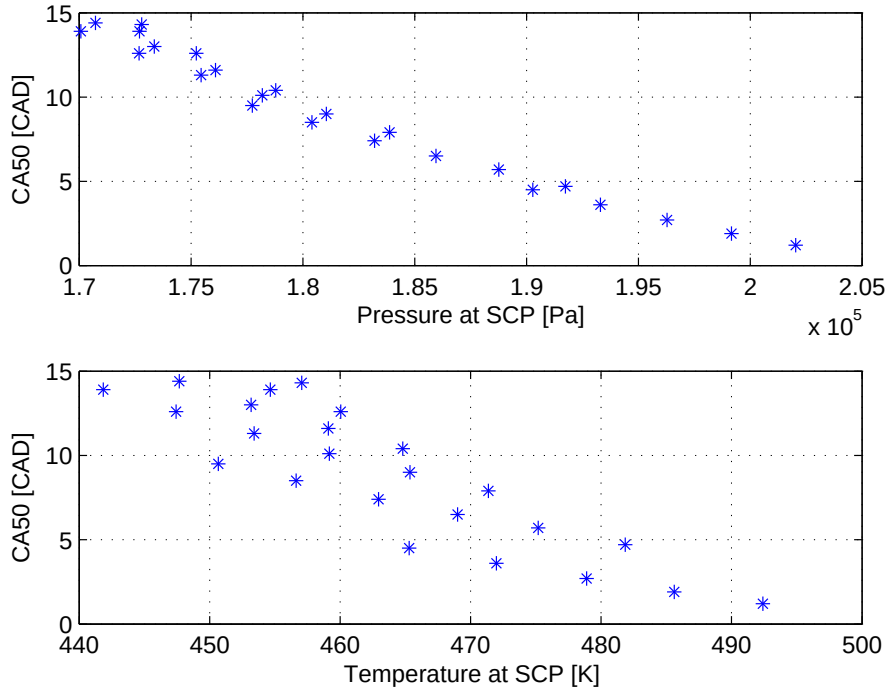

Figure 7.11: Dependency of CA_{50} on Pressure at SCP and Temperature at SCP

It's apparent that a tighter fit of the combustion model over the pressure may be more possible than over the temperature, which may lead to unexpected simulation results later on. As an example, by injecting more fuel, one may expect earlier combustion in the following cycles due to hotter gases, while the exhaust pressure may not be effected that much.
This is contrary to the experimental data shown earlier (Figure 7.7 and 7.6) where a change in combustion phasing with changed amount of fuel was observed. Thereby, a static mapping of exhaust pressure with combustion phasing might raise the accuracy at first glance, while the final model, on the other hand, would not predict the expected results.

It is therefore advisory to check the parameters for the simplified ignition model, and change the parameterization settings to gain the parameters that are expected. The values from equation 6.32 from [46] may serve here as a reference.

7.4 Linearization

This section explains the linearization approach of the readily parameterized control-oriented model that was introduced above.
In this work, linearization was accomplished in MATLAB with the *dlinmod* command, which perturbates each state and each input and tracks the state and output evolution.
Once the linearization is done, an LTI model of the following form is obtained:

$$\begin{aligned} x_{k+1} &= Ax_k + Bu_k \\ y_k &= Cx_k \end{aligned} \tag{7.32}$$

Note that the feedthrough matrix D is omitted here, which is attributed to the modeling approaches from above. Although there is almost a direct mapping from injected fuel to the power output (e.g. $IMEP$) which would yield such a matrix, this has been avoided by defining $IMEP$ as a state. This also makes sense from the point of view that it is affected by the exhaust pressure and some minor transients exist. Additionally, avoiding the feed-through matrix simplifies the control design.
Furthermore, despite of having a hybrid system, where the cylinders are in discrete-time and the exhaust in continuous-time, an overall discrete representation of the model has been obtained.

Additionally normalization of the matrices was done via transformation matrices, T_u, T_x and T_y such:

$$A_{norm} = T_x A T_x^{-1}, \quad B_{norm} = T_x B T_u^{-1}, \quad C_{norm} = T_y C T_x^{-1} \tag{7.33}$$

The values for the normalized matrices are:

$$A_{norm} = \begin{pmatrix} 0.2157 & -0.0583 & 0 & -0.1259 \\ -1.0601 & 0 & 0 & -0.2618 \\ -0.0389 & 0.0105 & 0.8765 & -0.0371 \\ -0.0242 & 0.0065 & -0.0911 & 0.8309 \end{pmatrix} \quad B_{norm} = \begin{pmatrix} 0 & 0 \\ 1.0518 & 0 \\ 0 & -0.0088 \\ 0 & -0.0430 \end{pmatrix}$$

$$C_{norm} = \begin{pmatrix} 0 & 1.0000 & 0 & 0 \\ 38.8106 & 0 & 0 & 0 \end{pmatrix} \qquad D_{norm} = D = \begin{pmatrix} 0 & 0 \\ 0 & 0 \end{pmatrix} \tag{7.34}$$

and the eigenvalues of the system-matrix A_{norm} are:

$$\lambda(A_{norm}) = \begin{pmatrix} -0.1617 \\ 0.3716 \\ 0.8005 \\ 0.9128 \end{pmatrix} \tag{7.35}$$

which are all inside the unit disc. Hence, the system is stable.
The input u_0, output y_0 and state vector z_0 are as follows:

$$u_0 = \begin{pmatrix} 16.9965 \\ 0.9010 \end{pmatrix} \quad x_0 = \begin{pmatrix} 369.52 \\ 4.76e+05 \\ 565.72 \\ 1.25e+05 \end{pmatrix}, \quad y_0 = \begin{pmatrix} 4.7584 \\ 9.5212 \end{pmatrix} \tag{7.36}$$

The following figure 7.12 shows a comparison of the non-linear model with the linearized one where the amount of fuel remained fixed, and the exhaust throttle angle was varied step-wise.

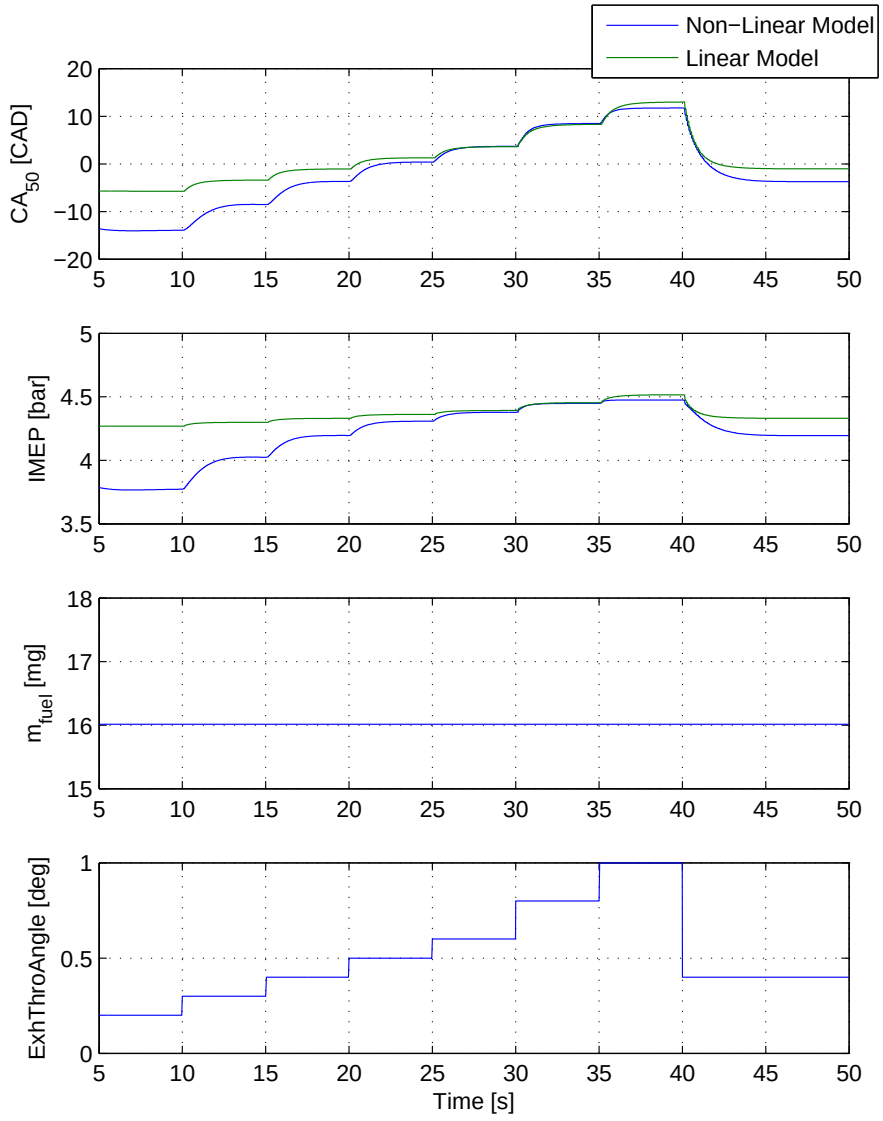

Figure 7.12: Comparison of the Linearized Model with the Non-Linear MVEM: CA_{50} Steps with fixed amount of Fuel injected @16mg

This figure shows that CA_{50} of the linearized model matches the non-linear model, where not only the transients were maintained, but also the magnitude. Also $IMEP$ keeps track, but only for lower values around $4.5bar$, while for other higher CA_{50} a clear difference can be seen, which shows stronger non-linearity characteristics when the point is moving further away from its linearisation point. To analyze this further, another trial was done with the same exhaust throttle actuation, but at different fuel injection amount of 18mg. This is shown in figure 7.13. Here, it can be seen that the behavior is the same as before, with strong deviation in combustion

phasing and engine load ($IMEP$), when the states are moving away from the linearization point. Note that combustion phasing has shifted slightly toward earlier phasings due to the higher amount of fuel injected.

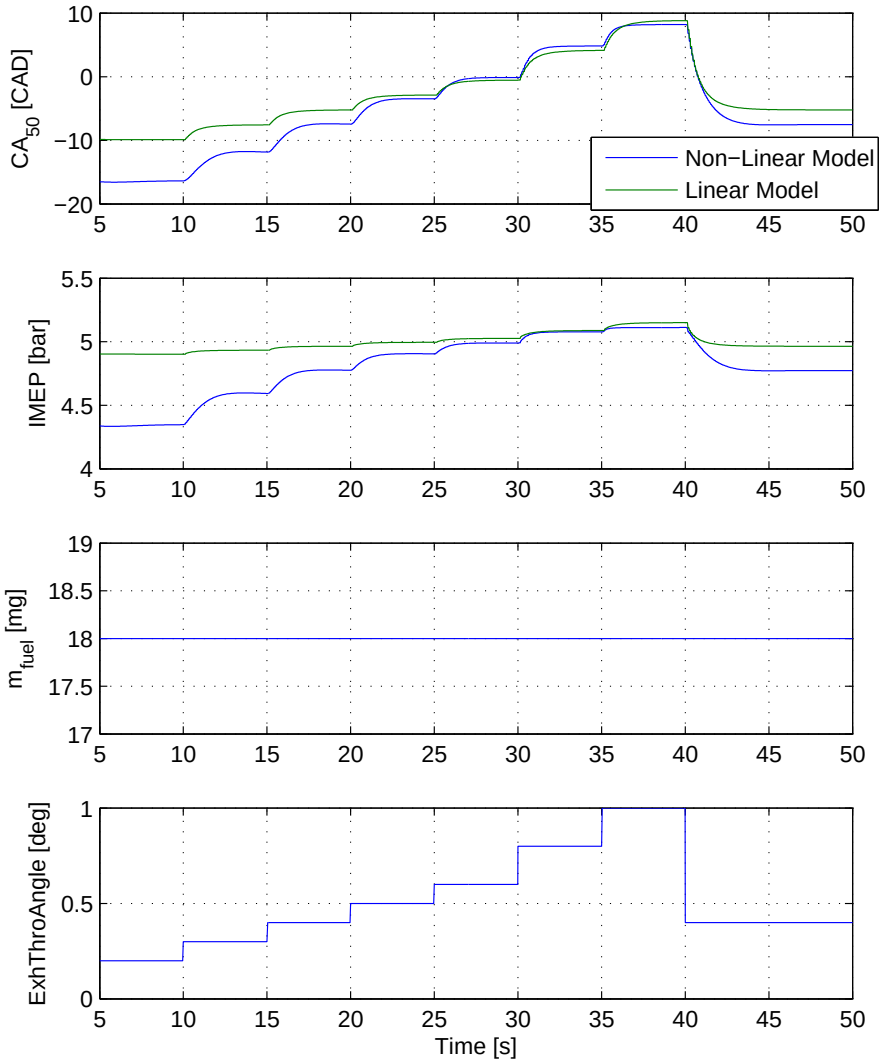

Figure 7.13: Comparison of the Linearized Model with the Non-Linear MVEM: CA_{50} Steps with fixed amount of Fuel injected @18mg

The next figure 7.14 shows step variations of the amount of fuel injected, while at the same time, the exhaust throttle was kept at an arbitrary and fixed value of around 1 degrees.
Here, it's apparent that the linearized model follows the non-linear model, not only with a similar magnitude, but especially with the same dynamics, though a clear offset can be seen, which remained almost constant for all simulated $IMEP$.
To clarify the non-linearity of the exhaust throttle actuation, the same analysis was done again with a different exhaust valve opening at 0.5 degrees, which is shown in the following figure

7.15.
Also displayed are, similar transients of the non-linear model with respect to the linear model, with some deviation due to non-linearity is also evident. This, however, is less than with exhaust throttle actuation, which may be considered as a stronger source of non-linearity than fuel injection, and its cross-coupling.

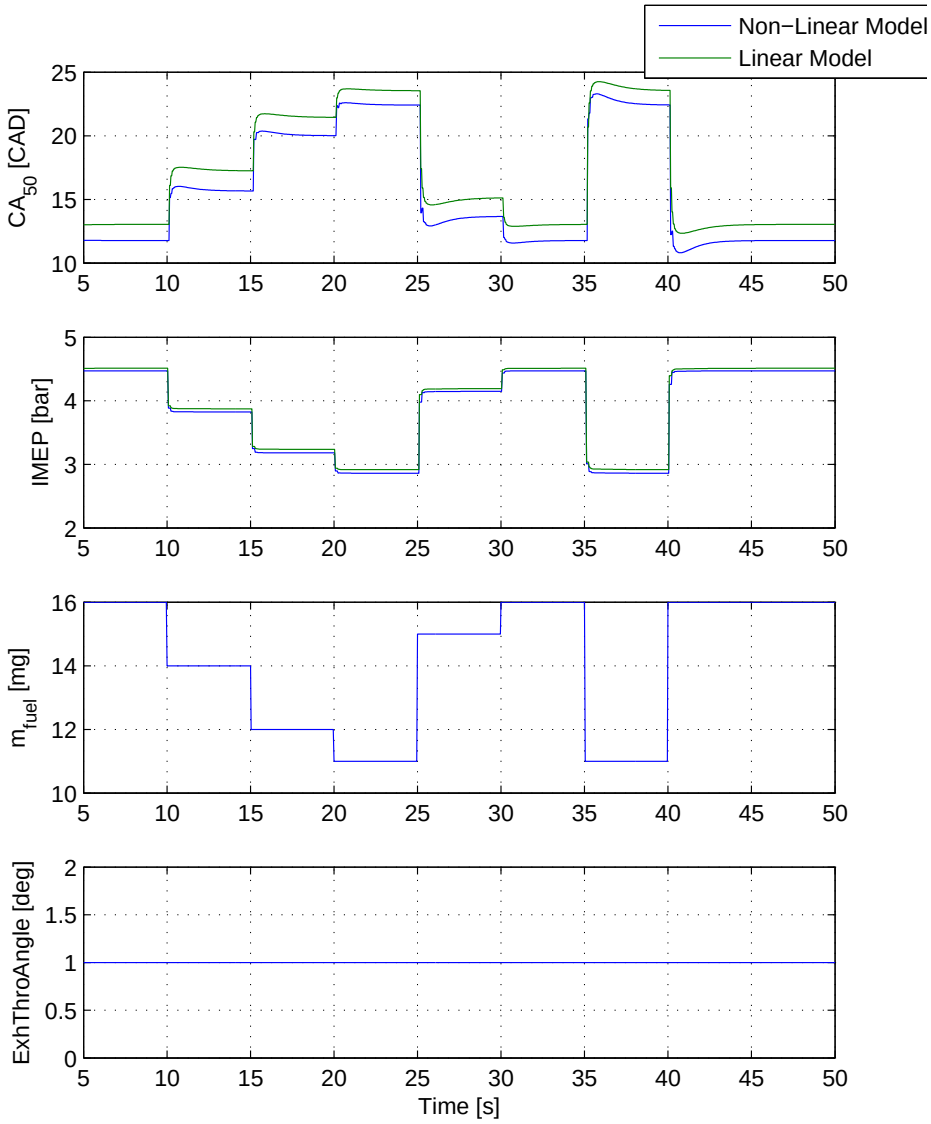

Figure 7.14: Comparison of the Linearized Model with the Non-Linear MVEM: $IMEP$ Steps with fixed exhaust valve angle@1deg

It becomes clear that control issues due to non-linearities may arise as soon as the operating point moves away from the linearization point.
Since the differences between the linearized and non-linear model only occur at unwanted operating points, one may nonetheless assume good dynamics of the closed-loop system.

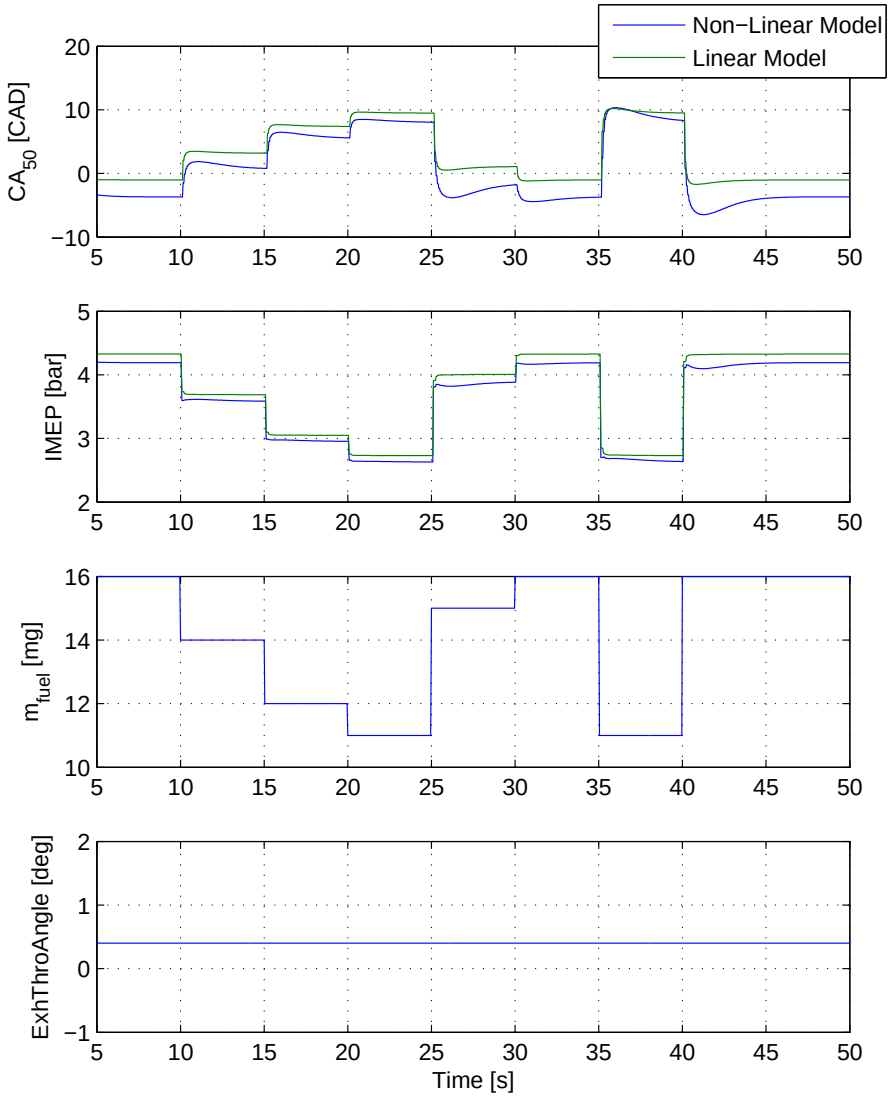

Figure 7.15: Comparison of the Linearized Model with the Non-Linear MVEM: $IMEP$ Steps with fixed exhaust valve angle@0.5deg

The poles and zeros of the linearized model are shown in the following figure 7.16, and for a better understanding, the poles and zeros of the converted linearized model in continuous time is shown in figure 7.17.

One can see that linearized model in itself is stable, and some non-minimum phase zeros exist, which only apply to the exhaust throttle actuation. These non-minimum zeros occur at the very beginning of the step input and at very small magnitudes, so that so that they do not dominate the overall transients.

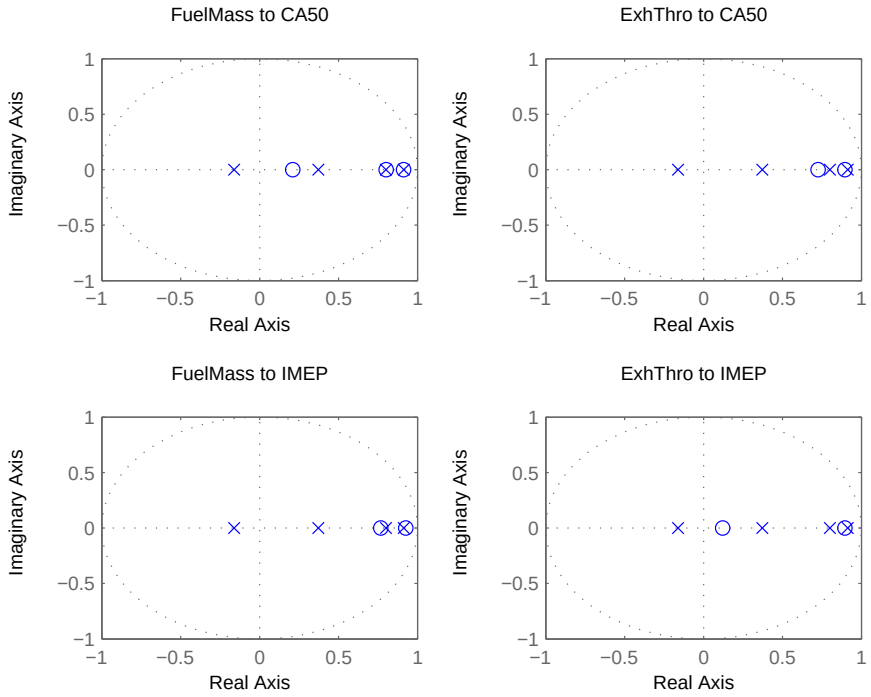

Figure 7.16: Maps of Poles (x) and Zeroes (o) of the discrete-time open system

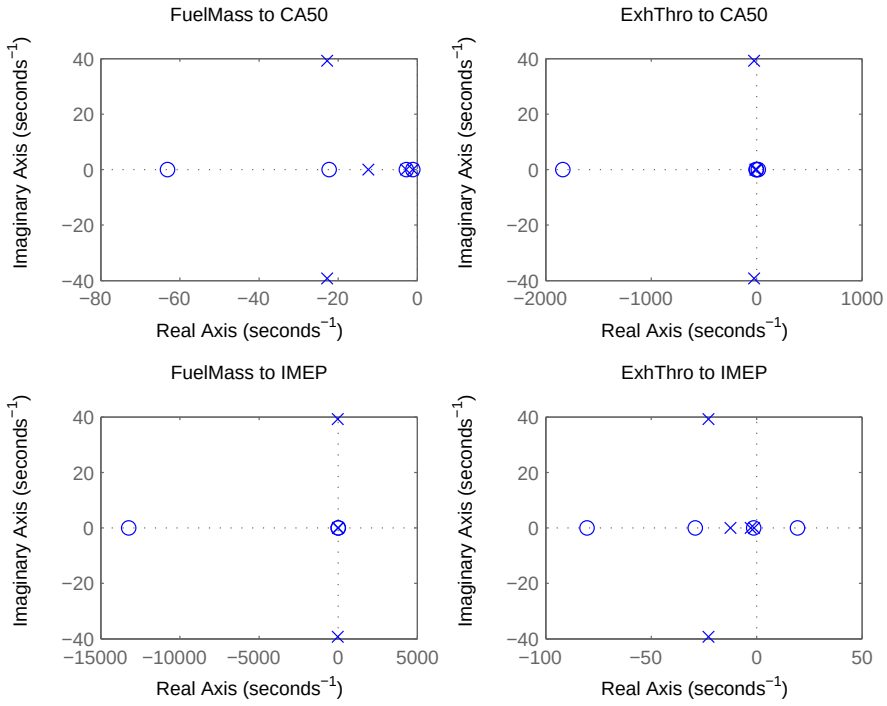

Figure 7.17: Maps of Poles (x) and Zeroes (o) of the equivalent continuous-time open system

7.5 Comparison to the reference model

In this section, the previously introduced mean-value model is compared to the more detailed 0-D engine model, as introduced above. This comparison is useful to further investigate the transients of both engine models, and deviation due to non-linearities to each other. Ideally, this would be done on a real-engine.
In this analysis, frequency plots of the reference model, which is here the 0-D model, were created by exciting the engine model with a sinusoidal input with changing frequency (chirp signal) for both inputs (amount of fuel and exhaust throttle angle) while measuring both outputs.
Thereby, the mean amount of fuel has been varied sinusoidally for each analysis, while the other actuator remained fixed at different levels, with the same being done for the mean exhaust throttle angle. This approach also allows for capturing the cross coupling between amount of fuel and combustion phasing (CA_{50}), as well as the influence of the exhaust throttle angle on the engine $IMEP$.

The analysis has been carried out at three different fuel levels, (low amount of fuel, medium and much fuel), at three different exhaust throttle angles (almost closed, medium open, and wider open), such that the exhaust value remain in an acceptable range, namely as $2\,CAD < CA_{50} < 14\,CAD$.
After that, the amplitude of the output for each signal was determined by a discrete Fast Fourier Transformation (FFT), which reads:

$$X_k = \Sigma_{j=1}^{N} x_j \omega_N^{(j-1)(k-1)} \tag{7.37}$$

where x_j is a signal vector, and the output signal was set in relation to its input signals, such:

$$G(i\omega)_{n,k} = \frac{|Y(i\omega)|}{|U(i\omega)|} \tag{7.38}$$

where the magnitude of the input always remained at 10%, which was the default setting for the input sinus excitation. Furthermore, the input and output have been normalized to their mean values.
The following plot 7.18 shows the Bode-plots from this analysis, where on the left column, the fuel input is shown, on the right column the exhaust throttle angle input, the upper row the combustion phasing output (CA_{50}), and the lower row the $IMEP$ output. Additionally, the linearized mean-value model is shown in dashed lines in each plot.
Also, it should be noted here that the magnitude is given in dezibel, defined as:

$$G(j\omega)_{[dB]} = 20 \cdot log(G(j\omega)) \tag{7.39}$$

In all plots, it can be seen that the bode-plots from the linearized mean-value engine model lie well within the ranges, measured at the reference model. It can be found outside for the upper right plots, which denotes $IMEP$-throttle coupling, but since the values are very low, it may be assumed that this is not of further concern. This may be more serious for the upper left plot, where a stronger deviation for higher frequencies can be seen. This may point to the omitted port-fuel modeling of the MVEM, and that a rather first other dynamics behavior is to be expected. This may lead to unwanted control behavior at extremely high gains, and should be handled with robust control design, or by explicitly including a first-order delay into the

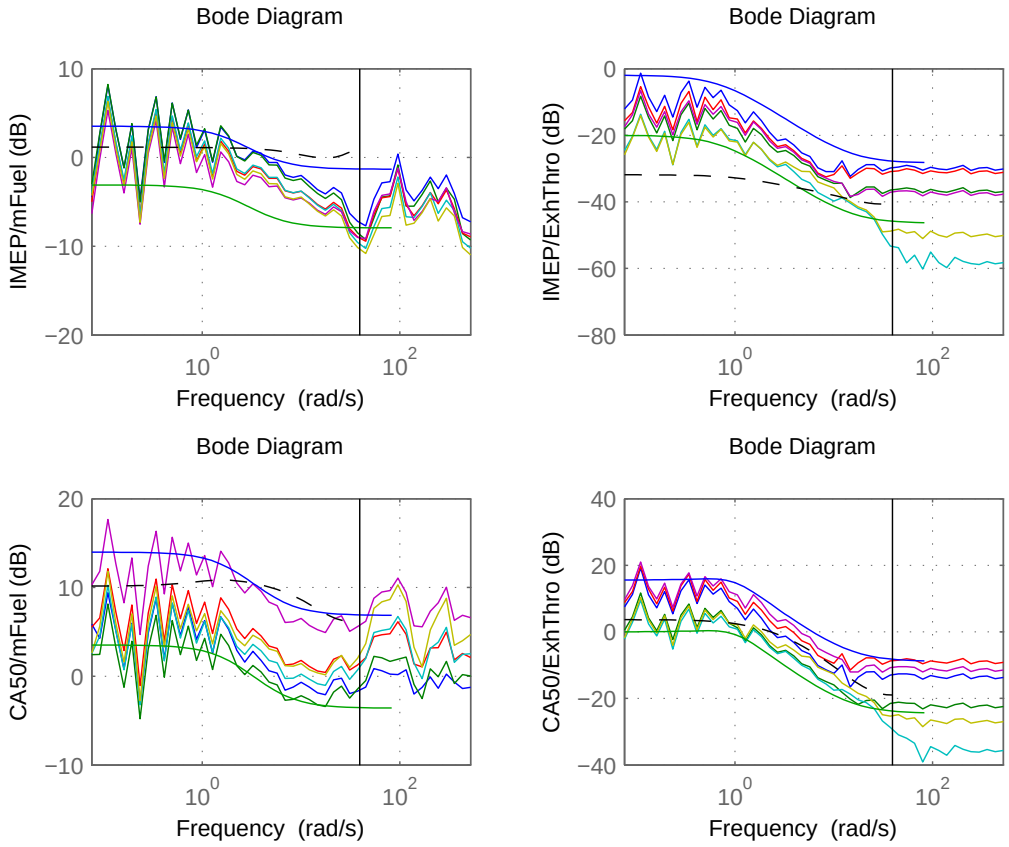

Figure 7.18: Bode-Plots of the linearized model and Frequency Responses of the Reference Model at Different Throttle Angles and Amount of Fuel Injeced

MVEM. As for the CA_{50}-throttle coupling, a clear first order dynamics can be seen which is captured well by the mean value model.

Chapter 8

Control design

Closed-loop control is essential for an HCCI engine to raise its robustness, especially with regard to changing atmospheric conditions, engine conditions, such as aging, or wall deposits, and different quality of fuel to name some of possible external disturbances. Additionally, internal disturbances due to cross-coupling between inputs and outputs which make control an HCCI engine further challenging. This would require either cascaded SISO loops, or more conveniently, a MIMO control concept. These control burdens are additionally complicated by the high sensitivity of HCCI combustion which depends on the in-cylinder conditions and is limited to a very narrow range so that tight control is needed. On top of all these points, classical control problems such as non-linearity issues need additionally to be considered. It is thereby desired to obtain a control concept that not only addresses these challenges sufficiently, but also facilitates desired engine performance in spite of stark engine transients in load and speed.
Several control concepts have been suggested for HCCI engines, which comprise mainly state-control, output control, robust control, and linear model-predictive control (MPC). These control approaches have been reported for common HCCI concepts, which are negative-valve overlap (NVO) and exhaust re-breathing. Contrary to that, for BDSC HCCI, hardly any closed-loop control concept has been reported.
Unlike common re-breathing strategies, like in the case of a BDSC HCCI engine, the main actuator for CA_{50} has been found in the exhaust throttle by regulating the exhaust pressure and thereby the EGR content. Here, actuation speed restrictions are given not only by the throttle actuation, but especially due to the slow and asymmetric change of exhaust pressure. Increasing the pressure by filling is thereby supposed to be slower than emptying the exhaust manifold by releasing exhaust gas into the atmosphere.

The purpose of this chapter is to find a control-concept, suitable for BDSC HCCI, where actuation concepts are first addressed, after which closed-loop controllers are presented.

8.1 Selection of Actuators

While NVO HCCI systems feature direct injection timing during the re-compression phase as a powerful combustion phasing control method, this is not possible in re-breathing and BDSC HCCI. During the intermediate re-compression phase of an NVO engine, chemical pre-reactions take place due to the higher in-cylinder temperatures, which continue during the compression phase until ignition sets in. By injecting fuel earlier during re-compression, combustion phasing

can be advanced and thereby actively controlled not only cylinder individual, but also on a cyclic basis. This concept can be further elaborated by using pre-injection during re-compression for combustion phasing and main injection at a later point within the engine cycle.
Since this actuation is not viable with BDSC, the employed port fuel injector can only regulate $IMEP$ and not CA_{50} simultaneously. However, due to the aforementioned cross-coupling, in which with varying amount of fuel, the temperatures level vary and with it combustion phasing, control of combustion phasing during $IMEP$ changes becomes mandatory.
In case of BDSC, only two main control approaches for combustion phasing have been suggested:

- Using the exhaust throttle to vary exhaust pressure, and thereby the amount of EGR
- Using secondary air injection for cooling the in-cylinder mixture during compression and thereby retarding combustion phasing

As mentioned in the introduction, secondary air is commonly used in SI engines during cold-start when more fuel is injected to stabilize combustion while the catalyst needs to be heated up. The injected air in the exhaust port then oxidizes unburned fuel fractions and reduces emissions. However, this actuation is switched off when the engine has reached its operating temperature.
The exhaust throttle is not common in SI engines, but nowadays it is found in Low-Pressure EGR (LPEGR) Diesel engines, where it raises the back-pressure to push more cold EGR back into the intake manifold. With this functionality in mind, it may become clear that a purpose of the exhaust throttle in BDSC HCCI is also to regulate the EGR content in the cylinder, similar to LPEGR, but with hot EGR gas and into the exhaust ports instead. However, with excessively high exhaust pressures, while unlike in boosted combustion engines intake pressures remain around atmospheric, pumping losses increase and decrease the power output and deteriorate the efficiency of the engine.
Contrary to this concept, common cam-phasing systems (Variable-Valve-Timings, VVT) are used for controlling EGR in NVO HCCI engines. This technology has been well established in common SI engines and together with the direct injection technique has become a de-facto standard with recent downsizing developments of SI combustion engines.

As a summary for control of BDSC HCCI, $IMEP$ is controlled by amount of fuel injected, but it also can be affected by the exhaust pressure. Exhaust pressure, in turn, is meant to regulate EGR inside the cylinders and is a powerful control actuation for combustion phasing. It, however, cannot control each cylinder individually, and due to the slow filling characteristics of the exhaust manifold, actuation may be slow. This aspect may be an issue if larger but faster CA_{50} transients are required which must be compensated for by suitable closed-loop control.

Secondary air does not pose much impact on $IMEP$, and it can regulate combustion phasing for each cylinder individually. Additionally, the air injection actuation is very fast on a cyclic basis so that modeling for control would only require static mapping, and its control authority range can be judged to be around 10 crank-angle degrees.
However, since this actuator requires a constantly running pump for building up the air injection pressure, this impairs the overall energy balance of the engine, and therefore decreases the efficiency of the engine.
One drawback of this control-concept is also that it hardly acts as a mid-range controller and

this is only possible if injection of secondary air is centered between no injection and maximum amount of injected air. Thus constant air injection would be necessary.

8.2 Output Control

A simple control concept, based on a MIMO output PI controller, has been tested with the engine model in AVL BOOST.
The control problem given here can be formulated as a MIMO problem. The exhaust pressure is utilized to control combustion phasing, which in return affects the $IMEP$. Secondary air has been additionally employed to allow for cylinder-individual control. Fuel injection has been kept fixed and $IMEP$ control skipped in this control trial.
The requirements here in this approach are a) that there is no linearized model needed, and b) possible cross-couplings between the cylinders should be avoided. The idea behind this approach is to use the static system output vector as:

$$y_0 = \begin{pmatrix} CA_{50}(1) \\ CA_{50}(2) \end{pmatrix} \tag{8.1}$$

where $CA_{50}(1)$ and $CA_{50}(2)$ are for cylinder $\#1$ and cylinder $\#4$ respectively.
The input vector was chosen as:

$$u_0 = \begin{pmatrix} t_{SecAir}(1) \\ t_{SecAir}(2) \\ \theta_{ExhThro} \end{pmatrix} \tag{8.2}$$

Where $t_{SecAir}(1)$ and $t_{SecAir}(2)$ are the injection timings for the secondary air pulses for each individual cylinder, and $\theta_{ExhThro}$ the exhaust throttle angle.
Although not strong coupling between the inputs and outputs exist in this case, a decoupling approach was nonetheless pursued here of which an introduction is given in [82].
Decoupling is achieved by using the inverse of the output vector 8.1 to obtain the following matrix:

$$S = y_0^{-1} \tag{8.3}$$

By applying a diagonal and positive definite weighting matrix R, similar to LQ design to emphasize some actuators:

$$R = \begin{pmatrix} r_{11} & 0 \\ 0 & r_{22} \end{pmatrix} \tag{8.4}$$

The gains for the PI controllers are found with

$$K_p = \alpha RS \tag{8.5}$$

and

$$K_I = \beta RS \tag{8.6}$$

The constants α and β have been added for fine-tuning on the system.
The results with the BOOST model are shown in figure 8.1 and 8.2.

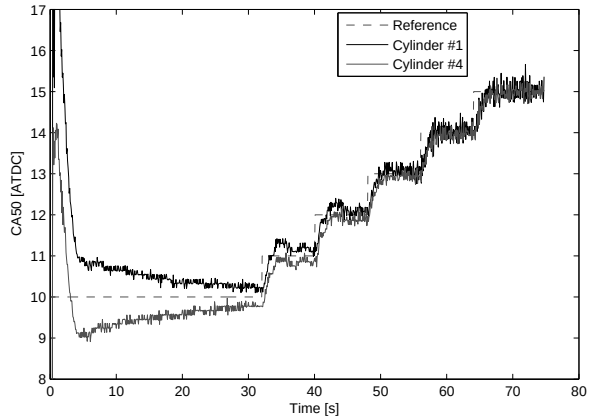

Figure 8.1: Tracking of CA_{50} with a MIMO PI Controller, tested on the BOOST model

It can be seen that the controller tracks the required outputs reliably, and combustion phasing differences are controlled out. The controller keeps combustion phasings together for both cylinders, even during reference changes. In figure 8.2 it can be seen that the secondary air control commands converge to a steady state value, which explain the diminishing differences between the two cylinders for CA_{50}, and that tracking is achieved by the exhaust throttle simultaneously. However, the plots for the exhaust throttle also show that the throttle actuation does not compensate for the slower exhaust transients by first opening the throttle wide before closing it again to ensure a faster pressure drop. Instead, it converges to a steady opening angle with each reference change, which causes the slow transients. In fact, by inspecting the figure 8.1, it becomes clear that the controller needs several seconds until it reaches a step-change of only one degree, which may be judged as fairly slow. In cases where the throttle first opens wider (in the first two step changes), this rather causes an overshoot in CA_{50}, which is still small here, but might become critical if the controller is tuned more aggressively.

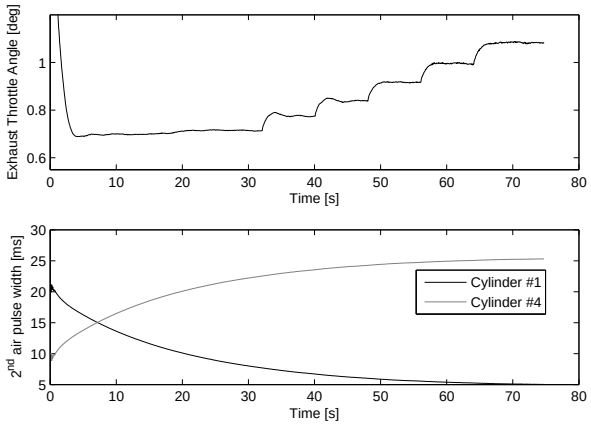

Figure 8.2: Control Commands of the MIMO PI Controller, tested on the BOOST model

This approach is simple and may achieve decoupling of coupled inputs and outputs in steady-state, a proper analysis tool is not given and stability or robustness cannot be judged by this method. Furthermore, tuning might become more cumbersome, if more actuation or

controlled variables are included in the design. However, the biggest drawback is that the dynamics of the system are not considered in the control design since only steady-state values are considered. In the design presented here, only unsatisfactory results were achieved and optimization would require lots of trial and error tests so that model-based design methods are to be preferred in control design.

8.3 Model-Based Control

Although the term model-based control may be misleading, it has commonly been referred in engine control to as a control scheme that incorporates a model in the control structure (e.g. [98]). This can be either as a model-predictive control, or as an observer that is used for state-feedback control.
In the following chapters, advanced control concepts will be analyzed for BDSC HCCI. First, a state controller with a Kalman-Filter and a linear feed-forward was implemented in Simulink and coupled with the 2-cylinder BOOST model for testing. The gains for the feedback control have been found by using Sliding-Mode Control (SMC) theory. Further control concepts that are introduced are sliding mode control with integral action, and robust controllers based on H_∞ optimization theory. Since computation times with the BOOST model were prohibitive for control analysis was done with the 0-D model introduced above.

8.3.1 Initial Considerations and Closed-Loop Control with BOOST

In this section, a trial of a model-based control on the BOOST model will be investigated. The controller designed here is a Sliding-Mode Control (SMC) with a Kalman-Filter for observing the states online. As explained in the introduction, since the controller is in discrete-time, a non-linear switching term is not necessary for reaching (quasi) sliding mode.
This controller has been tuned on the Mean-Value Engine Model (MVEM) that has been parametrized with identified data from the BOOST model. Although the exhausted enthalpy could not be determined on the BOOST model, it has been estimated from calculating the total amount of enthalpy within the cylinder before and after exhaust.
The plots in figure 8.3 show the transient results of the simplified model.

These plots show a similar behavior of the MVEM with the experiments. It can be seen that CA_{50} is very sensitive to fuel changes and that the reaction time is fast, where it settles within a few cycles to new values.

The controller was tuned by linearizing the MVEM and bringing the obtained state-space representation into regular form, where LQ optimization for finding the gains of the SMC. The controller has been hereby tuned aggressively so that it tracks the references in a very short time. In order to track the desired values for CA_{50} and $IMEP$, a feed-forward controller has been designed.
It should be noted at this point that difficulties arose when coupling the Simulink control model with the BOOST model in terms of time synchronization, which did not permit the use of an integrator or other dynamic controllers. Furthermore, since abnormal combustion was found during stark transients, in which CA_{90} appeared earlier than CA_{50} in the results and $IMEP$ drop for these cycles were found, combustion was kept fixed, which alleviated this problem. Since HCCI combustion is typically fast and does not vary as much as ordinary SI combustion,

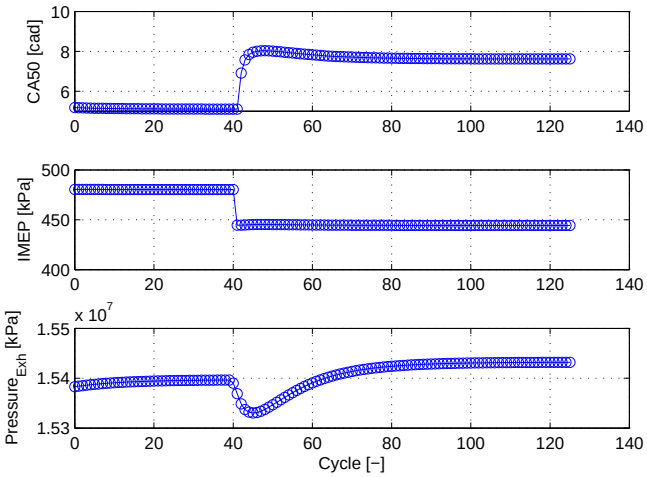

Figure 8.3: Step Input of the fuel of the simplified model

this was considered as a minor issue.
As for the coupling of the static controller with the BOOST model, it was ensured that cyclic coupling exist and the time-step size was set to neutral value of one in Simulink.
The following figure 8.4 shows the results for tracking CA_{50}, where the reference values are displayed in a dashed line.

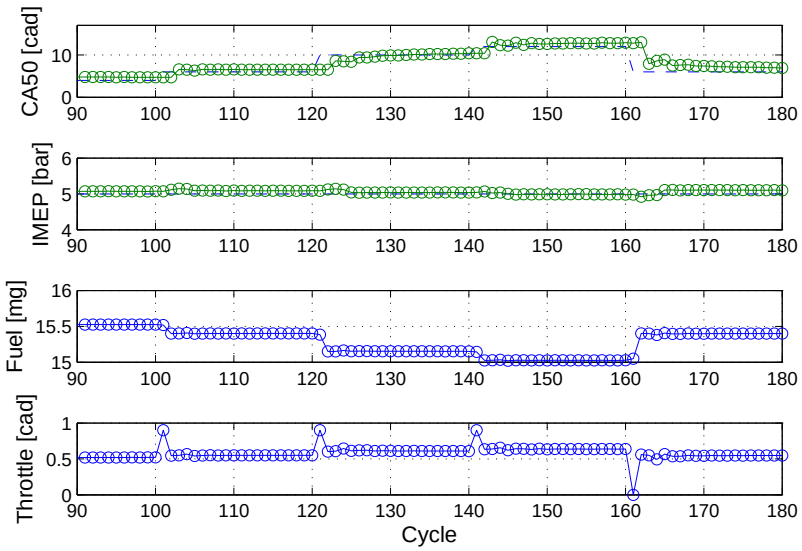

Figure 8.4: Tracking of CA_{50} with an SMC controller, tested on the BOOST plant

It can be clearly seen that the controller tracks the desired combustion phasing with an ideal response time of practically only one engine cycle. This may be attributed to the feed-forward controller and the fact that the fixed injected amount of fuel was around the linearisation point. On the other hand, the static feed-forward controller alone would not be able to track the reference value with such high dynamics. It is therefore clear that the feed-back controller

alone facilitates these transients. This especially becomes clear if one looks at the controlled actuation, where the controller opens or closes the exhaust valve quickly but then brings it back to a steady state point. This comes together with a slight change in amount of fuel injected, which has an impact on $IMEP$ and CA_{50}. Since, for example, with a commanded delay of CA_{50} the exhaust pressure is to be released, the pumping losses decrease and for a fixed $IMEP$, the amount of fuel can be decreased, which in turn delays the CA_{50}. In fact, a slight shift of $IMEP$ can be seen with each CA_{50} changes, which can be attributed to non-linearities, and an integrator becomes necessary to cancel out these discrepancies.
Although the dynamics seen here are very favorable for control of CA_{50}, step-wise control of $IMEP$ may become not as desired, as shown in figure 8.5.

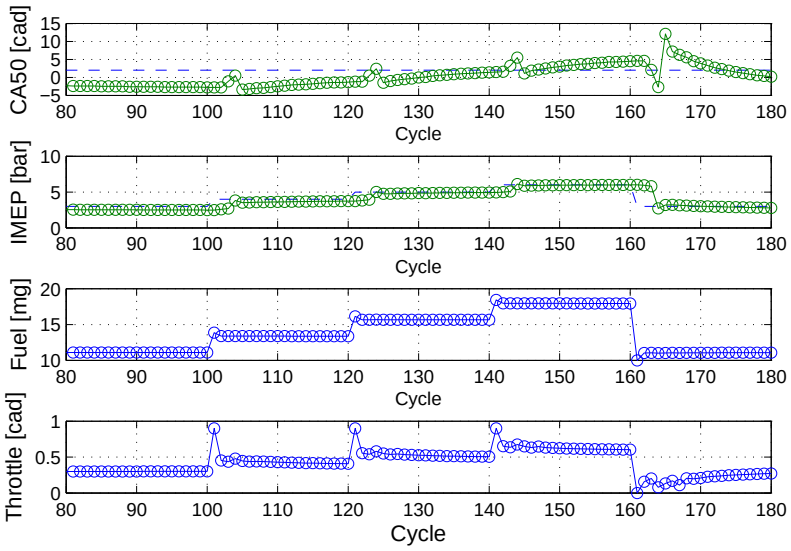

Figure 8.5: Tracking of $IMEP$ with an SMC controller, tested on the BOOST plant

Here it can be seen that the linear controller is able to track the desired $IMEP$ commands within one cycle as well, while rejecting the disturbances in CA_{50} that come with it. It however is not able to keep combustion phasing at a fixed value. Instead, it can be seen that it drifts to higher values the more fuel is injected. This clearly points at non-linearity issues which must be addressed in the control design, by including more robustness to ensure high gains for the sensitivity function at low frequencies.

Further control considerations are introduced in the following sections.

8.3.2 Robust Control

Robust Control, as introduced the introductory chapter, is a modern control scheme that gives the advantage of analyzing the control scheme before actual implementation. This allows for analyzing not only robust stability but also robust performance.
For the current control problem of a port-injection HCCI engine, unmodeled dynamics, model uncertainties, as well as cross-couplings between inputs and outputs may cause difficulties in control design.
To address the performance criterion, and recalling that the standard H_∞ includes an observer structure, the sensitivity function can be cast into the negative output-feedback form, which reads:

$$S(s) = \frac{1}{1 + P(s)K_\infty(s)} \tag{8.7}$$

where $P(s)$ is the plant, and $K_\infty(s)$ the dynamic feedback controller. It is easy to show that this sensitivity denotes the dynamics of the error between reference and system output so that this form can be used for analysis of disturbance rejection.
The upper limit of this function can be shaped by including an arbitrary transfer function such that the desired transients are achieved. Together, with additional transfer functions for the control- and plant outputs, the design procedure for the robust controller becomes straightforward. This approach is called the mixed sensitivity design and will be presented for BDSC HCCI next.

To begin with, modeling of the plant must be completed for robust H_∞ design by including a modeled uncertainty in the control design. For sake of simplicity, the multiplicative output uncertainty has been chosen here, which reads:

$$\tilde{P} = (I + \Delta_M(s)W_y(s))P_0(s) \tag{8.8}$$

with the unstructured uncertainty block Δ_M fulfilling the following inequality:

$$\| \Delta_M(s) \|_\infty \leq 1 \tag{8.9}$$

The dynamic uncertainty $W_y(s)$ is found by collecting data from the reference system (here: the 0-D engine model) for estimation of transfer functions $P(j\omega)$ and defining the $W_y(s)$ as the upper limit of all modeling errors for $s = j\omega$ as:

$$\left| \frac{P(j\omega) - P_0(j\omega)}{P_0(j\omega)} \right| \leq W_y(j\omega) \tag{8.10}$$

Note that on the left-hand side of equation 8.10 that the error has been normalized and is divided by the nominal plant $P_0(j\omega)$, which is in accordance to the definition 8.8.

Further to the uncertainty description $W_y(j\omega)$, a transfer function for tuning the error dynamics $e = r - y$ needs to be found. For this purpose, the shape function for the sensitivity function 8.7 can be chosen as a diagonal matrix as:

$$W_e = \begin{pmatrix} we_{11} & 0 & 0 & \cdots & 0 \\ 0 & we_{22} & 0 & \cdots & 0 \\ 0 & 0 & we_{33} & \cdots & 0 \\ & & \vdots & & \\ 0 & 0 & 0 & \cdots & w_{nn} \end{pmatrix} \tag{8.11}$$

with we_{ij} as a proper transfer function:

$$we_{ij} = \frac{s/M + \omega_B}{s + \omega_B A} \tag{8.12}$$

with M, ω_B and A as tuning parameters.
ω_B is here the corner frequency, where the $ln|we|$ crosses the 0 mark, the parameter A chosen to be small ($A << 1$) for tracking requirements, and the sensitivity peak M to include robustness. Typically M is around 2 or smaller.

A shaping function for tuning the control actuation, similar to shaping function the above may be used to obtain W_u and included in the control design. Alternatively, static constants instead of dynamic transfer functions can be included in the control design as well.

In order to obtain the W_t, which is the shaping function for the complementary sensitivity function:

$$T = \frac{P(s)K(s)}{1 + P(s)K(s)} \tag{8.13}$$

the following shaping function can be used:

$$wt_{ij} = \frac{s + \omega_B/M}{As + \omega_B} \tag{8.14}$$

where the tuning factors are the same as above.
The block diagram for the mixed sensitivity design is shown in the following figure:

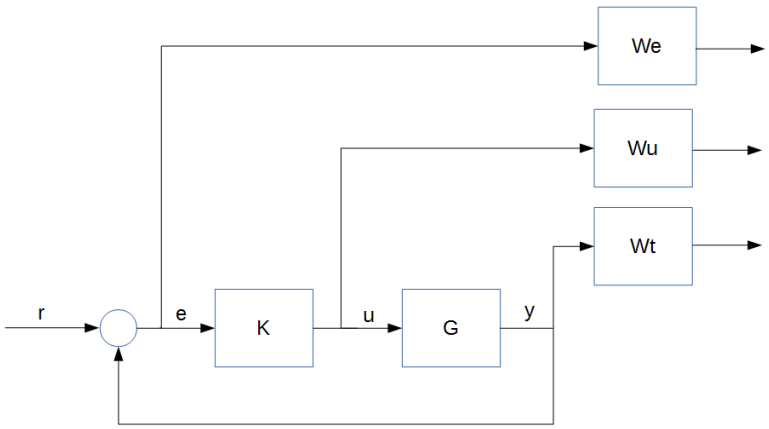

Figure 8.6: Mixed Sensitivity design

The estimation of the error from the linearized engine model, to its reference (here: the 0-D model), which not only includes unmodeled dynamics and inaccuracies but also the non-linearities, was accomplished by using the identification results, as presented in the previous chapter and shown in figure 7.18. For computing the relative output error, equation 8.10 has been utilized and an upper function was found by trial and error and fitting of a transfer function by hand.

The magnitude of the fitted bode function is shown in the following figure 8.7, with the upper bound in blue and a lower bound in green:

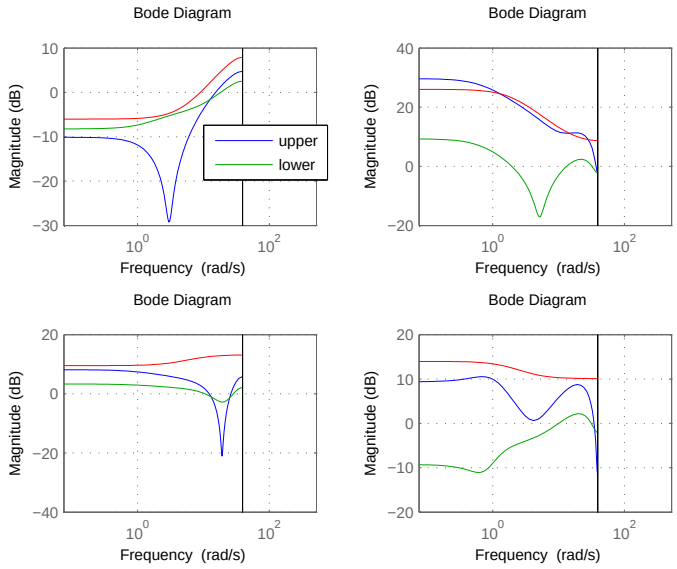

Figure 8.7: Error Estimation of Linearized Model in comparison to Reference Model

In a previous chapter, it was stated that the exhaust valve actuation brings rather slow dynamics in combustion phasing which should be compensated for by a feedback-controller. On the other hand, parasitic cross-coupling between fuel and combustion phasing, and throttle and power output are present.
The following figure 8.8 shows the step-input of the linearized plant, with the MATLAB command *step()*, where the $IMEP$ is shown in the upper row, CA_{50} in the lower row, the fuel actuation on the left column, and the exhaust throttle on the right column. Hence, the fuel-$IMEP$ relation is shown in the upper left corner with a fast response, and the throttle-CA_{50} in the lower right where a rather slow response can be seen. Note that the model and the results are normalized. On the other two plots, the cross-couplings show that the influence of throttle on $IMEP$ is rather low, while it is much stronger for fuel and CA_{50} which ought to be reduced by a suitable feedback control law, as well as the throttle actuation accelerated.

With the aim to fulfill the requirements of faster control response and cross-coupling minimization, a robust H_∞ has been synthesized here.
The controller has been designed via mixed sensitivity design as introduced above, where the weighting functions W_e, for both tracking errors (CA_{50} and $IMEP$) were formed with the weighting constants to meet the desired control performance with $\omega = 2\ rad/s$, $M = 2$,

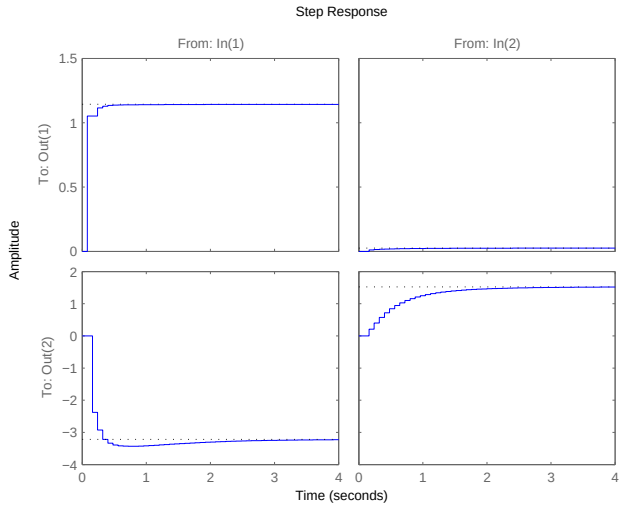

Figure 8.8: Step input into the linear MIMO model, with CA50 in the upper row, IMEP in the second row, and the fuel input in the first column and throttle in the second column

$A = 0.001$ for CA_{50}, and $\omega = 20\,rad/s$, $M = 2$, $A = 0.001$ for $IMEP$. A weighting function for the input signals have been omitted.
Although both transfer functions are very similar to each other, the following figure 8.9 shows the bode plots of each separately.

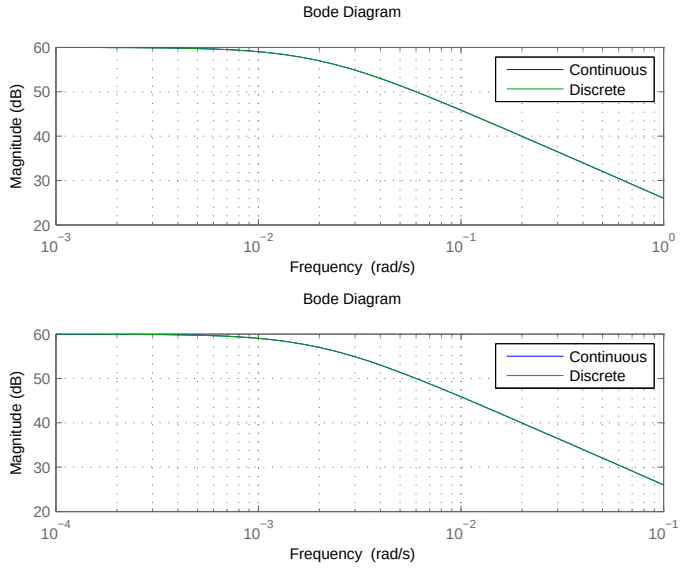

Figure 8.9: Weighting Functions for Tracking Requirements

An estimate of the the resulting closed-loop control performance on the linear plant with the MATLAB command *step()* is shown in figure 8.10, with $IMEP$ again in the upper row, and CA_{50} at the lower row. This plot shows as before collections of step-inputs into the closed-loop controlled system. Hence, the tracking on the upper left and lower right plots should reach the normalized value of one, while it should be kept around zero at the other two plots if cross-

coupling is reduced. The fuel is on the left hand side, and the exhaust throttle on the right hand side. Thus, the influence of fuel on $IMEP$ is in the upper left plot, and on CA_{50} on the lower left plot. Here, it is shown that the $IMEP$ step changes in a slower pace but still within an acceptable timescale. At the same time, the cross-coupling to CA_{50} has been extremely reduced. Another merit of the closed-loop can is apparent by inspecting the fast transients of CA_{50}, which show an initial fast approach to the reference value on a timescale within a only few engine cycles after which it slowly converges to the reference value. Since the fast transients exceed the first-order critical value of 63% after two time-steps, but slowly settles to its reference point, critical overshoots are avoided. Also, here, the cross-coupling is very low and $IMEP$ seems hardly affected.

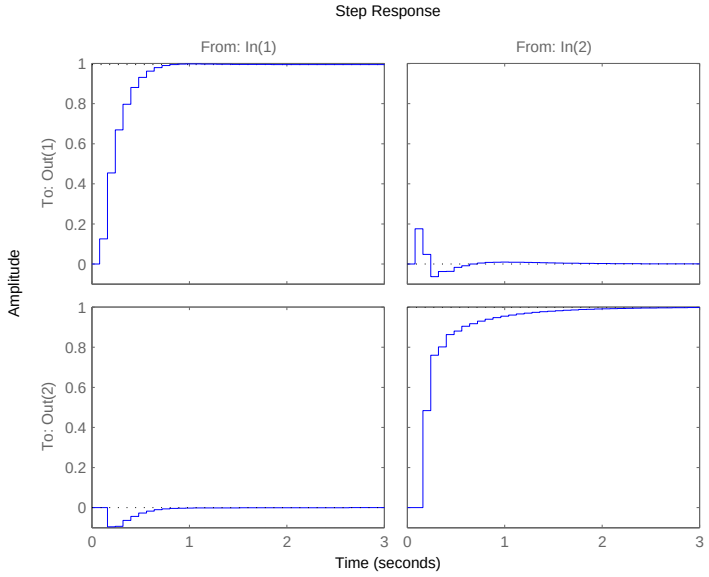

Figure 8.10: Step Input of the Closed-Loop H_∞ Controlled Linearized System

The resulting H_∞ controller that has been obtained here shows first favorable control dynamics, it is with 15 states somewhat too big and reducing the controller via Hankel singular values is considered here.
The following figure 8.11 shows the Hankel singular values plotted over the number of states.

This plot shows that one might expect similar control performance if the number of states are reduced. Here, reduction of half of the number of states seems feasible.

The following figure compares in Bode plots for the reduced controller on the augmented plant with the original one, and it is displayed that there is little difference between both controllers which gives confidence for the reduced H_∞ controller.

A few tracking reference step inputs have been tested on the linear model, and the results can be seen in the figure 8.13.

The $IMEP$ can be tracked within only a few time-steps where the fuel steps are rather smooth and less step-wise, while the exhaust throttle acts extremely fast and some chattering can be observed where some smaller oscillations at $IMEP$ step-changes are visible.
However, the step-changes in $IMEP$ do no interrupt CA_{50}, so that no severe cross-coupled disturbance can be seen. Hence, cross coupling is strongly minimized with this controller.

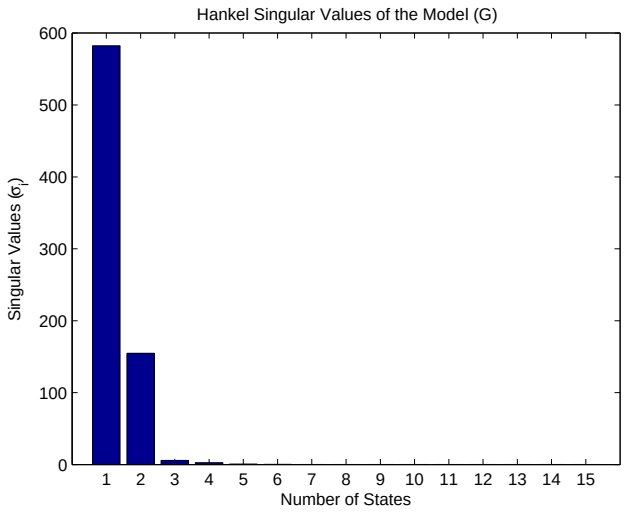

Figure 8.11: Hankel Values of the H_∞ controller

As another step, this controller has been applied to the non-linear model for test purposes as well, and the same reference tracking steps where done as in the linearized model.
This is shown in figure 8.14 where similar dynamics as with the linear model are seen, although some control performance deteriorates remarkably with late combustion phasing. Apart from these late phasings, it seems that the controller handles non-linearities well.

The controller has eventually been tested on the 0-D model as a reference, with CA_{50} tracking, while keeping $IMEP$ at a fixed value of 4 bar. This is shown in figure 8.15.

In this figure, it is apparent that the controller acts similar as with the non-linear mean-value engine model, and similar fast transients can be observed. Thereby, the exhaust throttle actuation is extremely fast, and some chattering can be seen as well. However, unlike in the non-linear model, some low-frequency oscillations are visible for the fuel injection actuation, especially during fast CA_{50} transients. As a second test, the controller has been tested with the same setting, but the regulated $IMEP$ has been kept at a value of 5 bar, and the results are shown in figure 8.15.

The controller behaves similar as with $IMEP = 4\,bar$ and little difference can be seen, which implies good robustness of the controller. However, as with the previous case, the exhaust throttle actuation is extremely fast, and high-frequency chattering is evident, while at the same time, low-frequency oscillations exist for the injector.
In a last trial, the combustion phasing has been kept fixed at a critical late value of 12deg ATDC, and $IMEP$ was tracked which is shown in figure 8.17. It, however may be concluded that this parameterization of the controller is not suitable for control of a BDSC HCCI engine and improvements need to be made by either further tuning the weighting functions, or by applying weighting functions for the input-signals to avoid the fast chattering. Although this approach has already shown promising control results, it does not consider estimated disturbances and modeling errors in the control-design, so that an approach with structured uncertainties will be introduced in the next section.
This is especially motivated by assessing the robustness criteria in this case with the estimated unstructured uncertainties.
By including the output uncertainty into the model as in table 3.1 and again shown here (for

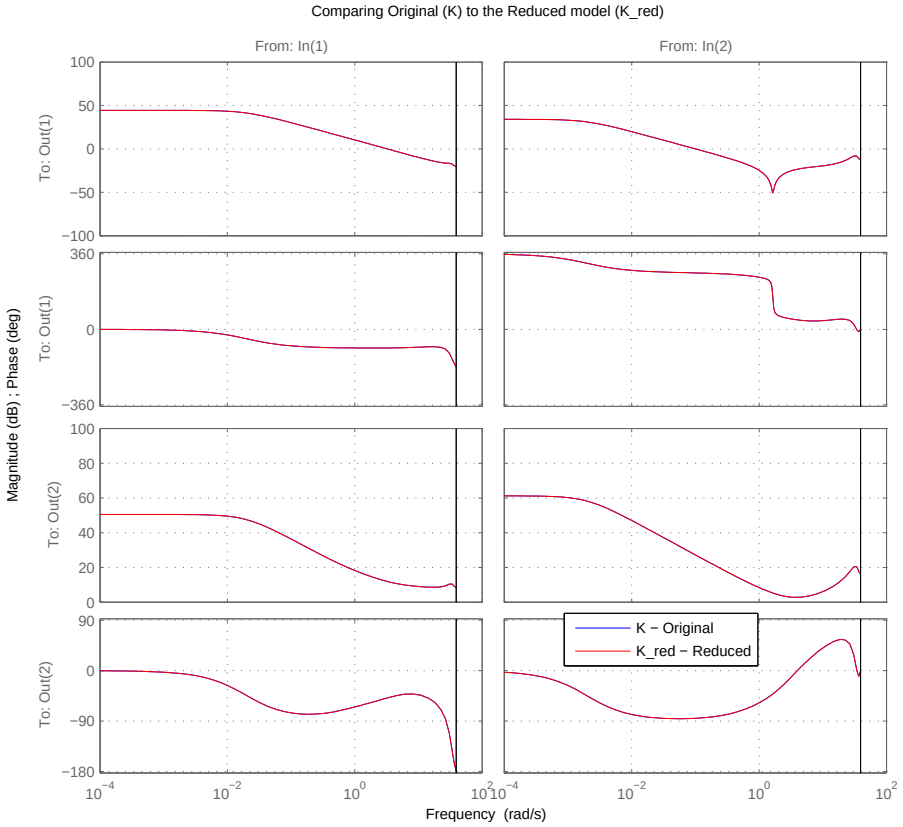

Figure 8.12: Bode Plots of the mixed-sensitivity system as in 8.6 for the Original H_∞ controller in comparison to the reduced one

$W_1 = 0$):

$$G_P = (I + \Delta W_2)G \tag{8.15}$$

(where G and G_P equal P and $\tilde{P}$ above) and computing the robustness criterion for this case, which is:

$$\| W_2 T \|_\infty < 1 \tag{8.16}$$

with T_O as the output complementary function, defined as

$$T_O = \frac{G_P K}{I + G_P K} \tag{8.17}$$

a value of 20.6388 is obtained, which is too large to guarantee robust control.
It may be disputed that the reason for this is the large uncertainty obtained from the reference model, whose infinity norm is already 20.6518, which itself is already normalized, but it may stem from the conflict of finding a tolerable CA_{50} uncertainty, especially around 0deg ATDC which increases the relative error remarkably.
This problem is addressed in the next section, where the uncertainty modeling is reviewed and a new structured uncertainty modeling presented, which is directly included in control design.

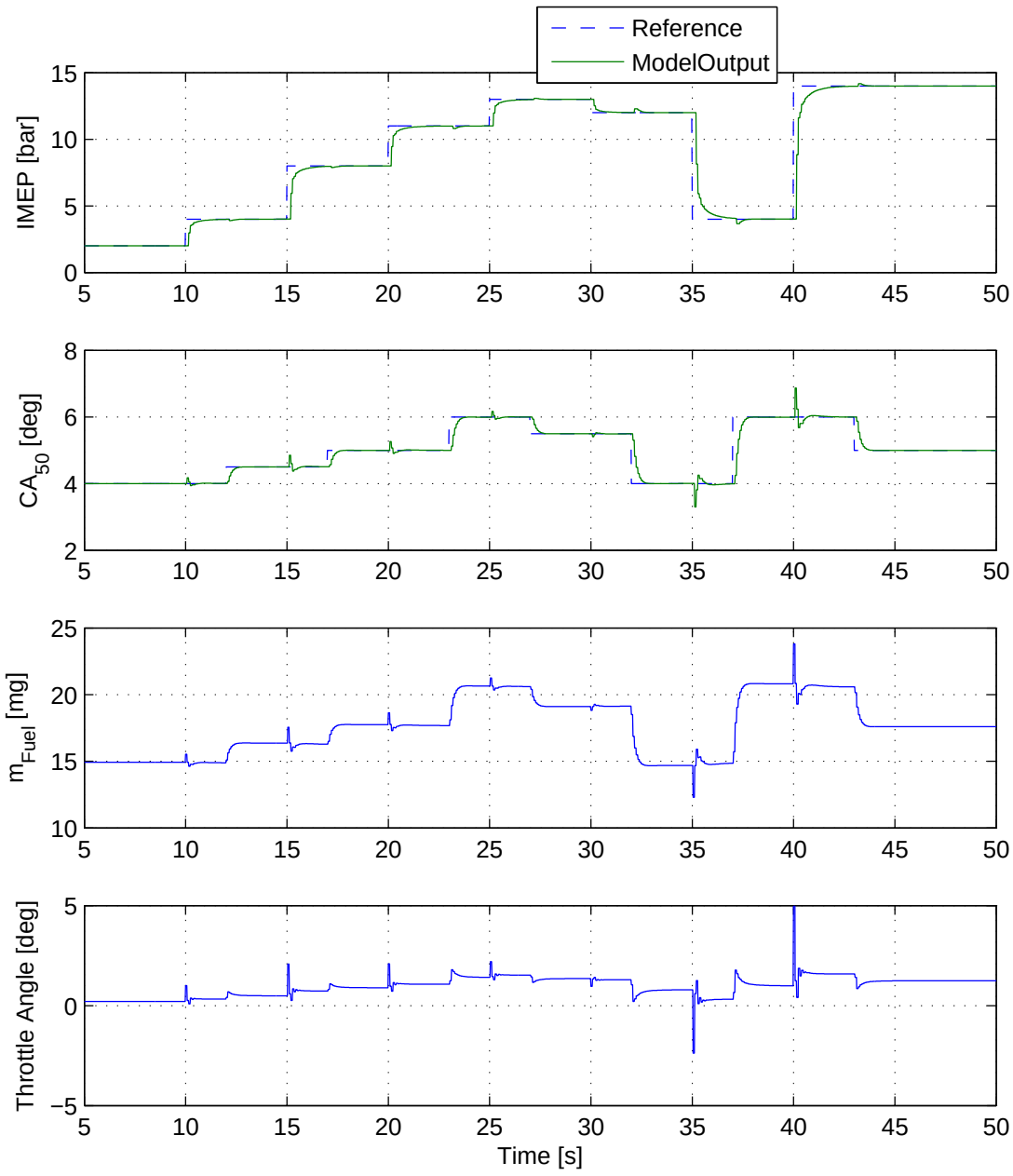

Figure 8.13: Closed-Loop control with an H_∞ controller of the linear plant

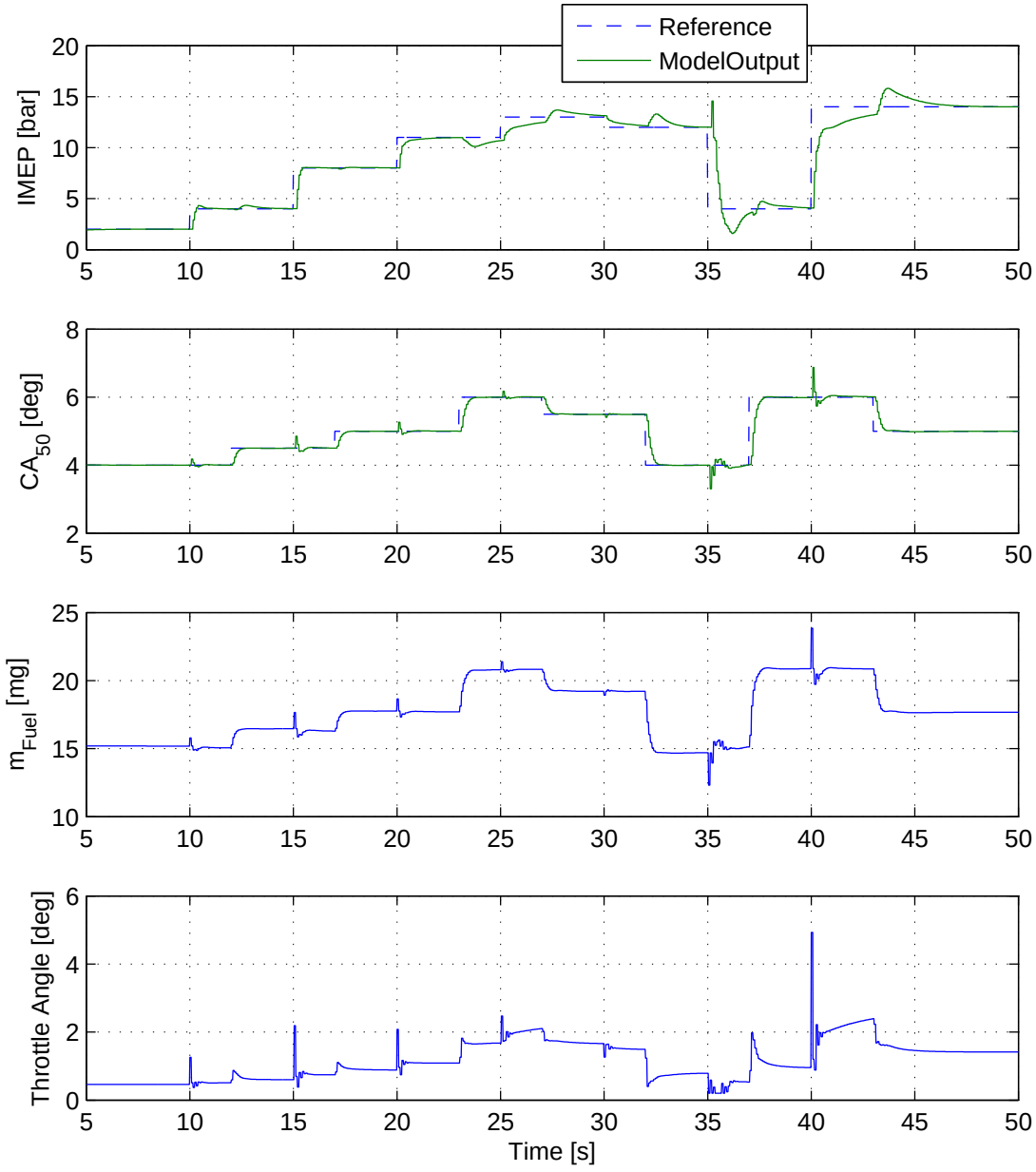

Figure 8.14: Closed-Loop control with an H_∞ controller of the nonlinear plant

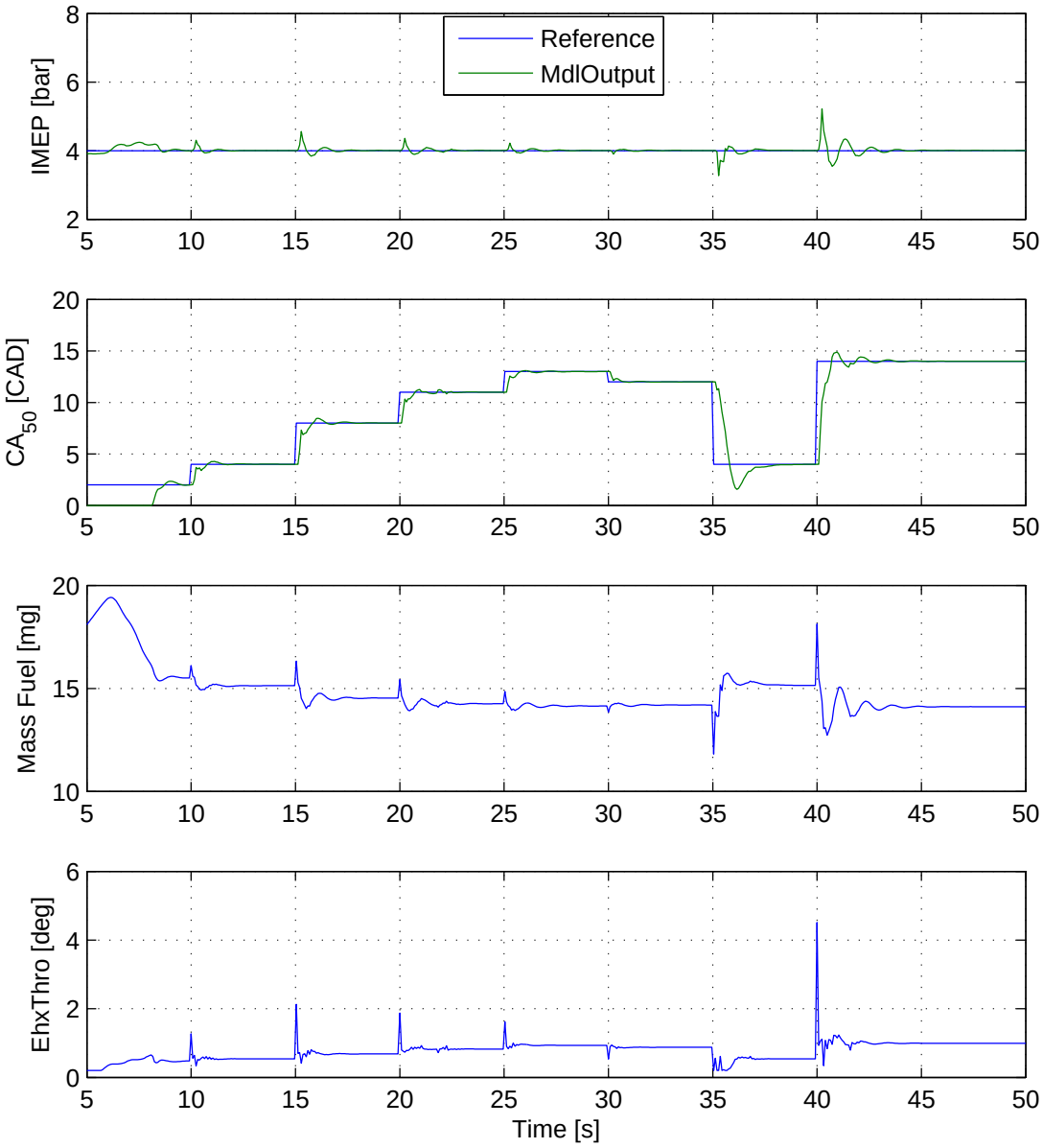

Figure 8.15: Closed-Loop control with an H_∞ controller at the 0-D Engine model with a constant $IMEP$ of 4 bar

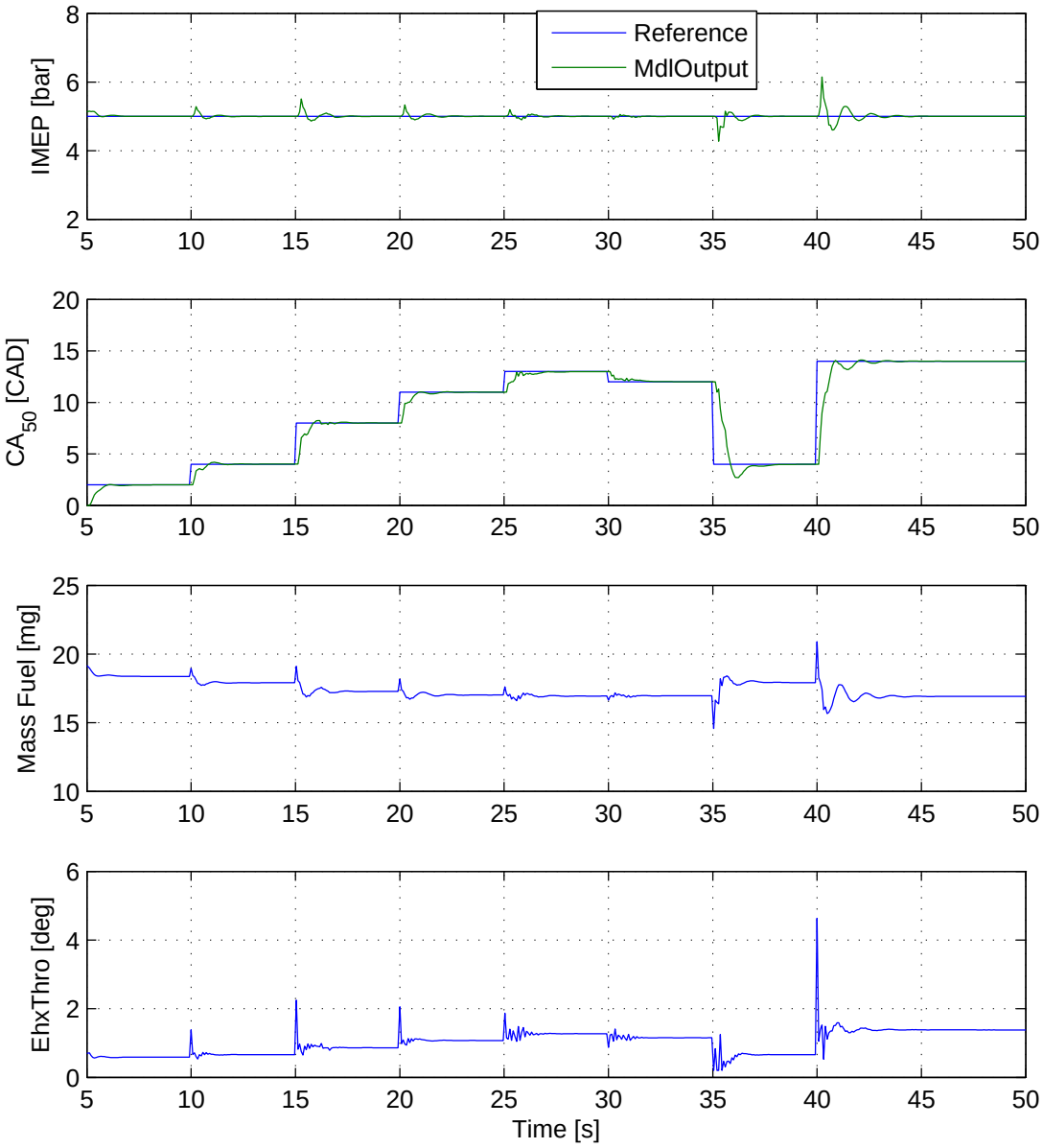

Figure 8.16: Closed-Loop control with an H_∞ controller at the 0-D Engine model with a constant $IMEP$ of 5 bar

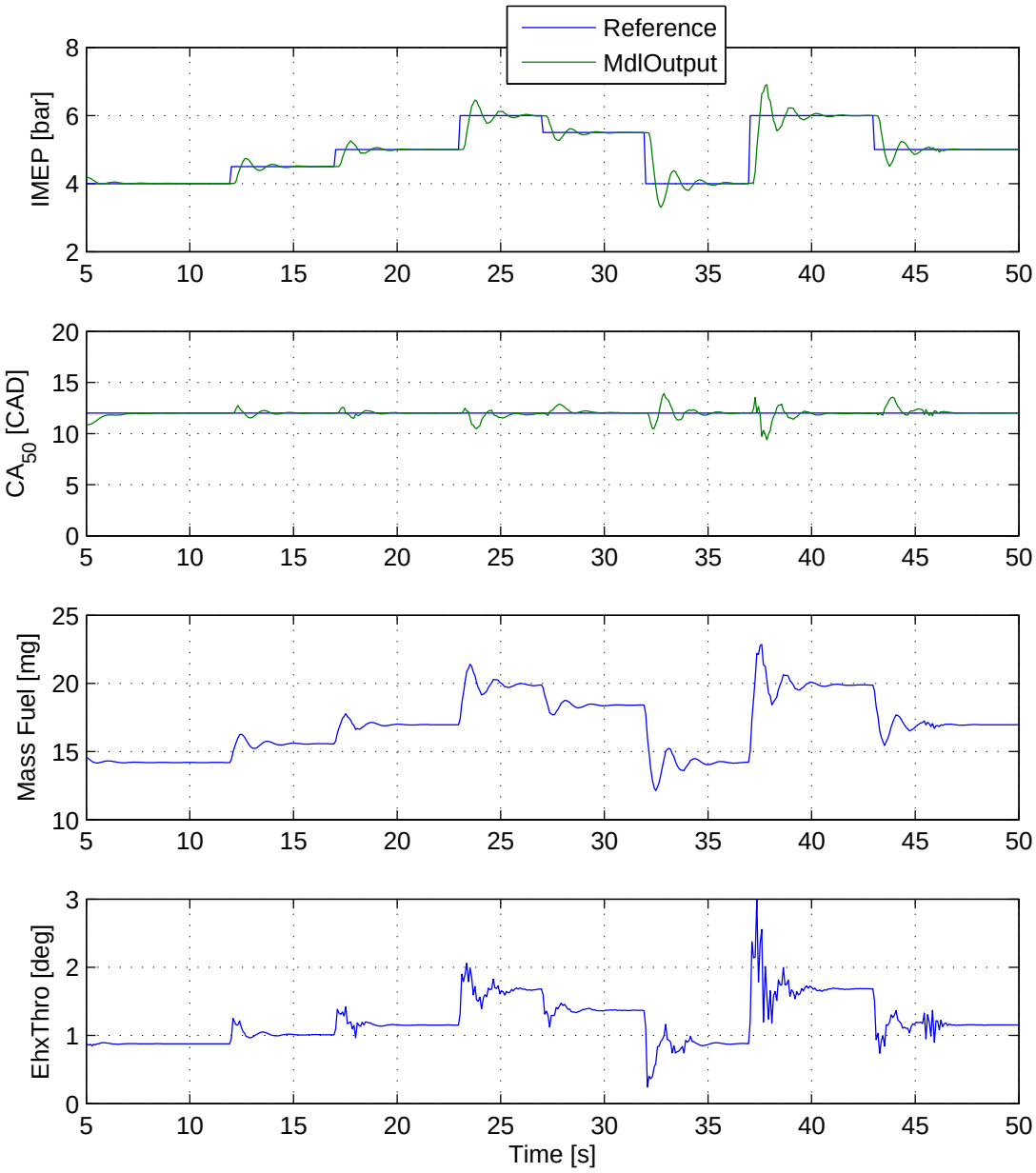

Figure 8.17: Closed-Loop control with an H_∞ controller at the 0-D Engine model with a constant CA_{50} of 12deg ATDC

μ Control Design

The H_∞ control scheme provides a comprehensive design framework including an observer structure, and by modeling uncertainty from the identification of the actual system (in this case here the 0-D model), robustness of the closed loop control can be estimated. However, as described in the fundamentals, the criterion for robustness might be too conservative and lead to sub-optimal controllers. The same issue holds for the robust performance estimation.
In the robust control analysis from last section, it was shown that the controller acted poorly on the target system, whereas it showed good performance on the non-linear Mean-Value Model.
A better approach for MIMO control design would be not only to model the disturbance as structured perturbations and to use μ analysis but also to include them in the control design.
In this work, the important states of the system have been modeled as the measured outputs. This motivates to relocate the output disturbances and incorporate them directly into the states for CA_{50} and $IMEP$, while the states of exhaust pressure and temperature were neglected. Modeling disturbance is hereby done on the linearized system, since the equations of the actual mean-value model are very complex and a clear uncertainty cannot be localized. In fact, variations may occur in every part of the model (e.g. temperature calculation, ignition model) and cannot be confined to a single parameter. Hence, the uncertainty is directly incorporated in the system matrix A of the linearized model, as shown in the following equation:

$$x_{k+1} = (A + \Delta A)\, x_k + B u_k \tag{8.18}$$

This approach allows for pulling out the uncertainties ΔA into an unstructured uncertainty block Δ with $\mid \Delta \mid \leq 1$. For the sake of simplicity, the disturbances directly modeled as percentage uncertainties and the bodeplots compared with the identification results from the reference model. The bode plots of the disturbed linear plant are shown in figure 8.18:

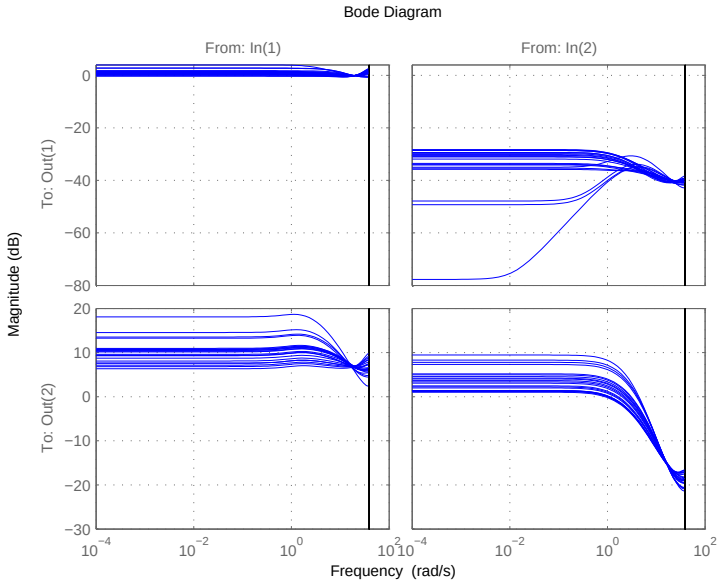

Figure 8.18: Bodeplots of the disturbed linear plant 8.18

The following figure shows the structured singular values of the open plant model.

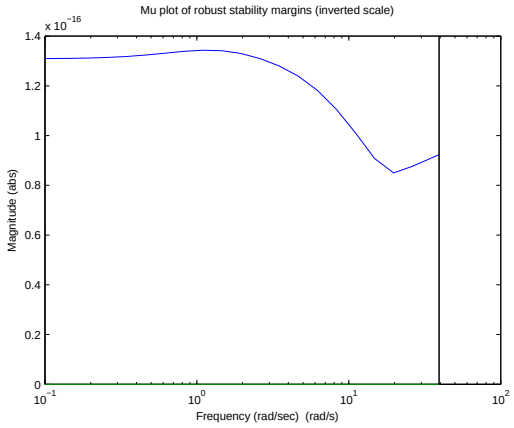

Figure 8.19: Singular Values of the disturbed plant

Here it can be seen that the estimated uncertainties do not de-stabilize the plant in any case and overall robustness with respect to disturbances is ensured, which makes control design more straightforward since a stabilizing controller is not required.
In order to incorporate these uncertainties directly into control design, the well-known D-K Iteration algorithm has been applied, where the bandwidth frequency for the weighting functions have been found by trial and error at 30rad/s, while the other parameters remained the same as with the H_∞ controller and the W_u was set to a static value of one.
The stability with the obtained μ controller is analyzed in the following figure which shows the singular values of the closed loop design.

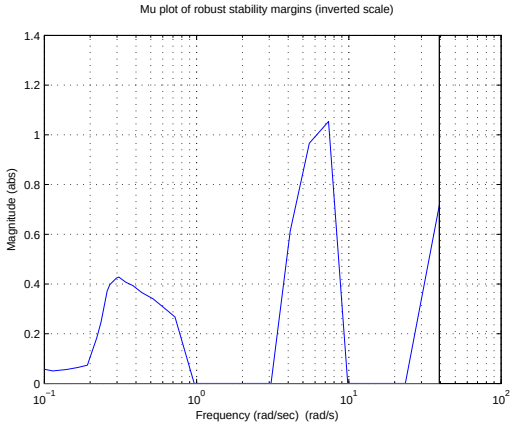

Figure 8.20: Singular Values of the closed-loop of the disturbed plant

It can be seen that the structured singular values fall far below the limit of one for almost all frequencies except for a small range where the value of one is crossed. By definition, this implies that robustness problems may occur, however, since the peak value is very close to the value of one. Furthermore, uncertainty ranges have been set generously wide. This peak can be lowered by tightening the tolerances a bit. Apart from this, the results here indicate robustness of the control scheme. Additionally, at some frequencies a value of zero can be seen, which shows that the plant cannot be destabilized if the input frequency stays within these ranges.

The controller designed here has an order 66 states which make online computation cumbersome and requires unnecessary computation resources. For order reduction, the Hankel approach was done here again, and Figure 8.21 shows the Hankel singular values of the μ controller.

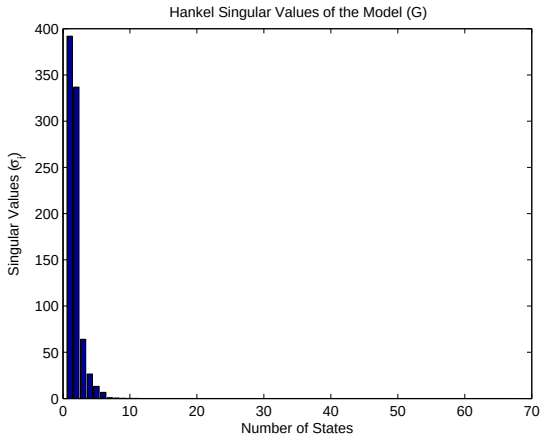

Figure 8.21: Hankel Singular Values of the μ controller

In this figure, the large number of controller states is evident. However, large Hankel singular values only appear at lower controller model states. Hence, it is conceivable to reduce the model states by a balanced model reduction algorithm.
By using the model balanced reduction algorithm, the states of the reduced controller have been limited to 12 states, albeit further reduction may be possible. To compare original with the reduced controller, the plots in figure 8.22 shows the magnitudes of the bode plots of both variants, where the reduced one is displayed in red.

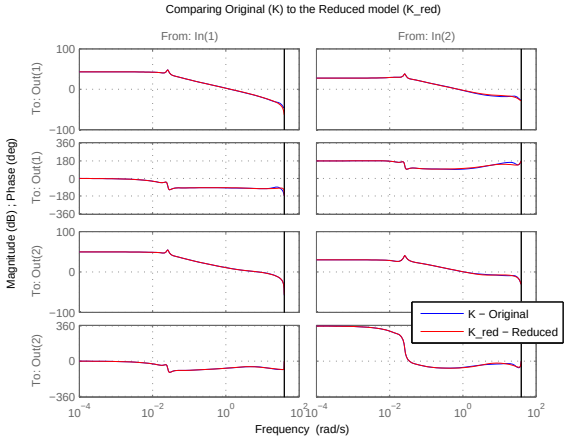

Figure 8.22: Hankel Singular Values of the μ controller

Here, it can be seen that both controllers are extremely similar such that it may be expected that the reduced controller works with similar effectiveness than the original controller.

Performance of the μ Controller

This section presents the performance results of the reduced μ controller, tested on the detailed 0-D model.
The following figure 8.23 shows the performance of CA_{50} control, while keeping $IMEP$ at a fixed value of $4bar$.

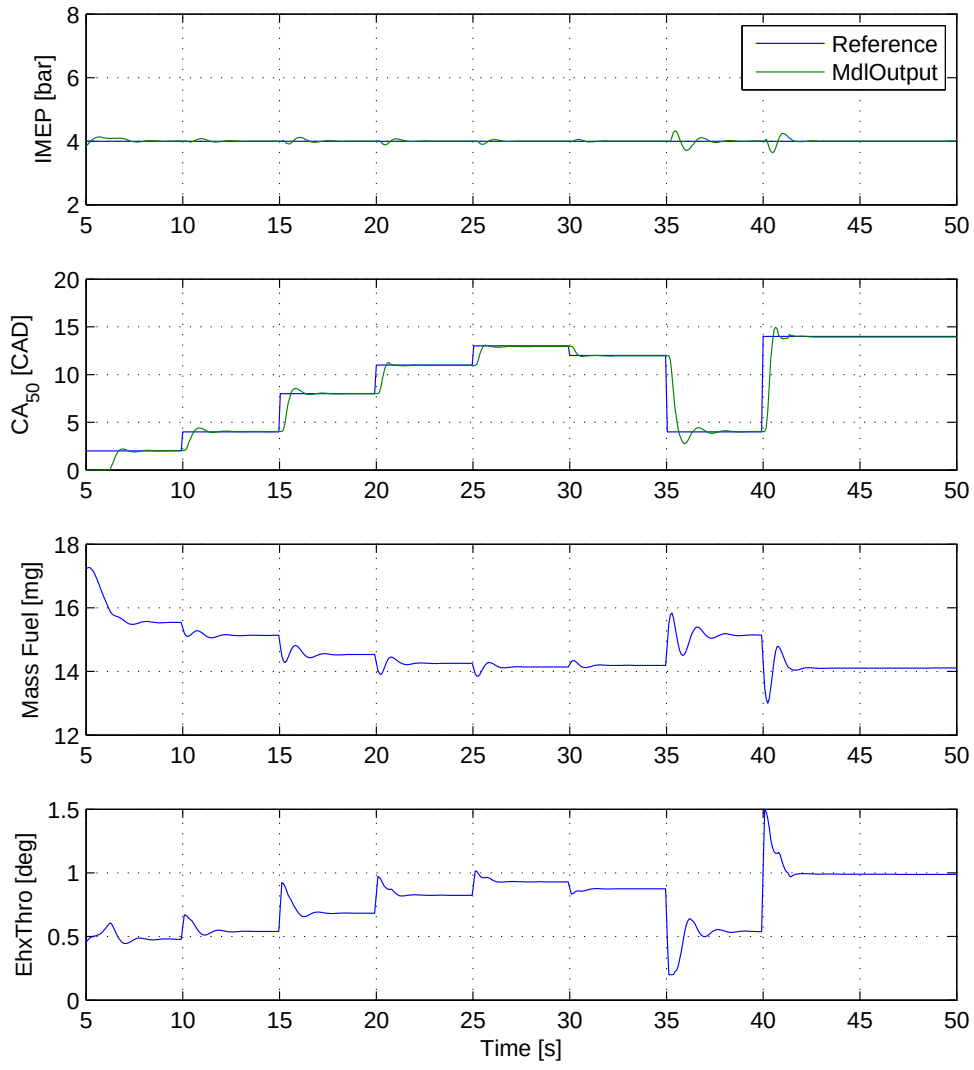

Figure 8.23: Tracking results of the reduced μ controller on the 0-D model

The controller is not only able to track the step changes in reference CA_{50} in less than one second and approaches the target value within even half of a second (or within a few cycles) with only very little overshoot, it is also able to regulate out the disturbances in $IMEP$. It can be seen that the controller performance is very similar during each step-change, despite of the bigger stretch in CA_{50}, where previously non-linearity concerns were expressed. It thereby

seems that the controller handles these challenges well. Even in the last step changes, which are challenging, not only due to the large change, but also since it steps to an extremely late combustion phasing, which are quite unstable and risks of misfire exist, are handled well.
The control performance can be judged as very good, and unlike the sliding-mode controller tested on the BOOST model, where strong linearities caused a weaker control performance when the operating points moved away from the linearization point, this issue has been entirely diminished with this control scheme.
The following figure 8.24 shows the performance of CA_{50} control with the same step-changes again, while keeping $IMEP$ at a much higher level of 6 bar.

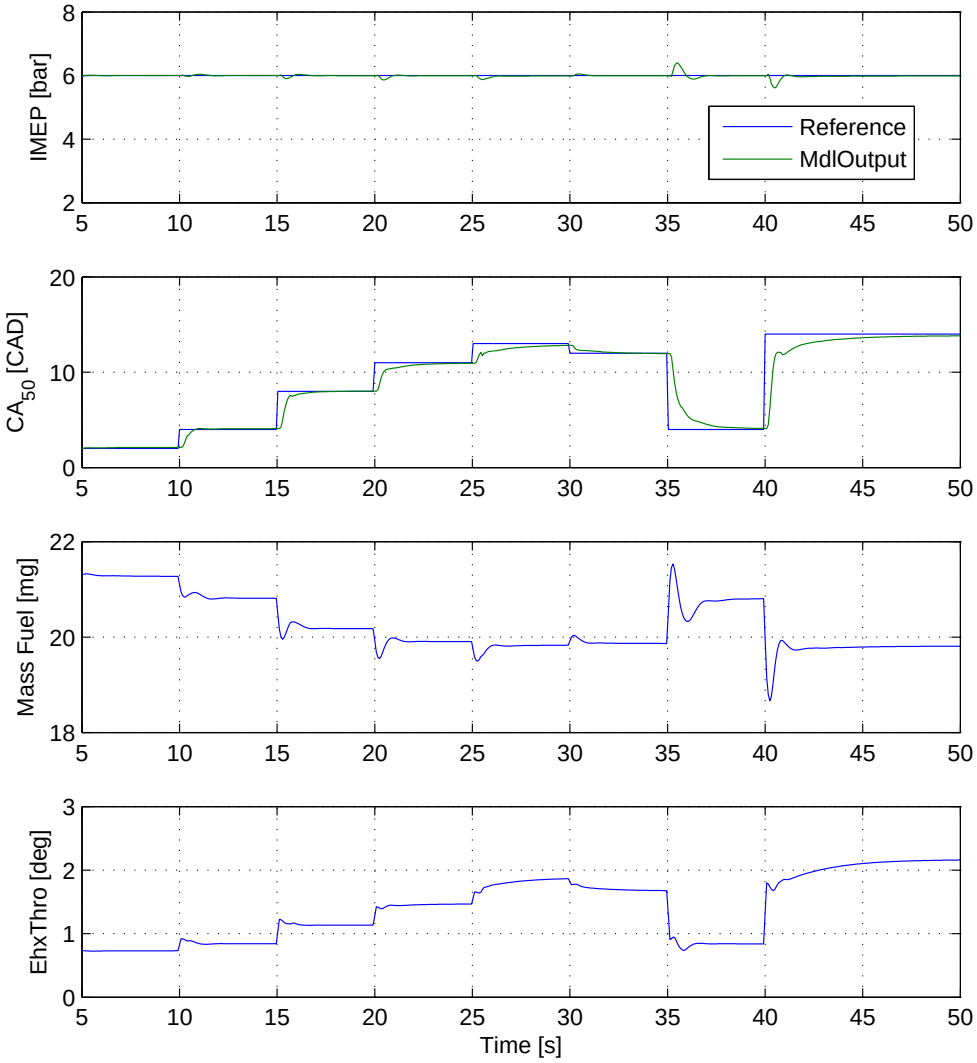

Figure 8.24: Tracking results of the reduced μ controller on the 0-D model

It can be seen in this figure that the controller shows very similar performance, although the transients at extreme points with late combustion phasings here are somewhat slower. The

initial fast transients still remain, but a slower approach to the reference value are visible. With these transients, no single overshoot can be observed here, and the initial transients still cross the critical 63% threshold only in a few cycles. At the same time, little disruption in $IMEP$ can be observed. In another trial, performance of $IMEP$ was tested, while CA_{50} is kept fixed at a late combustion phasing value of 12deg ATDC, which is a challenging control task due to the critical robustness problems in combustion, which can quickly result in misfire. The results are shown in figure 8.25.

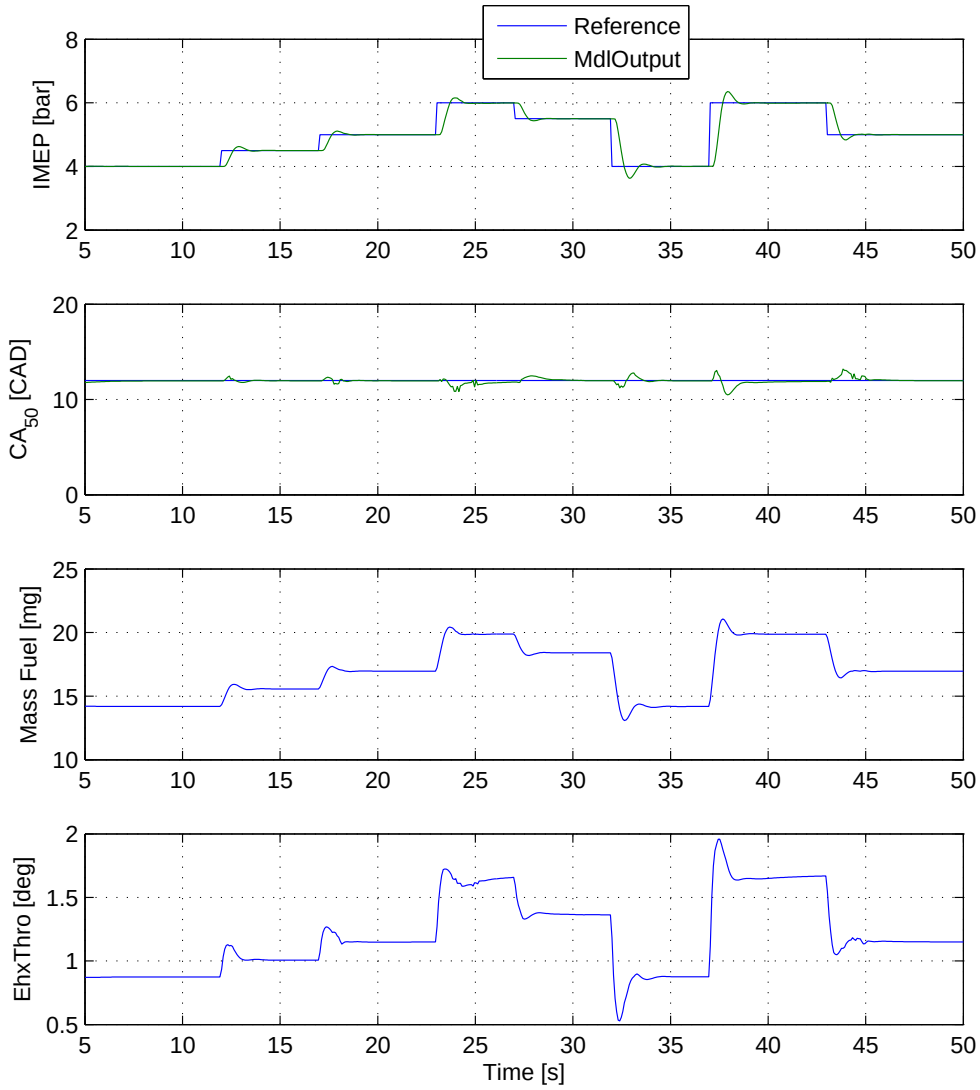

Figure 8.25: Tracking results of the reduced μ controller on the 0-D model

The controller tracks the $IMEP$ changes well and in a very fast time-scale similar to the combustion phasing one, while few overshoots can be seen. Additionally, combustion phasing is hardly affected and the controller keeps CA_{50} at its designated value. As mentioned earlier, this is a challenging task due to the strong cross-coupling from fuel to combustion phasing,

which is handled well with this controller.
A second test has been carried out with a reduced tracking reference of CA_{50} at a value of $7deg$ ATDC.
Figure 8.26 shows the results of $IMEP$ tracking, where similar dynamics can be found as in the previous case.

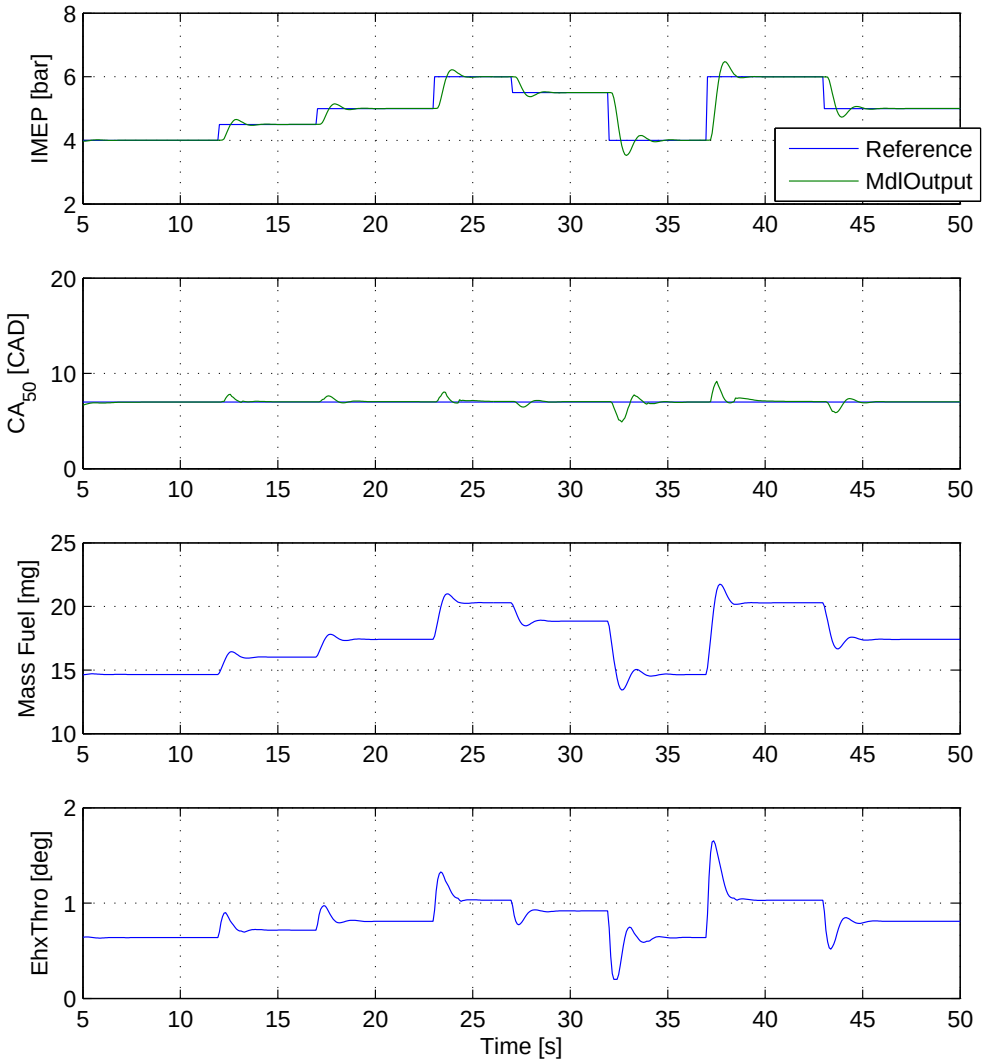

Figure 8.26: Tracking results of the reduced μ controller on the 0-D model

Also here, tracking of $IMEP$ was fairly fast, while disturbance rejection of CA_{50} is extremely good, and little variation could be found.

It can be concluded that this controller is a well-suited candidate for simultaneous control of $IMEP$ and CA_{50} of a BDSC HCCI engine, since its design is straightforward and the performance very good. Although optimization might be possible by a more aggressive tuning, this

however, might come at the expense of excessive control actuation which might cause excessive actuator wear, and in particular at presence of measurement noise on a real system, it might result in unexpected control performance. With this is mind, it may be concluded that this control scheme is suitable for BDSC HCCI.

Robustness of the μ Controller

The primary purpose of a robust closed-loop control scheme is to increase robustness of a BDSC HCCI engine. In this research, a framework for design of robust controllers for this particular engine has been proposed and demonstrated on the reference 0-D model in the previous section. The idea of using a MIMO controller is to avoid a more complicated cascaded multiple SISO-loop control scheme and simplify the overall control design process. Even more, by keeping the modeling effort simple and relying on robust control schemes further simplify the control design task remarkably, and by using the structured singular value approach, the control design engineer can already estimate control robustness and performance before the initial tests.

With all the advantages of a robust controller stated here and demonstrated previously, one particular characteristic of HCCI engines make robust control design inevitable and closed-loop robustness should be further analyzed. It is commonly agreed that HCCI combustion is extremely sensitive to disturbances, which may come from different atmospheric conditions (e.g. driving in snow vs. driving in a dessert); different fuels and fuel qualities, which is in particular true if the driver travels long distances in different countries; and where different legislation and driver preferences may require different kinds of fuel which impact HCCI combustion. Other uncertainties and external disturbances may arise due to production tolerances and aging of the combustion engine. Even deposits on cylinder walls stemming from combustion influence HCCI combustion very much ([51] and [50]).

To demonstrate the robustness of the proposed μ controller, varying ignition properties were emulated by changing the tuning factor of the ignition model varying to later and earlier ignition timings and the same tracking values for CA_{50} and $IMEP$ as before were applied to allow for a direct comparison.
The following figure 8.27 shows the control performance with fuel ignition at later timings. In this trial, the pre-exponential factor has been increased by nearly 90%, which causes a strong delay in ignition timing and is an extreme challenge for the controller.

The results in this figure show that the controller handles the disturbance well and little deterioration compared to the previous control task can be seen which is almost negligible. The good performance is quite surprising considering the stark ignition property change. Still, as before, some overshoot can be seen and the overall fast performance remains the same. Even the strong transients towards the end of the trial are handled extremely well and do not cause combustion instabilities at all. This even comes despite the fact that the ignition properties have been delayed largely, but the controller is able to keep combustion phasing in a very confined region. Apart from the good performance of the combustion phasing, regulation of $IMEP$ is hardly affected by the different combustion properties, although the tighter exhaust throttle actuation causes higher exhaust pressures, which in turn decrease pumping losses and deteriorate $IMEP$.

Figure 8.28 shows the same CA_{50} tracking at an $IMEP$ of six bar.

Here it can be seen that the controller works with very similar performance as for the undisturbed case, although the transients seem somewhat faster than in the undisturbed case. This may point at non-lineatities again, where later combustion phasing properties seem to cancel out these non-linearity issues with higher power outputs. Basically, no single overshoot can be seen despite of high tracking transients of CA_{50}, where at the same time regulation performance for $IMEP$ is almost the same. Overall confirms the good robust performance of the controller. In another control trial, investigation for earlier ignition timings have been investigated, where the ignition model has been tuned with a decrease by more than 60% of the pre-exponential factor of the ignition model. and the results are shown in figure 8.29.

The engine load $IMEP$ has been kept fixed again at 4 bar, while CA_{50}, which is more difficult to control, has been tracked.
Also here, it can be seen that the controller hardly deteriorates with different fuel ignition properties. In fact, the extremely good control performance is much the same as in the undisturbed case, such that CA_{50} step-changes are tracked in a very short time, whilst $IMEP$ disturbances are attenuated. For the sake of brevity, an investigation with $IMEP$ of six bar has been omitted here, but it may be expected here that the performance is very similar and the controller can handle the disturbance at higher loads as well.

These investigations show that the controller handles external disturbances and unknown plant properties well. This robustness investigation could be further expanded to different engine speeds and by applying the controller on different cam sets, of which three have been presented in this HCCI engine research. The control investigation here is only limited on the high loads cam specification and testing the control scheme at different cam sets is to be considered as a future task.
So is the testing of this controller at different speeds, which may be challenging to due different pressure wave characteristics, especially due to the blow-down pressure wave in the exhaust. However, also here, these disturbances affect in the end ignition timing, and with the investigation and considerations above, the proposed controller may handle this challenge too.

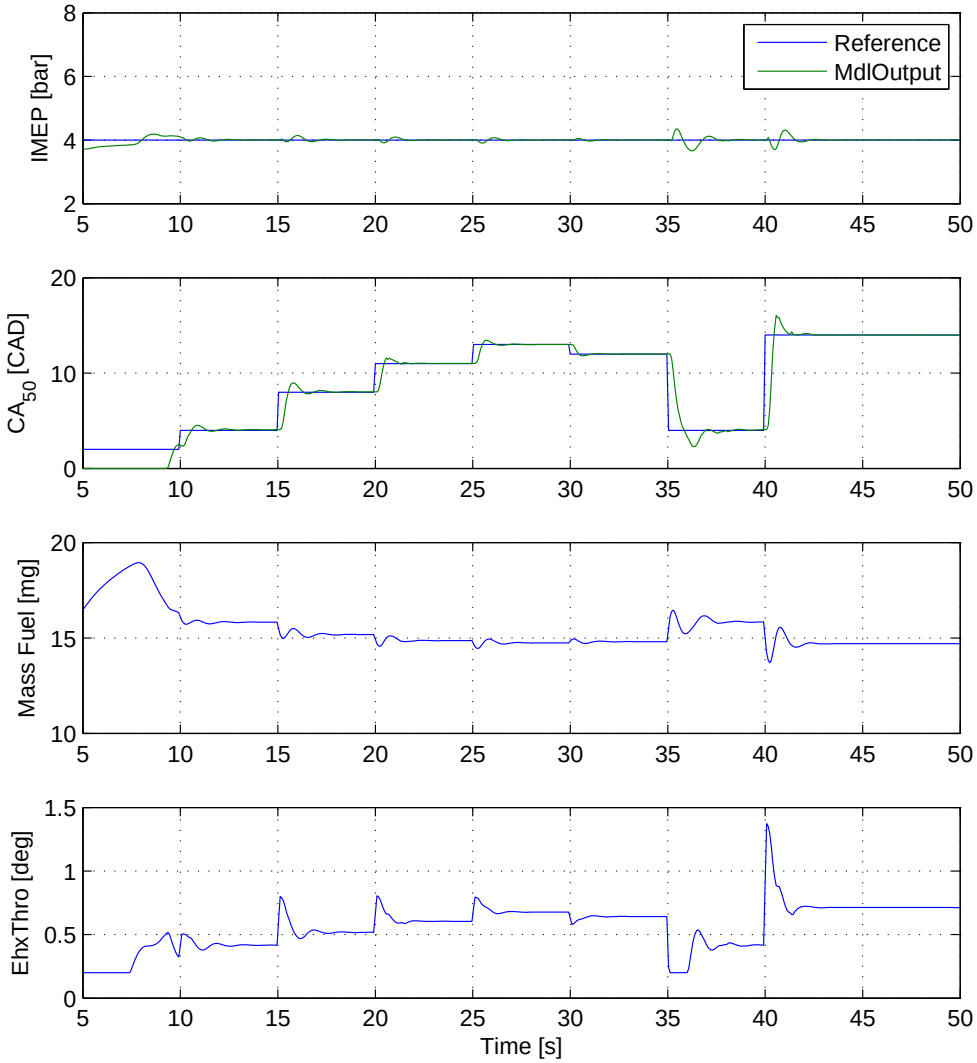

Figure 8.27: Tracking results of the reduced μ controller on the 0-D model with a modified ignition model with later combustion phasing

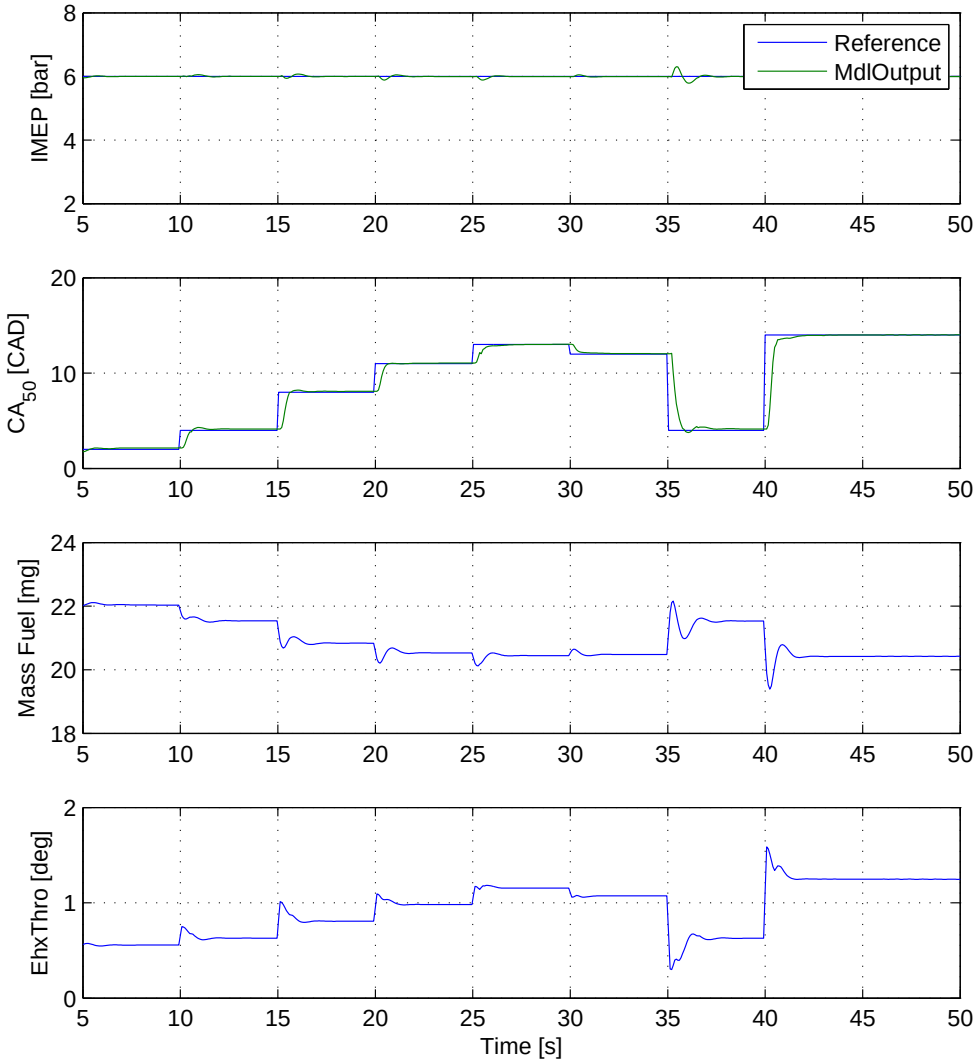

Figure 8.28: Tracking results of the reduced μ controller on the 0-D model with a modified ignition model with later combustion phasing

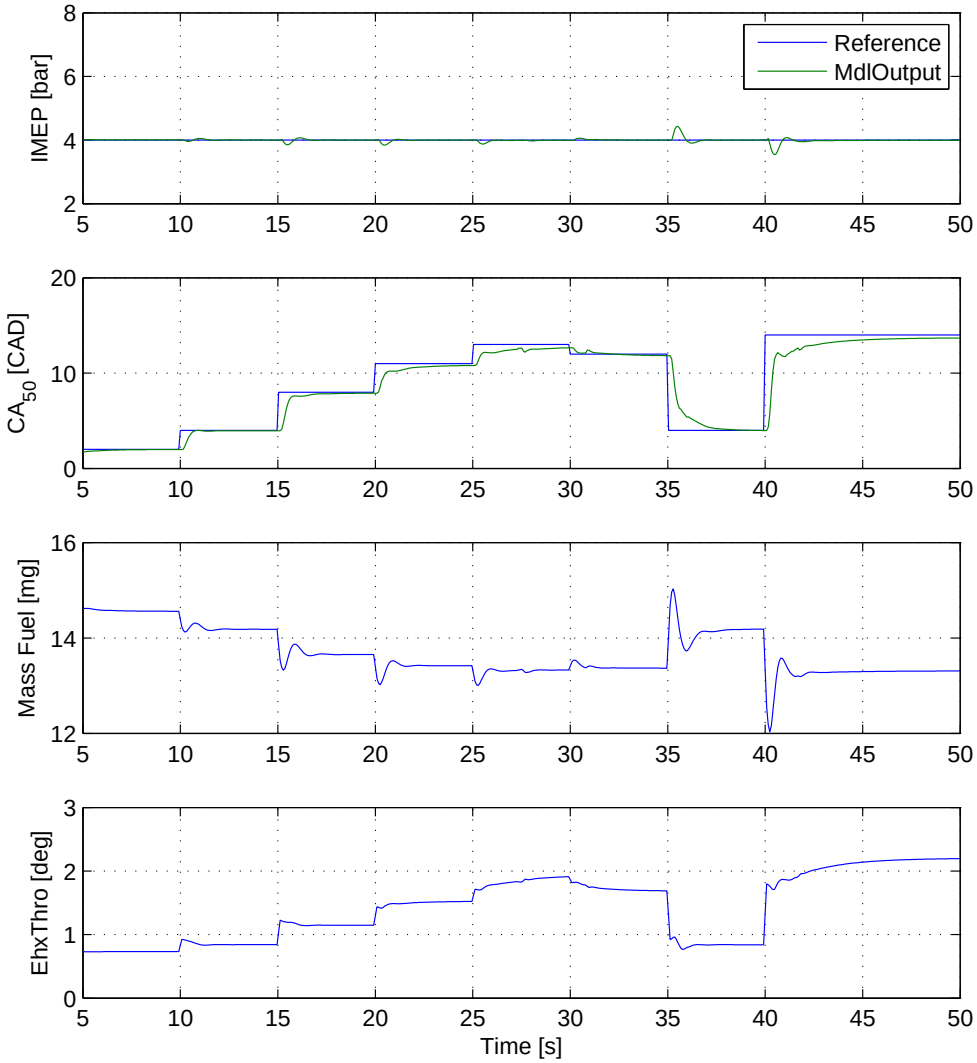

Figure 8.29: Tracking results of the reduced μ controller on the 0-D model with a modified ignition model with earlier combustion phasing

8.3.3 Sliding Mode Control

Sliding mode control (SMC) is a non-linear control scheme that has been used for automotive control as well (e.g. [2]). Its strength is the easy design and the inherent robustness, which comes from the non-linear switching algorithm.
So far, hardly any sliding-mode control scheme has been reported for HCCI control and it might be an alternative control concept to increase robustness of HCCI combustion. Since discrete-time SMC does not require a switching scheme to reach sliding-mode, the idea is to change the control performance at certain operating conditions by activating on the switching term. These might be when, for example, combustion phasing is too far off from the desired location and requires faster control actuation, while during transient operation, a rather smooth actuation is desired to avoid excessive control, actuation wear and unnecessary overshoots.
The underlying idea is depicted in the following figure:

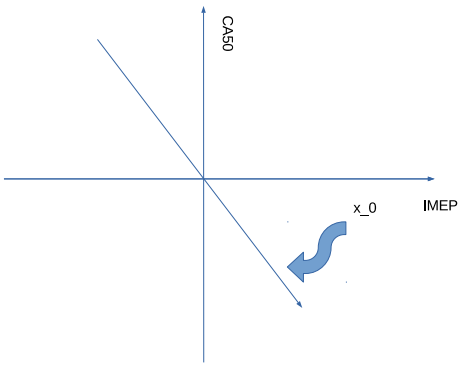

Figure 8.30: Idea of increasing robustness for SMC with HCCI

Here, the design plan is to find a controller that has desired slower dynamics when on the sliding manifold. Since the states already move parallel to the manifold and towards the origin as an equilibrium point with the equivalent control, the switching term might give an additional ”aggression” when activated and might be switched off when the states are close to the equilibrium point to avoid unwanted chattering. This might be only for a few cycles and might be useful in switching from one combustion mode to the other. In case of SI-HCCI switch, the first HCCI cycles will have an unfavorable combustion timing, preferably too early than too late to avoid misfire and a severe $IMEP$ drop. With too early combustion during the first cycles known, it might be a useful approach to tune the switching term of the sliding-mode controller such, that it aggressively moves the states towards the sliding manifold, which are designed such that they keep the states in a desired range.
A similar approach could be followed with the switch from HCCI to SI where the main objective is to bring the air/fuel ratio in an as short time as possible in a range around stoichiometric. This would ensure stable SI combustion and low NO_x emissions with a three-way catalyst (TWC).

While these advantages are promising for HCCI, this strategy might also be useful for other combustion concepts, such as lean SI with Lean-NOx-Trap (LNT), where frequent switching between lean combustion and stoichiometric to purge the catalyst is required.

To proceed with the control synthesis, the standard sliding control design used in this work will be explained here.

In its standard form, the controller consists of a linear controller, termed as the equivalent control u_{equ}, with the states as a feedback signal, and an additional switching term which switches between two positions, depending on where the states lie related to a pre-designed sliding manifold. Since this is a state-feedback controller, an observer or a Kalman estimator may be required, which is omitted in this investigation to analyze the possible control-performance.

Design of the sliding manifold is done in accordance to the dispcription in [28]). Although, the introduction here is given for time-continuous systems, it has been directly applied to the discrete-time system in this work.

Design of the Sliding Manifold

Given the linear model of an uncertain system:

$$\dot{x}(t) = Ax(t) + Bu(t) \tag{8.19}$$

with $rank(B) = m$ and the pair (A, B) is supposed to be controllable.
The switching function is defined as:

$$\sigma(t) = Sx(t) \tag{8.20}$$

with the sliding-manifold S that needs to be designed.
A standard way to find a sliding manifold is to transform the equation 8.3.3 into regular form, as:

$$\begin{aligned} \dot{z_1}(t) &= A_{11}z_1(t) + A_{12}z_2(t) \\ \dot{z_2}(t) &= A_{21}z_1(t) + A_{22}z_2(t) + B_2u(t) \end{aligned} \tag{8.21}$$

with transformed states $z_1(t)$ and $z_2(t)$, and the transformed matrices A_{11}, A_{12}, A_{21} and A_{22}. In this normal form of a state-space system, the inputs into the system do only affect the second equation, and it can be shown that disturbances acting only on this second equation can be entirely canceled out with this control scheme. This was already stated in the introduction and such disturbances are called "matched disturbances", while those fulfilling not the requirement are denoted as "unmatched".

The switching function becomes now:

$$s(t) = S_1z_1(t) + S_2z_2(t) \tag{8.22}$$

According to [28],the original system can be cast into normal form by employing a QR-decomposition of the input matrix B. By doing so, an orthogonal matrix T_r can be obtained, so that the change of coordinates is accomplished by:

$$z(t) = T_rx(t) \tag{8.23}$$

and the new input matrix B:

$$T_r B = \begin{pmatrix} 0 \\ B_2 \end{pmatrix} \tag{8.24}$$

while the system matrix A is changed too, as:

$$T_r A T_r = \begin{pmatrix} A_{t,11} & A_{t,12} \\ A_{t,21} & A_{t,22} \end{pmatrix} \tag{8.25}$$

The switching function is then composed of:

$$S T_r^T = [S_1 \; S_2] \tag{8.26}$$

Designing the sliding manifold S was accomplished by LQ design. In doing so, a positive-definite diagonal weighting matrix Q needs to be defined:

$$Q = \begin{pmatrix} q_{1,1} & 0 & \cdots & 0 \\ 0 & q_{2,2} & \cdots & 0 \\ \vdots & \vdots & \ddots & \vdots \\ 0 & 0 & \cdots & q_{m,n} \end{pmatrix} \tag{8.27}$$

where the weights $q_{n,m}$ for each objective are found by trial and error.
At this point, it should be noted that this control tuning task has been simplified here since the outputs of interests (combustion phasing CA_{50}, and $IMEP$) have been modeled directly as states in this work.

The weighting matrix has then to be transformed as well to match with the new transformed states z:

$$Q_t = T_s Q T_r^T = \begin{pmatrix} Q_{t,11} & Q_{t,12} \\ Q_{t,21} & Q_{t,22} \end{pmatrix} \tag{8.28}$$

where $Q_{t,21} = Q_{t,12}^T$ applies.

The objective in this LQ-approach is to minimize the following cost-function:

$$J = \frac{1}{2} \int_{t_s}^{\infty} \mathrm{z}_1^T Q_{t,11} z_1 + 2 z_1^T Q_{t,12} z_2 + z_2^T Q_{t,22} z_2 \, \mathrm{d}t \tag{8.29}$$

Defining

$$\hat{Q}_t = Q_{t,11} - Q_{t,12} Q_{t,22}^{-1} Q_{t,21} \tag{8.30}$$

and

$$\hat{A}_t = A_{t,11} - A_{t,12} Q_{t,22}^{-1} Q_{t,21} \tag{8.31}$$

the controller can be found by using the standard LQ optimization approach, with the cost function as given in the introduction (Equation 3.59), where

$$\begin{aligned} A &= \hat{A}_t \\ B &= A_{t,12} \\ Q &= \hat{Q}_t \\ R &= Q_{t,22} \end{aligned} \tag{8.32}$$

The resulting sliding manifold is obtained by:

$$\begin{aligned} M &= Q_{t,22}^{-1}(A_{12}^T P + Q_{t,21} \\ S_2 &= I \\ S &= S_2 \left[M \cdot I\right] T_r \end{aligned} \tag{8.33}$$

where P is the solution of the algebraic Riccati equation (ARE) and the corresponding state controller:

$$k_{smc} = (S \cdot B)^{-1} S \cdot A; \tag{8.34}$$

with $(S \cdot B)^{-1}$ as the Penrose-Moore pseudo inverse.
Since the non-linear switching term u_{nl} has been omitted here, the final feedback control scheme reads:

$$u_{equ} = k_{smc} \cdot x \tag{8.35}$$

A static feed-forward controller can be obtained with the state-controller k_{smc} by:

$$N_{ff} = (CI - A + Bk_{smc})^{-1} \cdot B) \tag{8.36}$$

In order to extend the controller with an integral action, and thereby to allow for reference tracking despite of model uncertainties, the following extended state-space model discrete-time systems has been created with an Euler-forward integral:

$$\begin{aligned} x_{k+1}^{(I)} &= x_k^{(I)} + Ts(r_k - y_k) \\ &= x_k^{(I)} - T_s C x_k + T_s r_k \end{aligned} \tag{8.37}$$

The augmented system then becomes:

$$\begin{pmatrix} x_{k+1}^I \\ x_{k+1} \end{pmatrix} = \begin{pmatrix} I & -T_s C \\ 0 & A \end{pmatrix} \begin{pmatrix} x_k^I \\ x_k \end{pmatrix} + \begin{pmatrix} 0 \\ B \end{pmatrix} u_k + \begin{pmatrix} T \\ 0 \end{pmatrix} r_k \tag{8.38}$$

The linear closed-loop system has the following eigenvalues:

$$\sigma = \begin{pmatrix} 0.0000 \\ 0.2289 \\ 0.6066 \\ 0.9661 \\ 0.8590 \\ 0.9148 \end{pmatrix} \tag{8.39}$$

To give the MIMO SMC design more flexibility, another diagonal matrix has been defined to allow for weighting of the control inputs, similar to the R-matrix of the LQ design approach.

The following weighting matrix has been found suitable for an acceptable trade-off between performance, and chattering and robustness:

$$Q = \begin{pmatrix} 1 & 0 \\ 0 & 3 \end{pmatrix} \tag{8.40}$$

The resulting control laws reads then:

$$\tilde{u_{equ}} = Q^{-1} \cdot u_{equ} \tag{8.41}$$

This approach is different than suggested in [107], where the diagonalization approach resulted in the following control law:

$$\tilde{u}_{equ} = Q^{-1} SB \cdot u_{equ} \tag{8.42}$$

However, since the term SB is nonetheless a constant, it has been omitted in the SMC design here.

SMC Control Performance

The controller introduced above has been coupled to the 0-D model and the performance results are presented in this section.
In figure 8.31, the first plot shows the same tracking problem of CA_{50} as before with fixed $IMEP$. The aim was to track step-wise changes in CA_{50}, in an acceptable control performance, while keeping $IMEP$ at a desired value, and to attenuate disturbances that come from the CA_{50} tracking steps.

In this figure, it is displayed that the controller tracks the CA_{50} very fast, within the order of only a few cycles. While disturbances on $IMEP$ occur, they remain in a very confined and acceptable range. It can also be seen that the controller brings back $IMEP$ within a few cycles only.
The actuation plots show that the controller uses for tracking of CA_{50} both actuators, fuel injection, and exhaust throttle to find the best possible dynamics. By retarding CA_{50} for example, the exhaust valve is opened quickly which causes the exhaust pressure to drop while $IMEP$ goes up. Consequently less fuel is required to keep $IMEP$ on a constant level and the amount injected is reduced. Furthermore, injecting less fuel helps to retard combustion phasing, since the in-cylinder temperature drops due to the lower combustion temperatures. In the previous chapters, it has been found that the dynamics of combustion phasing with fuel injection actuation are very fast so that theoretically a controller could be tuned that exploits these fast dynamics, to compensate for slower dynamics of other actuation (e.g. exhaust throttle) as well.
This, however, seems not to be the case for this controller, as can be seen by the actuation of the exhaust throttle. With every step-change, the exhaust throttle is actuated first and in a large step, before it switches back to a steady-state value. Some smaller after-actuation can be seen, which is due to the integrator of the controller, which corrects steady-state errors. In fact, this integral part of the controller has been kept slow in order not to influence the overall good performance of the controller.
The performance of this SMC could be further improved if a tuning strategy was chosen such that it includes some additional objectives in the control design. Here, it might be a useful approach to find a controller that minimizes the fuel consumption and keeps the injected amount

of fuel at the lowest level as possible. This could be done, for example, by implementing an additional algorithm that releases the exhaust pressure during steady-state run until an optimized point has been found, which can be considered as a future task.

In another test, the same CA_{50} tracking problem was analyzed again but with lower IMEP which was set here at a value of 4 bar. The results of this trial are shown in figure 8.32.
As with the case of 5 bar, the controller actuates very fast, and reaches the desired CA_{50} within a few cycles, while keeping the $IMEP$ at a fixed level. The disturbances on $IMEP$ that occur here are much lower than with the μ controller but they take several seconds until they reach their designated value.
It can be seen that the dynamics here at somewhat better than in the previous case, although the difference is minute. This, nonetheless, points at non-linearity issues, which have to be compensated by the robustness feature of the controller.

In a further trial, the control performance for $IMEP$ is tested, of which the results are shown in figure 8.33.
The plots in this figure shows step-wise changes of $IMEP$, while trying to keep combustion phasing at a designated level of 7 deg ATDC. The controller is able to track the $IMEP$ within one step, which may be attributed to the feed-forward part of the controller and the fairly linear characteristics of the fuel-to-$IMEP$ relation. However, a clear overshoot can be seen which controlled out after some seconds.
These general fast tracking dynamics on the other hand penalize the performance of CA_{50}, which are first disturbed, after which it takes a few cycles until they converge back to their set-value. As previously stated, this is due to the strong intercoupling between $IMEP$ and CA_{50}, the high sensitivity and high transients, which give challenges to the control design.
Since it is not advisable to amend the feed-forward terms, which would deteriorate steady-state tracking as a consequence, it would be a better idea to append a low-pass filter to the $IMEP$ reference command in order to loosen the tracking requirements and to bring more robustness into the CA_{50} regulation.

As a concluding remark, it can be stated that this controller is a suitable candidate for control of BDSC HCCI as well. Although an observer was omitted in this control scheme, and full state-feedback was assumed, this part must be re-considered before implementation on the real engine.

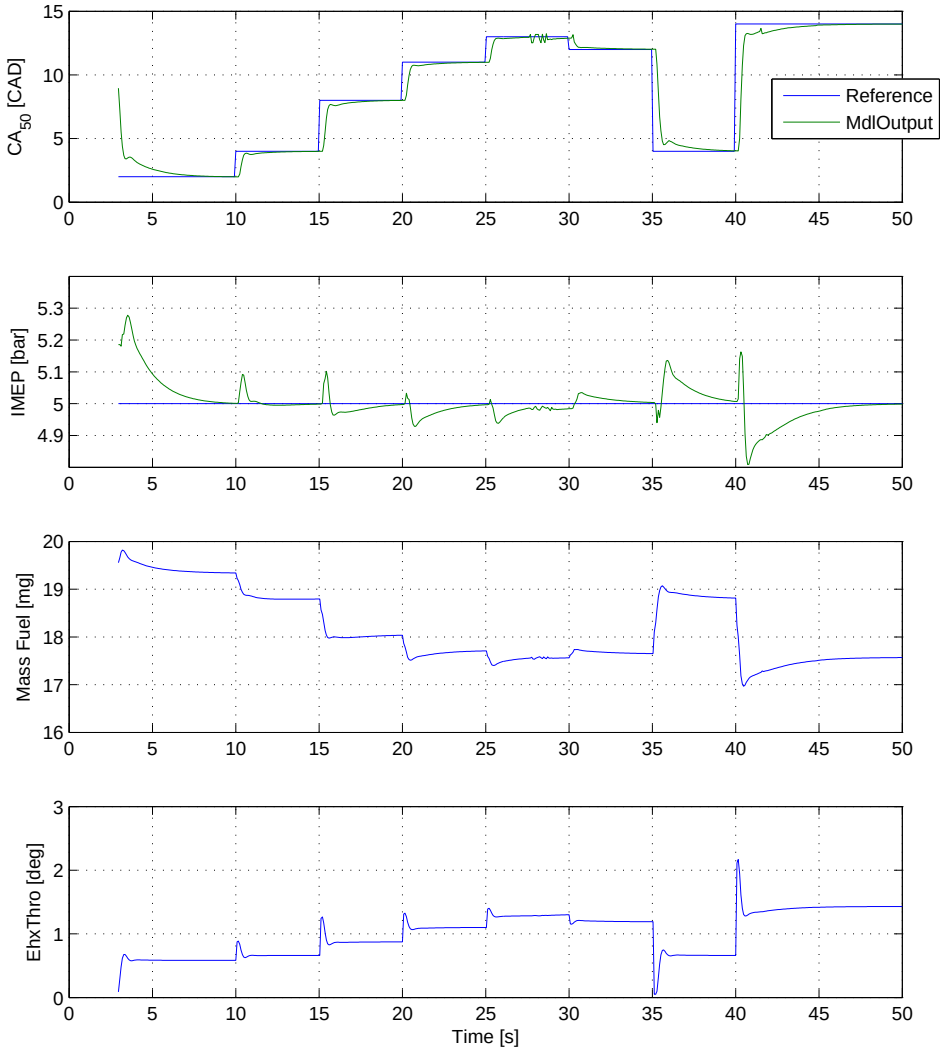

Figure 8.31: Closed-Loop Results on the 0-D model with SMC

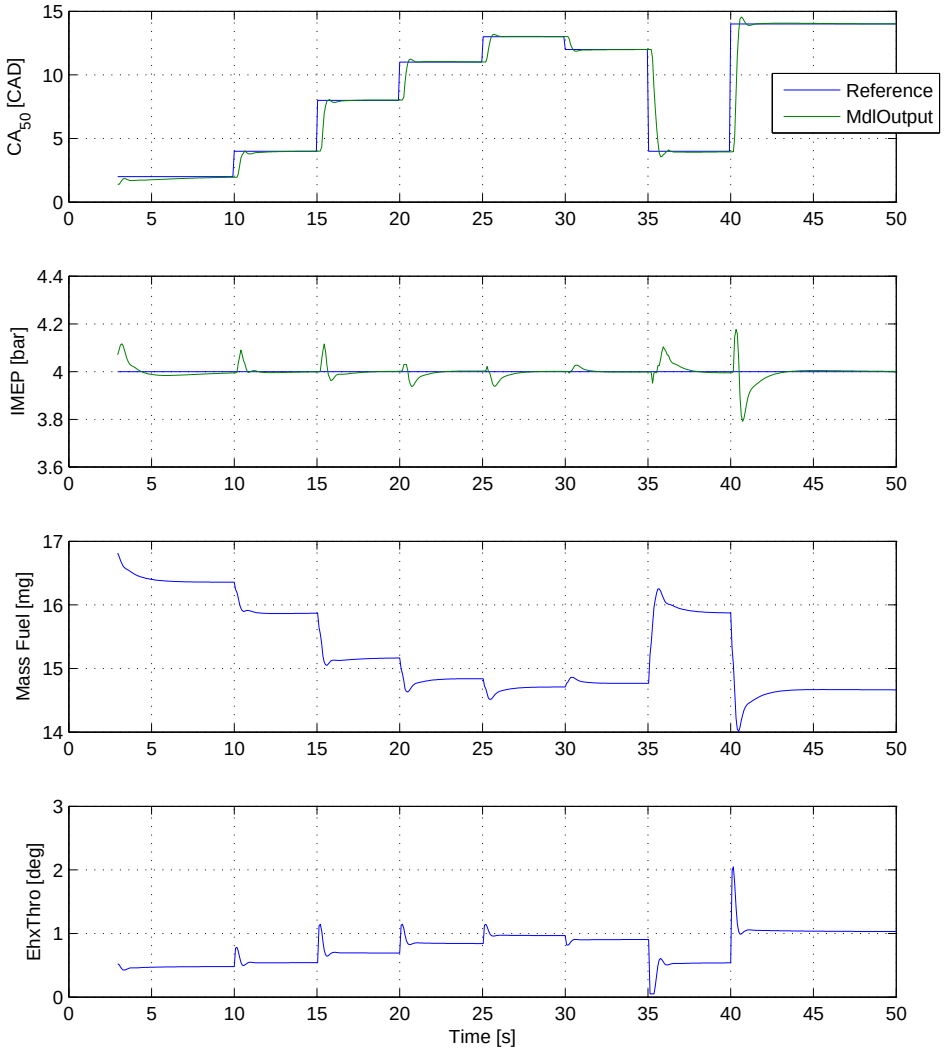

Figure 8.32: Closed-Loop Results on the 0-D model with SMC with a fixed $IMEP$ at 4 bar

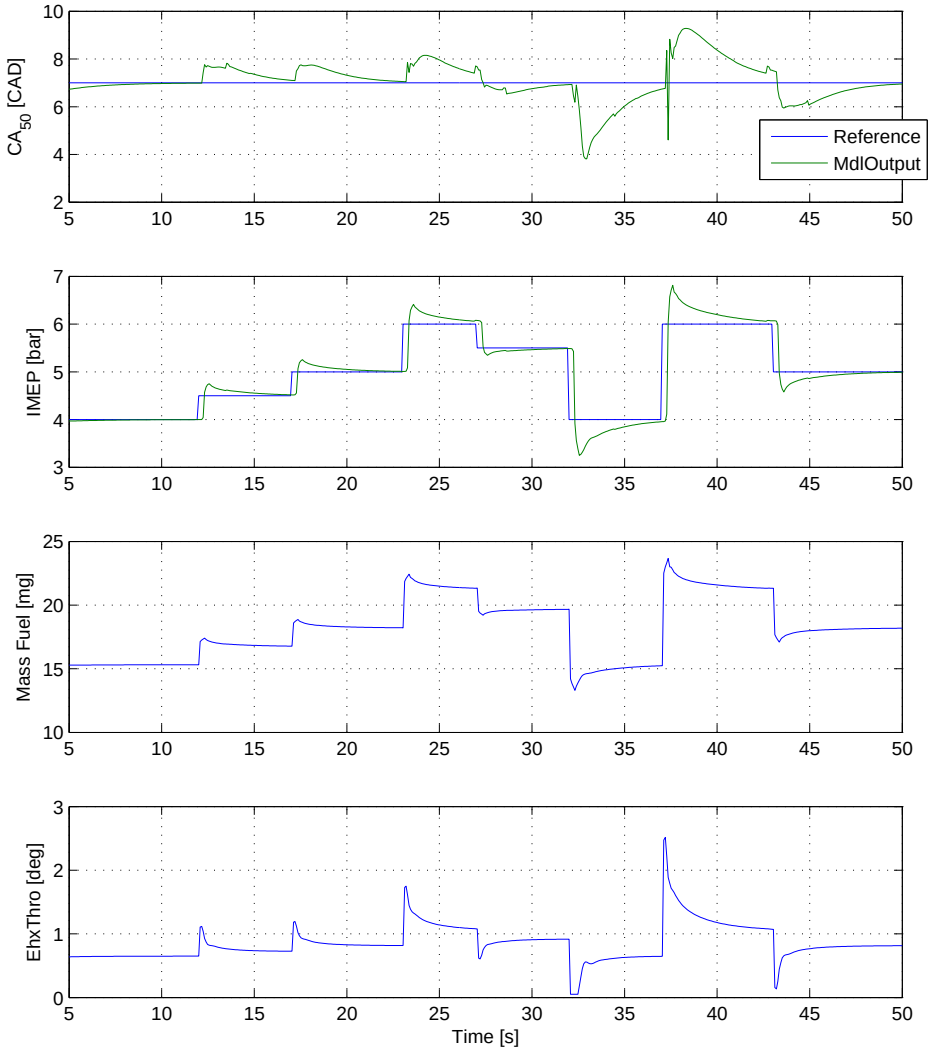

Figure 8.33: Closed-Loop Results on the 0-D model with SMC

Effectiveness of the Switching Term in SMC

In this section, the effectiveness of the non-linear switching term will be briefly analyzed. Since this term acts as an addition to the linear discrete-time state-feedback controller ([57]), it can be switched off if not required and may act as a supportive control term in order to alter the high transient of the closed-loop controlled system, while the actual core-controller, which is basically a linear state-feedback controller remains unchanged, as are the computed eigenvalues of the closed-loop system. Hence, the linear feedback control would keep its main characteristics, but its performance could be increased in critical situations, such combustion mode switch.
For this analysis, the Gao reaching scheme was utilized ([34]), and to avoid chattering, the signum function has been replaced by a smooth differential approximation ([28]), with -1 and $+1$ as upper and lower boundaries and defined as

$$sgn(\sigma) \approx u_\delta(\sigma) = \frac{\sigma}{\mid \sigma \mid + \delta} \tag{8.43}$$

for $\sigma = Sx$ and with a small constant δ.
The values for ϵ and q in equation 3.155 are:

$$\epsilon = \begin{pmatrix} 0.05 & 0 \\ 0 & 50 \end{pmatrix} \quad , \quad q = \begin{pmatrix} 1 & 0 \\ 0 & 0.1 \end{pmatrix} \tag{8.44}$$

Note that the ϵ term is the gain of the switching term, while the term q is not related to the signum function and is an additional term for the reaching phase. Therefore, in the Gao reaching scheme, the additional term also constitutes an additional linear term, which basically could be included in the overall linear control scheme. However, the additional tuning factor q hereby brings another degree of freedom in the control synthesis process and may help, if the basic linear controller does not give the desired fast transients.
Due to the feed-forward term of the controller for reference tracking, the equilibrium states are being shifted with every reference change and need to be canceled out in order to achieve a sliding motion on the sliding manifold at $\sigma = 0$. Hence:

$$\tilde{x} = x - x_{SS} = x - N_x r \tag{8.45}$$

The switching function is re-defined as $\sigma = S \cdot \tilde{x}$.
For the sake of simplicity, the analysis is carried out on the mean-value engine model.
Figure 8.34 shows a linear SMC controller without switching term. The tracking values for both, $IMEP$ and CA_{50} are shown in the first two plots and the two actuators in the third, while the switching function for both actuators is depicted in the last plot. These figures show again the aggressive tuning of the controller alone, which may mainly be attributed to the feed-forward control, but also on the feed-back term. Some stronger overshoots in combustion phasing can be seen, but also that the states have reached sliding motion within a few cycles, and remain there, despite disturbances due to tracking changes.
In figure 8.35, the same controller was augmented by the switching term after Gao, and with the tuning explained above, where the signum function was replaced by the continuous function 8.43. These plots show that the controller still acts fast for CA_{50}, but with fewer overshoots, while it somewhat slowed down $IMEP$. Inspecting the switching functions of the last plot makes clear that the reaching phase has slowed down overall. Figure 8.36 shows the same controller, but with the signum function for the switching term, which causes a strong chattering for

the exhaust throttle. Although this strong actuation may keep the states on the sliding manifold, this strong chattering causes also strong variations in combustion phasing, such that this control approach may be judged as unsuitable for HCCI.

As a concluding remark, it may be stated that the switching term can be a promising candidate for shaping the fast transients of a linear SMC controller, where an extremely aggressive controller could be moderated by a switching term that slows down the reaching-phase, or a slower controller could be made more aggressive. Consequently, a linear sliding-mode control with a switching term that can be deactivated brings more flexibility in the control design.
However, the observations made in this analysis confirm the statement of Hui and Zak ([57]) that for discrete-time sliding-mode controllers, the switching term becomes obsolete and should be utilized only if a compelling reason exists.

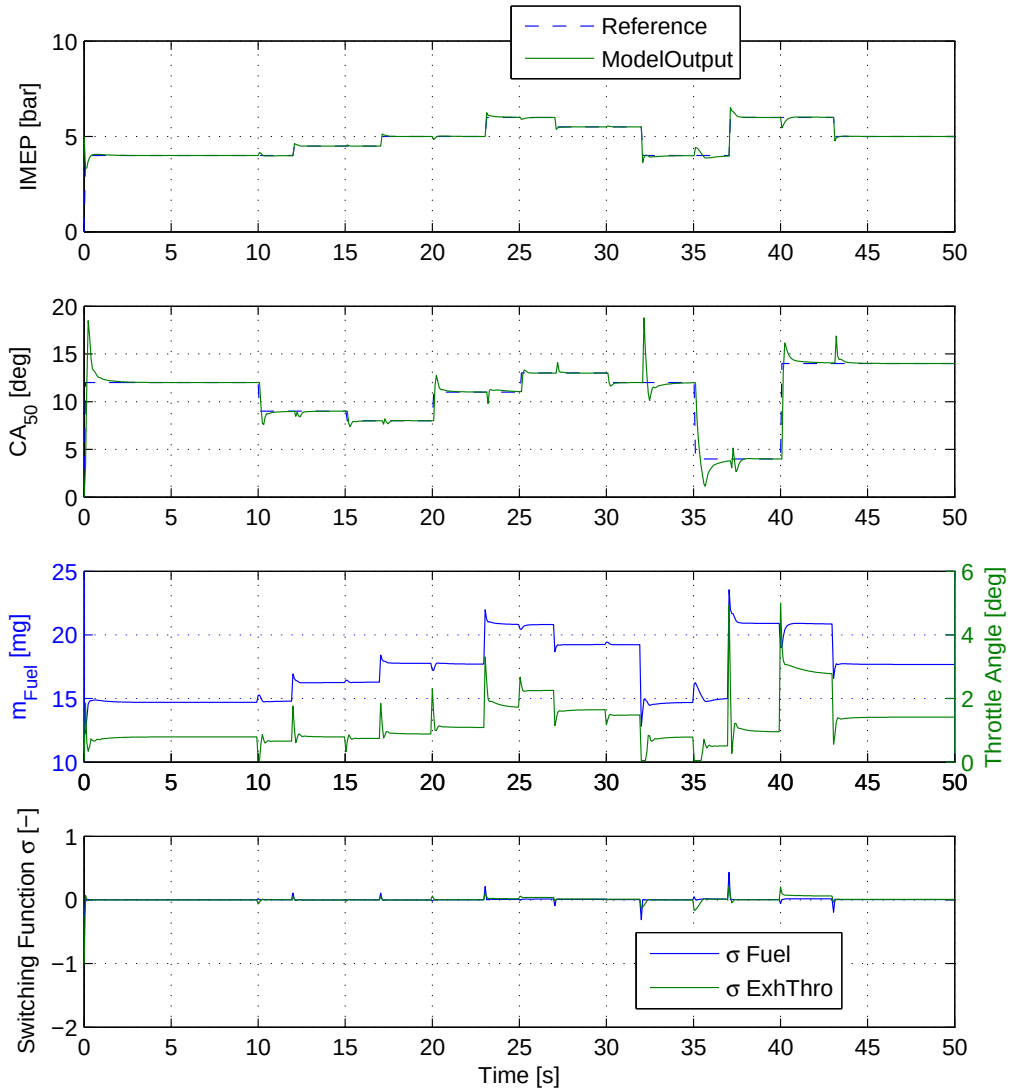

Figure 8.34: Closed-Loop Results on the MVEM with SMC without nonlinear switching term

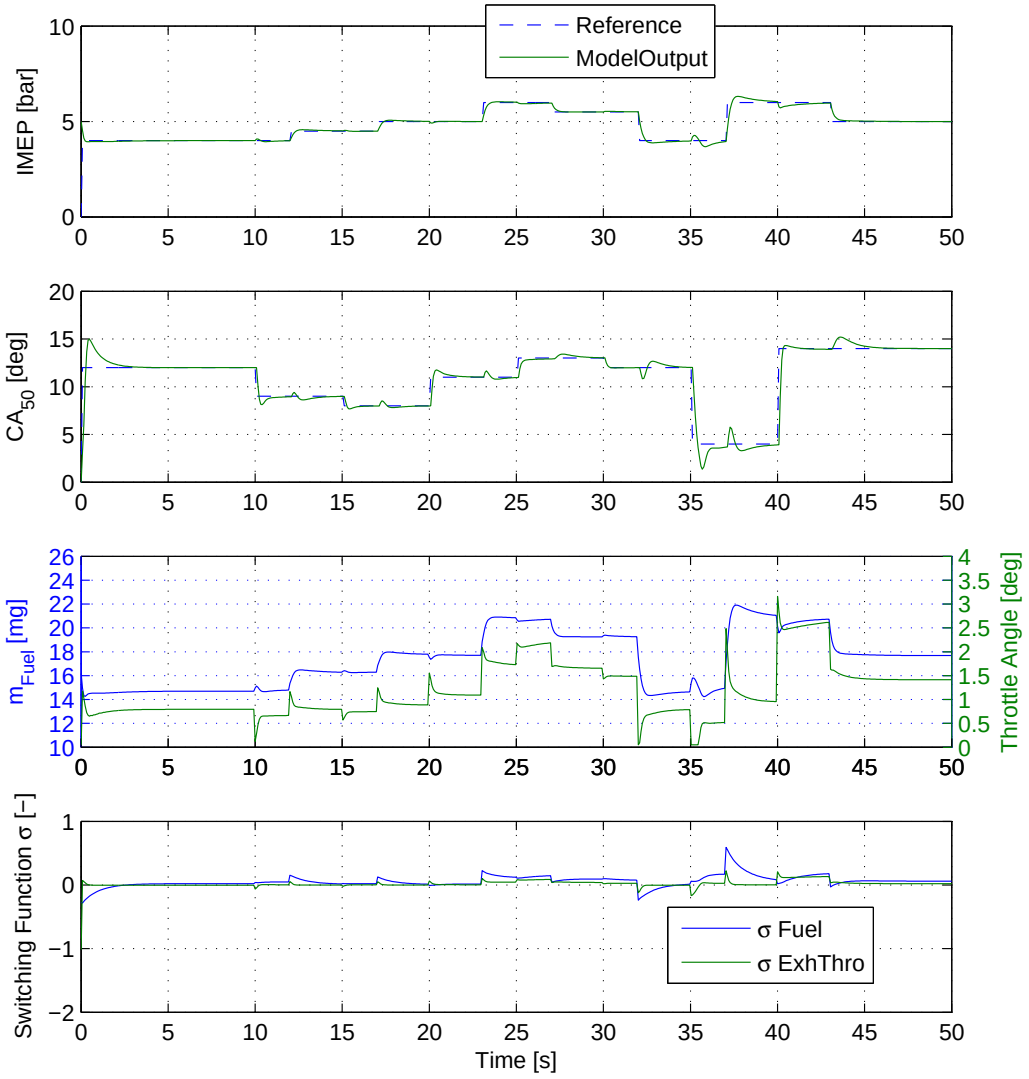

Figure 8.35: Closed-Loop Results on the MVEM with SMC with smooth approximation of the switching term

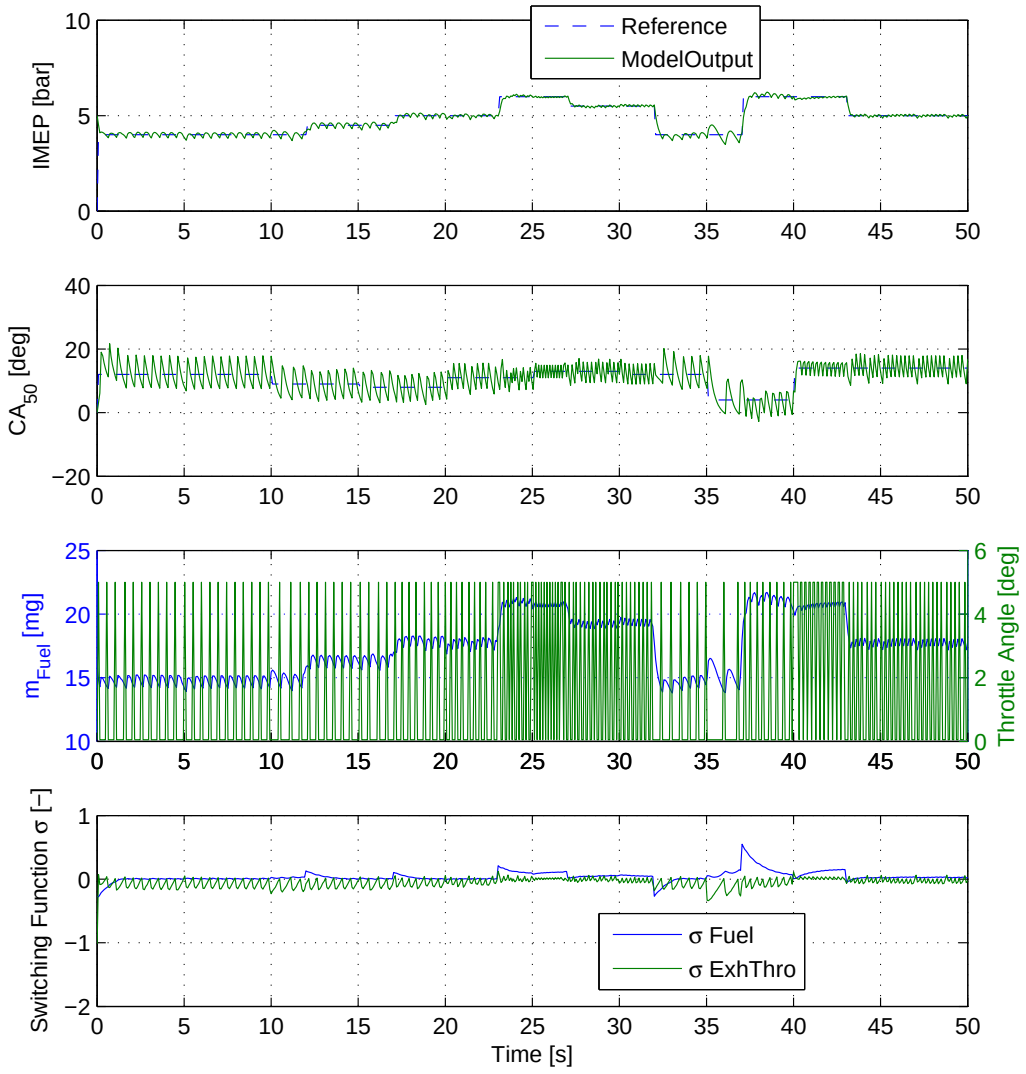

Figure 8.36: Closed-Loop Results on the MVEM with SMC switching term

Chapter 9

Combustion Mode Switch

Combustion mode switch between SI and HCCI is considered as a challenge, since the operating conditions of SI and HCCI are extremely different from each other. While HCCI can run in extremely lean modes, SI requires an air-fuel ratio around stochemiotry to ensure stable combustion. On the other hand, SI combustion becomes unstable if the EGR ratio becomes too high. Before a combustion mode switch with NVO system, the engine in SI mode has been driven up to 30% EGR before the actual switch. Common SI engines do not reach values higher than 10%.
Contrary to that, HCCI engines must be operated with high EGR gas contents to ensure that the temperature levels are high enough for proper ignition.
This fundamental difference between the two combustion modes makes the switch challenging.

9.1 Switch Considerations

HCCI and SI are conceptually different, as are the stable operating areas of both combustion modes.
In the previous sections it was introduced that stable HCCI requires enough amount of EGR, while at the same time it can be operated under unthrottled conditions at WOT. In fact, it is rather required to run HCCI in lean mode for dilution of the mixture and reduction of pressure rise rate, which causes audible noise.
Contrary to HCCI, SI requires tight intake air control which is confined by the amount of fuel injected. The air/fuel mixture should thereby not deviate too much from stoichiometric. Furthermore, EGR is introduced as a measure for reduction of raw NO_x emissions, but it is usually limited to 20% to avoid unstable combustion, and typically is operated at ratios less than 10%.
Therefore, a map can be drawn to illustrate the different operational ranges in dependency of air-to-fuel ratio and EGR ratio, which is depicted in the following figure 9.1.

Here, the range for stable SI combustion is shown in the lower left corner, and for HCCI in the upper right corner, where the air-to-fuel ratio is drawn at the bottom and the amount of EGR to the side.
Between the two operational ranges is an area, where neither stable SI, nor stable HCCI can be operated, and by inspecting this figure, it becomes intuitively clear that this unstable range has to be traversed during the switch, or if possible entirely avoided.

In the literature, several switching approaches have been presented, which have been gener-

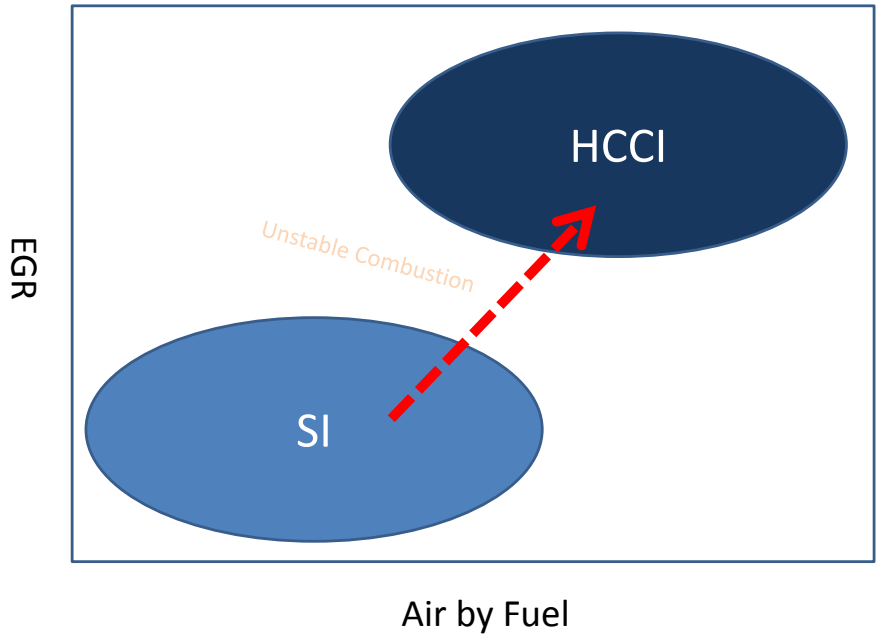

Figure 9.1: HCCI and SI Operation Maps

ally confined to open-loop controlled switches. This however may pose problems in terms of robustness of the switch, due to many and often unpredictable disturbances, such as torque variations, or changing atmospheric conditions, so that a closed-loop controlled switching scheme is deemed a better solution.
In the following sections, both open-loop switching strategies as well as closed-loop switches are presented, that have been reported recently in the literature.

9.2 Literature review

In the past years, several switching strategies have been presented in the literature, for both NVO and re-breathing systems, and both open-loop switching strategies as well as closed-loop switches are detailed in the literature presented in the following sections.

9.2.1 Open-Loop Switches

Hitachi

[72] analyzed the switching of a NVO HCCI. They first analyzed a direct switch from SI into HCCI and investigated the cause for the combustion instabilities. Not surprisingly, they found that the conditions of the first cycles are unfavorable for HCCI combustion. They found that the response times for EGR change are different than the air-fuel ratio, so that a compensation for this lag had to be included in the open-loop control strategy. They further identified stable SI conditions and their limits as well as stable HCCI limits and their conditions. It was shown that

there exists a gap between SI and HCCI, where neither stable SI, nor stable HCCI can be operated, and ideally this gap needs to be avoided. Their switching strategy consisted of steering the engine in SI to its boundary by first increasing the amount of EGR. In this region, the gap to HCCI has been found the narrowest such that traversing the gap might be the easiest. In order to reach HCCI combustion, the intake throttle was opened to increase the air-to-fuel ratio. With this strategy, the time response difference between EGR and air-to-fuel ratio can be minimized.

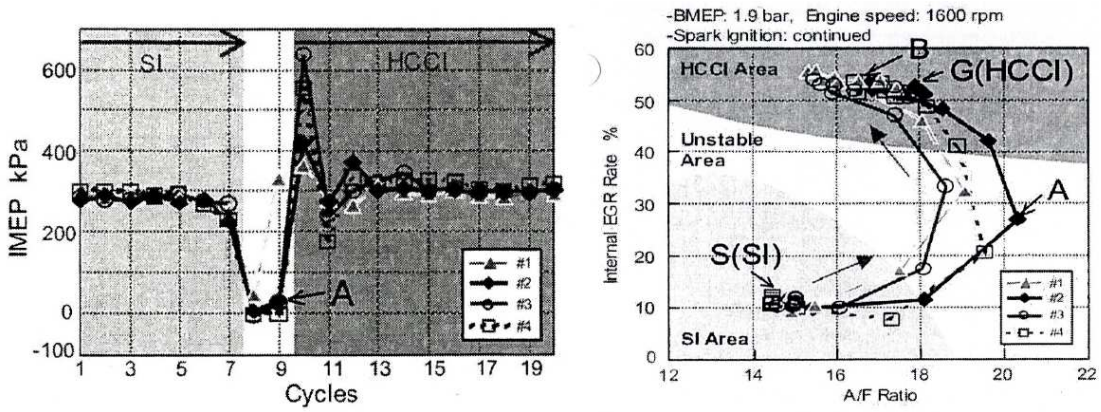

Figure 9.2: Results from a direct switch actuation from SI to HCCI ([72])

However, the subsequent cycles after SI were found a mix of SI combustion and HCCI combustion, which is not only unstable combustion but also difficult to control. Countermeasures were necessary to stabilize combustion in this region, which was utilizing double fuel injection together with the spark plug to promote HCCI combustion.
The overall switching has been demonstrated smooth although the control effort was quite large. Furthermore, the overall switching procedure took many cycles until stable HCCI was achieved.

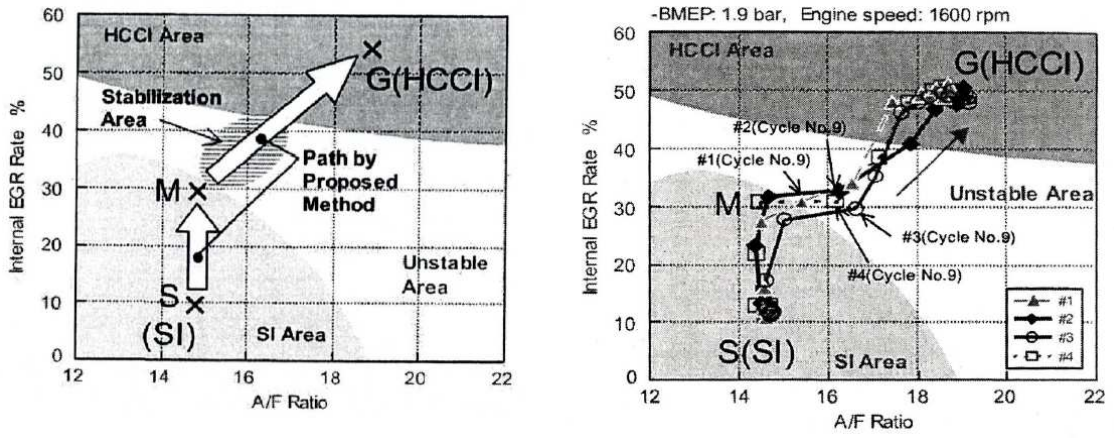

Figure 9.3: Proposed switching strategy for stable switch from SI to HCCI ([72])

Tianjinn University

Similar to the previous sub-section, researchers at Tianjinn University ([126]) analyzed a switch on an NVO system and reported similar combustion instabilities during the switch.

They defined an inversion point, which defines the transition from SI combustion to HCCI combustion within one combustion event in one cycle. This can be explained by an initial SI combustion which has been triggered by a spark, but due to the in-cylinder conditions closer to HCCI, this SI combustion becomes HCCI combustion, when the pressure and temperatures increase due to the initial SI combustion. This kind of hybrid combustion is also referred to as Spark-Assisted Compression Ignition (SACI), which can extend HCCI to much higher loads and holds a great promise to be implemented in future passenger cars.
The researchers concluded that for a stable switch, controlling this inversion point is necessary.

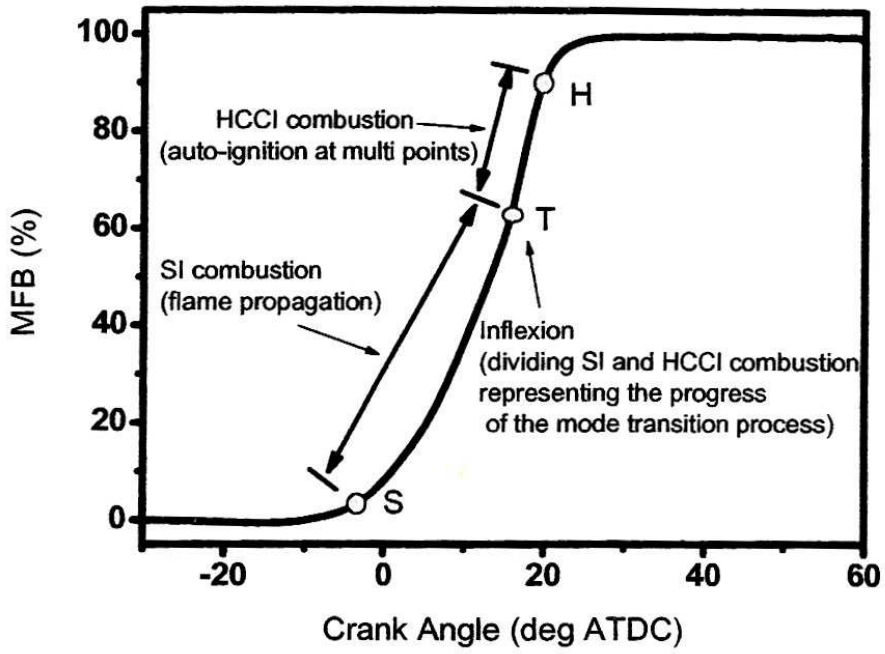

Figure 9.4: Definition of the Inflexion Point which marks the transition from SI combustion to HCCI during an combustion event ([126])

They conducted the experiments on a single cylinder engine with NVO strategy and mechanical, fully flexible valve sytem, which could be varied in lift and phasing for intake and exhaust stroke, which was taken from a Vanos system, and a Valvetronics sytem from BMW.
Three different operating points at different speeds (between 1000 and 3000 rpm) and loads (between 2.0 and 3.0 bar) were investigated where each of the points was at the edge of stable HCCI combustion.
By switching from SI to HCCI, it was observed that at higher engine speeds, it took around ten engine cycles until stable HCCI was observed. It was reported that high exhaust gases from SI would lead to early ignition timings in the first HCCI cycles, due to cyclic coupling. It was suggested, in order to keep the ignition timing at later crank angles, to precisely control the fuel-injection, spark timing, and to provide ultra-lean mixture.
During the switch, the inflexion point, as the point of transition between SI and HCCI combustion during one combustion even, was observed and it was stated that it is important to control the inflexion point during the mode switch. They observed that varying the spark timing did not have a remarkable influence on the inflexion point, but it was shown that the amount of EGR influenced the inflexion point. By increasing the EGR, it was observed that the inflexion point

moved towards start of combustion, and the HCCI part becomes bigger. However, at EGR ratios around 21% unstable combustion was achieved so that this EGR ratio was called RGF gap. By further increasing the EGR amount greater than 26%, it was shown that HCCI combustion dominated.
Therefore the authors concluded that for a successful combustion mode switch, the inflexion point had to be controlled by dynamically controlling EGR and by designing a hybrid release model which was not further elaborated.

University of Cambridge

A switch similar to that one from Hitachi was reported at University of Cambridge ([43] [69]), where an NVO system was utilized with two-stage cam profiles and double fuel direct injection. It was reported that a switch from SI to HCCI was possible within one cycle, while switching from HCCI to SI revealed some NIMEP fluctuations due to the delay in VVT shifting and a relatively slow change in MAP.
As a first test, the the engine was switched from SI to HCCI within one cycle, where it was observed that also the MAP increased within one engine cycle, starting from 5% WOT. Contrary to that, the transfer of the VVT system took approximately three engine cycles. This caused abnormal high AFR (air to fuel ratio), and insufficiently low EGR, which was too low, which resulted in large fluctuations in NMEP.
As a countermeasure to that, the intake throttle was delayed to reduce the excessive amount of AFR. Simultaneously, fuel injection was controlled. By using the spark, some cycles with initial SI combustion and HCCI combustion later in the compression stroke were detected.

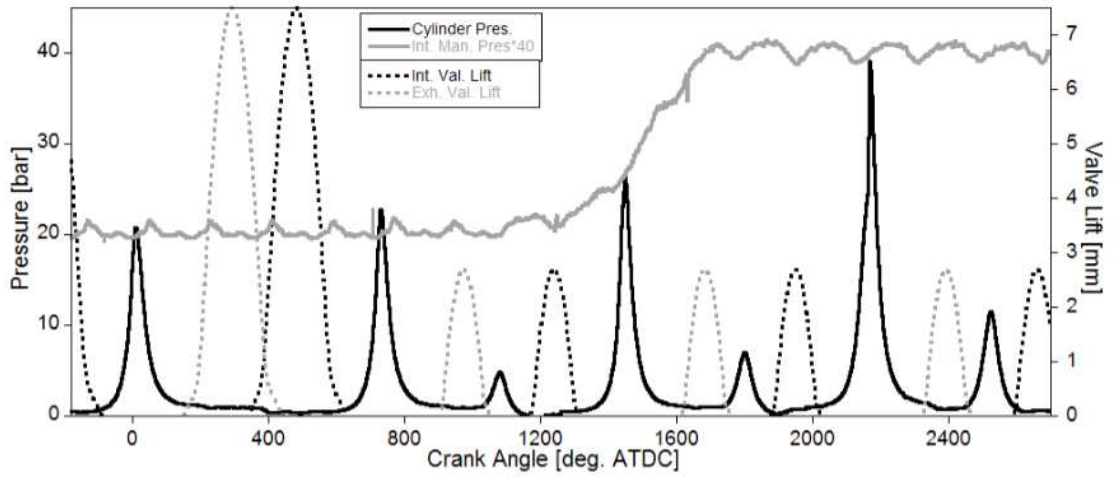

Figure 9.5: Valve Lift and pressure traces of cylinder and intake during the switch from SI to HCCI ([69])

By first moving the cylinder states to higher EGR of 32%, and by controlling hybrid SACI combustion during the switch, a smooth SI to HCCI transition could be accomplished in experiments and a simulation model that was able to simulate SACI.
This switch, together with the spark assisted HCCI, could be also investigated in simulation with a sophisticated simulation code using a so-called stochastic reactor model that was reported to

run in real-time. The results of the switch are shown in figure 9.5.
With the high EGR rate during SI and before the switch, together with the combustion stabilization measures, such as spark assist, this switching strategy resembles that of Hitachi considerably.

Robert Bosch GmbH

[120] analyzed in experiments are switch for an NVO HCCI. It utilizes closed-loop control, but only when the switch is completed.
Fuel injection timing was used to control combustion phasing so that a cylinder-individual control was possible. Exhaust valve closing time (EVC) was additional used for combustion phasing control, which however was not individual for each cylinder. Electro-hyrdraulic cam phasers with a two-stage valve lift switching with 4mm for low and 10mm for high was utilized in this 4-cylinder engine.
The noise during combustion change was recorded in a silence chamber, with optimized walls and floors, and by using six microphones.
Switching was done at 2000 and 3000 rpm and an $IMEP$ between 2 and 4 bar. The residual gas fraction (EGR) was for SI 10.1% and for HCCI 44.6%.
It was reported that for a stable combustion mode switch, a strategy for throttle, injection timing and valve lift switching was necessary. Additional ignition timing had to be calibrated which was considered more significant for higher loads. As a bottleneck, the time delay properties of the cam phasers, due to oil pressure transients, pulsation effect, and engine speed. For that reason, a two-step calibration strategy (pre- and post-step) was reported to deliver satisfactory results.
The pre-step was to move to the target combustion mode as fast as possible, by dethrottling the intake manifold. Thereby, the last SI was run as lean as possible.
During the post-step, the burn duration had to be increased to limit the pressure rise rate. This was influenced by fuel injection during the re-compression stroke, which reduced the in-cylinder temperature, due to evaporation and creating inhomogenities. By increasing the number of injection events during re-compression, the peak pressure could be shifted to later cycles, but the pressure peak could not be reduced. To reduce the pressure peak, the injection timing was advanced during re-compression.
This, ultimately, resulted in a switch with decreased combustion noise.

Stanford University

A team at Stanford University [86] analyzed a switching strategy in simulation of an exhaust re-breathing HCCI. Unlike the re-breathing HCCI presented in the introduction, where the exhaust valve re-opens during the intake stroke, the strategy is a little bit different here. In this engine, the exhaust valve remains open after the exhaust stroke and partly during the intake stroke to breath in exhaust gas from the exhaust port. The engine that had been modeled was equipped with a fully hydraulic valve system, which allowed for a direct switch between steady-state SI valve profiles, and steady-state HCCI valve profiles.
The cam profiles for SI and HCCI are shown in the following figure:

The analysis was carried out on a 0-D simulation model and a direct switch (”hard switch”) was simulated. It was shown that ignition advanced excessively during the first cycles, and it was assumed that this was due to the hot exhaust gases that were carried over from the last SI

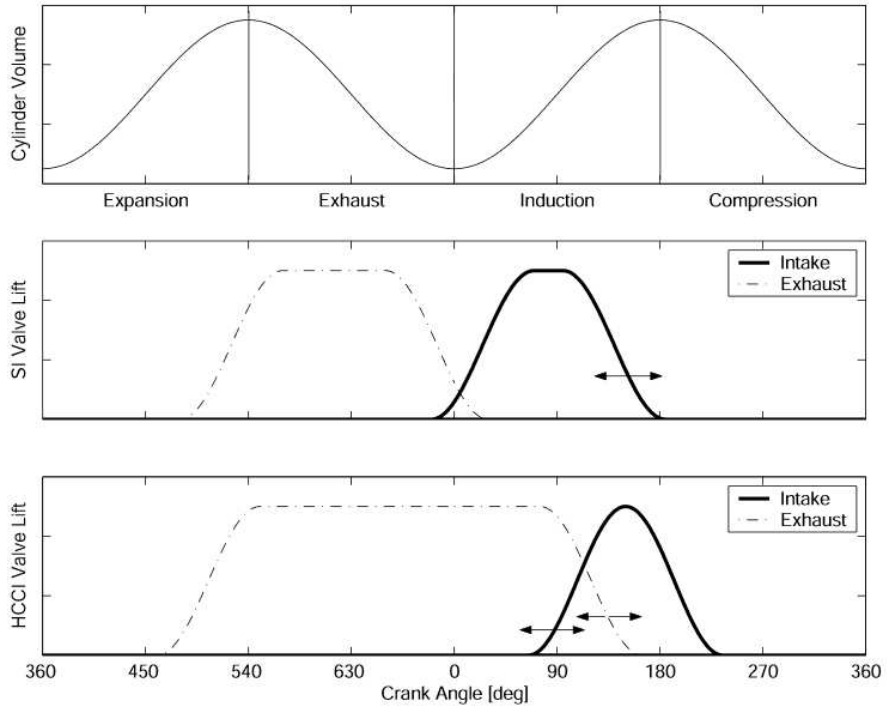

Figure 9.6: Valve Lift and Actuation of a Re-Breathing HCCI ([86])

cycle.
In order to shift ignition to later values, it was concluded that the amount of EGR had to be controlled dynamically during the switch. Therefore, the exhaust valve closing time was advanced during the first cycles to earlier phasings to avoid an excessive amount of EGR and to keep combustion phasing in a desired range. At the same time, the intake valve was actuated as well to limit the amount of fresh reactants to be drawn in and thereby the work output of the engine.
The result of this switch was that too early combustion could be avoided during the first cycles, and that the overall switch could be stabilized.
The results from the simulation model are shown in Figure 9.8. Here the last SI cycle is shown, with low peak pressure, and the first HCCI cycle with a desired phasing, such that the combustion does not occur too early. The subsequent cycles move towards steady-state, until a peak pressure of more than 50 bar is reached. It is shown here that the overall switching process in order to compensate for the exhaust gas dynamics took around four cycles.

The authors concluded that such a open-loop scheduling would be difficult to design for each single operating point and that a closed-loop control scheme would be a better solution for a robust combustion mode switch.

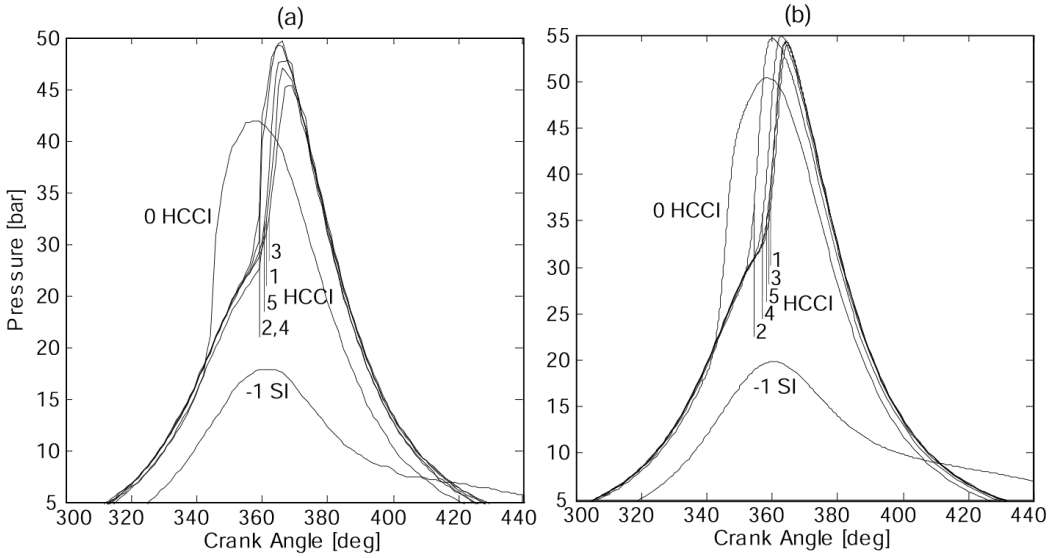

Figure 9.7: Comparison of a hard switch of experiments (a) and results from simulation (b) of a Re-Breathing HCCI ([86])

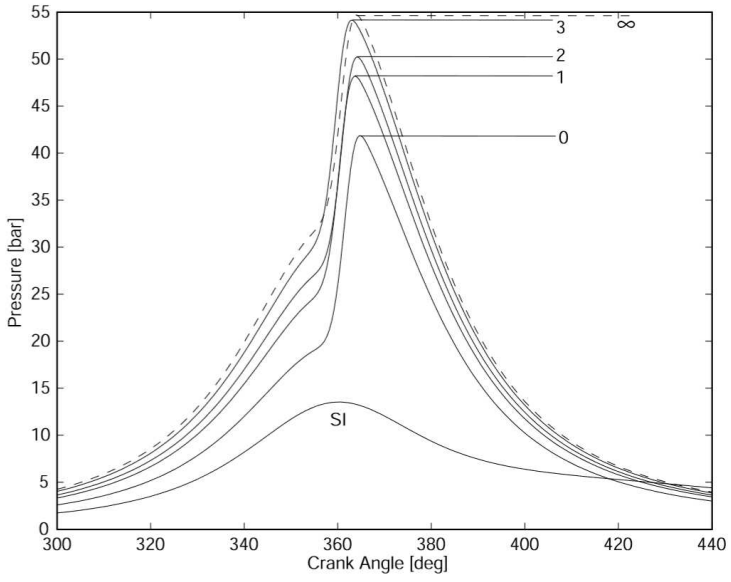

Figure 9.8: Successful smooth switch from simulation of a Re-Breathing HCCI ([86])

9.2.2 Closed-Loop Switches

Lund University

First attempts of using a closed loop controller directly for the switching process was reported at Lund University ([7]). The HCCI engine employed here was a NVO system, with fully flexible hydraulic valve actuation. A closed-loop LQR state-controller was designed to control combustion phasing as well as the IMEP and it was switched on a few cycles after the first HCCI cycle. In order to compensate for excessive amount of fuel burnt, due to fuel wall film effects, the port fuel injector was switched off for one cycle before the switch.
The MIMO LQR controller with a Kalman-Filter was compared to PI controllers, of which two were used separately for control of combustion phasing and $IMEP$ during the switch. The actuation is hereby mass fuel and NVO. The LQ controller was designed by system identification. While the model-based controller would be switched on three cycles after the switch, the PI was activated one cycle later than that, namely after four cycles.

The experimental results with the two PI controllers are shown in Figure 9.9.

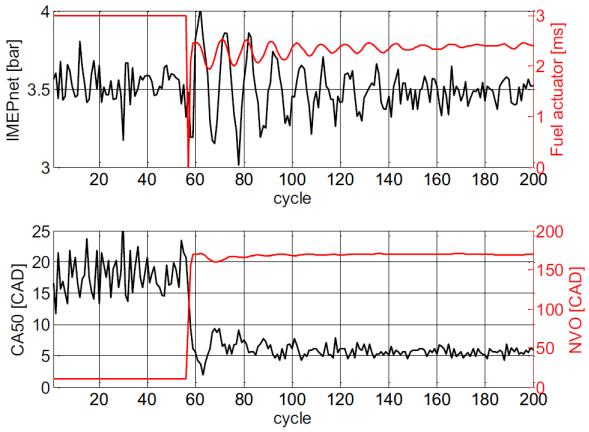

Figure 9.9: Closed-loop controlled switch with two PI controllers of and NVO HCCI ([7])

Here it can be clearly seen that the controller tends to oscillate in amount of fuel injected, while this obviously also affects combustion phasing which oscillates too. It is hereby obvious that both controllers do not work satisfactorily together and that the NVO controller is not able to reject the disturbances which come from the fuel injected.
Although no abnormal combustion (too early or late) cannot be detected in this plot, the overall switch cannot be judged as successful due to the instabilities that arose and the high variations in $IMEP$.

In comparison to that, the model-based LQ controller has been tested on the engine. The results are shown in Figure 9.10.

Additionally, the fuel injection was stopped for one cycle to compensate for the fuel film dynamics and the controller was switched on after three cycles.
These plots display a significantly smoother switch where no fluctuations are observed. In fact the smooth transition of combustion phasing can be judged as superb where it reaches quickly a steady-state phasing with no remarkable undershoot.

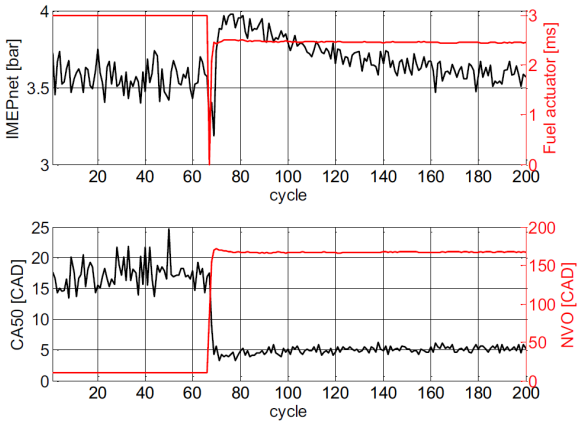

Figure 9.10: Closed-loop controlled switch with the model-based controller of and NVO HCCI ([7])

As for $IMEP$ on the other hand, it is apparent that it first drops, which may be due to the fuel injection deactivation, then remarkably overshoots of about 0.5 bar from the set-point. After this a slow convergence of more than eighty cycles can be seen, while combustion phasing can be successfully kept on its desired value.

Possible improvements in control design were addressed and it was concluded that using a direct injection would give greater control authority and more precision than a port injector with the deactivation strategy.

Robert Bosch RTC

A closed loop switch was also attempted at Bosch RTC [100] in a research with the author on a single cylinder engine with fully flexible hydraulic valve actuation and direct injection.
In a previous work, a closed-loop control concept for controlling of combustion phasing by varying injection timing during re-compression was already reported in [95] and [96].
The same control concept has been utilized and refined and in order to feedback the first signal for HCCI, a state observer for in-cylinder temperature and oxygen has been devised and included in the controller. The HCCI controller was then switched on on the first HCCI cycle in order to stabilize combustion during the switch. At the same time, the intake and exhaust valve were gradually moved cycle-by-cycle to attain a negative overlap position after the switch. The movement of the valves during the switch were included as a known disturbance into the closed-loop controller.
The overall feed-forward and feedback controller was implemented in a real-time prototyping system and tested on the single-cylinder engine.
Although a bit of SACI combustion was found during the switch, for which no control existed, the controller performed well and at different operating points.
Figure 9.11 shows the pressure traces of the open-loop controlled switch, where some cycles with too early combustion can be seen together with strong ringing. In this switch, the valve timings for both, intake and exhaust were opened gradually, until steady-state HCCI is achieved and injection timing was kept fixed.
In the closed-loop case, where the valve timings were still controlled in open-loop, but the in-

jection timing closed-loop control was switched on during the switch, a much tighter range of the pressure traces can be found, with much less ringing, which shows the advantage of a closed-loop system for combustion phasing during the control switch.

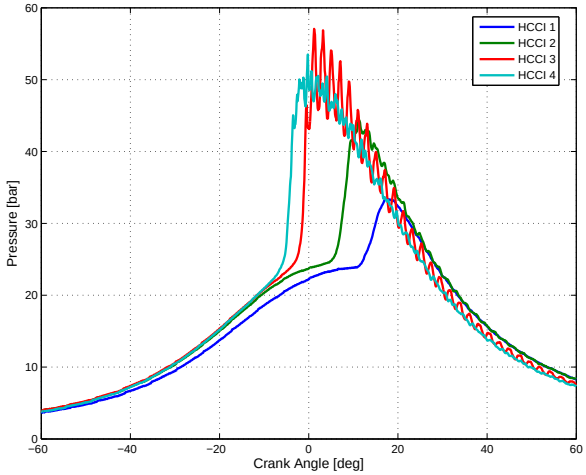

Figure 9.11: Pressure Traces of the open-loop controlled switch ([100])

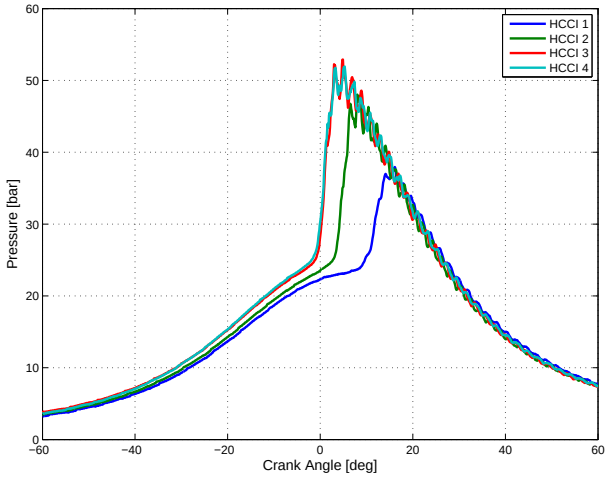

Figure 9.12: Pressure Traces of the closed-loop controlled switch ([100])

Michigan State University

A closed-loop control concept was presented and tested in a simulation environment at Michigan State University [127]. The model used for the analysis was a control-oriented 0-D model that capable to simulate spark assisted compression ignition (SACI) by implementing a two-zone combustion model, which was denoted here as hybrid combustion. The model was prepared for real-time simulation so that a physical control unit could be tested in a hardware-in-the-loop (HIL) environment.

The engine under investigation was a NVO HCCI engine, with a two stage cam shaft with two distinct valve timings and lifts for the intake and exhaust valve, with external cooled EGR, and both port fuel and direct injectors.
The controller has been split into an individual cylinder $IMEP$ control via injection duration consisting of a feed-forward controller and a PI feedback law. The feed-forward controller was tuned automatically by a self learning algorithm, which could be done during cruising in engine steady-state operation or during the calibration process. This self-learning algorithm ensured precise tracking of the required $IMEP$.
In addition to the $IMEP$ controller, it was required to control the air-to-fuel as well in order to ensure stable combustion during the hybrid combustion cycles. Since it was assumed that the air drawn into the cylinder can be estimated online by knowing the intake valve closing volume of a cylinder and by assuming the intake pressure inside the cylinder. Therefore, it was decided to control the intake manifold absolute pressure (MAP) for an indirect control of the air-to-fuel ratio. By using a simplified MAP simulation model an LQI controller was synthesized to track the desired MAP.
Several hybrid cycles were found during the switch and an HCCI ratio x_{HCCI} between 0 and 1 was defined where 0 was pure SI combustion, and 1 was pure HCCI combustion, with values between 0 and 1 denoting hybrid combustion.
A direct switch from SI to HCCI was simulated such that the x_{HCCI} ratio jumped from 0 to 1 within one cycle, which brought unstable combustion and severe $IMEP$ drops due to the response time properties of the intake and exhaust cams. In order to show the significance of hybrid combustion during the switch for the overall stability of the switch, an open loop test has been performed and a transition through several hybrid cycles enforced by scheduling spark timing, external EGR valve opening, intake and exhaust valve timing and lift. This measure could stabilize $IMEP$ during the mode switch.

University of Michigan

Another closed-loop controller for the switch from SI to HCCI was presented at University of Michigan [104]. The engine under investigation was a recompression internal EGR (NVO) gasoline. This paper addresses the fact that so far, combustion mode switches were only a combination of open-loop switching strategies, with closed-loop control aid. It was claimed that a combustion mode switch often involves a complex actuation of many control inputs which have a mutual influence through cross-coupling between inputs and outputs so that the control strategies are complex. Therefore, an open-loop scheduled switching strategy may work well in one operating point but may become impractical at other operating points so that it becomes difficult to cover the entire range of possible switching conditions.
The base model is a mean-value engine model that was able to simulate SI and HCCI combustion.
The controller was designed to track, among others, a reference intake manifold pressure since the in-cylinder mass-flow is mainly determined by the intake pressure and the target values were read from tables. This should ensure fast transients of the air-to-fuel ration during the switch. Additionally the air-to-fuel ratio λ had to be closed-loop controlled, as well as net mean effective pressure ($NMEP$) and combustion phasing CA_{50}.
This gives the following reference vector:

$$r = \begin{pmatrix} p_{In} \\ NMEP \\ \lambda \\ \theta_{50} \end{pmatrix} \tag{9.1}$$

It should be noted that controlling λ at higher values during the last SI cycle may be desired to reduce the amount of hot EGR for the first HCCI cycle and to avoid excessive amount of fuel when the intake pressure rises.
The chosen control inputs are: throttle angle ϕ_t, fuel mass m_f, positive valve overlap PVO and start of fuel injection ϕ_{SOI} during HCCI mode. The input vector therefore becomes:

$$u = \begin{pmatrix} \phi_t \\ m_f \\ \phi_{sp} \\ PVO \\ \phi_{SOI} \end{pmatrix} \tag{9.2}$$

The model has been linearized around the intended steady-state operating point after the combustion mode switch, and a linear LQI controller was designed.
The controller was tested in simulation, and the results of the switch are shown in figure 9.13, with a comparison between open-loop and closed-loop switch.

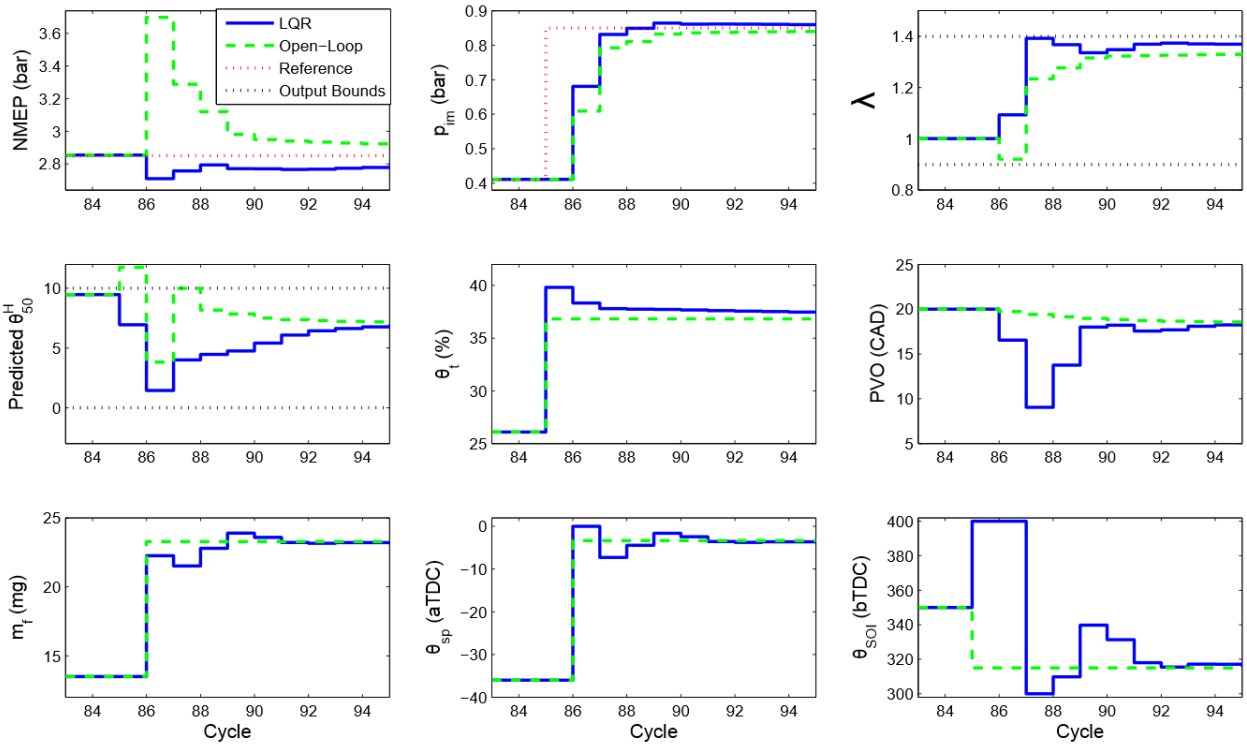

Figure 9.13: Comparison of Closed-Loop switch and open-loop controlled switch ([104])

The open-loop switch is shown in dashed green, while the closed-loop switch is shown in blue.

9.3 Switch Considerations for BDSC HCCI

Switching from SI to HCCI is a challenge, not only due to the different combustion modes, but also a highly dynamics process where control of combustion phasing becomes difficult.
Typically, the exhaust temperature during SI cycles are higher than in comparable HCCI cycles so that if the normal amount of EGR is trapped inside the cylinder, the ignition would be much more advanced due to the hotter mixture. With the subsequent cycles, the temperature would decrease until steady-state HCCI is achieved.
The following section investigates what control actuation may be required to facilitate a smooth combustion mode switch for a BDSC engine.

Combustion Model Analysis

In this section, the question on what in-cylinder contents need to be controlled during a combustion mode switch is investigated and was published in [90].
During the switch, starker transients in in-cylinder conditions than in normal transient operation of an HCCI engine may occur, due to the strongly varying intake pressure, as well as strongly varying exhaust pressure in case of BDSC HCCI and other possible influences. The question arises here: what in-cylinder conditions would lead to premature combustion, and what cylinder conditions would lead to delayed combustion (or misfire)? It remains unclear whether, for example, a very high air-to-fuel ratio could compensate the high exhaust temperatures from the last SI cycle and to attenuate abnormal combustion.
The ignition model presented above, which was derived from the ignition delay correlation 6.32, was used for the analysis of the ignition conditions, which reads:

$$KM = \int_{\theta}^{\theta_{ign}} A_{pre} \cdot P^{B} \left(\frac{F}{G}\right)^{C} \left(\frac{A}{G}\right)^{D} exp\left(\frac{-E}{R \cdot T}\right) d\theta \tag{9.3}$$

where A_{pre} is a pre-exponential factor,F and A, the mass of fuel and air respectively and G the total amount of gas inside the cylinder. E is the activation energy, R the gas constant, and T the in-cylinder temperature. During simulation, ignition is defined as the point during the compression phase when the integral in equation 9.3 reaches a pre-defined constant KM, which served here as a tuning factor for the model.
The ignition model presented here has been used in HCCI switch considerations so that it is assumed that it can be used for switching analysis.
In this equation, it can be seen that ignition depends on in-cylinder pressure and temperature, as well as the gas composition, consisting of air-to-fuel ratio A/G and fuel-to-gas ratio F/G. By inspecting this equation alone, it is not entirely clear what variables are really influential and whether variables can be entirely ignored by calibration a switching strategy.
The model used here is the BOOST 1-D engine model, as introduced above, and the ignition model was included in a BOOST function, which is written in a programming language that resembles the language C. As a default integrator was not included in the software, a numerical trapezoidal scheme was implemented in the user code. The wall-heat transfer model was selected as the Hohenberg, which suits HCCI better than the standard Woschni, as presented in [55], and the intake and exhaust pipes were modeled as in a reference model, provided in the simulation software suite GT-Power. The injector was implemented as a port fuel injector, and two cylinders of the overall four were deactivated by deactivating gas exchange and fuel

injection for the affected cylinders.
In order to tune the ignition model as presented above, a single cylinder model was developed as well, which was "cut-off" on the intake and exhaust side, at around $700mm$ away from the cylinders, where measurements of the intake and exhaust pressure were applied as boundary conditions. Thereby, the influence of the intake and exhaust model were excluded. For combustion, a standard single Wiebe function was used, with the ignition model presented above, and the combustion duration directly taken from the experiments for each considered case. Flow discharge coefficients were taken as provided from experiments without any further manipulation.
The following figure shows the steady-state cases it was tuned for in comparison with the experimental data.

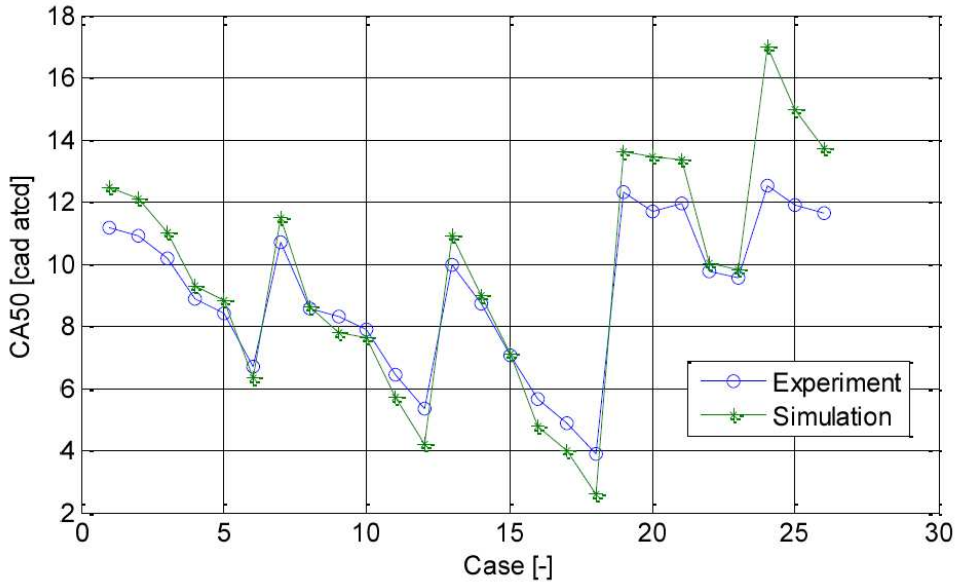

Figure 9.14: Step Input of the linearized system

The results show a fairly good match with experimental data such that it was considered that this ignition model suits an ignition analysis.
In order to clarify the ignition influence problem, an analytic analysis has been carried out on the ignition model 9.3.
First, the sensitivity of the ignition model was investigated where the normalized sensitivity of a function is defined as in [60]

$$S(u) = \frac{u_{OP}}{y_{OP}} \cdot \frac{\partial y}{\partial u} \tag{9.4}$$

where u is the input of the considered function, and y the output. The underscore denotes the considered operating point, which is necessary for normalization. The necessity of normalization becomes clear if one considers the different magnitudes of the variables. Pascal as an example, is much higher than Kelvin.
For analysis of the ignition model, the inverse integrand was analytically investigated with the MATLAB Symbolic Toolbox (MuPAD).
The outcome of this analysis is shown in figure 9.15:

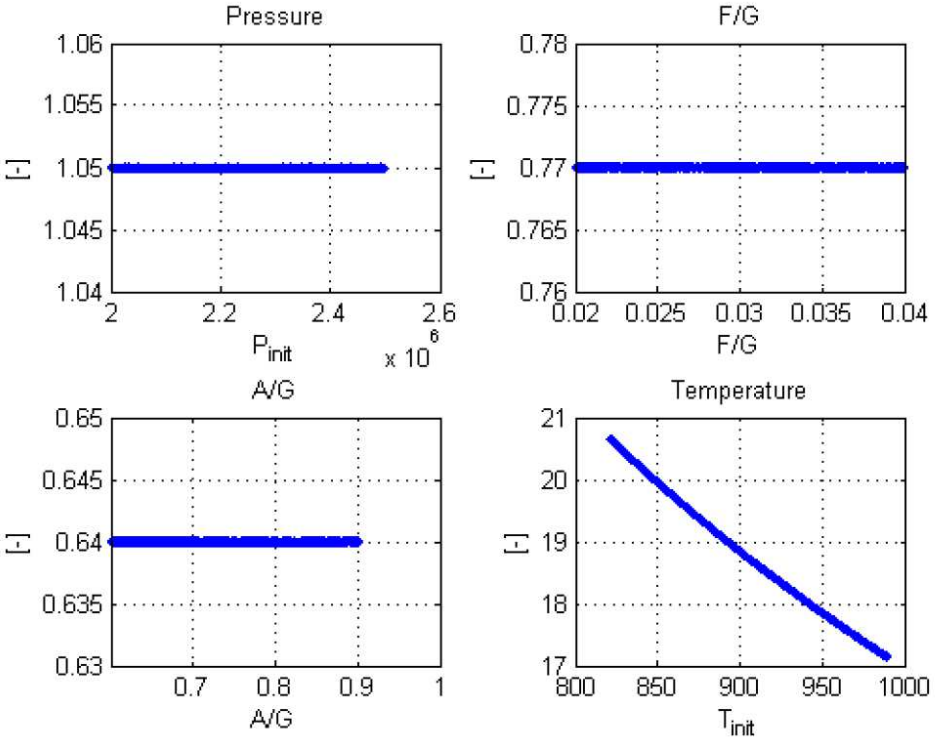

Figure 9.15: Sensitivity analysis of the ignition model

Here, the upper left figure shows the sensitivity of the pressure term in the ignition model in dependency of the considered pressure range. The upper right the sensitivity of the F/G ratio and the lower left the A/G ratio. The temperature sensitivity is shown in the lower right plot. Unsurprisingly that for pressure F/G and A/G term the sensitivity is constant, as they correspond to their respective exponents in the equation. It is also apparent that the pressure has the highest sensitivity of all those three variables, and the A/G the lowest. Therefore, it may be concluded that the gas composition terms F/G and A/G can be ignored. Contrary to that, the temperature sensitivity is not only varying and decreasing with higher temperatures, it is also up to 21 times higher than the pressure sensitivity, which implies the strong temperature influence on ignition. With this in mind, it seems clear that temperature is a key factor for controlling combustion. It is however not clear whether pressure for example could compensate for abnormal temperatures which would cause abnormal combustion.
For calibration of a open-loop switching algorithm, it would be desirable to have the in-cylinder condition target to ensure stable combustion for each switch.
For the analysis, the compression part of the control-oriented mean-value model as presented above was utilized, and the ignition model was included with a trapezoidal integration scheme. This is different from the control-oriented model above, where no integral was used for prediction of CA_{50}. Integration has been commenced at $40deg$ BTDC, which is a point during compression where it can be expected that not much fuel has been converted yet.
In order to conduct a useful analysis of the switching model, a Monte-Carlo approach has been utilized in which initial conditions at 40 deg BTDC were randomly set.
The range for these variables at $20deg$ BTDC is given in table 9.1. For integration from $40deg$ BTDC, the values have been back-calculated from the values in the table, by using polytropic

expansion 7.7 and 7.6.

Variable	Range
In-Cylinder Temperature (at 20BTDC)	790.0 - 870.0 [K]
In-Cylinder Pressure (at 20BTDC)	20.0 - 25.0 [bar]
Air/Gas	0.6 - 0.9 [-]
Fuel/Gas	0.02 - 0.04 [-]

Table 9.1: Ranges of the variables for ignition model investigation

The following figure 9.18 shows the result of this analysis in scatter plots, where the arrangement of the sub-plots are the same as in the sensitivity analysis, with the pressure on the top left, the F/G on the top-right, the A/G on the bottom left, and the temperature on the bottom right.

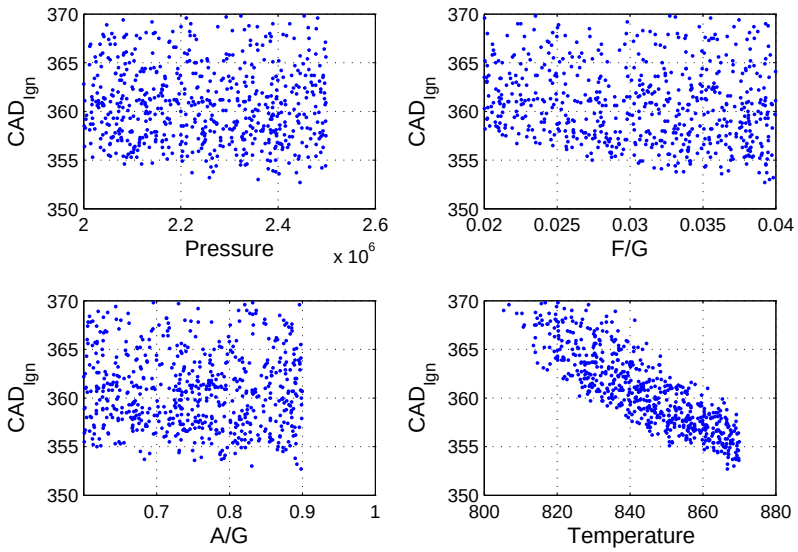

Figure 9.16: Scatter Plot of the ignition model analysis

In these plots, a real trend cannot be seen in either pressure, F/G nor in A/G. It seems as if none of these variable has such a great impact on ignition that it could be used for precise ignition control. For the temperature, however, there seems to be a clear trend with earlier ignition with higher temperatures. Also, all ignition timings seem to be confined in a tight cloud, which becomes even tighter with higher temperatures. This implies that ignition ranges become tighter at higher temperatures, with less variability and higher variability at lower temperatures, such that the influence of the other three variables becomes more influential with lower in-cylinder temperatures. This might be a key factor for cycle-to-cycle variability in HCCI.
The following figure 9.17 shows a plot of the distribution of the ignitions as histograms.

Here it can be seen that from a range of thousand samples, more than 30% are far beyond 360 degrees(TDC), which implies misfire. Normally, an ignition timing before TDC is desired for a stable ignition range.

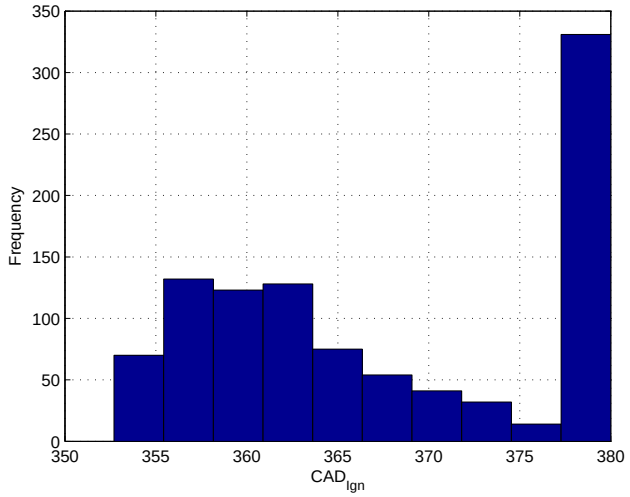

Figure 9.17: Histogram of the frequencies of ignition points

In this plot, it is also shown that a peak gathers around TDC, but with occurrences less than 15%.
With the results from the sensitivity analysis and the scatter plot in mind, it may be clear that tightening the temperature range alone would prevent misfires, while the other variables are neglected.

In a second analysis, the temperature has been confined to a range between 850K and 870K for $20deg$ BTDC, while the ranges of the other variables remained as before.
After narrowing the temperature range, the following results were obtained:

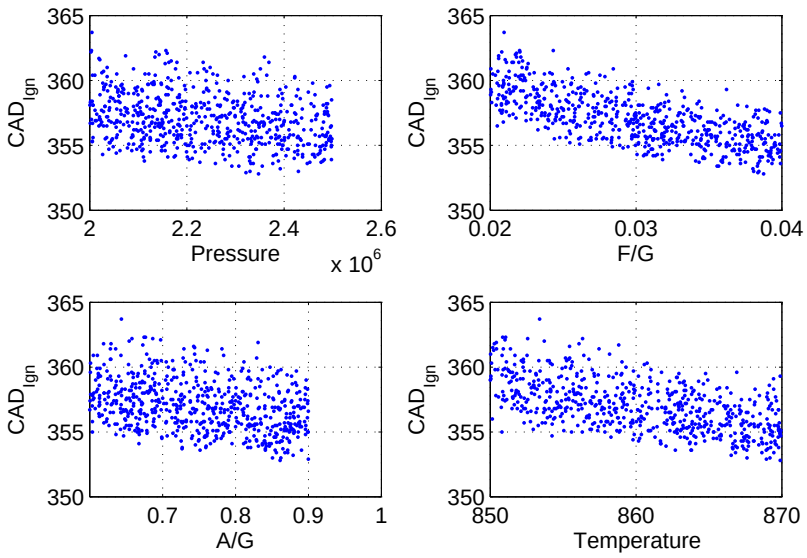

Figure 9.18: Scatter Plot for Ignition with tighter temperature range

Here, a clear accumulation before TDC can be seen, and no case of misfire can be found.

Also, unlike the previous analysis, a clearer trend for all four variables can be seen such that the ignition is more advanced the higher the respective value is. Hence, all four variables show a negative trend with higher values.
Although in a real engine, or engine simulation, all four variable are somewhat interconnected to each other (e.g. higher temperature causes higher pressure), this influence could be excluded in this analysis by using the Monte-Carlo approach. The distribution of the ignition was found as shown in figure 9.17.

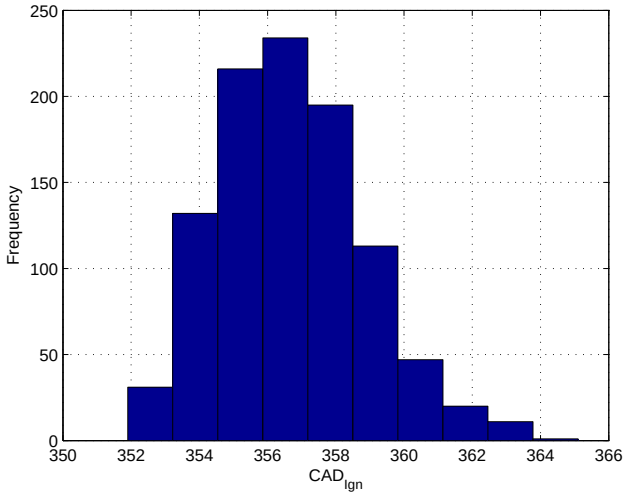

Figure 9.19: Histogram of frequencies of ignition points at tighter in-cylinder temperature range

In this plot, a peak of more than 20% occurrences are gathered before TDC, which is a fairly desirable ignition timing. The latest ignitions were found at values smaller than 366 deg CAD, and with a frequency close to zero.

These analyses demonstrate the necessity of precise temperature control during stark HCCI transients, such as a switch, and it seems obvious that temperature cannot be compensated with other measures at all. However, NOx has not considered, which is abundant during SI combustion and in the last SI cycle before the switch.
With these observations, it becomes obvious that control actuators for control of in-cylinder temperature are vital for the switch.
In case of BDSC, these actuators may be:

- Exhaust throttle
- External (Cooled) EGR
- Secondary air injector
- Direct Injection (Fuel evaporation)
- Variable Valve Lift for EGR

Although in NVO HCCI, direct injection timing is a powerful combustion phasing actuator and helps greatly during the combustion mode switch (e.g. [100]), BDSC has not been found

suitable for direct injection due to the necessary higher exhaust pressure to compensate for the charge cooling from evaporation. Hence, direct injection timing as a control knob is excluded for BDSC HCCI.
Variable valve lift for the exhaust re-breathing seems to be a feasible control actuation for controlling the amount of exhaust during the switch effectively. A fully flexible and cylinder-individual actuator, however, would require a sophisticated and expensive electromagnetic or hydraulic valve system. Fully mechanical systems may be an option, but since the engine is equipped with a Honda VTEC system only, the focus in this work is on fuel injection mainly for $IMEP$ control, the exhaust throttle and the actuation of the EGR lift, where for demonstration purposes, a fully flexible lift will be considered as well. All other actuators have been excluded.

To demonstrate the considerations above, a combustion mode switch has been tested with the BOOST model, of which a "hard switch" is performed, where it is directly switched into HCCI with no further combustion control. In comparison with that, a more elaborate actuation, where it was aimed to keep the in-cylinder temperature in a confined range.
Figure 9.20 shows the considered combustion mode switch actuation.

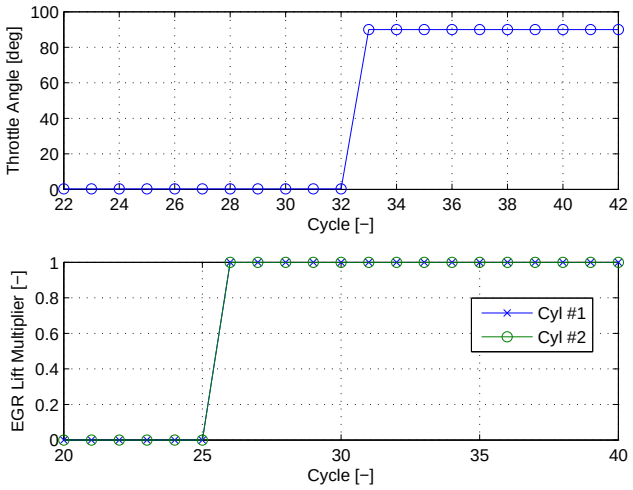

Figure 9.20: Direct Switch from SI to HCCI - Inputs

This figure shows that the exhaust valve lift opens in one cycle, which was assumed possible with the employed Honda VTEC system. Furthermore, the intake-throttle opening is shown, where it is obvious that the throttle opens a few cycles later, such that less fresh air is inducted into the cylinders and more EGR can subsequently enter the cylinders. This leads to extremely high temperatures, and according to the observations above, should lead to extremely early combustion.
This can be confirmed in the figure 9.21, which shows the combustion phasing in the first plot as CA_{50}, the in-cylinder temperature at 20deg BTDC and the air/fuel ratio for the two cylinders.

Here, extremely high temperatures, which exceed 2000K and almost reach 2500K in the first HCCI cycle, can be seen, which lead to extremely early combustion at less than 20deg BTDC. Such high temperatures not only cause early ignitions but may also increase NO_x emission due to the extremely high combustion temperatures. Therefore, it is clear that this temperature

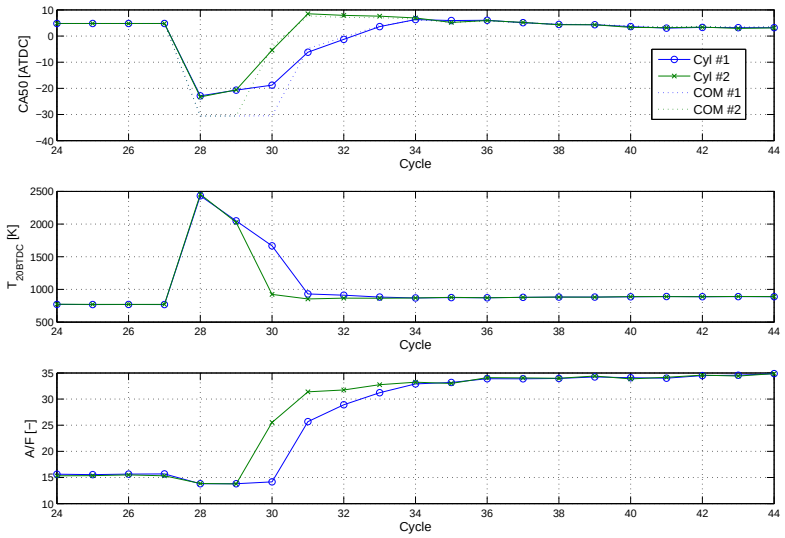

Figure 9.21: Direct Switch from SI to HCCI - Outputs

stems from the combustion event itself. The temperature settles within three cycles towards its final steady-state point, while at the same time, the air/fuel ratio rises due to the increased intake manifold pressure. Therefore, the fall of the in-cylinder temperature is caused by a mix of the increased fresh air and lowering exhaust temperatures due to the increased dilution with not only air, but also with EGR.

In order to keep combustion phasing in a desired phasing, it is assumed that the temperature needs to be controlled. Since both cylinders have shown different combustion phasings, which may be due to the different fresh air dynamics of the intake flows, it was decided to compensate for both separately by controlling each cylinder individually.
Here, a fully variable EGR valve lift has been chosen for its simplicity when tuning the combustion mode switch.
By keeping the lift open but low, less EGR flows into the cylinder, and the temperatures in the cylinders are kept low. As such, the fuel should ignite later.
Such an actuator was implemented into the engine model, and tested for the combustion mode switch.

The actuation for the switch is shown in figure 9.22, which shows that the EGR valve lift are opened gradually and not rapidly within one engine cycle as in the previous test. This figure also shows that the intake throttle was actuated with the same timings as before, such that the first HCCI cycle would be operated with less air so that more EGR could potentially enter the cylinders. However with the reduced valve lift in the first two cycles, this EGR mass-flow has been restricted so that the in-cylinder temperatures should be limited too. This can be seen in the second plot of the second figure 9.23 where it shown that the in-cylinder temperature has been kept on a level close to the desired steady state value. This has kept combustion in a desirable range of after TDC but before 10deg ATDC for CA_{50}. The EGR valve lifts for subsequent cycles have been tuned in a similar way to keep temperature and combustion phasing in the

required range, such that the overall combustion mode switch could be improved.
Although it may be said that the switch can be more optimized by fine-tuning the valve lifts, it should be emphasized that this is a time-consuming task on a simulation model that was not designed for control but rather a faster simulation model, or directly on the real target engine.

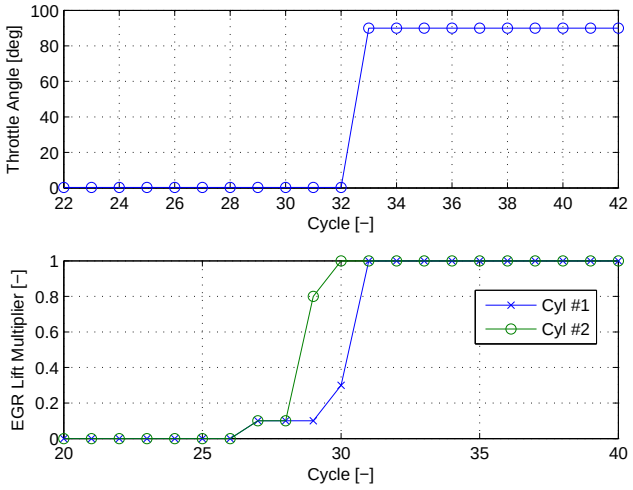

Figure 9.22: Complex-Actuated Switch from SI to HCCI - Inputs

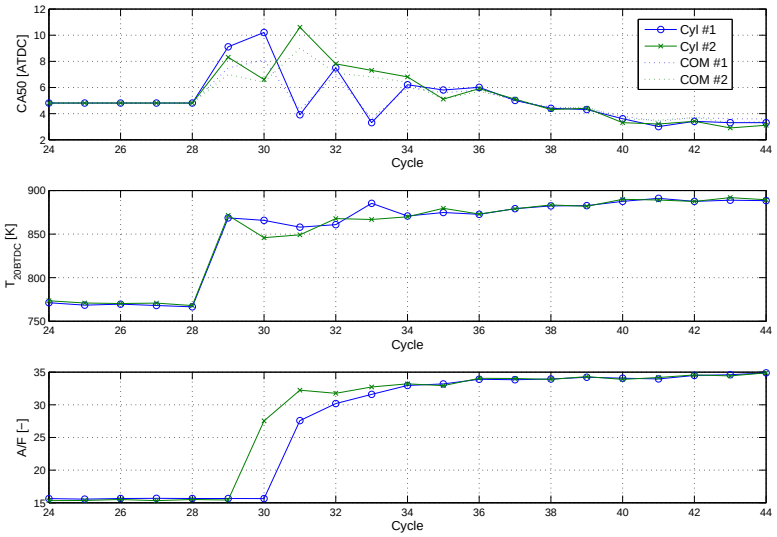

Figure 9.23: Complex-Actuated Switch from SI to HCCI - Outputs

The findings above have lead to another idea to compensate for the extremely high temperatures by utilizing cold EGR to replace hotter EGR from the re-breathing stroke. Since the re-breathing occurs well after the intake stroke, the idea is to fill the cylinders with additional EGR, either by replacing some of the air, or by boosting EGR additionally to the air. The first approach would increase the heat capacity of the mixture, while the second one would also achieve this, and additionally, would increase dilution due to higher in-cylinder mass before

EGR re-breathing.
The idea behind this concept is depicted in figure 9.24.

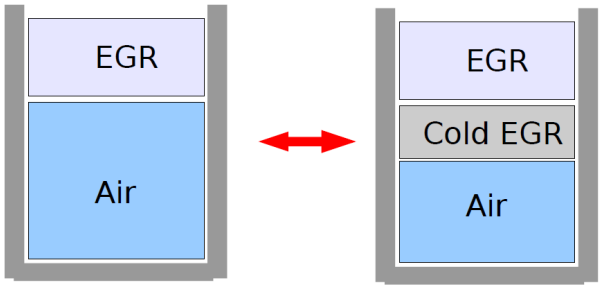

Figure 9.24: Schematic of the idea behind introducing cold (external) EGR

For that reason, it was suggested to equip a BDSC HCCI engine an external low-pressure EGR loop to release EGR into the intake manifold. However, since the exhaust manifold is throttled to higher pressures, this feature could be utilized for a high-pressure EGR concept instead. An inter-cooler, as depicted in this figure would cool the hot exhaust gases before entering the intake manifold.
A suitable EGR-release timing before the switch would compensate for possible slow EGR dynamics.

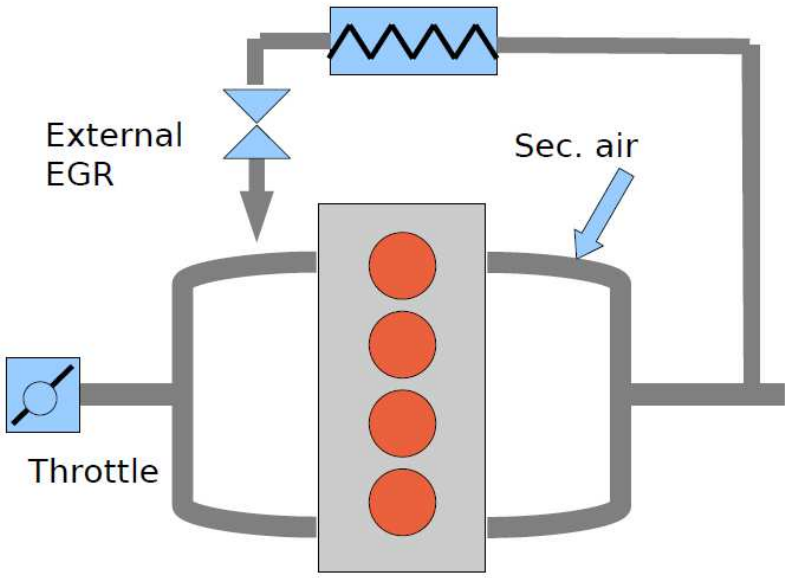

Figure 9.25: Cold EGR Engine schematics

Direct Combustion Mode Switch from SI to HCCI - Avoiding the Unstable Combustion Area

Common NVO HCCI engines have been reported to transverse an unstable combustion area between SI and HCCI where none of these combustion modes can be operated under stable conditions. Since stable combustion control in this region may be difficult to realize, the idea of directly switching into HCCI by skipping the unstable area has been suggested. Figure 9.26 shows this switching idea where a direct switch from SI to HCCI without traversing the unstable area implied by a red arrow and in comparison with the strategy proposed by [72] for NVO systems.

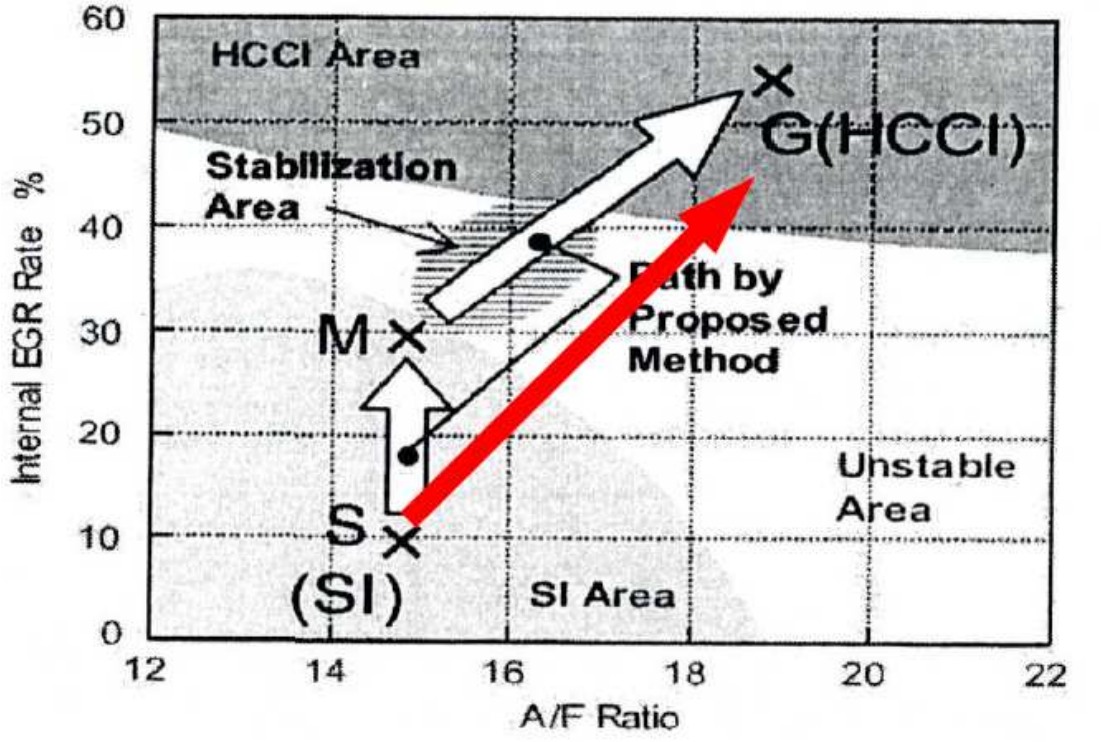

Figure 9.26: Idea of direct switch in comparison to method of Hitachi [72]

By assuming that the EGR valve lift, based on the Honda VTEC system, can be fully opened or closed within one cycle, it may be considered possible to switch to HCCI within one cycle. This is different from conventional mechanical NVO systems, which have some slower response time, and where a direct switch may be more difficult. Driving through the unstable area, in which a hybrid combustion of SI and simultaneous HCCI (Spark Ignited Compression Ignition - SACI), has been observed requires control competences for SACI. However, control of SACI has been not reported as of yet. Hence, it may be considered that a direct switch to HCCI is easier to control.

However, the observations from the previous section have stated that in-cylinder temperature dynamics need to be controlled after the first HCCI cycle and that the switch is not completed once HCCI combustion has been reached. Therefore, such a direct HCCI switch basically doesn't exist, and pre-switch control as well as post-control must be considered. Pre-switch

might be preparations a few cycles before switching into HCCI, such as cold EGR introduction, as suggested above. Post-switch control is a clearly precise combustion phasing control until steady-state HCCI has been reached. Therefore, the operational areas for SI and HCCI, as shown in figure above 9.26, is measured in steady-state engine conditions, such that the HCCI area is not entirely correct for transient HCCI. Due to the higher temperatures after the switch and its dynamics of several cycles, EGR must be first limited such that the admissible area for EGR is first confined in a small area, which increases with the subsequent cycles, until steady-state conditions are achieved.
This depicted shown in figure 9.27, where a change of the operational map is plotted over time. First, a small HCCI area is depicted, which increases with time.

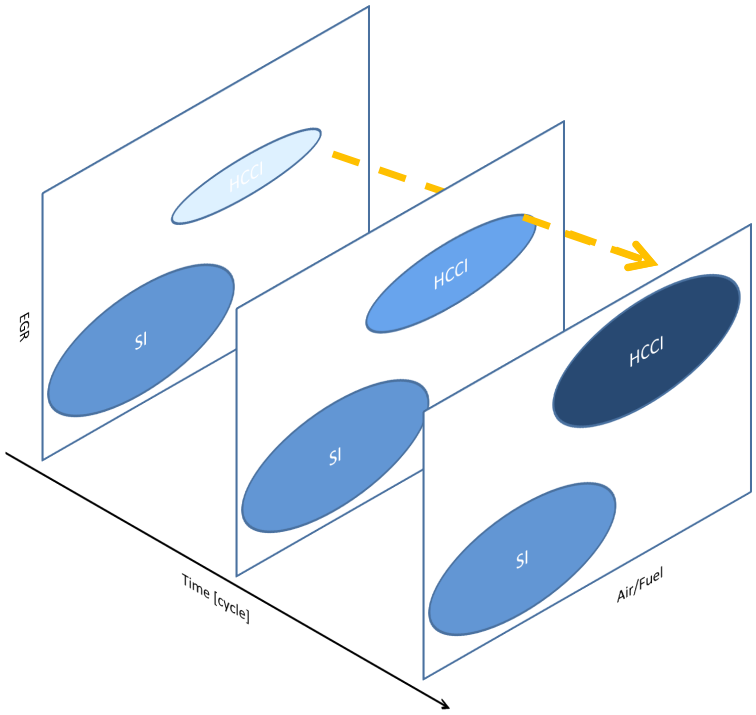

Figure 9.27: Transient HCCI and SI Operation Maps

In case of BDSC HCCI, these transients may even be prolonged due to the slow exhaust manifold dynamics as mentioned and demonstrated in the closed-loop control sections. To compensate for these unwanted dynamics, such a feedback controller can be employed.

Experimental Data of SI-HCCI Switch

Experiments have been conducted and a switch from SI to HCCI analyzed, of which a high load switch with cold EGR will be briefly outlined in this section.
In addition to that, numerical analysis with a 4-cylinder full-engine model with the software GT-Power have been carried out to analyze control strategies for the switch from SI to HCCI whilst keeping the HCCI combustion phase in a desired range.
The open-loop switching control strategy was here to actuate intake and exhaust throttle simultaneously with the aim to keep combustion and combustion phasing in a desired range.
The actuation and results are shown in figure 9.28, which were published in paper [119].
These figures show that the intake and exhaust throttles were actuated rapidly, such that the intake and exhaust pressures could be changed within one engine cycle. The first plot shows the intake pressure and throttle angle, where it can be seen that it is opened as fast as possible, such that the intake pressure reaches atmospheric pressures within one cycle. Simultaneously, the exhaust pressure has been closed before the switch, to increase the exhaust pressure. Obviously, this was done to ensure HCCI ignition in the first cycles, where under unthrottled exhaust conditions, misfire might have been simulated. The exhaust pressure was then opened after the switch to decrease the exhaust pressure in order to bring steady-state HCCI in a suitable range.
Combustion phasings, as shown as CA_{50} in the plots are for first cycles extremely early of less than 15deg BTDC, which may be attributed to the extremely high exhaust pressure before the switch, which was found here close to 2bar.
Although it was stated that in the paper that too early combustion was found, it remains unclear whether reduced exhaust pressure before the switch would lead to a more acceptable combustion phasing. In fact, if under unthrottled exhaust conditions before the switch, misfire would occur, then a switching strategy with the exhaust throttle actuation only would be theoretically possible.

Together with this numerical analysis, experiments have been carried out as well, which were reported in [5]. Here, intake- and exhaust throttle actuation was utilized, but since even ignition was observed even for unthrottled exhaust conditions before the switch, combustion was deemed too difficult to control, and cooled external EGR was introduced in the intake manifold, as suggested in a previous section.
The figures 9.31, 9.29, 9.32, and 9.30 show the results of these experiments. The results of CA_{50} show, despite of strong cyclic variations, a fairly smooth transition, where it is also shown that without ignition timing control, ignition would gradually move to unwanted earlier phasings. To overcome this, the exhaust throttle was opened in open-loop and exhaust pressure decreased to bring back combustion phasing to desired values of around 10deg ATDC.

To suggest switching improvements and increase of switching robustness despite of disturbances, the following section will introduce closed-loop switching considerations in simulation.

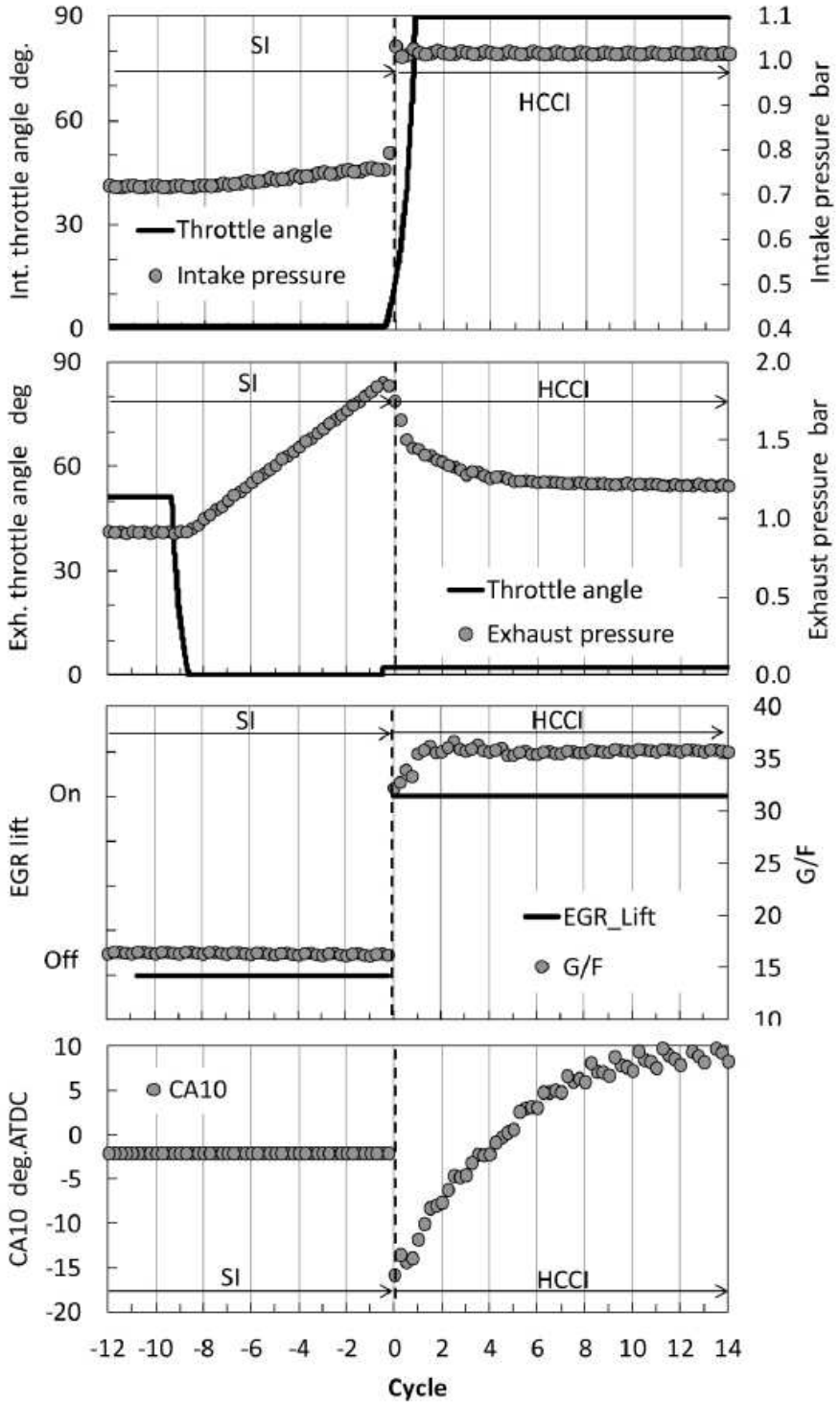

Figure 9.28: Simulation Results of the switch from SI to HCCI with GT-Power ([119])

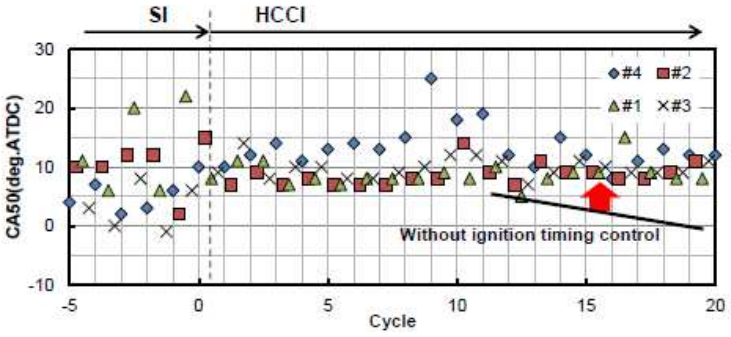

Figure 9.29: Experimental Data of Switch including cold EGR and open-loop exhaust throttle actuation - CA_{50}

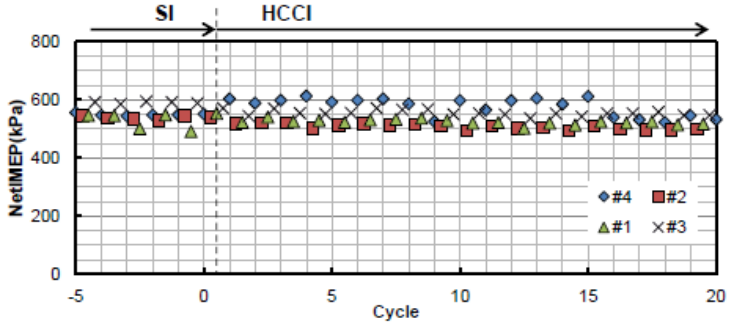

Figure 9.30: Experimental Data of Switch including cold EGR and open-loop exhaust throttle actuation - $IMEP$

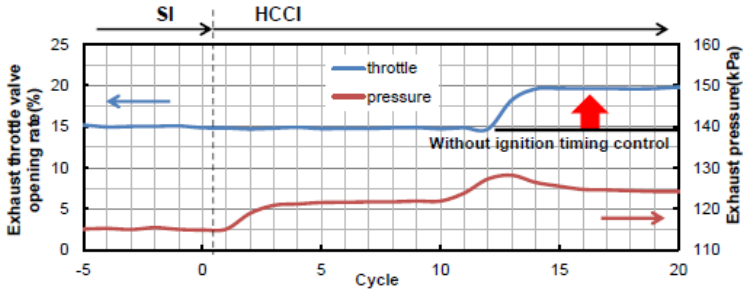

Figure 9.31: Experimental Data of Switch including cold EGR and open-loop exhaust throttle actuation - Exhaust Pressure

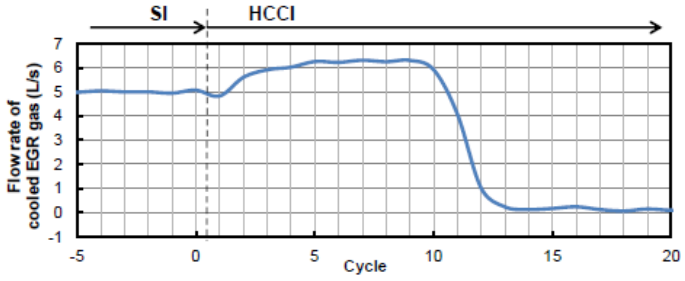

Figure 9.32: Experimental Data of Switch including cold EGR and open-loop exhaust throttle actuation - Cold EGR Introduction

9.3.1 Closed-Loop Switch Control with μ control

In this section, the μ controller, as presented in a previous section, is analyzed here for the switch.
As introduced in this section, robust control theory is a fairly new theory which gives a better insight of the control robustness and performance before actual implementation and skips the design of an observer that is usually needed for state feedback. This overall makes control design very convenient and is the motivation for analyzing the control performance during the combustion switch.
Therefore, the μ-controller has been implemented here, set to inactive during SI mode, and activated during combustion mode switch. The controller has also been activated one cycle before HCCI, so at the last SI cycle, in order to give the controller authority over the controlled variables, exhaust pressure and IMEP before the switch.
Figure 9.34 shows the open-loop switch for comparison at the selected operating point, which is at $IMEP$ of around 4 bar.

The exhaust pressure here was driven to 1.6 bar, which is fairly high and leads to early combustion in the first HCCI cycles, before combustion converges to a later phasing when the in-cylinder temperatures have been settled. In fact, the exhaust pressure rises here even more, due to the unthrottled HCCI operation, which advances HCCI combustion again. In this trial, CA_{50} has been even found before TDC due to the high exhaust pressure. It is clear that the exhaust pressure needs to be controlled dynamically after the switch in order to avoid this drift to early combustion.

To improve this switch, the μ-controller has been implemented and tuned such that it smoothly controls $IMEP$ and CA_{50}. The goal is hereby to improve the switch by keeping combustion phasing in a particular range, preferably between TDC and around 12deg ATDC. It is also required to keep $IMEP$ robustly near the operating point. This is a major challenge with BDSC since the exhaust pressure changes for control of CA_{50} simultaneously affect $IMEP$ due to the pumping losses.

The controller has been switched on one cycle before the first HCCI cycle, and the reference points were set to $IMEP = 5bar$ and $CA_{50} = 7degATDC$. Since an HCCI feedback signal is not yet available for the first HCCI cycle, an artificial feedback signal was introduced for the first cycle, imitating the early combustion around $CA_{50} = -10degATDC$, while IMEP was set to $5\ bar$. The results of this switch are shown in figure 9.34.
Here, the reaction of the controller can be seen, where it reduces the amount of fuel, possibly as a measure to retard combustion phasing, but especially opens the exhaust throttle rapidly, which causes a pressure drop. As a consequence, $IMEP$ is interrupted a little, but combustion phasing have been shifted to early values ATDC, which is a great improvement to the open-loop switch. Subsequently, combustion phasing moves to later timings before it converges to its designated set-point of 7 degrees ATDC. In order to control out the $IMEP$ interruption, the controller reacts with higher fuel amount. However, due to the rather slow tuning of the controller, it needs a few cycles to settle to its steady-state point.

Overall, the controller is able to control combustion phasing and $IMEP$ simultaneously, despite of the high transients and disturbances that occur during the switch. It is shown that the switch is completed in about one second.

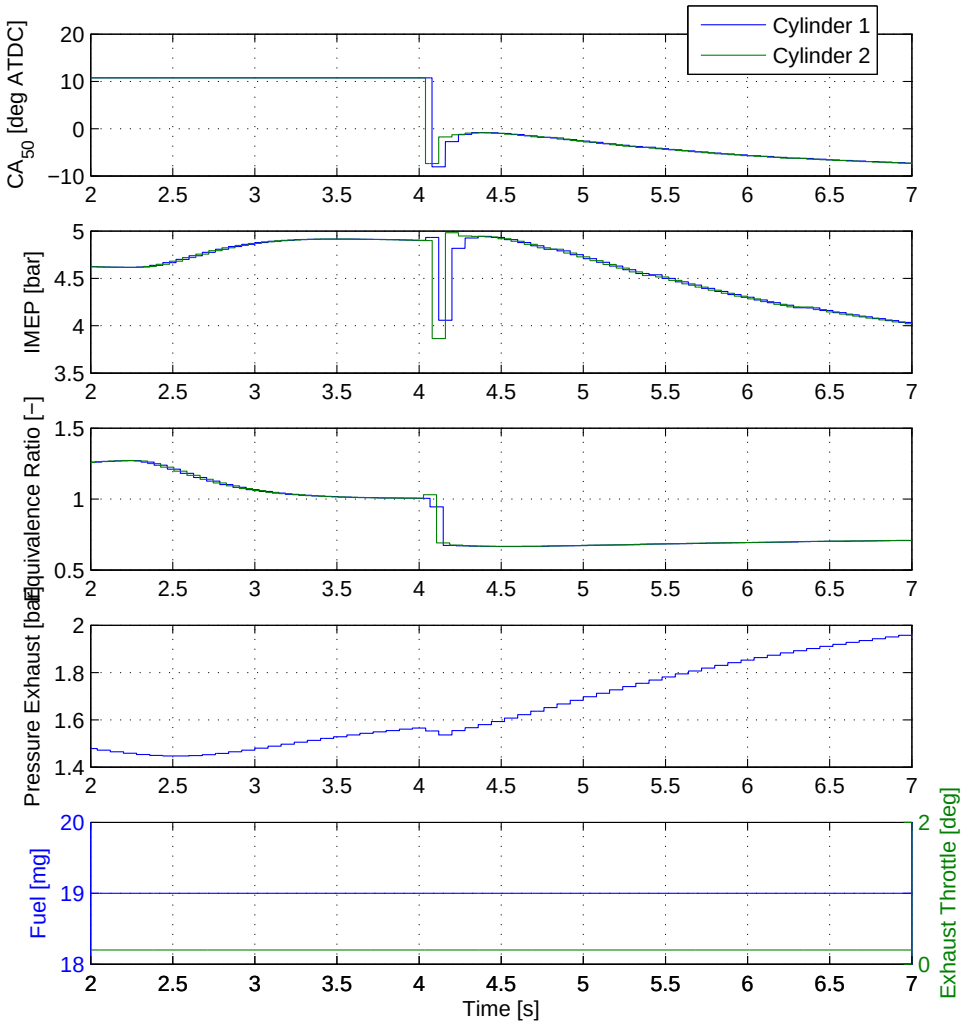

Figure 9.33: Open-Loop switch, with fixed control actuation

Another test has been carried out with the same control strategy but at a lower $IMEP$ of 4 bar and where the first feedback signal for $IMEP$ has been reduced to 4 bar accordingly. The results of this switch are presented in figure 9.36.
Same as with the previous test, the controller opens the exhaust throttle quickly, but hardly changes the amount of fuel injected. CA_{50} has been found here in a favorable range for the first HCCI cycles. $IMEP$ on the other hand make a bigger jump to higher values, which may be due to the de-throttling of the intake with constant amount of fuel injected. As with the previous case, the $IMEP$ deviates to higher values, which may additionally be due to the decreasing exhaust pressure, but it moves back to its set-point of 4 bar within one second.

To avoid the excessive rise of the $IMEP$ rise during the switch, the initial signal feedback signal can be amended. Here, the initial $IMEP$ has been changed to 5 bar instead of the previous 4 bar, which may be justified due to the un-throttling disturbance from the intake, and assuming that during normal combustion, $IMEP$ would increase around this value.

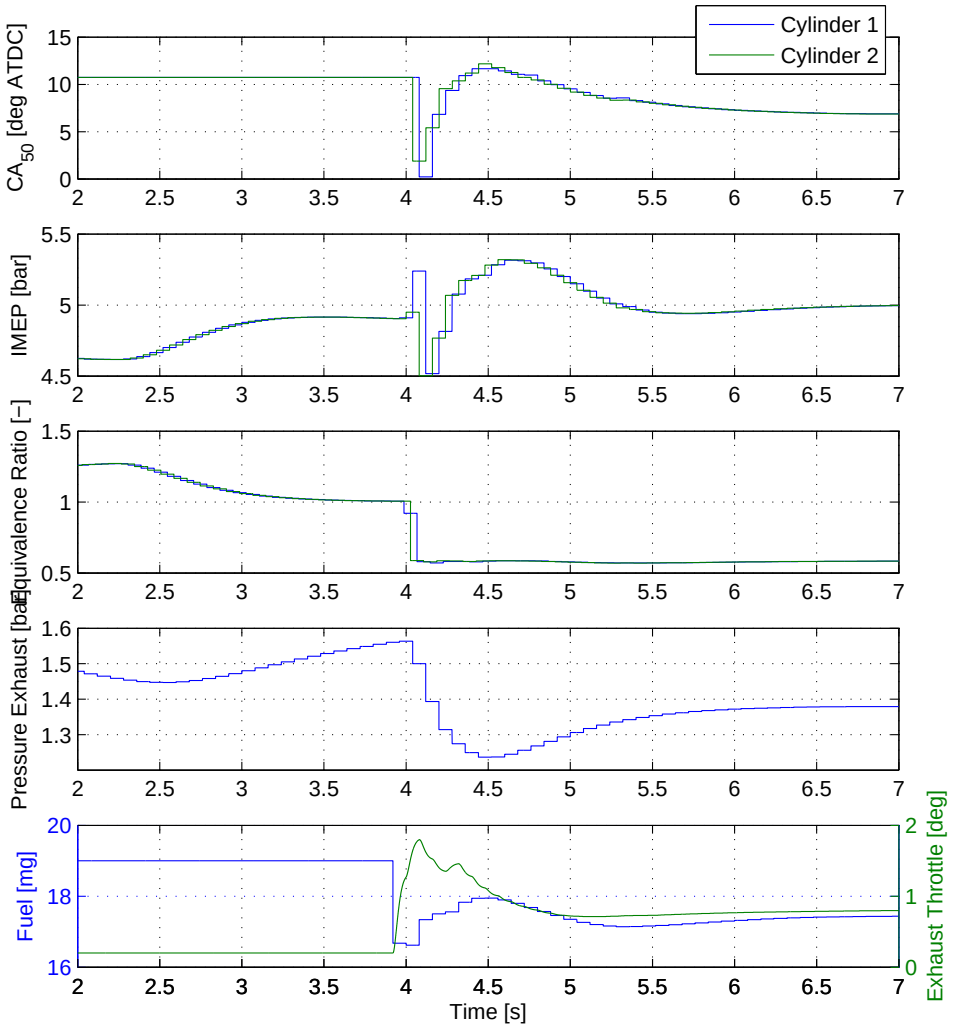

Figure 9.34: Closed-Loop controlled switch with a robust μ controller at $IMEP = 5\ bar$

The results are shown in figure 9.36 which shows a significant improvement, while combustion phasing is hardly affected.

9.3.2 Closed-Loop Switch Control with SMC

In order to make this switch smoother, the sliding mode controller, which was introduced above, was employed in the next switch.
Here, the SI mode was run in open-mode again. The closed-loop controller was then switched on for the first HCCI cycle.
However, a feedback problem exists, since for the first HCCI cycle, the combustion phasing is unknown. For that reason, an artificial state vector was inserted for first HCCI cycle so that the controller can perform properly.
The tracking references were set to a point, close to the linearization point, and in accordance

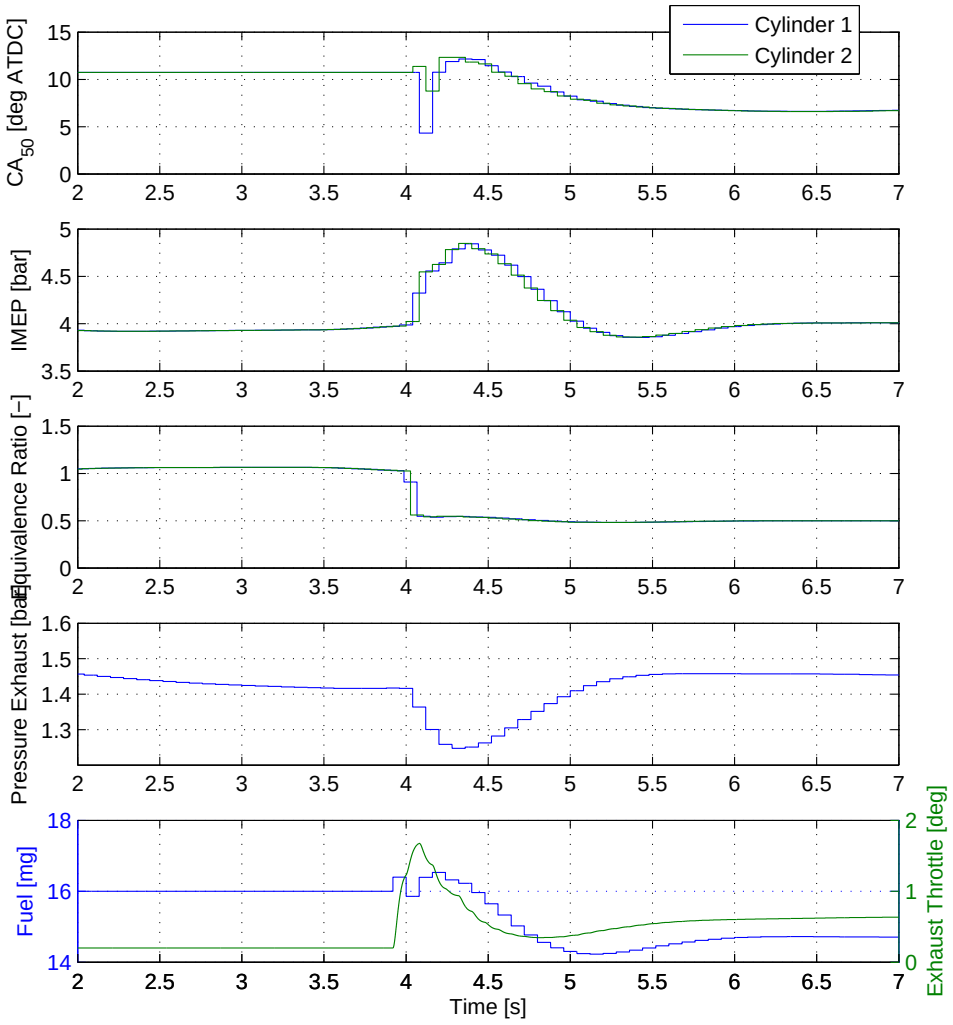

Figure 9.35: Closed-Loop controlled switch with a robust μ controller at $IMEP = 4\ bar$

to the SI $IMEP$. Therefore, the reference is set at $CA_{50} = 8$ and $IMEP$ at 4 bar.
The results of this switch are shown in the following figure 9.37.

In comparison to the open-loop switch, it is evident that the controller effectively controls combustion phasing and the power output. The controller first opens the exhaust throttle in order to delay combustion but also increases the amount of fuel injected for two cycles to meet the $IMEP$ demand. Thereby, $IMEP$ goes back to its reference values, with some minor overshoots before it completely settles.
At the same time, combustion phasing first undershoots for one cycle, before it jumps up to its required value, where it remains. After roughly half of a second the controller converges slowly to a steady-state value, which takes several seconds due to the slow integral part of the controller.
Both, CA_{50} and $IMEP$ remain fixed, while the exhaust pressure has been automatically adjusted to meet the tracking demands.

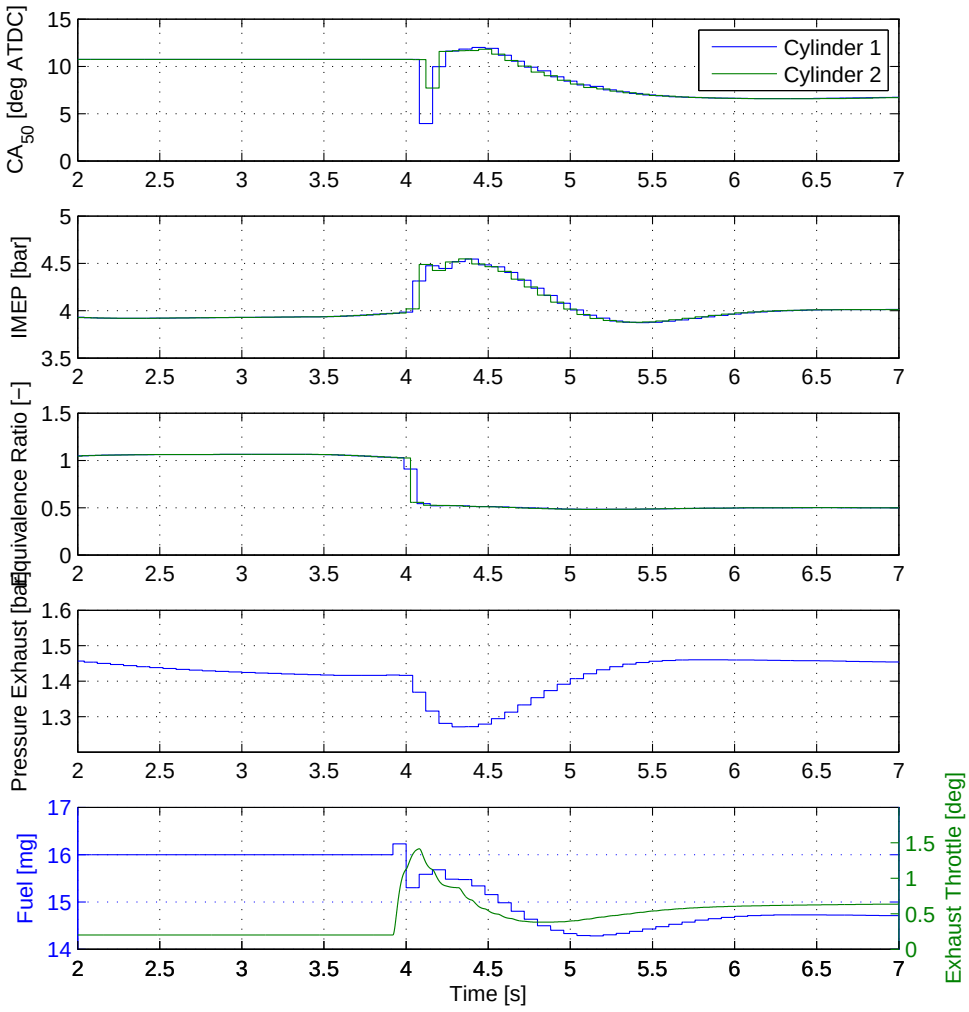

Figure 9.36: Closed-Loop controlled switch with a robust μ controller at $IMEP = 4\ bar$ with adjusted initial feedback signal

This shows the effectiveness and usefulness of a closed-loop control scheme for the combustion mode switch.
In a second trial, the exhaust pressure has been decreased before the switch, and during SI, by opening the angle of the throttle a little bit more.
The results of this switch are shown in the following figure 9.38.

Here, the initial pressure was 0.1 bar lower than before at about 1.4 bar before the switch. As a consequence, the first ignitions are a little later than before, with the next cycles with delayed phasing, which however, are still in an acceptable range. The controller acts quickly and brings back the combustion phasing to its desired value within only a few cycles. This is accomplished by closing the exhaust valve briefly before re-opening to reach a steady-state value.

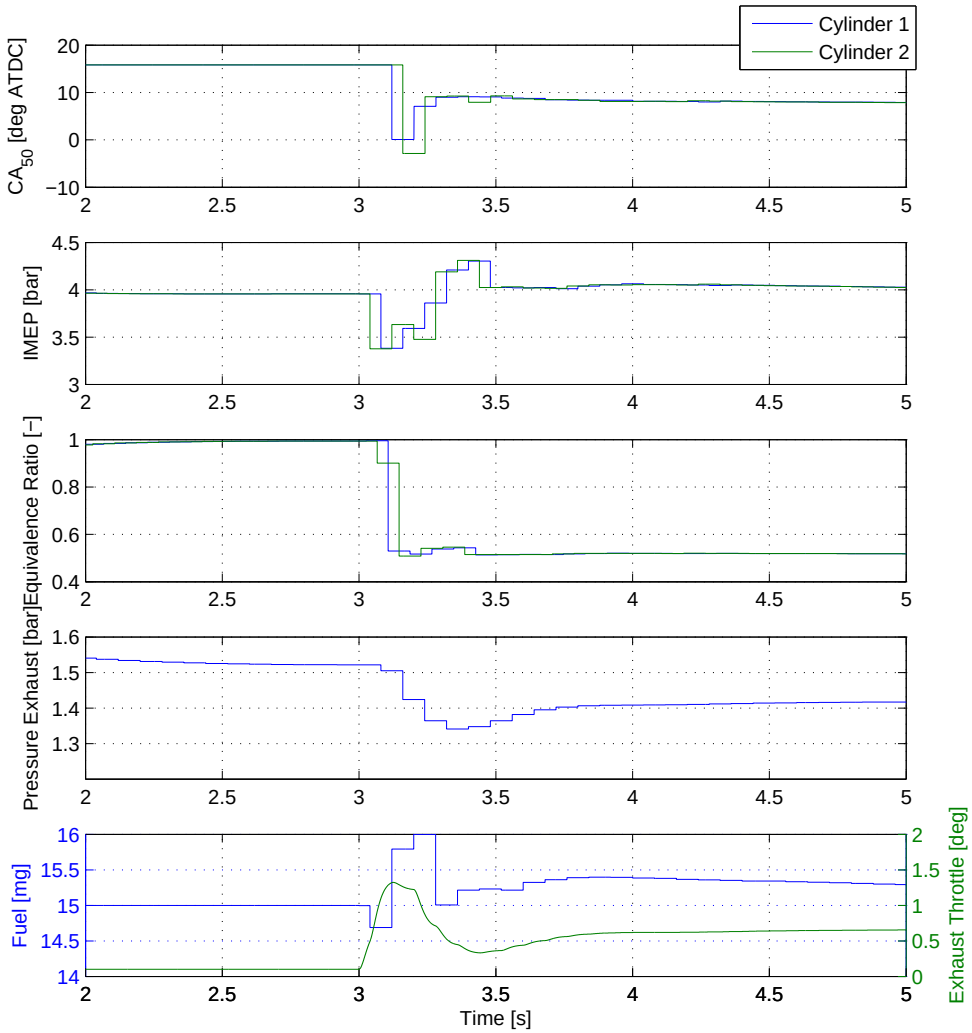

Figure 9.37: Closed-Loop switch with SMC

9.3.3 Concluding Remarks on the Closed-Loop Controlled Switch

In the previous two sections, two control strategies for a smooth switch from SI to HCCI were presented.
Both consisted of a feedback controller that is deactivated during SI but activated for HCCI to control combustion phasing and the $IMEP$ as a proxy for the power output during the combustion mode switch.
A sliding-mode controller (SMC) was tested first, which consisted mainly of a linear state-feedback and a sporadically non-linear switching control that was predominantly switched off. This controller took advantage of the modeling approach, in which the states are essentially measurable and an observer can be omitted. This, however, would require a temperature signal from the exhaust manifold, or a manipulated feedback signal from e.g. the exhaust port. If the engine scheme would not make use of the exhaust manifold for combustion phasing control, but rather other control actuators that act directly on the states $IMEP$ and CA_{50}, such as the

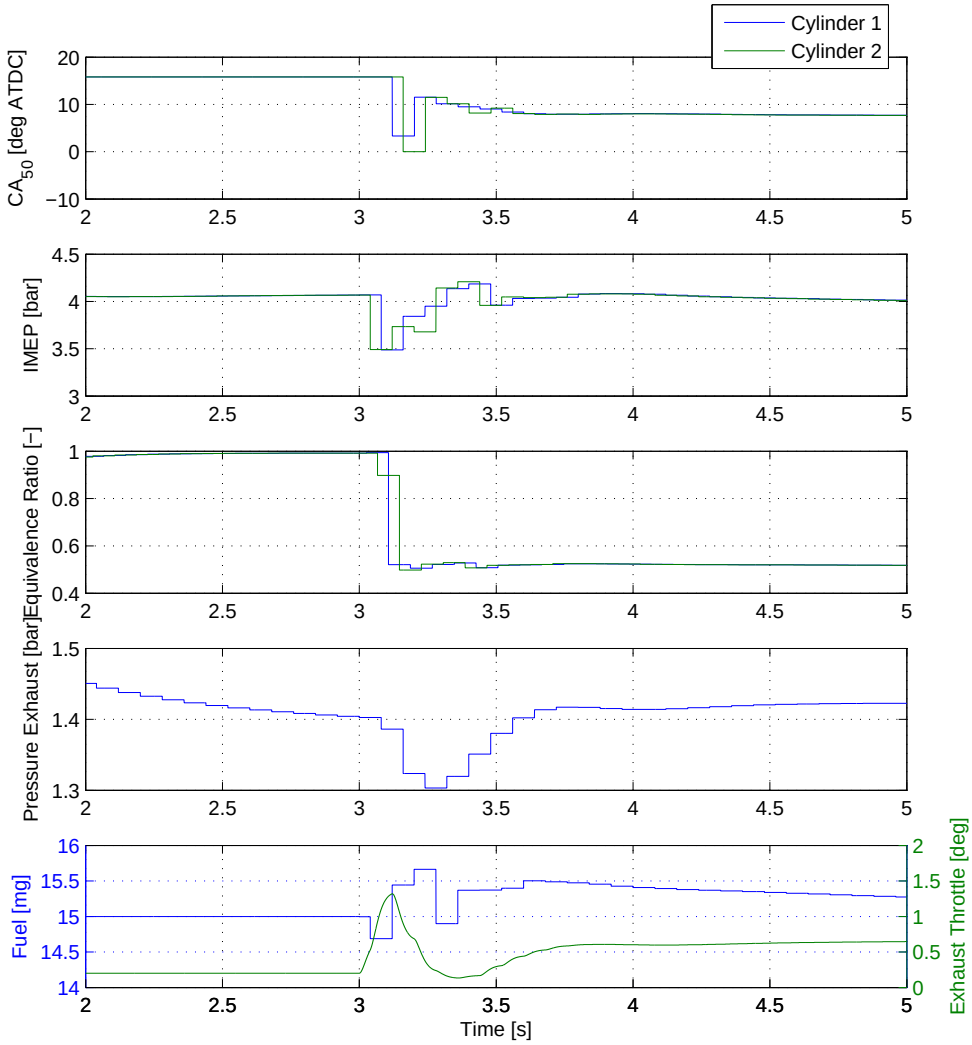

Figure 9.38: Closed-Loop switch with SMC at lower intial exhaust pressure

secondary air and fuel injector.
In comparison to this controller, an H_∞ controller has been designed and employed as an aid for the combustion mode switch. By the nature of this kind of controller, a state-feedback is already included in the overall control scheme, which makes control design convenient. Unlike the SMC presented before, this control requires as a feedback signal only the error vector of the controlled outputs. The design objective can be met by mixed sensitivity design, and with the right choice of the weights for sensitivity function, a suitable controller can be obtained. This controller was utilized for the control of the combustion mode switch as well.

Both controllers have shown a substantial improvement over an open-loop control approach. While the latter could not prevent premature combustion for the first cycle, after which a rather acceptable progression in $IMEP$ and CA_{50}, which however lasted only for a few cycles. After that, due to the increasing exhaust pressure caused the raised intake pressure, the combustion

phasing advances to unwanted values. It is clear that active control, or better closed-loop control is necessary after the switch.

Chapter 10

Conclusion and Outlook

With all the benefits that HCCI provides, there are still some obstacles to be tackled. Extension HCCI to higher speeds and especially to higher loads was the aim of BDSC. However, it did not show any feasible control actuation. While control of $IMEP$ remains at the fuel injection, as in any other combustion engine, CA_{50} can be controlled by exhaust pressure and secondary air injection and indication for cold EGR exist. While the first actuator lowers the efficiency due to increased pumping losses, it is powerful enough to control combustion phasing at a wide range. An additional drawback of this actuation is that it cannot regulate each cylinder individually. This, on the other hand, is possible with secondary air injection. Secondary air injection is a common system which is used during warm-up of the engine. However, it is switched off after this phase. Since pressurized air is injected into the exhaust port, compressing the air costs additional energy. Although this actuator may cover a range of up to 10 degrees in combustion phasing variation, mid-range control becomes difficult, since secondary air can only retard combustion phasing. Hence a mid-point must be maintained by permanently injecting air. Cold-EGR may be considered as an alternative although very little is known about response time properties and it cannot regulate each cylinder individually. While it has shown effective during the combustion mode switch from SI to HCCI, it may be replaced by exhaust pressure actuation during normal BDSC HCCI operation.
While actuation existed, control of a BDSC HCCI engine has been considered as difficult, mainly due to modeling difficulties. Furthermore, attempts were made to use a full-engine 1-D simulation model, built in the commercial code GT-Power by Gamma Technologies, as a model-based control concept for this particular HCCI engine to be made ready for a production ECU.

In response to that, this work suggest control-oriented modeling approaches and feasible control concepts. Here, some tools which a indispensable for control design are introduced. First, to comply with 0-D modeling approaches that a common in control engineering, a 0-D model for the BDSC engine was introduced, which had been extended to be able to simulate the blow-down pressure wave. Comparison with experimental data showed good agreement in the range considered. Although other loads and especially speed ranges were not considered in this work, the model created here proved useful for rapid control testing with control algorithms in a continuous time-domain, which could be directly implemented on a real-engine. Furthermore, it proved useful for gaining information for model-reduction for obtaining a mean-value engine model (MVEM), which was subsequently introduced in this work. For this specific engine

model variant, the inclusion of a pressure wave model for the blow-down pressure was found unnecessary so that the model could be strongly reduced. This helps greatly for initial control testing on a non-linear model due to its high simulation performance and low testing times. Furthermore, since such a cycle-resolved low-order model can be linearized to obtain a state-space description for the BDSC HCCI engine for control design, further simplifications were implemented. First, the ignition model has been reduced to a simple correlation for CA_{50} in dependency of only pressure and temperature. By doing so, additional states could be omitted to reduce the controller order. It was further mentioned that the correlation could be inverted such that from knowing CA_{50} and the in-cylinder pressure at some point in a cycle alone, the temperature at the same point could be back-calculated. Since temperature is the dominant driving force for combustion phasing, it may be intuitive to define it as a state, with the modeling approach introduced above, this state can be converted into CA_{50} instead. This, and by introducing $IMEP$ as an additional state, the two cylinder states are both measurable and an online-estimator can be omitted for those two variables. This, however, is not true for the exhaust states, of which feedback sensing is rather uncommon due to sensor dynamics or production costs.
A parameterization scheme for the given mean-value model was presented, which automatically tunes the model and the unknown parameters for each necessary case. While one set of parameters may cover a wider range of operating points, this may not be possible for all necessary points, especially with respect to the exhaust pressure wave characteristics at different engine speeds. This, however, would not pose a serious problem since parameters for different regions could be stored in look-up tables (LUTs) and changed during simulation according to the operating point.
With this mean-value model, controllers for feedback control of CA_{50} and $IMEP$ were synthesized and tested on a more detailed 1-D engine model on the commercial code BOOST from AVL. Here, it could be shown that the synthesized sliding-mode controller, with a Kalman Filter a feed-forward term for tracking and no switching term employed tracked the combustion phasing step-changes well, while it was not able to keep it at the same phasing when $IMEP$ was changed. It was assumed that this is due to non-linearities of the system, and it was further investigated by testing a robust H_∞ controller, which includes an integral action, and other SMC concepts. Due to the high computations times of the 1-D BOOST model, this analysis was further conducted on the 0-D model.
In this work, it was shown that despite the common notion of a BDSC HCCI being a difficult task to model for control, it has been shown that such a control-oriented model is feasible, and comparisons with reference data have not only proven its potential for accuracy but also showed that the simplified model is able to re-produce the transients, which are important for control design.

In another step of this work, feasible switching control switching strategies for switching between SI and HCCI modes have been discussed and compared to work for other HCCI engine concepts. Here, the idea of a direct switch from SI to HCCI by avoiding hybrid combustion or the unstable area between SI and HCCI, was introduced. For the case of a direct switch into HCCI, it was pointed out that unfavorable combustion due to premature or delayed ignition may cause power output drop, unacceptable audible noise or even misfire. For analyzing the conditions of such abnormal combustion, the ignition model was analyzed and eventually the dominance of temperature for ignition been pointed out. It was thereby concluded that control-

ling the temperature during a combustion mode switch from SI to HCCI can only be successful if temperature inside the cylinder is tightly controlled cycle-by-cycle.
Since open-loop switching strategies may be difficult to find for each single operating point and conditions, closed-loop switches were investigated and promising results could be shown on the 0-D engine model. Although it remains unclear whether the approaches presented here would work alone or need a third actuator, such as the cold-EGR, the control-concept is considered easily extendable by including this additional actuation in the control approach. This could be done by an additional feed-forward term or by extending the control-oriented model to cold-EGR.
The latter is also true for cyclic variation in CA_{50}, where an additional actuator could be added to the already existing model. Although not shown in this work, secondary air has also been tested by including it into the EGR correlation to account for the cooling effects. Thereby, a controller with additional secondary air could be created and tested. If the dominant cause for these variations is understood, these physics could be included in the model as well to obtain a higher order model which is capable of simulating combustion variations.

Although the control approaches shown in this work are considered effective for increasing the operational robustness of a BDSC HCCI and helping bringing this engine closer into production, it is the author's regret that none of these concepts were tested in experiments to find guidelines for further steps in research.

Therefore, the next steps would be testing the controllers in experiments. This is not only for investigating the performance of the controllers but especially for analyzing the robustness features at different operating conditions. Additionally, since the controllers have been only tested in simulation at a certain $IMEP$ range with a pre-defined cam-set and at one engine speed only, it would be useful to test the robustness of the controllers by application at different loads and speeds and to identify the limitation of the controllers.
Once the performance and robustness has been confirmed, it would be useful to implement the closed-loop scheme to simplify the switch from SI to HCCI and to increase the robustness. The same applies to switch from HCCI to SI, where a tight air/fuel ratio control is required and this could be ensured by suitable closed-loop control design as well.
Once a set of closed-loop controllers has been set, a further step would be the development of a supervisory controller which decides the combustion mode switching conditions and timings where a high-frequency switching between both combustion modes should be avoided.

Bibliography

[1] G. K. Fraidl A. Fuerhapter, W.F. Piock. Csi - controlled auto ignition - the best solution for the fuel consumption - versus emission trade-off? In *SAE 2003-01-0754*, 2003.

[2] Melih Cakamakci A. Galip Ulsoy, Huei Peng. *Automotive Control Systems*. Cambridge Press, 2012.

[3] H. Werner M. Schultalbers A. Kwiatkowski, J.P. Blath. Application of lpv gain scheduling to charge cotntrol of a si engine. In *Conference on Computer-Aided Control Systems Design*, 2006.

[4] Stanislav V. Bohac Adam Vaughan. An extreme learning machine approach to predicting near chaotic hcci combustion phasing in real-time. Technical report, University of Michigan, 2013.

[5] Yosuke Akiyama. *Invesitagation of combustion mode switches of a blowdown supercharge HCCI einge (in Japanese)*. Master's Thesis, Chiba University, 2013.

[6] Eitan Tadmor Alexander Kurganov. New high-resolution central schemes for nonlinear conservation laws and convection?diffusion equations. *Journal of Computational Physics, 160, 241?282*, 2000.

[7] Per Tunestål Rolf Johansson Bengt Johansson Anders Widd, Patrick Borgqvist. Investigating mode switch from si to hcci using early intake valve closing and negative valve overlap. In *SAE 2011-01-1775*, 2011.

[8] Rolf Johansson Anders Widd, Per Tunestal. Physical modeling and control of homogeneous charge compression ignition (hcci) engines. In *Proceeding of the 47th IEEE Conference on Decision and Control*, 2008.

[9] Toshio Yamada Norio Uesugi Atsushi Morita, Kiochi Hatamura. A study on hcci (homogeneous charge compression ignition) gasoline engine supercharged by exhaust blow down pressure (third report). *Review of Automotive Engineering 29 (2008) 061-064*, 2008.

[10] Per; Johansson Bengt Aulin, Hans; Tunestal. Control of a turbo charged nvo hcci engine using a model based approach. In *2009 IFAC Workshop on Engine and Powertrain Control, Simulation and Modeling*, 2009.

[11] Janardhanan S. Bandyopadhyay, B. *Discrete-time Sliding Mode Control A Multirate Output Feedback Approach*. Springer, 2006.

[12] Andrej Bartoszewicz. Discrete-time quasi-sliding-mode control strategies. *IEEE Transactions on Industrial Electronics*, 1998.

[13] Alessando Beghi, Lorenzo Nardo, and Marco Stevanato. Observer-based discrete-time sliding mode throttle control for drive-by-wire operation of a racing motorcycle engine. *IEEE Transactions on Control Systems Technology*, 14, 2006.

[14] Ferdinand Svaricek Benedikt Alt. Robust control design for automotive applications: A variable structures control approach. *Challenges and Paradigms in Applied Robust Control*, 2011.

[15] J. Bengtsson, P. Strandh, R. Johansson, P. Tunestal, and B. Johansson. Hybrid modelling of homogeneous charge compression ignition (hcci) engine dynamics - a survey. *International Journal of Control*, 2007.

[16] Johan Bengtsson, Magnus Gäfvert, and Petter Strandh. Modeling of hcci engine combustion for control analysis. In *43rd IEEE Conference on Decision and Control*, 2004.

[17] Rowland S. Benson. *The Thermodynamics and Gas Dynamics of Internal-Combustion Engines, Volume I.* Clarendon Press, 1982.

[18] Daniel Blom, Maria Karlsson, Kent Ekholm, Per Tunestal, and Rolf Johansson. Hcci engine modeling and control using conservation principles. In *SAE Paper 2006-01-1086*, 2006.

[19] Per Tunestal Bengt Johansson Gustaf Sarner Markus Alden Carl Wilhelmsson, Andreas Vressner. Combustion chamber wall temperature measurement and modeling during transient hcci operation. In *SAE 2005-01-3731*, 2005.

[20] Frederick L. Dryer Charles K. Westbrook. Simplified reaction mechanisms for the oxidation of hydrocarbon fuels in flames. *Combustion Science and Technology - COMBUST SCI TECHNOL , vol. 27, no. 1-2, pp. 31-43, 1981*, 1981.

[21] Anna G. Stefanopoulou Chia-Jui Chiang. Sensitivity analysis of combustion timing and duration of homogeneous charge compression ignition (hcci) engines. In *Proceedings of the 2006 American Control Conference*, 2006.

[22] Anna G. Stefanopoulou Chia-Jui Chiang. Sensitivity analysis of combustion timing of homogeneous charge compression ignition gasoline engines. *Journal of Dynamic Systems, Measurement and Control*, 2009.

[23] Mrdjan Jankovic Chia-Jui Chiang, Anna G. Stefanopoulou. Nonlinear observer-based control of load transitions in homogeneous charge compression ignition engines. *IEEE Transactions on Control Systems Technology, Vol. 15, No. 3*, 2007.

[24] Elbert Hendricks Michael Struwe Christian Winge Vigild, Karsten P.H. Andersen. Towards robust h-infinity control of an si engine's air/fuel ratio. In *SAE Paper 1999-01-0854*, 1999.

[25] Elbert Hendricks Michael Struwe Christian Winge Vigild, Karsten P.H. Andersen. Electronic throttle and wastegate control for turbocharged gasoline engines. In *American Control Conference*, 2005.

[26] J.-M. Kang J. A. Eng T.-W. Kuo D. J. Rausen, A. G. Stefanopoulou. A mean-value model for control of homogeneous charge compression ignition (hcci) engines. *Journal of Dynamic Systems, Measurement, and Control; Vol. 127*, 2005.

[27] M. M. Konstantinov D.-W. Gu, P. Hr. Petkov. *Robust Control Design with MATLAB*. Springer, 2005.

[28] Christopher Edwards and Sarah K. Spurgeon. *Sliding Mode Control: Theory and Applications*. Taylor and Francis, 1998.

[29] Li Jiang Erik Hellstrom, Anna G. Stefanopoulou. Reducing cyclic dispersion in autoignition combustion by controlling fuel injection timing. In *IEEE 51st Annual Conference on Decision and Control (CDC)*, 2012.

[30] Li Jiang Erik Hellstrom, Anna G. Stefanopoulou. Cyclic variability and dynamical instabilities in autoignition engine with high residuals. *IEEE Transactions on Control System Technology*, 2013.

[31] Jie Zhang Fang-yi Jiang, Shi-lun Gao. Prototyping hardware-in-the-loop simulation of diesel engine on linux system with automatic code generation. In *SAE 2008-01-1735*, 2008.

[32] D. N. Assanis G. Q. Zhang. Manifold gas dynamics modeling and its coupling with single-cylinder engine models using simulink. *Journal of Engineering for Gas Turbines and Power*, 2003.

[33] Yue-Yun Wang G. Rizzoni, Sergey Drakunov. On-line estimation of indicated torque in ic engines via sliding mode observers. In *Proceedings of the American Control Conference*, 1995.

[34] Weibing Gao, Yufu Wang, and Abdollah Homaifa. Discrete-time variable structure control systems. *IEEE Transactions on Industrial Electronics*, 1995.

[35] Michael L. Workmann Gene F. Franklin, J. David Powell. *Digital Control of Dynamic Systems*. Addison-Wesley, 2001.

[36] J I Ghojel. Review of the development and applications of the wiebe function: a tribute to the contribution of ivan wiebe to engine research. *Int. J. Engine Res. Vol. 11*, 2010.

[37] Peter Miller Robert Norris Anthony Truscott GianCarlo Pacitti, Steven Aphlett. Real-time crank-resolved engine simulation for testing new engine management systems. *SAE Int. J. Passeng. Cars - Mech Syst., Volume 1, Issue 1*, 2008.

[38] Bengt Johansson Goran Haraldsson, Per Tunestal. Transient control of a multi cylinder hcci engine during a drive cycle. In *SAE 2005-01-0153*, 2005.

[39] Bengt Johansson Jari Hyvonen Goran Haraldsson, Per Tunestal. Hcci combustion phasing with closed-loop combustion control using variable compression ratio in a multi cylinder engine. In *JSAE 20030126; SAE 2003-01-1830*, 2003.

[40] Bengt Johansson Jari Hyvonen Goran Haraldsson, Per Tunestal. Hcci closed-loop combustion control using fast thermal management. In *SAE 2004-01-0943*, 2004.

[41] Benoit Bellicaud Guillaume Colin, Yann Chamaillard. Robust control for the air path of a downsized engine. *Journal of Automobile Engineering*, 2011.

[42] Lino Guzella and Christopher H. Onder. *Introduction to Modeling and Control of Internal Combustion Engine Systems*. Springer, 2004.

[43] Simon Regitz Jonathan Etheridge Markus Kraft Hao Wu, Nick Collings. Experimental investigation of control method for si-hcci-si transition in a multi-cylinder gasoline engine. In *SAE 2009-10PFL-0546*, 2009.

[44] Ibrahim Haskara, Cem Hatipoglu, and Ümit Özgüner. Sliding mode compensation, estimation and optimization methods in automotive control. *Springer (Book Chapter?)*, 2002.

[45] K. Hatamura. A study on hcci (homogeneous charge compression ignition) gasoline engine supercharged by exhaust blow down pressure. In *2007-01-1873*, 2007.

[46] X. He, M.T. Donovan, B.T. Yigler, T.R. Palmer, S.M. Walton, M.S. Wooldridge, and A. Atreya. An experimental and modeling study of iso-octane ignition delay times under homogeneous charge compression ignition conditions. *Combustion and Flame*, 2005.

[47] Thorsten Schnier Jihong Wang Guohong Tian He Ma, Hongming Xu. A real-time control oriented hcci combustion model in 4-stroke hcci/si gdi engine and model-based fast calibration development. In *SAE 2012-01-1123*, 2012.

[48] Stefanopoulou A. Vavra J. Babajimopoulos A. Assanis D. Hellstrom, E. Understanding the dynamic evolution of cyclic variability at the operating limits of hcci engines with negative valve overlap. *SAE Int. J. Engines 5(3)*, 2012.

[49] E. Hendricks and S Sorenson. Mean value modelling of spark ignition engines. In *900616*, 1990.

[50] Sarikoc F. Schumann F. Kubach H. et al. Hensel, S. Investigations on the heat transfer in hcci gasoline engines. In *SAE Paper 2009-01-1804*, 2009.

[51] Sarikoc F. Schumann F. Kubach H. et al. Hensel, S. A new model to describe the heat transfer in hcci gasoline engines. In *SAE Paper 2009-01-0129*, 2009.

[52] John B. Heywood. *Internal Combustion Engine Fundamentals*. McGraw-Hill, 1988.

[53] Masahiro Ohba Shigeyuki Hosoe Ferfei Zhang Hiroaki Kuraoka, Naoto Ohka. Application of h-infinity design to automotive fuel control. In *American Control Conference*, 1989.

[54] G. Hohenberg. Advanced approaches for heat transfer calculations. In *SAE 790825*, 1979.

[55] H. Walmsley B. Head G.T. Kalghathi C. Sorusbay H.S. Soyhan, H. Yasa. Evaluation of heat transfer correlations for hcci engine modeling. *Applied Thermal Engineering*, 2009.

[56] Adam F. Jungkunz Jun-Mo Kang J. Christian Gerdes Hsien-Hsin Liao, Nikhil Ravi. Representing recompression hcci dynamics with a switching linear model. In *American Control Conference*, 2010.

[57] Stefen Hui and Stanislaw H. Zak. On discrete-time variable structure sliding mode control. *Systems & Control Letters*, 1999.

[58] Matt Warner Benoit Despujols Iakovos Papadimitriou, John Silvestry. Development of real-time capable engine plant models for use in hil systems. *SAE Int. J. Passeng. Cars - Electron. Electr Syst., Volume 1, Issue 1*, 2008.

[59] Ümit Özgüner Vadim Utkin Ibrahim Haskara. On sliding mode observers via equivalent control approach. *Int. J. Control*, 1998.

[60] R.W. Dibble J. Warnatz, U. Maas. *Combustion, Physical and Chemical Fundamentals*. Springer, 1996.

[61] Bengt Johansson Jan-Ola Olsson, Per Tunestal. Closed-loop control of an hcci engine. In *SAE 2001-01-1031*, 2001.

[62] Julia H. Buckland Ilya V. Kolmanovsky Huei Peng Jessy W. Grizzle Jeffrey A. Cook, Jing Sun. Automotive powertrain control - a survey. *Asian Journal of Control*, 2006.

[63] Nan Jia, Jihong Wang, Keith Nuttall, Jianlin Wei, Hongming Xu, M.L. Wyszynski, Jun Qiao, and Michael J. Richardson. Hcci engine modeling for real-time implementation and control development. *IEEE/ASME Transactions on Mechatronics*, 2007.

[64] Leyi Wang Jing Sun, Yong Wha Kim. Aftertreatment control and adaptation for automotive lean burn engines with hego sensors. *International Journal of Adaptive Control and Signal Processing*, 2004.

[65] Michael Guenthner Joerg Reissing Andreas Mueller Christian Donn Johannes Franz, Frank Schwarz. Closed-loop control of an hcci multi-cylinder engine and corresponding adaption strategies. In *SAE 2009-24-0079*, 2009.

[66] Rolf Johansson, Per Tunestal, and Anders Widd. *Modeling and Model-based Control of Homogeneous Charge Compression Ignition (HCCI) Engine Dynamics*, chapter 6. Springer-Verlag, 2010.

[67] Allen Tannenbaum John Doyle, Bruce Francis. *Feedback Control Theory*. Macmillan Publishing Co., 1990.

[68] John Moskowa John Lahti. Dynamic engine control for hcci combustion. *SAE Int. J. Engines 5(3)*, 2012.

[69] Markus Kraft Hao Wu Nick Collings Jonathan Etheridge, Sebastian Mosbach. A detailed chemistry simulation of the si-hcci transition. In *SAE 2010-01-0574*, 2010.

[70] Jyh-Shin Chen Man-Feng Chang Jun-Mo Kang, Chen-Fang Chang. Concept and implementation of a robust hcci engine controller. In *SAE 2009-01-1131*, 2009.

[71] Zoran Filipi Dennis Assanis Tang-Wei Kuo Paul Najt Rod Rask Junseok Chang, Orgun Guralp. New heat transfer correlation for an hcci engine derived from measurements of instantaneous surface heat flux. In *2004-01-2996*, 2004.

[72] Yamaoka S. Kumano K. Sato S Kakuya, H. Investigation of a si-hcci combustion switching control method in a multi-cylinder gasoline engine. In *SAE 2008-01-0792*, 2008.

[73] Stefan Pischinger Kai Hoffmann-Dirk Abel Karl Georg Stapf, Dieter Seebach. Aspects of gasoline controlled auto ignition - development of a controller concept. *MTZ 04/2009 Volume 79*, 2009.

[74] Hassan K. Khalil. *Nonlinear Systems, Third Edition*. Pearson Education International Inc., 2001.

[75] Susanne Köhl and Dirk Jegminat. How to do hardware-in-the-loop simulation right. In *SAE Paper 2005-01-1657*, 2005.

[76] Uwe Kiencke and Lars Nielsen. *Automotive Control Systems*. Springer, 2005.

[77] V. Krishnaswami, C. Siviero, F. Carbognani, G. Rizzoni, and V. Utkin. Application of sliding mode observers to automobile powertrain diagnostics. In *Proceedings of the 1996 IEEE International Conference on Control Applications*, 1996.

[78] Nakamura Y. Kugimachi, Y. and N. Iida. Model-based combustion control of a hcci engine using external egr and the exhaust rebreathed. In *SAE 2014-32-0079*, 2014.

[79] Xiaoqiu Li and Stephen Yurkovich. Sliding mode control of delayed systems with application to engine idle speed control. *IEEE Transactions of Control Systems Technology*, 9, 2001.

[80] Ångström H. Kalghatgi G. Möller C. Lindström, F. An empirical si combustion model using laminar burning velocity correlations. In *SAE Technical Paper 2005-01-2106*, 2005.

[81] Jan Lunze. *Regelungstechnik 1 - Systemtheoretische Grundlagen, Analyse und Entwurf einschleifiger Regelungen*. Springer, 2004.

[82] Jan Lunze. *Regelungstechnik 2 - Mehrgroessensysteme, Digitale Regelungen*. Springer, 2008.

[83] Uwe Mackenroth. *Robust Control Systems*. Springer, 2004.

[84] Shawn Midlam-Mohler Yann Guezennec-Giorgio Rizzoni Marcello Canova, Renaud Garcin. A control-oriented model of combustion process in a hcci diesel engine. In *2005 American Control Conference*, 2005.

[85] Adam F. Jungkunz J. Christian Gerdes Matthew J. Roelle, Nikhil Ravi. A dynamic model of recompression hcci combustion including cylinder wall temperature. In *ASME 2006 International Mechanical Engineering Congress and Exposition*, 2006.

[86] J. Christian Gerdes Matthew J. Roelle, Gregory M. Shaver. Tackling the transition: A multi-mode combustion model of si and hcci for mode transition control. In *Proceedings of IMECE?04 2004 International Mechanical Engineering Conference and Exposition*, 2004.

[87] Sungbae Park Aleksandar Kojic Jasmit Ahmed Maxim V. Subbotin, Karl Lukas Knierim. Modeling and control of a two stroke hcci engine. In *American Control Conference*, 2008.

[88] Keith Glover Merten Jung. Calibratable linear parameter-varying control of a turbocharged diesel engine. *Transactions on Control Systems Technology, Vol 14, No. 1*, 2006.

[89] David J.N. Limebeer Michael Green. *Linear Robust Control*. Pearson Education, Inc., 1995.

[90] Yasuo Moriyoshi Michael Jagsch, Tatsuya Kuboyama. Control-oriented modeling and model-based control of a blowdown supercharge (bdsc) hcci engine. *JSAE*, 2013.

[91] Tielong Shen Jianqiu Li Munang Hong, Minggao Ouyang. Model-based pi feedback control of engine torque. In *International Conference on Control and Automation*, 2010.

[92] Jung D. Nakamura, Y. and N. Iida. Closed-loop combustion control of a hcci engine with re-breathing egr system. *SAE Int. J. Engines 6(4)*, 2013.

[93] Daniel L. Flowers Francisco Espino-Loza Miroslav Krstic Nick J. Killingsworth, Salvador M. Aceves. Hcci engine combustion-timing control: Optimizing gains and fuel consumption via extremum seeking. *IEEE Transactions on Control Systems Technology, Vol. 17, No. 6*, 2009.

[94] Luca Carmignani Stefano Di Palma Nicolo Cavina, Francesco Migliore. Development of a control-oriented engine model including wave action effects. In *SAE 2009-24-0107*, 2009.

[95] Adam F. Jungkunz Chen-Fang Chang-Han Ho Song J. Christian Gerdes Nikhil Ravi, Hsien-Hsin Liao. Modeling and control of an exhaust recompression hcci engine using split injection. *Journal of Dynamic Systems, Measurement, and Control*, 2012.

[96] Adam F. Jungkunz Christian Gerdes Nikhil Ravi, Hsien-Hsin Liao. Modeling and control of exhaust recompression hcci using split injection. In *American Control Conference*, 2010.

[97] Adam F. Jungkunz J. Christian Gerdes Nikhil Ravi, Matthew J. Roelle. A physically based two-state model for controlling exhaust recompression hcci in gasoline gines. In *International Mechanical Engineering Conference and Exposition - IMECE2006-15331*, 2006.

[98] Hsien-Hsin Liao Adam F. Jungkunz-Chen-Fang Chan Sungbae Park J. Christian Gerdes Nikhil Ravi, Matthew J. Roelle. Model-based control of hcci engines using exhaust recompression. *IEEE Transactions on Control Systems Technology, Vol. 18, No. 6*, 2010.

[99] J. Christian Gerdes Nikhil Ravi, Matthew J. Roelle. Controller-observer implementation for cycle-by-cycle control of an hcci engine. In *International Mechanical Engineering Conference and Exposition - IMECE2007-42371*, 2007.

[100] Joel Oudart Nalin Chaturvedi David Cook Aleksandar Kojic Nikhil Ravi, Michael Jagsch. Closed-loop control of si-hcci mode switch using fuel injection timing. In *ASME 2013 Dynamic Systems and Control Conference*, 2013.

[101] D.E. Foster P. Najt. Compression-ignited homogeneous charge combustion. In *SAE830264*, 1983.

[102] Marco Tonetti Enrico Lanfranco Paolo Fiorani, Agostino Gambarotta. A real-time model for the simulation of transient behaviour of automotive diesel engines. In *SAE 2006-01-3007*, 2006.

[103] Anna Stefanopolou Li Jiang Srinath Gopinath Patrick Gorzelic, Erik Hellstrom. A coordinated approach for throttle and wastegate control in turbocharged spark ignition engines. In *Control and Decision Conference*, 2012.

[104] Anna Stefanopolou Li Jiang Srinath Gopinath Patrick Gorzelic, Erik Hellstrom. Model-based feedback control for an automated transfer out of si operation during si to hcci transitions in gasoline engines. In *ASME 2012 5th Annual Dynamic Systems and Control Conference joint with the JSME 2012 11th Motion and Vibration Conference*, 2012.

[105] S. Pischinger. *Vorlesungsumdruck Verbrennungsmotoren Band II (in German)*. Lecture Material, RTWH Aachen, 2013.

[106] N. ; Oudart J. ; Cook D. ; Doran E. ; Kojic A. ; Pimpare M.; Ravi, N. ; Chaturvedi. Control-oriented physics-based modeling of engine speed effects in hcci. In *Decision and Control (CDC), 2012 IEEE 51st Annual Conference on*.

[107] Gregory P. Matthews Raymond A. DeCarlo, Stanislaw H. Zak. Variable structure control of nonlinear multivariable systems: A tutorial. *Proceedings of the IEEE, Vol. 76, No.3*, 1988.

[108] A. Aldawood S. Mosbach and M. Kraft. Real-time evaluation of a detailed chemistry hcci engine model using a tabulation technique. *Combustion Science and Technology*, 2008.

[109] K. Shoda P Do Jo S. Kato S. Onishi, S. Hong Jo. Active thermo-atmosphere combustion (atac) - a new combustion process for internal combustion engines. In *SAE790501*, 1979.

[110] Zimmer T. Bachhuber M. Scheller M. et al. Schauer, F. Development of a model-based hcci control strategy for an engine with a fully variable valve train. In *SAE 2013-01-1667*, 2013.

[111] Herbert Schuette and Markus Ploeger. Hardware-in-the-loop testing of engine control units - a technical survey. In *SAE Paper 2007-01-0500*, 2007.

[112] Tino Schulze, Markus Wiedemeier, and Herbert Schuette. Crank angle - based diesel engine modeling for hardware-in-the-loop applications with in-cylinder pressure sensors. In *SAE Paper 2007-01-1303*, 2007.

[113] Gegory Matthew Shaver. *Physics-Based Modeling and Control of Residual-Affected HCCI Engines using Variable Valve Actuation*. PhD thesis, Stanford University, 2005.

[114] Gregory M. Shaver, Matthew J. Roelle, and J. Christian Gerdes. Modeling cycle-to-cycle dynamics and mode transition in hcci engines with variable valve actuation. *Control Engineering Practice*, 2006.

[115] J.C. ; Jain P. ; Caton P.A. ; Edwards C.F. Shaver, G.M.; Gerdes. Modeling for control of hcci engines. In *American Control Conference, 2003. Proceedings of the 2003 (Volume:1)*, 2003.

[116] Ian Postlehwaite Sigurd Skogestad. *Multivariable Feedback Control - Analysis and Design*. John Wiley & Sons, 2001.

[117] Jason S. Souder and J. Karl Hedrick. Adaptive sliding mode control of air-fuel ratio in internal combustion engines. *International Journal of Robust and Nonlinear Control*, 2003.

[118] Keith Glover Themi Petridis Stelios Karagiorgis, Nick Collings. Dyanmic modeling of combustion and gas exchange process for controlled auto-ignition engines. In *Proceedings of the 2006 American Control Conference*, 2006.

[119] Koichi Hatamura Toshio Yamada Junichi Takanashi Yasuhiro Urata Tatsuya Kuboyama, Yasuo Moriyoshi. A study of control strategy for combution mode switching between hcci and si with the blowdown supercharging system. In *SAE Paper 2012-01-1122*, 2012.

[120] Roland Karrelmeyer Tobias Nier, Andre Kulzer. Analysis of the combustion mode switch between si and gasoline hcci. In *SAE 2012-01-1105*, 2012.

[121] Vadim Utkin. Variable structure systems with sliding modes. *IEEE Transactions on Automatic Control*, 1977.

[122] Giorgio Rizzoni Vasanth Krishnaswami. Vehicle steering system state estimator using sliding mode observers. In *Proceedings of the 34th Conference on Decision and Control*.

[123] William T. Vetterling Brian P. Flannery William H. Press, Saul A. Teukolsky. *Numerical Receipes in C - The Art of Scientific Computing - Second Edition*. Cambridge University Press, 1992.

[124] G. Woschni. A universally applicable equation for the instantaneous heat transfer coefficient in the internal combustion engine. In *SAE 670931*, 1967.

[125] Schauer F. Yamasaki, Y. and G. Wachtmeister. Development of dynamic models for an hcci engine with fully variable valve-train. In *SAE 2013-01-1656*, 2013.

[126] Nenghui Zhou Tao Chen Hua Zhao Yan Zhang, Hui Xie. Study of si-hcci-si transition on a port fuel injection engine equipped with 4vvas. In *SAE 2007-01-0199*, 2007.

[127] Xiaojian Yang and Guoming G. Zhu. Si and hcci combustion mode transition control of an hcci capable si engine.

[128] Kemin Zhou, John C. Doyle, and Keith Glover. *Robust and Optimal Control*. Prentice Hall, 1995.